Abstract

LI, QIFU. Modeling and Finite Element Analysis of Smart Materials. (Under the direction of Dr. Stefan Seelecke.)

This dissertation consists of two parts, the modeling of piezoceramic (PZT) actuators and the finite element implementation of a shape memory alloy (SMA) model and the subsequent thermo-mechanically coupled multifield analysis of several devices, such as tensile wire and cantilever beam actuators. Both models are based on similar free energy expressions and allow for a unified treatment of a number of active materials.

PZT actuators have been widely used in positioning applications due to their high bandwidth, high resolution, compact and light weight characteristics. However PZT materials also exhibit some inherent undesirable nonlinear effects like hysteresis, creep and frequency dependent response. To improve the performance of PZT actuators, these effects need to be taken into account. In this dissertation, based on a free energy model for perfect single crystal PZT materials and motivated by its extension to homogenized model for polycrystalline materials, a parameterization method is developed to model the hysteresis behaviors of polycrystalline PZT materials. In the parameterization method, the effective barrier is assumed to be a function of the phase fraction. Major loop effective barriers are identified from experimental polarization-electric field diagrams as functions of the phase fraction. Minor loops are constructed by major loops using a linear mapping method and a bookkeeping algorithm. A robust algorithm, which preserves the simple structure and efficiency of the original perfect single crystal model, is implemented to simulate the rate dependent minor loop behavior of the PZT materials and compared to experimental data.

Shape memory alloys (SMAs) represent another type of smart materials that have been extensively used in many engineering applications due to their unique material properties, and new devices like SMA microactuators are constantly being developed. To facilitate these new development, an efficient computational tool like the finite element method has to be used in order to simulate the highly nonlinear, load-history and temperature dependent responses of SMA materials. In this dissertation, a 1-D free energy SMA model is

implemented into the finite element software package FEMLAB using its general PDE form by treating the evolution equations of phase fractions as degenerated PDEs coupled with the mechanical equilibrium equation and the heat transfer equation. First, without including the latent heat effect and neglecting the heat transfer equation, simulations are conducted for SMA bars to demonstrate that the model can predict the low temperature quasiplastic and high temperature superelastic behaviors as well as shape memory effect.

The finite element implementation is then expanded by including the nonlinear transient heat transfer equation with the phase transformation induced latent heat as a coupling term. In contrast to the so-called staggered iteration approach, where the individual fields are solved for in a decoupled way within an iteration, FEMLAB allows for a fully coupled solution. This approach generally provides for a robust and efficient solution even in the case of strong coupling between the fields. A number of different applications are then studied for the first time using such a coupled multi-field approach. The particular focus is on the effects of inhomogeneous fields and the strong coupling between thermal and mechanical fields. Tensile simulations of an SMA wire under different thermal boundary conditions with different loading rates are conducted to demonstrate the inhomogeneity and rate effects of the system responses. By including the Joule heating, the performance of an SMA wire actuator under different thermal boundary conditions is studied.

The 1-D free energy model is also implemented into FEMLAB to study the inhomogeneous SMA beam bending problems by using the Euler-Bernoulli beam bending theory. The SMA beam bending problem is modeled as a system of first order PDEs and boundary conditions are implemented as Dirichlet boundary conditions. Detailed analysis is presented for inhomogeneous bending behavior of an SMA cantilever beam under constant temperatures and thermo-mechanical loading, respectively. The rate-dependent responses of an SMA cantilever beam due to strong thermo-mechanical coupling are also studied. Finally, using traditional incremental finite element method, the 1-D free energy model is also implemented into the finite element program ANSYS using its BEAM188 element and the user defined material subroutine USERMAT, which also serves as a validation tool for the FEMLAB implementation. Convergence behavior is studied systematically.

Modeling and Finite Element Analysis of Smart Materials

by

Qifu Li

A dissertation submitted to the Graduate Faculty of
North Carolina State University
in partial fulfillment of the
requirements for the Degree of
Doctor of Philosophy

Mechanical Engineering

Raleigh

August 2006

Approved By:

Dr. Gregory D. Buckner	Dr. Clement Kleinstreuer
Dr. Stefan Seelecke Chair of Advisory Committee	Dr. Ralph C. Smith

To my wife, *Bei Lu*

Biography

Qifu Li was born on October 1 1975, in Guangxi, China. He received his BS and MS degrees from the Aerospace Engineering and Mechanics Department at Harbin Institute of Technology, China, in 1997 and 1999, respectively. He enrolled in the graduate school at NC State University in the spring of 2003, to pursue his Ph. D degree in Mechanical Engineering.

Acknowledgments

I would first like to express my deepest appreciation to my advisor, Dr. Stefan Seelecke, for all his support, encouragement, and guidance throughout this research. It has been an honor and a pleasure to work with you.

I would also like to thank my committee members, Dr. Gregory Buckner, Dr. Clement Kleinstreuer and Dr. Ralph Smith, for being on my committee and supporting me. Additionally, I would like to take this opportunity to thank Dr. Fen Wu for supporting my first year of study.

I would like to thank my fellow graduate students, Alex York, Davis Brian and Matthew Pausley. You guys are great! A special thank you goes to Alex for helping me to correct some typos and errors in the first part of this dissertation.

Last but not least, I want to thank my wife, Bei Lu. Thank you for your constant support and encouragement. You have always been my relief during the toughest of my times.

Table of Contents

List of Figures **vii**

1 Introduction **1**
1.1 Motivation and Objectives 1
1.2 Background 2
1.2.1 PZT Modeling 2
1.2.2 SMA Modeling and Finite Element Simulations 3
1.3 Dissertation Outline 6

2 Hysteresis Modeling of PZT Materials **8**
2.1 Free Energy Model for Perfect Single Crystal PZT Materials 8
2.1.1 Free Energy 9
2.1.2 Average Polarization 10
2.1.3 Kinetics of Phase Transformations 11
2.2 Homogenized Energy Model of Polycrystal PZT 12
2.2.1 Stochastic Distributions of Energy Barrier and Internal Electric Field 13
2.2.2 Implementation and Discussion 15
2.3 Parameterization Method 15
2.3.1 Concept of Parameterization: Representative Single Crystal 16
2.3.2 Identification of Effective Barrier $E_c(x_+)$ from Experimental Data . 17
2.3.3 Implementation Details 18
2.3.4 Construction of Minor Loops: Linear Mapping Method 18
2.3.5 Minor Loop Implementation: Book-keeping Algorithm 22
2.4 Simulation Results 28
2.4.1 Rate Effects 28
2.4.2 Minor Loop behaviors 29
2.4.3 Relaxation Behaviors 35
2.5 Summary 35

3 Finite Element Analysis of SMA Components **38**
3.1 Free Energy SMA Model 39
3.1.1 Free Energy 41

3.1.2 Constitutive Stress-Strain Relationship 44
3.1.3 Evolution of Phase Fractions 44
3.1.4 Balance of Internal Energy 46
3.1.5 Summary of Model Equations 46
3.2 Finite Element Analysis of SMA Bars and Wires Using FEMLAB 47
3.2.1 Implementation 49
3.2.2 Quasi-static Analysis without Latent Heat 53
3.2.3 Coupled Thermo-mechanical Analysis 67
3.3 Finite Element Analysis of SMA Beam Bending Using FEMLAB 89
3.3.1 Implementation 93
3.3.2 Inhomogeneous Bending Analysis under Constant Temperatures . . 97
3.3.3 Thermo-mechanical Loading 120
3.3.4 Coupled Thermo-mechanical Analysis 123
3.4 Finite Element Analysis of SMA Beam Bending Using ANSYS 139
3.4.1 Finite Element Implementation 140
3.4.2 Parameter Study 144
3.5 Summary 150

4 Conclusions **152**

List of References **155**

List of Figures

2.1 $PbTiO_3$ cystal lattice cells with positive and negative polarization 9
2.2 (a) Gibbs free energy $G(E, P)$ for increasing field E; (b) P-E diagram for a single crystal PZT with uniform lattice. [25] 10
2.3 (a) Nonuniform PZT lattice structure; (b) Free energies associated with lattice widths (i) and (ii); (c) Variations in hysteresis kernel due to different free energies. [25] 13
2.4 Full loop P-E diagram at the slow rate: $0.05kV/mm/s$ 18
2.5 Identified $E_c(x_+)$ 19
2.6 Identification of P_R and s 19
2.7 Full-loop simulation using the identified effective barrier $E_C(x_+)$ at the slow rate of 0.05 $kV/mm/s$ 20
2.8 Scheme of linear mapping 21
2.9 Scheme of book-keeping algorithm 23
2.10 Iteration scheme for loading direction 27
2.11 Iteration scheme for unloading direction 27
2.12 Block diagram of parametrization method implementation 28
2.13 E vs. t at rates of $0.05kV/mm/s$, $0.5kV/mm/s$ and $5.0kV/mm/s$ 29
2.14 Full-loop P-E responses for different loading rates: (a) simulation; (b) experiment. 30
2.15 Electric field input for the first order reversal minor loops 31
2.16 First order reversal: (a) simulation; (b) experiment. 32
2.17 Electric Field inputs for second order reversal at rates of $0.05kV/mm/s$, $0.5kV/mm/s$, $5.0kV/mm/s$ 32
2.18 Second order reversal: (a), (b) and (c) are simulation responses; (d), (e) and (f) are respective experimental results. 33
2.19 Second order reversal at different rates. 34
2.20 Relaxation simulations for $V_D = 1.0e-21/m^3$ and $\tau_x = 0.2s$: (a)-(c) applied fields at rates of $0.05kV/mm/s$, $0.5kV/mm/s$, $5.0kV/mm/s$; (d)-(f) time responses of the polarization at respecitive loading rates; (g)-(i) P vs. E at different rates 36

2.21 Relaxation experiments: (a)-(c) applied fields at rates of $0.05kV/mm/s$, $0.5kV/mm/s$, $5.0kV/mm/s$; (d)-(f) time responses of the polarization at respecitive loading rates; (g)-(i) P vs. E at different rates 37

3.1 Lattice configurations in austenitic phase A and martenstic twin phases M_+, M_-. 40
3.2 Piecewise quadratic Helmholtz free energy function $\psi(\varepsilon, T)$. 40
3.3 Gibbs free energy landscapes under thermo-mechanical loadings: (a) Under zero stress: temperature induced transformation; (b) At low temperature: stress induced marternsitic transformation; (c) At high temperature: stress induced martensitic transformation. 43
3.4 Material parameters identification through two tensile tests at different temperature T_L and T_U. 43
3.5 Temperature dependent stress-strain relation. 48
3.6 SMA bar 50
3.7 Quasiplasticity at low temperature T=273K: (a) Applied force; (b) Strain distribution along x during the loading process; (c) Strain distribution along x during the unloading process; (d) Global tip force vs. tip displacement; (e) Stress-strain relation at point $x = 0$; (c) Time histories of phase fractions x_+ and x_-. 54
3.8 Superelasticity at high temperature T=353K: (a) Applied force vs. time; (b) Strain distribution along x during the loading process; (c) Strain distribution along x during the unloading process; (d) Global tip force vs. tip displacement; (e) Stress-strain relation at point $x = 0$; (c) Time histories of phase fractions x_+ and x_-. 55
3.9 Shape memory effect (SME): (a) F vs. time; (b) T vs. time; (c). Strain reponse vs. time; (d) Stress-stain relation. 57
3.10 Evolution of phase fractions of shape memory effect (SME): (a) x_A vs. time; (b) x_+ vs. time; (c). x_- vs. time. 58
3.11 Themomechanical coupling with constant mechanical loading: (a) F vs. time; (b) T vs. time; (c) strain vs. time; (d) strain-temperature diagram. 59
3.12 Evolution of phase fractions of themomechanical coupling: (a) x_+ vs. time; (b) x_- vs. time; (c) x_A vs. time; (d) Gibbs free energy landscape favoriting M_+ well. 60
3.13 SMA bar with varying cross-section 61
3.14 SMA bar with varying cross-section at $T = 273K$: (a) Force and displacement vs. time; (b) Force vs. displacement. 62
3.15 Phase fraction evolution of different positions A and B for a SMA bar with varying cross-section at $T = 273K$: (a) x_+ vs. time; (b) x_- vs. time 62
3.16 Stress and strain responses of different positions A and B for a SMA bar with varying cross-section at $T = 273K$: (a) stress vs. time; (b) strain vs. time. 63

3.17 SMA bar with varying cross-section at $T = 350K$: (a) Force and displacement vs. time; (b) Force vs. displacement. 63
3.18 Phase fraction evolution of different positions A and B for a SMA bar with varying cross-section at $T = 350K$: (a) x_+ vs. time; (b) x_- vs. time 64
3.19 Stress and strain responses of different positions A and B for a SMA bar with varying cross-section at $T = 350K$: (a) stress vs. time; (b) strain vs. time. 64
3.20 SMA bar with nonuniform temperature distribution 65
3.21 Displacement response for a SMA bar with nonuniform temperature distribution: (a) Applied tip force and tip displacement vs. time; (b) Applied tip force vs. tip displacement. 66
3.22 Phase fraction evolution of different positions A, B and C for a SMA bar with nonuniform temperature distribution : (a) x_+ vs. time; (b) x_- vs. time 66
3.23 Strain reponse and stress-strain relation of different positions A, B and C for a SMA bar with nonuniform temperature distribution : (a) strain vs. time; (b) stress-strain relation. 67
3.24 Tensile test of SMA wire with controlled displacement. 71
3.25 Tensile test of SMA wire with insulated boundary condtion at temperature $T_0 = 253K$: (a) controlled displacement input; (b) temperature response of the SMA wire; (c) stress response of the SMA wire; (d) evolution of phase fractions x_+ and x_-. 72
3.26 Tensile test of SMA wire with insulated boundary condtion at temperature $T_0 = 333K$: (a) controlled displacement input; (b) temperature response of the SMA wire; (c) stress response of the SMA wire; (d) evolution of phase fractions x_+ and x_-. 73
3.27 Controlled displacement input for three different rates: (a) $\dot{u}(t)/L_0 = 0.7 \times 10^{-4}/s$;(b) $\dot{u}(t)/L_0 = 0.7 \times 10^{-3}/s$;(c) $\dot{u}(t)/L_0 = 0.7 \times 10^{-2}/s$. 74
3.28 Evolution of temperature distribution along the SMA wire for three different loading rates during the loading and unloading processes: (a) and (b) for the loading rate of $0.7\times10^{-4}/s$; (c) and (d) for the loading rate of $0.7\times10^{-3}/s$;(e) and (f) for the loading rate of $0.7 \times 10^{-2}/s$. 75
3.29 Evolution of latent heat distribution along the SMA wire for three different loading rates during the loading and unloading processes: (a) and (b) for the loading rate of $0.7\times10^{-4}/s$; (a) and (b) for the loading rate of $0.7\times10^{-3}/s$;(a) and (b) for the loading rate of $0.7 \times 10^{-2}/s$. 76
3.30 Evolution of phase fraction x_+ distribution along the SMA wire for three different loading rates during the loading and unloading processes: (a) and (b) for the loading rate of $0.7 \times 10^{-4}/s$; (a) and (b) for the loading rate of $0.7 \times 10^{-3}/s$;(a) and (b) for the loading rate of $0.7 \times 10^{-2}/s$. 78

3.31 Evolution of strain distribution along the SMA wire for three different loading rates during the loading and unloading processes: (a) and (b) for the loading rate of $0.7 \times 10^{-4}/s$; (a) and (b) for the loading rate of $0.7 \times 10^{-3}/s$;(a) and (b) for the loading rate of $0.7 \times 10^{-2}/s$. 79
3.32 Time responses of temperature and stress at the middle point of the SMA wire for three different loading rates: (a) and (b) for the loading rate of $0.7 \times 10^{-4}/s$; (a) and (b) for the loading rate of $0.7 \times 10^{-3}/s$;(a) and (b) for the loading rate of $0.7 \times 10^{-2}/s$; (a), (c) and (e) are temperature responses; (b), (d) and (f) are stress responses. 80
3.33 Time responses of strain of the SMA wire at three different points $x = 0mm$, $x = 1.5mm$ and $x = 3mm$, and their corresponding stress-strain relations: (a) and (b) for the loading rate of $0.7 \times 10^{-4}/s$; (a) and (b) for the loading rate of $0.7 \times 10^{-3}/s$;(a) and (b) for the loading rate of $0.7 \times 10^{-2}/s$. 81
3.34 Stress-strain relations: (a) engineering stress-strain responses of three different loading rates; (b) engineering stress-strain response vs. stress-strain respones at three different position for rate $\dot{u}(t)/L_0 = 0.7 \times 10^{-4}/s$; engineering stress-strain response vs. stress-strain respones at three different position for rate $\dot{u}(t)/L_0 = 0.7 \times 10^{-3}/s$; engineering stress-strain response vs. stress-strain respones at three different position for rate $\dot{u}(t)/L_0 = 0.7 \times 10^{-2}/s$. . 82
3.35 Superelastic responses of SMA wire tensile experiments at different displacement rates (Shaw et al [68]): (a) $1 \times 10^{-4}/s$; (b) $1 \times 10^{-3}/s$; (c) $1 \times 10^{-2}/s$. 83
3.36 Controlled displacement input at low temperature $T_0 = 253K$ with fixed temperature boundary conditions. 84
3.37 Tensile test of SMA wire with fixed temperature boundary condtions at $T_0 = 253K$: (a) evolution of temperature distribution along x during the loading process; (b) evolution of temperature distribution along x during the cooling process; (c) evolution of laten heat distribution along x; (d) temperature response at the middle point $x = 30mm$. 85
3.38 Tensile test of SMA wire with fixed temperature boundary condtions at $T_0 = 253K$: (a) evolution of phase fractions x_+ and x_-; (b) stress response. . . . 86
3.39 SMA wire actuator 86
3.40 SMA wire actuator with insulated boundary conditions: (a). applied voltage vs. time; (b) temperature responses vs. time for different spring stiffness; (c) displacement reponses for different spring stiffness; (d) displacment-temperature relations for different spring stiffness. 87
3.41 SMA wire actuator with insulated boundary conditions: (a) evolution of phase fractions for the case with $K_B = 0.1E_MA/L$; (b) evolution of phase fractions for the case with $K_B = 0.4E_MA/L$; (c) time history of latent heat absorbed and released; (d) stress reponses vs. time. 88

3.42 SMA wire actuator with fixed temperature boundary conditions: (a) temperature distribution along the wire during the heating process; (b) temperature distribution along the wire during the cooling process; (c) temperature history at the middle point $x = 30mm$; (d) displacement response of SMA actuator. 90
3.43 SMA wire actuator with fixed temperature boundary conditions: (a) phase fraction x_+ distribution along the wire during the heating process; (b) phase fraction x_+ distribution along the wire during the cooling process; (c) strain distribution along the wire during the heating process; (d) strain distribution along the wire during the cooling process; 91
3.44 Comparison of SMA actuator displacement reponses between the insulated boundary conditions and fixed temperature boundary conditions under the same applied voltage. 92
3.45 Displacement responses of a SMA wire actuator (Chang et al [69]): (a) insulated boundary condition; (b) fixed temperature boundary condition. . 92
3.46 SMA cantilever beam 93
3.47 Illustration of Gauss integration 95
3.48 SMA cantilever beam with 8 integration points 97
3.49 Quasiplastic behavior of SMA beam bending at low temperature $T = 273K$: (a) Applied tip force and tip displacement response vs. time; (b) Tip force vs. tip displacment. 101
3.50 Contour plots of SMA beam bending at low temperature $T = 273K$ during the loading process: (a) stress contour plots; (b) strain contour plots; (c) phase fraction x_+ contour plots; (d) phase fraction x_- contour plots at $F = 1200N,\ 2100N,\ 3000N$, respectively. 102
3.51 Contour plots of SMA beam bending at low temperature $T = 273K$ during the unloading process: (a) stress contour plots; (b) strain contour plots; (c) phase fraction x_+ contour plots; (d) phase fraction x_- contour plots at $F = 3000N,\ 1500N,\ 0N$, respectively. 103
3.52 SMA beam bending at low temperature $T = 273K$: phase fraction, stress and strain distributions of different layers along the length of the beam at $t = 1s$ with $F = 3000N$: (a) x_+ vs. x; (b) x_- vs. x; (c) stress vs. x; (d) strain vs. x. 104
3.53 SMA beam bending at low temperature $T = 273K$: phase fraction, stress and strain distributions of different layers along the length of the beam at $t = 2s$ with $F = 0N$: (a) x_+ vs. x; (b) x_- vs. x; (c) stress vs. x; (d) strain vs. x. 105
3.54 SMA beam bending at low temperature $T = 273K$: evolution of phase fractions for different layers at the clamped end: (a) x_+ vs. time; (b) x_+ vs. time from $t = 0.25$ to $0.4s$; (c) x_- vs. time; (d) x_- vs. time from $t = 0.25$ to $0.4s$. 106

3.55 SMA beam bending at low temperature $T = 273K$: time history of stress and strain responses of different layers at the clamped end: (a) stress vs. time; (b) stress vs. time from $t = 0.25$ to $0.4s$; (c) strain vs. time; (d) strain vs. time from $t = 0.25$ to $0.4s$. 107
3.56 SMA beam bending at low temperature $T = 273K$: stress and strain distribution of different layers through the thickness at the clamped end: (a) stress distribution from $t = 0.25$ to $0.36s$; (b) strain distribution from $t = 0.25$ to $0.36s$; (c) stress distribution from $t = 0.37s$ to $0.4s$; (d) strain distribution from $t = 0.37s$ to $0.4s$. 108
3.57 Quasiplastic behavior of SMA beam bending at low temperature $T = 273K$: (a) stress-strain response of the $1st$ layer; (b) stress-strain response of the $2nd$ layer; (c) stress-strain response of the $3rd$ layer; (d) stress-strain response of the $4th$ layer. 109
3.58 Superelastic behavior of SMA beam bending at high temperature $T = 333K$: (a) Applied tip force and tip displacement response vs. time; (b) Tip force vs. tip displacment. 111
3.59 Superelastic behavior of three point bending test: applied force vs. midspan deflection (Auricchio and Sacco [55]). 111
3.60 Contour plots of SMA beam bending at high temperature $T = 333K$ during the loading process: (a) stress contour plots; (b) strain contour plots; (c) phase fraction x_+ contour plots; (d) phase fraction x_- contour plots at $F = 1950N$, $2400N$, $3000N$, respectively. 112
3.61 Contour plots of SMA beam bending at high temperature $T = 333K$ during the unloading process: (a) stress contour plots; (b) strain contour plots; (c) phase fraction x_+ contour plots; (d) phase fraction x_- contour plots at $F = 3000N$, $1200N$, $900N$, respectively. 113
3.62 SMA beam bending at high temperature $T = 333K$: (a) evolution of phase fraction x_+ for different layers at the clamped end; (b) evolution of phase fraction x_- for different layers at the clamped end; (c) time history of stress for different layers at the clamped end; (d) time history of strain for different layers at the clamped end. 114
3.63 Superelastic behavior of SMA beam bending at high temperature $T = 333K$: (a) stress-strain response of the $1st$ layer; (b) stress-strain response of the $2nd$ layer; (c) stress-strain response of the $3rd$ layer; (d) stress-strain response of the $4th$ layer. 115
3.64 Stress contour plots of SMA beam bending at high temperature $T = 333K$ during the loading process at $F = 1950N$ for two different numbers of integration points ($NintP = 8, 16$) and two different numbers of elements ($Ne = 250, 500$). 116

3.65 Strain contour plots of SMA beam bending at high temperature $T = 333K$ during the loading process at $F = 1950N$ for two different number of integration points ($NintP = 8, 16$) and two different number of elements ($Ne = 250, 500$): (a) complete plots; (b) zoom-in plots. 117
3.66 Phase fraction x_+ contour plots of SMA beam bending at high temperature $T = 333K$ during the loading process at $F = 1950N$ for two different numbers of integration points ($NintP = 8, 16$) and two different numbers of elements ($Ne = 250, 500$): (a) complete plots; (b) zoom-in plots. 118
3.67 Phase fraction x_- contour plots of SMA beam bending at high temperature $T = 333K$ during the loading process at $F = 1950N$ for two different numbers of integration points ($NintP = 8, 16$) and two different numbers of elements ($Ne = 250, 500$): (a) complete plots; (b) 119
3.68 SMA beam bending under thermo-mechanical loading: (a) applied force, temperature and displacement response vs. time; (b) displacement vs. temperature. 123
3.69 Contour plots of SMA beam bending under thermo-mechanical loading during the cooling process: (a) stress contour plots; (b) strain contour plots; (c) phase fraction x_+ contour plots; (d) phase fraction x_- contour plots at $T = 302.5K$, $287.5K$, $250K$, respectively. 124
3.70 Contour plots of SMA beam bending under thermo-mechanical loading during the heating process: (a) stress contour plots; (b) strain contour plots; (c) phase fraction x_+ contour plots; (d) phase fraction x_- contour plots at $T = 250K$, $325K$, $337K$, respectively. 125
3.71 SMA beam bending under thermo-mechanical loading: phase fractions, stress and strain distribution of different layers along the length of the beam at $t = 2s$ with low tempature $T = 250K$: (a) x_+ vs. x; (b) x_- vs. x; (c) stress vs. x; (d) strain vs. x. 126
3.72 SMA beam bending under thermo-mechanical loading: evolution of phase fractions for different layers at the clamped end: (a) x_+ vs. time; (b) x_+ vs. time from $t = 1.55s$ to $1.85s$; (c) x_- vs. time; (d) x_- vs. time from $t = 1.55s$ to $1.85s$. 127
3.73 SMA beam bending under thermo-mechanical loading: time history of stress and strain responses of different layers at the clamped end: (a) stress vs. time; (b) stress vs. time from $t = 1.5$ to $1.85s$; (c) strain vs. time; (d) strain vs. time from $t = 1.5$ to $1.85s$. 128
3.74 SMA beam bending under thermo-mechanical loading: stress and strain distribution of different layers through the thickness at the clamped end: (a) stress distribution from $t = 1.5s$ to $1.64s$; (b) strain distribution from $t = 1.5s$ to $1.64s$; (c) stress distribution from $t = 1.64s$ to $1.85s$; (d) strain distribution from $t = 1.64s$ to $1.85s$. 129

3.75 SMA beam bending under thermo-mechanical loading: time history of phase fraction, stress and strain responses of different layers at the clamped end during heating from $t = 2.35s$ to $2.72s$: (a) x_+ vs. time; (b) x_- vs. time (c) stress vs. time; (d) strain vs. time. 130
3.76 SMA beam bending under thermo-mechanical loading: stress-strain responses at the clamped end (starts from $t = 1s$): (a) the $1st$ layer; (b) the $2nd$ layer; (c) the $3rd$ layer; (d) the $4th$ layer. 131
3.77 SMA cantilever beam 134
3.78 Applied tip forces vs. time: (a) $rate = 0.35N/s$; (b) $rate = 0.035N/s$. . . . 134
3.79 Tip force-tip displacement responses under the thermal boundary condition of $T_x(0,t) = T_x(L,t) = 0$. 135
3.80 Evolution of phase fraction x_+ along the length of the SMA beam at different layers (in the half section subjected to tensile stresses) under the thermal boundary condition of $T_x(0,t) = T_x(L,t) = 0$: (a) $rate = 0.35N/s$; (b) $rate = 0.035N/s$. 136
3.81 Evolution of latent heat and temperature along the length of the SMA beam under the thermal boundary condition of $T_x(0,t) = T_x(L,t) = 0$: (a) $rate = 0.35N/s$; (b) $rate = 0.035N/s$. 137
3.82 Tip force-tip displacement responses under the loading rate at $0.35N/s$ for two different thermal boundary conditions. 137
3.83 Evolution of phase fraction x_+ along the length of the SMA beam at different layers (in the half section subjected to tensile stresses) under the loading rate at $0.35N/s$: (a) $T_x(0,t) = T_x(L,t) = 0$; (b) $T(0,t) = T_0$ and $T_x(L,t) = 0$. . 138
3.84 Evolution of latent heat and temperature along the length of the SMA beam under the loading rate at $0.35N/s$: (a) $T_x(0,t) = T_x(L,t) = 0$; (b) $T(0,t) = T_0$ and $T_x(L,t) = 0$. 139
3.85 ANSYS implmentation using the element beam188 and usermat.f 143
3.86 ANSYS beam section cell mesh(* - integration point): (a) 1x 4 cells; (b) 1x 8 cells. 144
3.87 Axial loading at low and high temperatures: (a) Low temperature at $T = 273K$; (b) High temperature at $T = 353K$. 145
3.88 Comparison between the results of ANSYS and FEMLAB for the SMA cantilever beam bending: (a) Applied tip force vs. time; (b) force-displacement diagram at low temperature $T = 273K$; (c) force-displacement diagram at high temperature $T = 333K$. 146
3.89 Force convergence criterion with different substeps: (a) Low temperature at $T = 273K$; (b) High temperature at $T = 333K$. 147
3.90 Displacement convergence criterion with different substeps: (a) Low temperature at $T = 273K$; (b) High temperature at $T = 333K$. 148
3.91 Displacement convergence criterion with different element numbers: (a) Low temperature at $T = 273K$; (b) High temperature at $T = 333K$. 148

3.92 Displacement convergence criterion with different integration points: (a) Low temperature at $T = 273K$; (b) High temperature at $T = 333K$. 149
3.93 Effects of minimum cutoff tangential Young's modulus $Et_{\min}$: (a) force-displacement diagrams at low temperature at $T = 273K$; (b) iteration number vs. time at low temperature $T = 273K$; (c) force-displacement diagrams at high temperature at $T = 333K$; (d) iteration number vs. time at high temperature $T = 333K$. 150

Chapter 1

Introduction

1.1 Motivation and Objectives

Due to their fast frequency response, high resolution, compact and light weight characteristics, piezoceramic (PZT) actuators have been widely used in positioning applications, such as atomic force microscope (AFM) [1], etc. PZT materials also exhibit some inherent undesirable nonlinear effects like hysteresis, creep, frequency dependent response [2, 3]. At low drive levels, PZT actuators exhibit moderately nonlinear responses and these nonlinear effects can be compensated effectively through feedback controllers [4, 5]. PZT actuators, however, can be considered to behave linearly only to about 15% of their maximum field strength [6]. To improve the performance of positioning devices to a higher level by using the full capacities of the PZT actuators, these nonlinear effects of PZT materials need to be incorporated in models and subsequent control designs.

The first objective in this dissertation is to develop a computationally efficient model to model the rate dependent hysteresis behaviors of the polycrystalline PZT materials. The model has potential to be used in control applications such as time optimal control design [7].

Shape memory alloys (SMAs) represent another type of smart materials that have been extensively used in many engineering applications due to their two unique material properties: the superelasticity (at high temperature, SMAs can generate and recover large deformations during loading and unloading cycles) and the shape memory effect (SME) (upon heating, SMAs can recover the large residual deformation generated at low temperature)

[8, 9]. Medical device applications include endovascular stents, or orthodontic wires for correction of teeth malpositions [10, 11]. They are also used as hysteresis-induced damping materials in civil structures [12, 13, 14]. More recently, due to its high work output per volume, SMAs have been fabricated as microactuators using thin film techniques [15, 16, 17]. The large surface to volume ratio of SMA thin films allows fast cooling compared to bulk SMA materials. This increases the bandwidth of the SMA actuator dramatically. Some interesting applications include microgrippers,micropumps, microcantilever switches and scanners [18, 19, 20, 21]. SMAs also exhibit a complex temperature-dependent hysteresis behavior. Typically, SMA actuators are driven by electric current heating and convective cooling to trigger phase transformations between martensite and austenite. These generate the actuator deformations/forces, resulting in a thermo-mechanically coupled problem. To facilitate the development of these new devices, an efficient computational tool such as finite element method (FEM) has to be used.

The second objective in this dissertation is to implement the free energy model developed by Muller, Achenbach and Seelecke [22, 23, 24] into finite element programs to simulate SMA components under different mechanical and thermal loading conditions and obtain a better understanding of their working mechanism.

1.2 Background

1.2.1 PZT Modeling

Hysteresis models for PZT materials can be roughly categorized as microscopic or mesospopic models and macroscopic models based on energy principles and phenomenological principles [25]. Microscopic models are formulated at the grain or lattice level like [26] and are not suitable for macroscopic engineering applications such as controls due to their large number of required parameters and high computational cost. Macroscopic hysteresis models are typically low order and based on phenomenological principles or energy principles and aiming for engineering design applications. One macroscopic model is the Preisach model [27, 28], which is based on purely phenomenological principles. Due to its mathematical generality [29], the Preisach model can be used to characterize the hysteresis behaviors for a wide range of materials. However, the lack of physical parameters makes it difficult to

incorporate frequency, temperature and load dependencies and adapt to changing operating conditions. Other macroscopic models like the model of Chen and Lynch [30] and the domain wall models of Smith and Hom [31] and Smith and Ouneies [32] are derived from energy principles, which provide a good compromise between microscopic models and purely phenomenological models.

In [25, 33], Smith and Seelecke develop a free energy model for perfect single cystalline PZT materials, which is a direct extension from the SMA models of Achenbach and Muller [22, 23]. The perfect single crystal model is extended to model polycrystalline materials by using a stochastic homogenization method. Two distributions for the internal fields and coercive fields are used to incorporate the effects of inhomogeneities and nonuniform electric fields in the materials. An effective numerical implementation of the model is also proposed in [25] by neglecting thermal activation, which is computationally efficient but loses the time dependent characteristics of the energy model. An efficient implementation algorithm employing lookup tables is aslo developed in [34], which incorporates relaxation mechanisms and electromechanical coupling. In [35], Smith et al extend the homogenized model by using the general densities instead of lognormal and normal densities used in [25] and employ optimal parameter estimations to get a better curve fitting with experimental data. A unified framework for modeling hysteresis in ferroic materials was established by Smith et al in [33] and Smith in [36].

1.2.2 SMA Modeling and Finite Element Simulations

During the last two decades, numerous models have been developed for SMAs. Early efforts go back to Tanaka [37, 38, 39]. The model uses the fraction of martensite as an internal variable and gives a phenomenological equation of state for its dependence on stress and temperature in the form of an exponential function. Liang and Rogers [40] later modified the model by using a cosine law for the martensite fraction. However, both versions are only applicable to predict the superelastic behaviors of the SMAs. Brinson [41] improved the model by introducing a decomposition of the martensite fraction into twinned and detwinned martensite such that the quasiplastic behavior can be predicted as well. The model was further refined by Bekker and Brinson [42, 43] by using a phase diagram based approach. Boyd and Lagoudas [44] have developed a model that is derived from

irreversible thermodynamics. The model follows the guidelines of the classical theory of rate-independent plasticity with yield conditions triggering the phase transformations and is formulated in a three-dimensional setting. Closed form solutions for damping capacity and actuator efficiency are obtainable from the model. A drawback, however, is the large number of material parameters to be determined. Furthermore, due to its provenance from the classical theory of plasticity, the dissipation potential is not chosen from physical reasoning but rather from mathematical arguments like convexity properties. Based on generalized plasticity theory, Aurichio and Taylor [45] developed a model to predict the superelastic behavior of SMA materials.

All these models above are rate independent and their suitability for the simulation of SMA actuator applications is very limited. The same holds for the recent micromechanical models [46, 47, 48, 49], which, based on the self-consistent average methods, are too complex to be used for the simulation of mostly one-dimensional SMA actuators. In this dissertation, the focus is on a one-dimensional model accounting for both thermodynamic and mechanical aspects.

A noticeable model in this respect has been developed by Ivshin and Pence [50, 51] and Wu and Pence [52]. The model evolves from careful thermodynamic consideration. Despite a certain lack of physical reasoning, the model appears to be quite powerful with respect to the simulation of SMA actuator behavior. It includes an energy balance with contributions from convective heat exchange, latent heats and external heat sources, and a number of interesting simulations are displayed in [51].

One of the latest models for SMA wires is developed by Shaw [53]. The model is capable to simulate both superelastic and shape memory behaviors of SMAs. The model also takes into account the unstable phase transformation behaviors by including the strain gradient effects and by allowing softening transformation paths. The energy balance and latent heat effects are also included in the model, which also makes it suitable for the simulation of SMA actuators.

Another model that has recently been applied to SMA actuator applications has originally been developed by Achenbach and Müller [22], Achenbach [23] and Seelecke and Müller [24]. It uses ideas from statistical thermodynamics and describes the evolution of

two martensite fractions based on the theory of thermally activated processes. The coupling with the balance of energy including latent heat effects due to the phase transformation makes it possible to reproduce the time-dependent length change of an electric current heated SMA wire under an arbitrary time-dependent load. The attractiveness of the model is based on the fact that the complete load- and temperature-dependent hysteretic behavior of SMAs is derived from the energy function alone without any additional loading/unloading criteria. The model can represent both shape memory effect and superelasticity of SMA materials. A very limited number of material parameters used to construct the free energy can be identified from only two tensile experiments conducted at two different temperatures. Together with a convenient mathematical structure in the form of an ODE system, allowing for robust numerical integration, these features make the model an attractive candidate for the simulation of SMA actuators and their control behavior.

Due to their complex temperature-dependent and hysterestic behavior, numerical methods like the finite element method must be used in order to predict the responses of SMA structures and devices. Many simulations of SMA structures and devices using FEM have been reported in literature (see, e.g. [54] [55] [56] [57] [58] [59] [60] [61] [62]). However, most of these simulations have been conducted under the assumption of isothermal or homogenous temperature fields without including the nonlinear transient heat transfer into the problems. By neglecting the latent heat effects, Amalraj et al [61] studied the phase transformation of an SMA wire by solving the heat transfer equation and equation of mechanical deformation separately using the Galerkin finite element method. Using a very simplified SMA model, Krevet and Kohl [62] conducted a 3D finite element simulation of an SMA microactuator by solving an electro-thermo-mechanically coupling problem sequentially. Typically, SMA actuators are driven by electric current heating and convective cooling with environment and the latent heats due to the phase transformation have to be taken into account. In order to conduct simulation of SMA actuators, one has to solve a nonlinear transient thermo-mechanically coupled problem. If the variation of the resistivity of SMAs with temperature and mechanical loading is also considered, the problem will become an electro-thermo-mechanically coupled problem. This will be investigated in this dissertation.

1.3 Dissertation Outline

The detailed outline of this dissertation is as follows:

Chapter 2 presents the hysteresis modeling of PZT materials using parameterization method. First, brief overviews are given of the free energy model for perfect single crystal PZT materials and its extension to polycrystalline materials. Then based on these models, a modified parameterization method is developed to model the hysteresis behaviors of the polycrystalline PZT materials. Following the introduction of the concept of the parameterization method, the effective barriers of the major loops are identified from the experimental polarization-electric field diagram as functions of the phase fraction, and then minor loops are constructed by the major loops using linear mapping method and bookkeeping algorithm. A robust algorithm is implemented into FORTRAN program using the Radua5 ODE solver. The model is used to simulate the rate dependent minor loop behavior of the PZT materials, which is subsequently compared to experimental data.

Chapter 3 presents the finite element analysis of SMA components. First, a brief overview is given of the 1-D free energy SMA model and an explicit stress-strain expression is derived for a displacement-driven finite element implementation. Then, the model is implemented into the finite element software package FEMLAB using its general PDE form by treating the evolution equations of phase fractions as degenerated PDEs coupled with the mechanical equilibrium equation. First, without including the latent heat effect and neglecting the heat transfer equation, simulations are conducted for SMA bars with uniform cross-section, non-uniform cross-section and non-uniform temperature distribution to validate the finite element implementation and demonstrate the capabilities of the free energy SMA model. The finite element implementation is then expanded by including the nonlinear transient heat transfer equation with the phase transformation induced latent heat included. Tensile simulations of an SMA wire under different thermal boundary conditions with different loading rates are conducted to demonstrate the inhomogeneity and rate effects of the system responses. By including the Joule heating, the performance of an SMA wire actuator under different thermal boundary conditions is studied. Following the finite element analysis of bars and wires, similar scheme is used to implement the 1-D free energy model into FEMLAB to study the inhomogeneous SMA beam bending problems.

After the implementation, we present the detailed analysis of inhomogeneous bending behaviors of an SMA cantilever beam under constant temperatures and thermal-mechanical coupling loading, respectively. Finally, using traditional incremental finite element method, the 1-D free energy model is also implemented into finite element program ANSYS using its BEAM188 element and user defined material subroutine USERMAT, which also serves as a validation tool for the FEMLAB implementation. We study convergence behavior and accuracy for different convergence criteria in ANSYS as well as other relevant parameters such as element, substep and integration point number.

Finally, Chapter 4 presents a summary of the main results and remarks on the future work.

Chapter 2

Hysteresis Modeling of PZT Materials

This chapter presents the hysteresis modeling of polycrystalline PZT materials using parameterization method. First, we introduce the free energy model for perfect single crystal PZT materials and the homogenized model for polycrystalline materials. Then based on these models, a parameterization method is developed to model the hysteresis behavior of the polycrystal PZT materials. Following the introduction of the concept of the parameterization method, major loop effective barriers are identified from experimental polarization-electric field diagram as functions of the phase fraction, and minor loops are constructed by major loop using a linear mapping method and a bookkeeping algorithm. A robust algorithm is implemented to simulate the rate-dependent minor loop hysteresis behavior of the polycrystalline PZT materials. The simulation results are then compared with experimental data.

2.1 Free Energy Model for Perfect Single Crystal PZT Materials

To model the polarization P vs. electric field E hysteresis behavior of the PZT material at the domain level, a free energy model is developed by Smith and Seelecke et al [25]. The model is based on the theory of thermally activated processes and statistical mechanics under the assumption that the dipoles in a single crystal with uniform lattice cells have only two orientations, which are denoted as (+) and (-), depending on whether the Ti^{4+} ion is displaced upward ($+180°$) or downward ($-180°$) with respect to the center of symmetry as

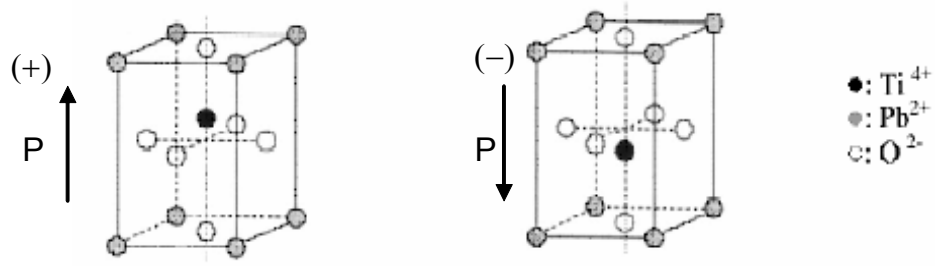


Figure 2.1: $PbTiO_3$ cystal lattice cells with positive and negative polarization

shown in Figure 2.1. The similar free energy model was originally developed by Muller and Achenbach [22, 23] for the perfect single crystal SMA materials.

2.1.1 Free Energy

For a fixed temperature, the Helmholtz free energy for the single crystal is constructed by three parabolae

$$\psi(P) = \begin{cases} \frac{1}{2}s(P+P_R)^2, & P \le -P_I \\ \frac{1}{2}s(P_I - P_R)(\frac{P^2}{P_I} - P_R)^2, & |P| < P_I \\ \frac{1}{2}s(P-P_R)^2, & P \le P_I \end{cases} \tag{2.1}$$

Physical parameters P_R, P_I denote the remnant polarization and the polarization at the onset of the domain switching, which correspond to the minimum location and the inflection point of the Helmholtz free energy (3.2), and s is the reciprocal of the slope of the $P-E$ curve as shown in Figure 2.2. They have the following relation with the coercive field E_c

$$E_c = s(P_R - P_I) \tag{2.2}$$

The Gibbs free energy is expressed as

$$G(E,P) = \psi(P) - EP \tag{2.3}$$

where EP is the electrostatic energy due to the applied electric field E. The applied electric field changes the landscapes of the Gibbs free energy and the barrier will be eliminated

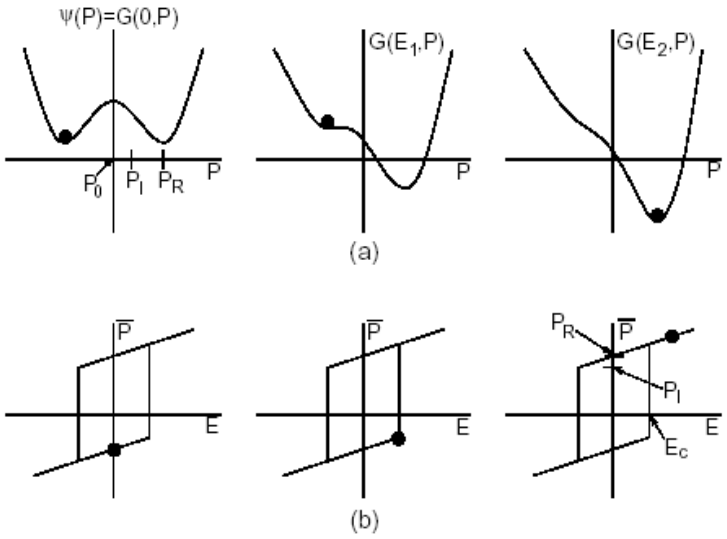


Figure 2.2: (a) Gibbs free energy $G(E, P)$ for increasing field E; (b) P-E diagram for a single crystal PZT with uniform lattice. [25]

if the applied field is strong enough. The elimination of the barrier causes the domain to switch from one orientation to the other. For instance, a switching process started with full $-180°$ phase for increasing the applied field is illustrated in Figure 2.2. Once the applied field E is greater than the coercive field E_c, the energy barrier between the two phases will disappear which causes switching from the $-180°$ phase to the $+180°$ phase. The energy model predicts the almost instantaneous jump between the two phases for the perfect single crystalline materials.

2.1.2 Average Polarization

With the existence of thermal activation, the probability for reaching the energy level G is given as the Boltzmann density

$$\mu(G) = Ce^{GV_D/kT} \tag{2.4}$$

where T is the temperature, k is the Boltzmann's constant, V_D is the activation volume and C is an constant chosen to yield a probability of 1 when $\mu(G)$ is integrated over all admissible

input values. The expected polarizations due to dipoles with different orientations are given as

$$\langle P_+ \rangle = \frac{\int_{P_I}^{\infty} P e^{-G(E,P,T)V_D/kT}\, dP}{\int_{P_I}^{\infty} e^{-G(E,P,T)V_D/kT}\, dP} \approx \frac{E}{s} + P_R \tag{2.5}$$

$$\langle P_- \rangle = \frac{\int_{-\infty}^{-P_I} P e^{-G(E,P,T)V_D/kT}\, dP}{\int_{-\infty}^{-P_I} e^{-G(E,P,T)V_D/kT}\, dP} \approx \frac{E}{s} - P_R \tag{2.6}$$

For a perfect single crystal PZT material with uniform electric field, the average polarization is given as

$$\overline{P} = x_+ \langle P_+ \rangle + x_- \langle P_- \rangle \tag{2.7}$$

where x_+ and x_- denote the fractions of dipoles with positive and negative orientations, respectively.

2.1.3 Kinetics of Phase Transformations

In the model, the evolution of the phase fractions x_+ and x_- is governed by the following rate law, and the sum of phase fractions x_+ and x_- is equal to 1

$$\dot{x}_+ = -x_+ p^{+-} + x_- p^{-+} \tag{2.8}$$

under the constraint of

$$x_+ + x_- = 1 \tag{2.9}$$

The rate of change of x_+ is the sum of a loss due to dipoles jump from the $+180°$ phase to the $-180°$ phase, and a gain due to dipoles jump from the $-180°$ phase to the $+180°$ phase. The number of jumps are proportional to the phase fractions x_+ and x_-. The quantities $p^{\alpha\beta}$ in (3.18) are transition probabilities. For instance, p^{+-} is the transition probability from the +180 phase to the −180 phase. Transition probabilities are computed as the product of the probability of achieving the energy required to overcome the energy barrier and the frequency at which jumps are tempted [25]. They are given as

$$p^{+-} = \frac{1}{\tau_x} \frac{e^{-G(E,P_I,T)V_D/kT}}{\int_{P_I}^{\infty} e^{-G(E,P,T)V_D/kT}\ dP} \tag{2.10}$$

$$p^{-+} = \frac{1}{\tau_x} \frac{e^{-G(E,-P_I,T)V_D/kT}}{\int_{-\infty}^{-P_I} e^{-G(E,P,T)V_D/kT}\ dP} \tag{2.11}$$

where τ_x is the relaxation time of the PZT material. The ratio V_D/kT determines the fluctuation of the polarization about the equilibrium values due to the thermal activation. The rate dependence of the hysteresis response is determined by the ratio V_D/kT and the relaxation time τ_x.

We can simplify the expressions for the transition probabilities using the relationship in (2.2), by expressing them as functions of the coercive field E_c

$$p^{+-} = \frac{2}{\tau_x} \frac{\sqrt{\alpha}}{\sqrt{\pi}} \frac{1}{\operatorname{erf} cx[\frac{\sqrt{\alpha}}{\eta}(E_c - E)]} \tag{2.12}$$

$$p^{-+} = \frac{2}{\tau_x} \frac{\sqrt{\alpha}}{\sqrt{\pi}} \frac{1}{\operatorname{erf} cx[\frac{\sqrt{\alpha}}{\eta}(-E_c + E)]} \tag{2.13}$$

where

$$\operatorname{erf} cx(x) = \frac{e^{-x^2}}{\operatorname{erf} c(x)} \tag{2.14}$$

is the scale complement error function and

$$\operatorname{erf} c(x) = \frac{2}{\sqrt{\pi}} \int_x^{\infty} e^{-x^2} dx \tag{2.15}$$

is the complement error function.

2.2 Homogenized Energy Model of Polycrystal PZT

The model given by (2.7) and (3.18) is valid only for perfect single crystal PZT materials under assumptions of homogeneous and isotropic material properties and uniform electric fields through out the materials. The single crystal model predict instantaneous domain switching at the coercive field E_c as shown in Figure 2.2. In general, inhomogeneities of the polycystalline PZT materials can yield variations in the local material response as well as the

nonuniform electric field. To capture the more gradual transition of the domain switching and characterize the minor loop behavior in polycrystalline PZT materials, a homogenized energy model was developed by Smith and Seelecke et al [25] by incorporating the effects of inhomogeneities and nonuniform electric fields in the materials .

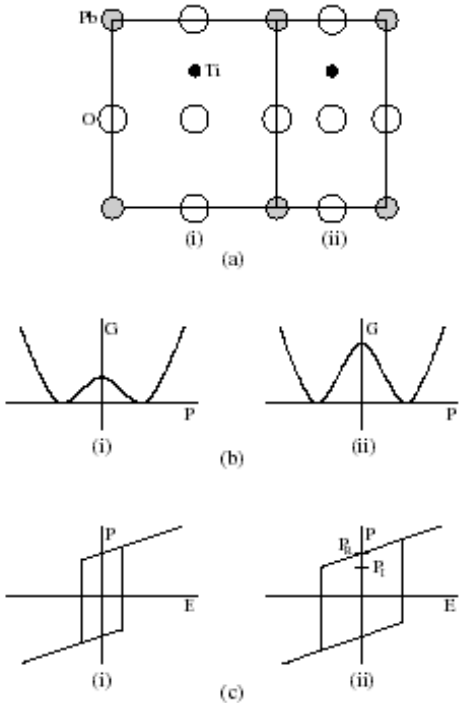


Figure 2.3: (a) Nonuniform PZT lattice structure; (b) Free energies associated with lattice widths (i) and (ii); (c) Variations in hysteresis kernel due to different free energies. [25]

2.2.1 Stochastic Distributions of Energy Barrier and Internal Electric Field

To account for the inhomogeneities, the local coercive field E_c and the effective electric fields E_e throughout the material are assumed to be stochastic distributions instead of fixed values. As illustrated in Figure 2.3, different Helmholtz free energy profiles corresponds to the different lattice widths, which result in variations in hysteresis kernel. Lattice cells with different widths see different energy barriers, which corresponds to different coercive field

E_c. The local coercive field E_c is assumed to have a stochastic distribution. Under these conditions, the global polarization is given by

$$P(E) = \int_0^\infty \overline{P}(E, E_c) f_1(E_c)\ dE_c \tag{2.16}$$

where $\overline{P}$ is the local polarization given in (2.7), and $f_1(E_c)$ is a probability density function defined in $[0,\ \infty)$. In [25], the distribution of the local coercive field E_C is assumed to be a log-normal distribution. Generalized densities are also used by Hatch [**?**] to better fit the experimental data. And Zhong [63] used a clipped normal distribution with the mean value $\overline{E}_c$ as

$$f_1(E_C) = c_1 e^{-(E_C - \overline{E}_C)^2/b_1} \tag{2.17}$$

The constant c_1 can be determined by

$$c_1 = \frac{1}{\int_0^\infty e^{-(E_C - \overline{E}_C)^2/b_1}\ dE_C}$$

To incorporate the effect of the nonuniform electric fields due to the interactions of neighboring dipoles, the effective field E_e is assumed to be a perturbation about the external applied field E. The global polarization is then given by

$$P(E) = \int_{-\infty}^\infty \overline{P}(E + E_e, E_C) f_2(E_e)\ dE_e \tag{2.18}$$

where $\overline{P}$ is given in (2.7), and

$$f_2(E_e) = c_2 e^{-E_e^2/b_2} \tag{2.19}$$

is the normal distribution of the effective field E_e. The constant c_2 can be determined by

$$c_2 = \frac{1}{\int_{-\infty}^\infty e^{-E_e^2/b_2}\ dE_e} \tag{2.20}$$

Combining two distributions in (2.17) and (2.18), the global polarization for the polycrystalline PZT materials with varying coercive fields E_c and effective fields $E_e$is given as

$$P(E) = \int_0^\infty \int_{-\infty}^\infty \overline{P}(E + E_e, E_c) f_1(E_c) f_2(E_e)\ dE_e dE_c \tag{2.21}$$

2.2.2 Implementation and Discussion

Numerical integration is used to approximate the integral in the model (2.21). Gauss-Legendre quadrature is used on the semi-infinite domain and the Gauss-Hermite quadrature is used on the infinite domain [25],[63]. The approximation of (2.21) by the numerical integration is given as

$$P(E) = \sum_{i=1}^{N_i} \sum_{j=1}^{N_j} \overline{P}(E + E_{e_j}, E_{C_i}) f_1(E_{c_i}) f_2(E_{e_j})\ w_i v_j \tag{2.22}$$

where E_{e_j}, E_{c_i} are the integration points associated with respective quadrature formulae, and w_j, v_i are the corresponding weights.

For each combination of E_{e_j} and E_{C_i} used to evaluate the $\overline{P}(E + E_{e_j}, E_{C_i})$, an ODE (3.18) needs to be solved. This results in a total of $N_i \times N_j$ ODEs need to be solved simultaneously in order to compute the global polarization P in (2.22), which is very computationally expensive if $N_i \times N_j$ becomes a large number. Typically, to get a reasonably smooth simulation curve, hundreds of ODEs must be solved together [63]. A simplified implementation is developed in [25] by neglecting the thermal activation, which is much more computationally efficient but loses the time dependent characteristics of the energy model. Recently, an efficient implementation algorithm employing lookup tables is also developed in [34], which incorporates relaxation mechanisms and electromechanical coupling. Motivated by the above homogenized energy model, the next section develops an alternative computationally efficient parameterization method, which preserves the dynamic characteristics of the free energy model.

2.3 Parameterization Method

In this section, based on the homogenized energy model, an alternative computationally efficient method called parameterization method is developed. First, we introduce the concept of the parameterization method, which parameterizes the coercive field E_c as a function of phase fraction x_+.

2.3.1 Concept of Parameterization: Representative Single Crystal

For the quadrature implementation of the homogenized energy model (2.22), many physical single crystalline domains are considered and each having a barrier E_{ci} and a effective field E_{ej}. The effective barrier, which can be negative, is defined as $E_c^e = E_c - E_e$. The domains with an equal effective barrier E_c^e will transform together. The applied field $\triangle E$ overcoming $\triangle E_c^e$ will cause a corresponding phase fraction change of $\triangle x_+$. The value of $\triangle x_+$ depends on the number of domains with corresponding effective barrier, which is determined by the probabilities of two distributions of E_c and E_e (2.21). Motivated by this, instead of looking at an ensemble of many physical domains, the parametrization method starts with a different perspective by creating a "representative" domain. This representative domain is the one that is most likely to transform next for a given phase fraction x_+ and given applied electric field. Depending on how many domains have already transformed, this domain will see a constantly changing barrier $E_c^e(x_+)$. The effective barrier $E_c^e(x_+)$ is now parametrized as a function of the phase fraction x_+. This eliminates the need to solve many ODEs for different domains and reduces the implementation to only one ODE for the representative domain. This makes the parametrization method is very computationally efficient.

The equations of parameterization are summarized as (from now on, we drop the superscript e from the effective barrier $E_c^e(x_+)$)

$$\overline{P} = x_+ \left(\frac{E}{s} + P_R \right) + (1 - x_+) \left(\frac{E}{s} - P_R \right) \tag{2.23}$$

$$\dot{x}_+ = -x_+ p^{+-} + x_- p^{-+} \tag{2.24}$$

$$p^{+-} = \frac{2}{\tau_x} \frac{\sqrt{\alpha}}{\sqrt{\pi}} \frac{1}{\operatorname{erf} cx[\frac{\sqrt{\alpha}}{s}(E_c(x_+) - E)]} \tag{2.25}$$

$$p^{-+} = \frac{2}{\tau_x} \frac{\sqrt{\alpha}}{\sqrt{\pi}} \frac{1}{\operatorname{erf} cx \left\{ \frac{\sqrt{\alpha}}{s} [-E_c(x_+) + E] \right\}} \tag{2.26}$$

The only difference compared with the single crystal model in section 2.1 is that the constant coercive field E_c is now replaced by the parameterized effective barriers $E_c(x_+)$.The effective barrier $E_c(x_+)$ needs to be calculated from the current phase fraction value x_+

and the loading history. The next step is to determine how to identify the effective barriers $E_c(x_+)$ and how to construct the minor loops.

2.3.2 Identification of Effective Barrier $E_c(x_+)$ from Experimental Data

To implement the parameterization method, we need to construct the effective barrier curves $E_c(x_+)$ for both loading and unloading paths. Instead of assuming an analytical expression for the $E_c(x_+)$ as in [63], here, we identify the effective barrier from the experimental data directly. By assuming that effective barrier $E_c(x_+)$ is independent of the loading rates, we can treat the $E(x_+)$ curve to be equal to $E_c(x_+)$ at very slow loading rates. Through experiments, we can measure the polarization $P(E)$ curve, and in the model, $P(E, x_+)$ is calculated as

$$P(E, x_+) = 2P_R x_+ + \frac{E}{s} - P_R \tag{2.27}$$

which is a linear function the phase fraction x_+.

So the unmeasurable phase fraction $\hat{x}_+$ can be estimated from the measurable polarization P and electric field E as

$$\hat{x}_+(E, P) = \frac{1}{2P_R}(-\frac{E}{s} + P + P_R) \tag{2.28}$$

and the estimated effective barrier $\hat{E}_c(x_+)$ is

$$\hat{E}_c(\hat{x}_+) \approx E \tag{2.29}$$

Figure 2.4 shows the full loop experimental data of a PZT151 stack actuator under a very slow loading rate of 0.05 $kV/mm/s$ [64]. The points of $[\max(E), \max(P)]$and $[\min(E), \min(P)]$ in Figure 2.4 are assumed to correspond to the states of $\hat{x}_+ = 1$ and $\hat{x}_+ = 0$, respectively. Figure 2.5 is the identified effective barrier $\hat{E}_c(\hat{x}_+)$ curves using (2.28) and (2.29). Notice that in order to identify the effective barrier $\hat{E}_c(\hat{x}_+)$, the two parameters, the remnant polarization P_R and the reciprocal of the $P(E)$ curve s, need to be determined first from the experimental $P - E$ diagram as shown in Figure 2.6. These two parameters are chosen such that the estimated phase fraction $\hat{x}_+(E, P)$ given in (2.28) is within $[0, 1]$. We call the identified $E_c(x_+)$ curves as the major loop, which includes a

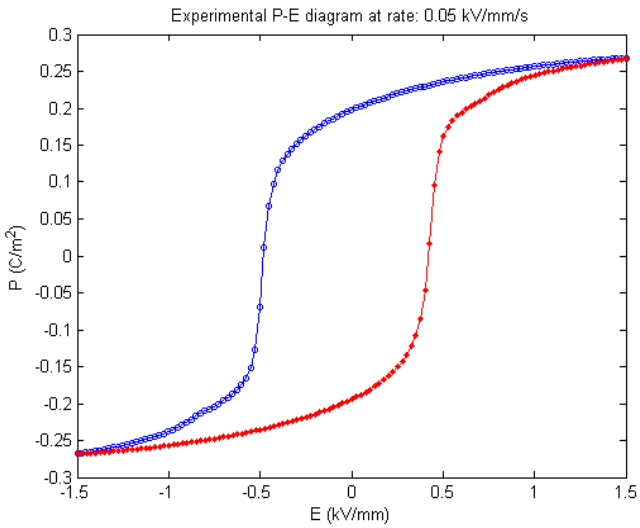


Figure 2.4: Full loop P-E diagram at the slow rate: $0.05kV/mm/s$

loading path $E_c^+(x_+)$ (in the direction of increasing electric field E) and an unloading path $E_c^-(x_+)$ (in the direction of decreasing electric field E) .

Using the above identified effective barrier $E_c(x_+)$, the simulation result is shown to match the experimental data perfectly as shown in Figure 2.7.

2.3.3 Implementation Details

To calculate the effective barrier $E_c(x_+)$, the current phase fraction value x_+ and information of the loading history are needed. As stated in the previous section, only the major loop curves of the effective barrier $E_c(x_+)$ have been identified from the experimental data. We use the major loop to construct the minor loops by using a linear mapping method and implementing a book-keeping algorithm to record and update the minor loop reversal points such that the loading history can be tracked.

2.3.4 Construction of Minor Loops: Linear Mapping Method

After identifying the effective barriers $E_c(x_+)$, the minor loops are constructed by the major loop using the linear mapping method. The scheme of a linear mapping is shown in Figure

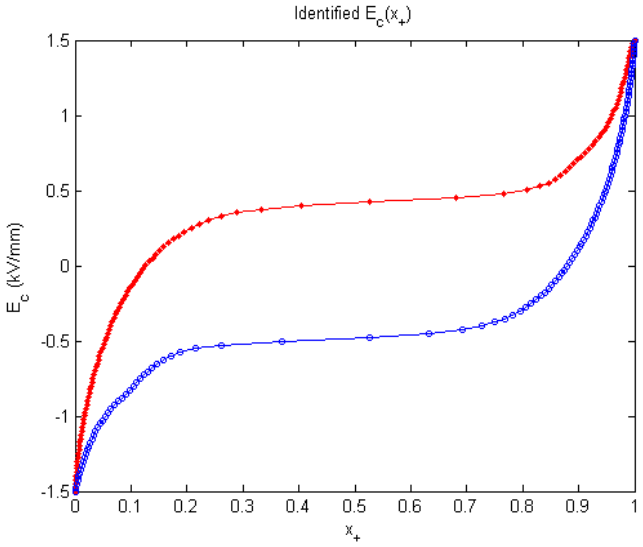


Figure 2.5: Identified $E_c(x_+)$

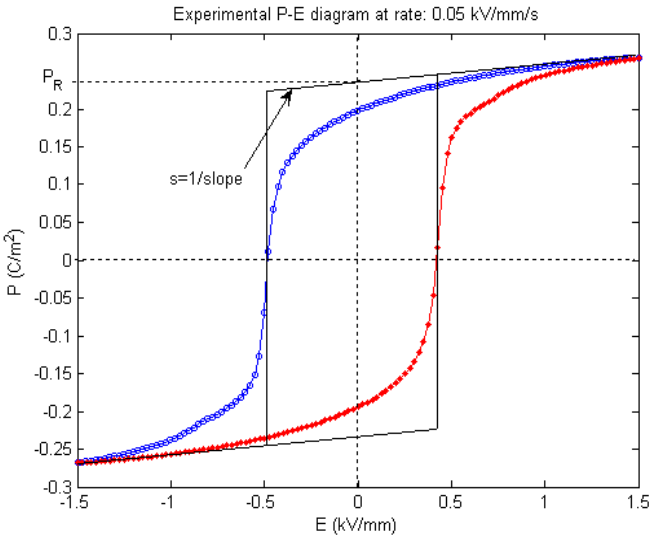


Figure 2.6: Identification of P_R and s

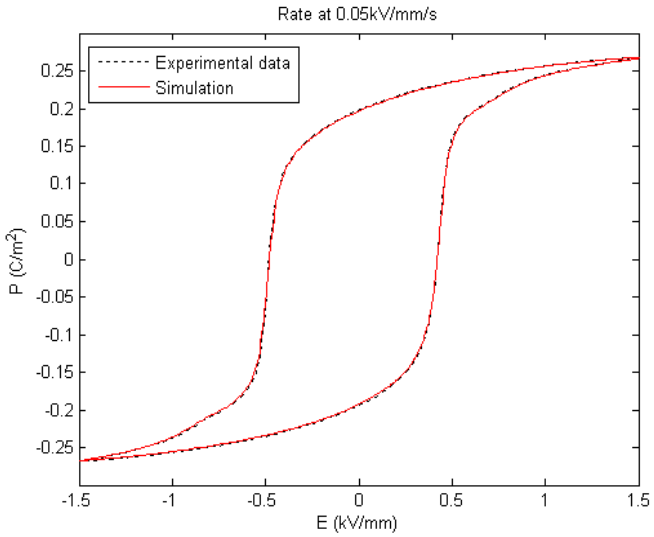


Figure 2.7: Full-loop simulation using the identified effective barrier $E_C(x_+)$ at the slow rate of 0.05 $kV/mm/s$

2.8. The minor loop loading and unloading paths are generated by mapping corresponding portions of major loop loading and unloading paths, respectively.

For the construction of the minor loops, we use the same function for the major loop and scale it to fit between reversal points. We have identified the effective barrier major loop loading path identified as a group of discrete points as

$$E_c(x_{+major}) = f(x_{+major}) : \begin{bmatrix} x_{+major}(1) = 0 & E_c(1) \\ x_{+major}(2) & E_c(2) \\ \vdots & \vdots \\ x_{+major}(N) = 1 & E_c(N) \end{bmatrix} \tag{2.30}$$

And its inverse is

$$x_{+major} = f^{-1}\left[E_c(x_{+major})\right] : \begin{bmatrix} E_c(1) & x_{+major}(1) = 0 \\ E_c(2) & x_{+major}(2) \\ \vdots & \vdots \\ E_C(N) & x_{+major}(N) = 1 \end{bmatrix} \tag{2.31}$$

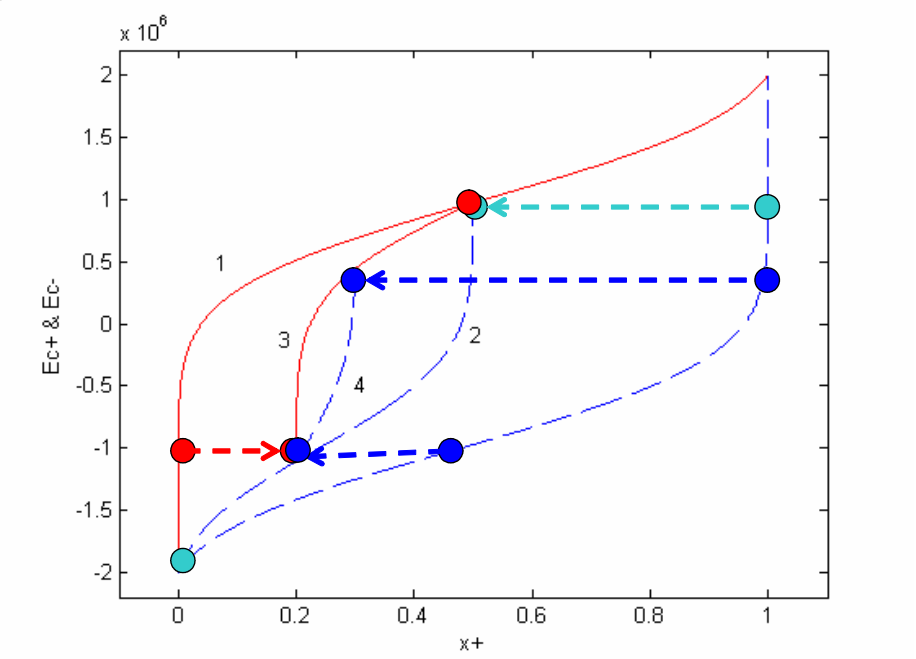


Figure 2.8: Scheme of linear mapping

Using the linear mapping, the minor loop is defined as

$$E_c(x_+) = f(mx_+ + p) \tag{2.32}$$

where m and p are two scale factors that need to be determined. The inverse of the (2.32) is given as

$$mx_+ + p = f^{-1}\left[E_C\left(x_+\right)\right] \tag{2.33}$$

which is a linear function of m and p. The values of m and p can be determined by the known lower reversal point $(x_+^L,\ E_c^L\left(x_+\right))$ and upper reversal point $(x_+^H,\ E_c^H\left(x_+\right))$.

$$mx_+^L + p = f^{-1}\left[E_c^L\left(x_+\right)\right] = x_{+major}^L \tag{2.34}$$

$$mx_+^H + p = f^{-1}\left[E_c^H\left(x_+\right)\right] = x_{+major}^H \tag{2.35}$$

where H and L denote the high and low end reversal points, respectively. Solving the above linear equations (2.34) and (2.35), we have

$$\Rightarrow \begin{cases} m = \frac{x_{+major}^H - x_{+major}^L}{x_+^U - x_+^L} \\ p = \frac{x_+^H x_{+major}^H - x_+^L x_{+major}^L}{x_+^U - x_+^L} \end{cases} \tag{2.36}$$

For example, for the major loop itself, $x_+^L = x_{+major}^L = 0$, $x_+^H = x_{+major}^H = 1$, we have scale factors $m = 1,\ p = 0$.

After the scale factors $m,\ p$ are determined, the value $x_+ \in [x_+^L,\ x_+^H]$ corresponds to $x_{+major} = mx_+ + p$ and then the value x_{+major} is used to calculate the value of the effective barrier $E_c\left(x_+\right)$ using linear interpolation for the identified major loop data.

2.3.5 Minor Loop Implementation: Book-keeping Algorithm

To track the loading history of the effective barrier $E_c\left(x_+\right)$, a book-keeping algorithm is needed to record the minor loop reversal points. First, the minor loop behaviors to be modelled are illustrated in Figure 2.9. The arrows indicate the possible loading (with phase fraction x_+ increasing) and unloading directions (with phase fraction x_+ decreasing). For

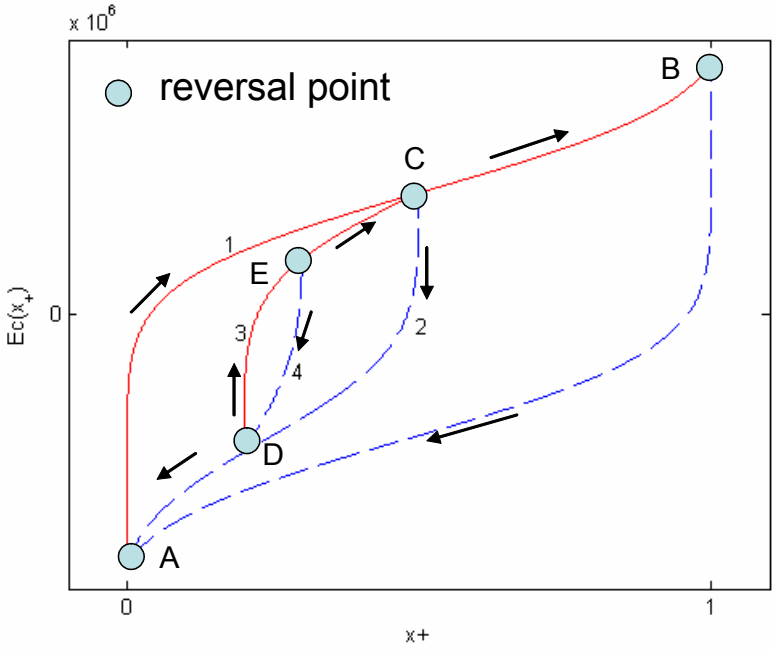


Figure 2.9: Scheme of book-keeping algorithm

example, if the loading starts at point A, $Ec(x_+)$ will go along path 1, which is the major loop loading path, called level 1 curve. At point C, if switching from loading to unloading occurs, it will follow the level 2 unloading path CA, which is constructed by a linear mapping of the corresponding portion of the major loop unloading path. If the unloading continues, the minor loop will close at the start point A. This is called the first order reversal minor loop. But if switching from unloading to loading occurs again at point D, it will follow the level 3 loading path DC. If the loading continues, the minor loop will close at point C and $Ec(x_+)$ jumps from level 3 curve to level 1 curve and continues on it. This is called second order reversal minor loop. The minor loop is closed at point C. Or if switching from loading to unloading occurs again at point E, $Ec(x_+)$ will need to follow the level 4 unloading path ED, and if the unloading continues, the minor loop will close at point D and $Ec(x_+)$ jumps from the level 4 curve to the level 2 curve and continues on it. First, we need to establish a criterion to detect the switching between the loading and unloading.

Loading and unloading criterion

x_+: current convergence value; $prev_x_+$: previous convergence value

If $x_+ > prev_x_+$ then

$\Rightarrow$ set $current_direction = increase$

If $x_+ < prev_x_+$ then

$\Rightarrow$ set $current_direction = decrease$

Else

$\Rightarrow$ set $current_direction = previous_direction$

Then we need a book-keeping algorithm to store and update the reversal points to track the loading and unloading history.

Global variables

nL: level number indicating the current $Ec(x_+)$ path

$x_+^H(nL)$ $E_c^H(nL)$: high end point of the nL-th level $Ec(x_+)$ path

$x_+^L(nL)$ $E_c^L(nL)$: low end point of the nL-th level $Ec(x_+)$ path

$prev_x_+$: previous convergence value of x_+

$prev_E_c$: previous convergence value of $E_c(x_+)$

$prev_direction$: previous loading direction

Switching from loading to unloading: level number increases by 1

If ($current_direction$ is not equal $prev_direction$)

and ($current_direction = decrease$) then

$\Rightarrow$ update the level number indicating the current $Ec(x_+)$ path as

$$nL = nL + 1$$

$\Rightarrow$ update the high end point of the nL-th level $Ec(x_+)$ path as

$$x_+^H(nL) = prev_x_+; \quad E_c^H(nL) = prev_E_c$$

$\Rightarrow$ update the low end point of the nL-th level $Ec(x_+)$ path as

$$x_+^L(nL) = x_+^L(nL-1); \quad E_c^L(nL) = E_c^L(nL-1)$$

$\Rightarrow$ call the subroutine $E_c^-(E_c, x_+, x_+^L(nL), E_c^L(nL), x_+^H(nL), E_c^H(nL))$

to calculate effective barrier $E_c(x_+)$

$\Rightarrow$ set $prev_direction = current_direction$

$\Rightarrow$ set $prev_x_+ = x_+$

$\Rightarrow$ set $prev_E_c = E_c$

Switching from unloading to loading: level number increases by 1

If ($current_direction$ is not equal $prev_direction$)

and ($current_direction = increase$) then

$\Rightarrow$ update the level number indicating the current $Ec(x_+)$ path as

$$nL = nL + 1$$

$\Rightarrow$ update the high end point of the nL-th level $Ec(x_+)$ path as

$$x_+^H(nL) = x_+^H(nL-1); \quad E_c^H(nL) = E_c^H(nL-1)$$

$\Rightarrow$ update the low end point of the nL-th level $Ec(x_+)$ path as

$$x_+^L(nL) = prev_x_+; \quad E_c^L(nL) = prev_E_c$$

$\Rightarrow$ call the subroutine $E_c^+(E_c, x_+, x_+^L(nL), E_c^L(nL), x_+^H(nL), E_c^H(nL))$

to calculate effective barrier $E_c(x_+)$

$\Rightarrow$ set $prev_dir = current_dir$

$\Rightarrow$ set $prev_x_+ = x_+$

$\Rightarrow$ set $prev_E_c = E_c$

Keep loading: continues in the current nL-th level curve
or closes the minor loop and jumps back to the (nL − 2) level curve:

If ($current_direction = prev_direction$) and ($current_direction = increase$) then

If $(x_+ > x_+^H(nL))$ then

$\Rightarrow$ update the level number indicating the current $Ec(x_+)$ path as

$$nL = nL - 2$$

$\Rightarrow$ call the subroutine $E_c^+(E_c, x_+, x_+^L(nL), E_c^L(nL), x_+^H(nL), E_c^H(nL))$
to calculate effective barrier $E_c(x_+)$

set $prev_dir = current_dir$

set $prev_x_+ = x_+$

set $prev_E_c = E_c$

Keep unloading: continues in current nL-th level curve
or closes the minor loop and jumps back to the (nL − 2) level curve:

If ($current_direction = prev_direction$) and ($current_direction = decrease$) then

If $(x_+ < x_+^L(nL))$ then

$\Rightarrow$ update the level number indicating the current $E_c(x_+)$ path as

$$nL = nL - 2$$

$\Rightarrow$ call the subroutine $E_c^-(E_c, x_+, x_+^L(nL), E_c^L(nL), x_+^H(nL), E_c^H(nL))$
to calculate effective barrier $E_c(x_+)$

$\Rightarrow$ set $prev_dir = current_dir$

$\Rightarrow$ set $prev_x_+ = x_+$

$\Rightarrow$ set $prev_E_c = E_c$

The reversal points only need to be updated at convergence values. As indicated in equations (2.24), (2.25) and (2.26), the model is highly nonlinear. Iterations are needed to reach the convergence solution. During each iteration, the reversal points and level numbers which are used to calculate the effective barrier $E_c(x_+)$ are kept unchanged. The iteration schemes for loading and unloading directions are illustrated in Figure 2.10 and Figure 2.11, respectively.

The above minor loop algorithms of the parametrization method are then implemented into a Fortran program. An unconditionally stable and very efficient ODE solver Radau5

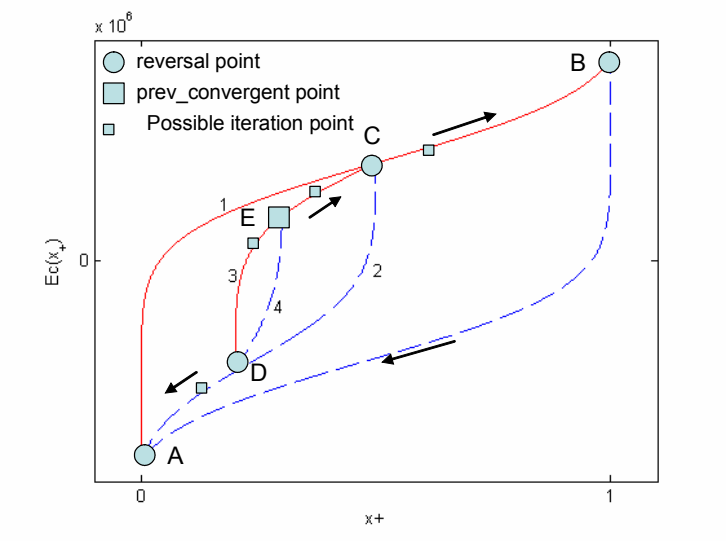


Figure 2.10: Iteration scheme for loading direction

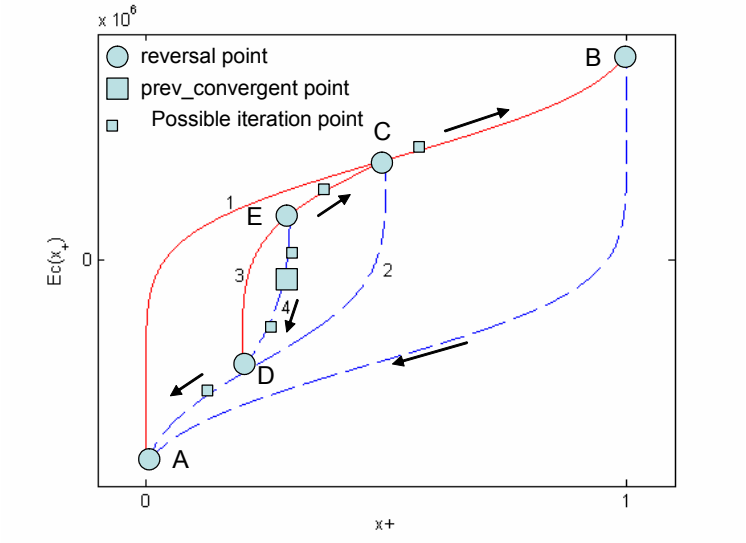


Figure 2.11: Iteration scheme for unloading direction

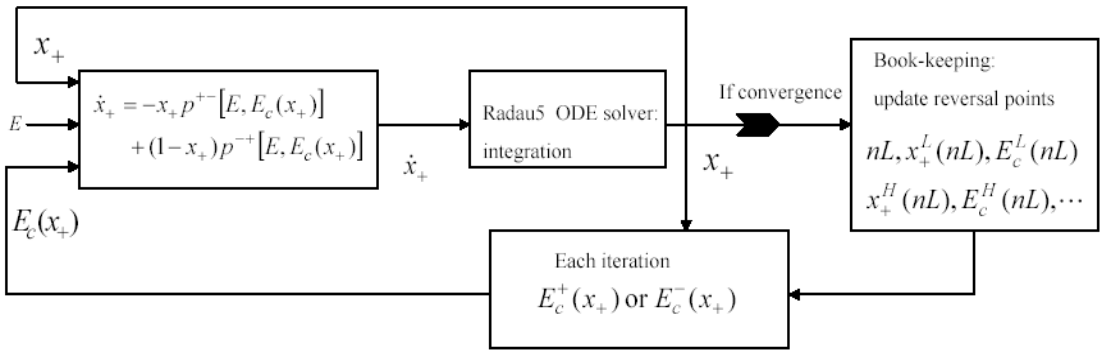


Figure 2.12: Block diagram of parametrization method implementation

developed by Harrier and Wanner [71], is to used to integrate equation (2.24). It is based on an implicit Runge-Kutta scheme and is particularly suited for stiff systems. The scheme of the complete implementation can be summarized in Figure 2.12

2.4 Simulation Results

After implementing the parametrization method into Fortran program. In this section we will demonstrate the efficiency of the implementation by illustrating some simulation results of rate dependent responses and minor loop behaviors of the PZT materials. The model parameters are fit with the experimental data [64] for PZT PIC-151 stack actuator made by Physik Instrumente. The identified major loop effective barriers are shown in Figure 2.5. The simulation results are also compared to the corresponding experimental results. All the experimental results in the following sections are taken from [64].

2.4.1 Rate Effects

First, we study the rate dependent effects of the PZT model by doing full major loop simulations at different loading rates. The applied electric fields E used are shown in Figure 2.13. The electric field E starting at the saturation field $1.5kV/mm$ are unloaded to $-1.5kV/mm$ and loaded back to $1.5kV/mm$ through a full-loop at rates of $0.05kV.mm/s$, $0.5kV.mm/s$ and $0.5kV.mm/s$, respectively.

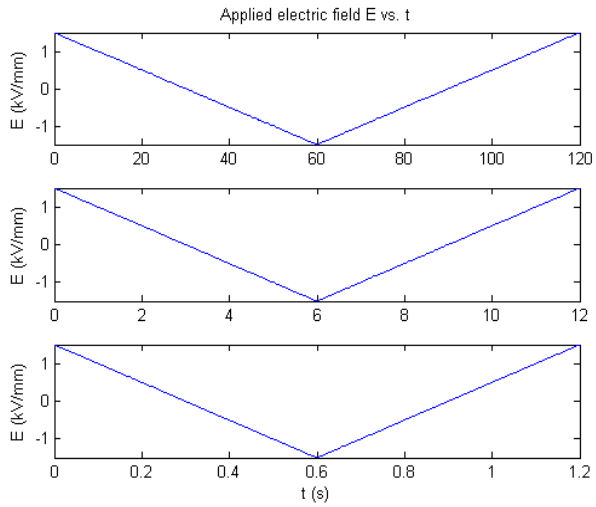


Figure 2.13: E vs. t at rates of $0.05kV/mm/s$, $0.5kV/mm/s$ and $5.0kV/mm/s$

Initial conditions for the simulation are:

$nL = 1$, $x_+^H(1) = 1$, $E_c^H(1) = 1.5e6V/m$, $x_+^L(1) = 0$, $E_c^L(1) = -1.5e6V/m$,

$prev_x_+ = 1$, $prev_E_c = 1.5e6V/m$, $prev_dir = DEC$.

All the subsequent simulations use the same initial conditions. We choose the activation volume $V_D = 1.0e-21/m^3$ and the relaxation time $\tau_x = 0.2s$. Figure 2.14(a) shows the simulation results of polarization vs. electric field. We can see that the hysteresis loop becomes wider as the loading rate increasing. This is due to delayed response of the domain switching to the faster loading. This rate dependent behavior of the PZT actuator is also clearly demonstrated in the corresponding experimental results in Figure 2.14(b). The results show that the parametrization method can reflect the rate dependent behavior of the PZT actuator

2.4.2 Minor Loop behaviors

The simulation starts from $x_+ = 1$, the state of fully $+180°$ polarity at an electric field of $1.5kV/mm$. The loading and unloading history of the applied field is shown in Figure 2.15. The constant rate for this simulation is set to be $0.05kV/mm/s$. The reversal points

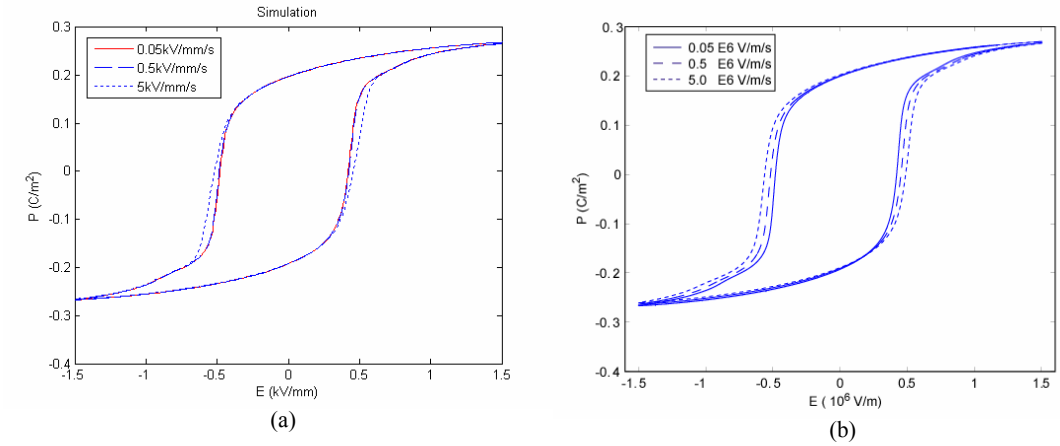


Figure 2.14: Full-loop P-E responses for different loading rates: (a) simulation; (b) experiment.

of the applied fields are chosen at $0kV/mm$, $0.35kV/mm$, $0.43kV/mm$, $0.50kV/mm$ and $0.8kV/mm$. A comparison of the simulation results with the experimental results is shown in Figure 2.16. The simulation result of the model gives the overall representation of the first order reversal behavior of the PZT actuator as demonstrated by the experimental results. We can see that the model does not reproduce the minor loops accurately. The simulation predicts instantaneous reversal of polarization with the switching direction of the applied electric field. However, the experimental result in Figure 2.16(a) shows that at the region close to the zero polarization region, the polarization does not reverse immediately with the switching direction of the applied electric field. Experimental evidences given in [64] indicates that there is a third phase, the 90° phase, which is between the $+180°$ phase and the $-180°$ phase, and the 90° phase has a longer switching time than the $\pm 180°$ phases. The particles that have switched from the $-180°$ phase into the 90° phase will not jump back to the original $-180°$ phase immediately at the time of switching applied field, instead they continue on toward the $+180°$ phase causing the rounded shape of polarization curve at the reversal point near the zero polarization region. It is noticed that some minor loop shown in the simulation is outside the major loop. This is due to minor loops in effective barrier $E_c(x_+)$ curves in the parametrization method are constructed by linear mapping

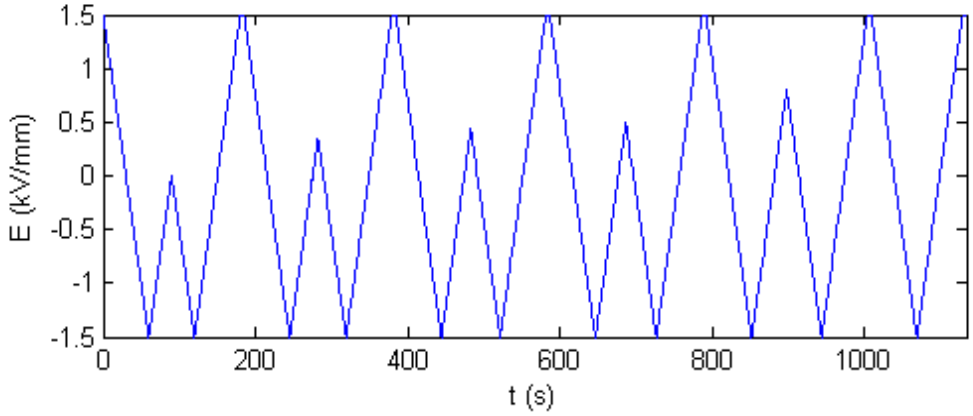


Figure 2.15: Electric field input for the first order reversal minor loops

of the corresponding portions of the major loop loops, which has no guarantee that minor loops are stay inside the major loop. So the minor loop outside the major loop in effective barrier $E_c(x_+)$ curves will produce the minor loop outside the major loop of P-E hysteresis curves.

More complicated second order reversal minor loop behaviors at different loading rates are shown in Figure 2.17 and Figure 2.18. The time histories of the applied fields at rates at $0.05kV/mm/s$, $0.5kV/mm/s$, $5.0kV/mm/s$ are shown in Figure 2.17. In this example, the second order reversal minor loops are produced by partial loading along the major loop and then partial unloading and then loading again to reach out the unloading points as illustrated in 2.17. The resulted minor loops for these loading and unloading inputs are shown in Figure 2.18: (a)-(c) are simulation results; (d)-(f) are corresponding experimental results. The results clearly indicate the rate dependent behaviors of the PZT actuator. Due to the delayed response of the domain switching to the applied field, the minor loops of the P-E hysteresis responses are shifted and do not close with the increased rates, especially at the transition region around the coercive field. The simulation results of the parametrization model reflect the changes of the rate dependent minor loop behaviors as illustrated in Figure 2.19.

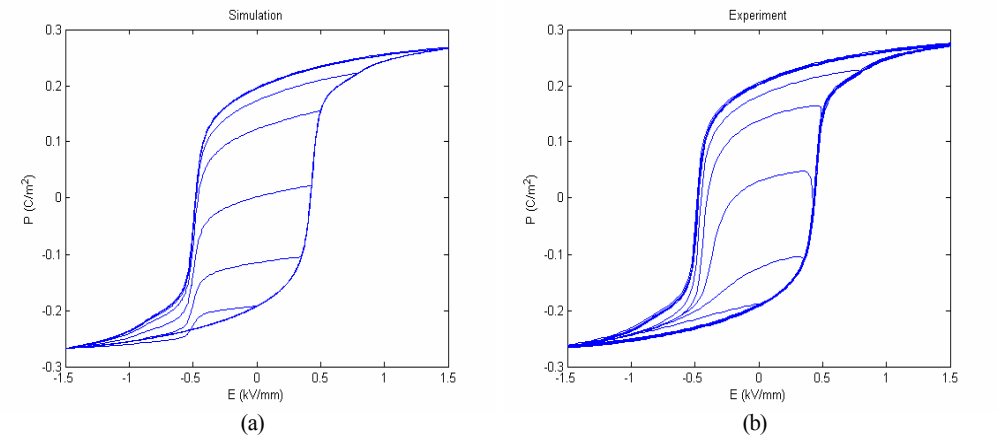


Figure 2.16: First order reversal: (a) simulation; (b) experiment.

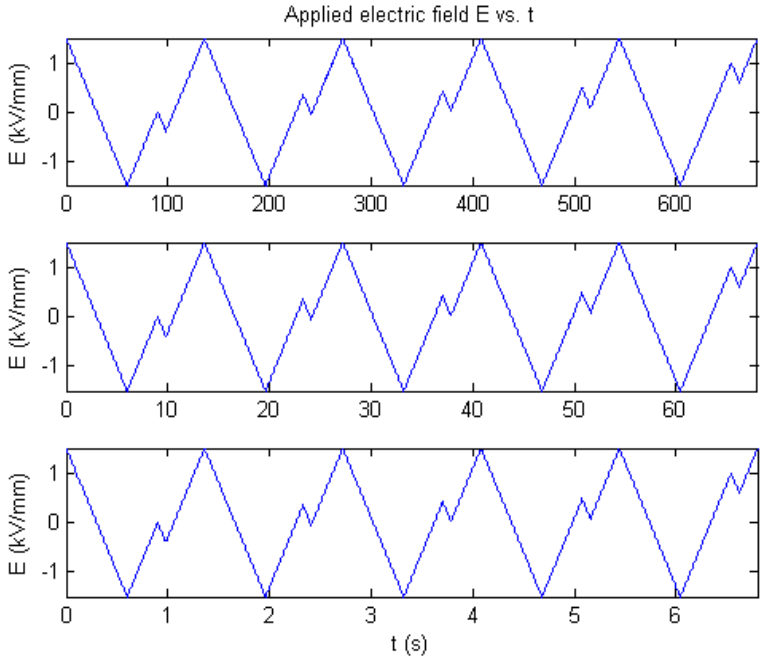


Figure 2.17: Electric Field inputs for second order reversal at rates of $0.05kV/mm/s$, $0.5kV/mm/s$, $5.0kV/mm/s$

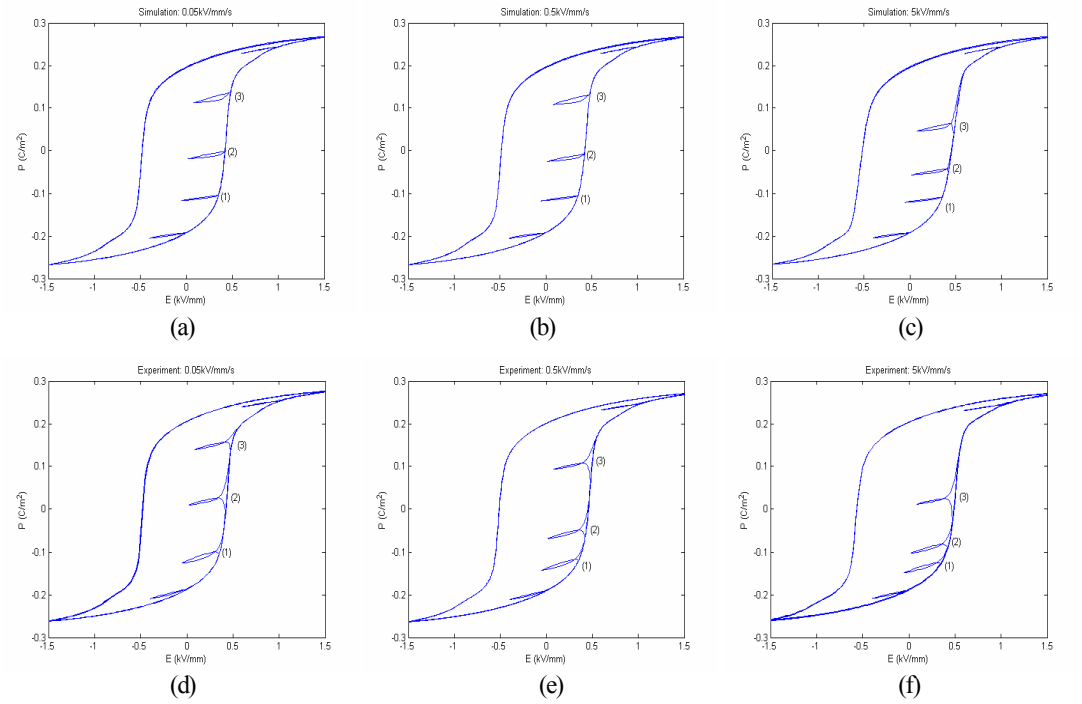


Figure 2.18: Second order reversal: (a), (b) and (c) are simulation responses; (d), (e) and (f) are respective experimental results.

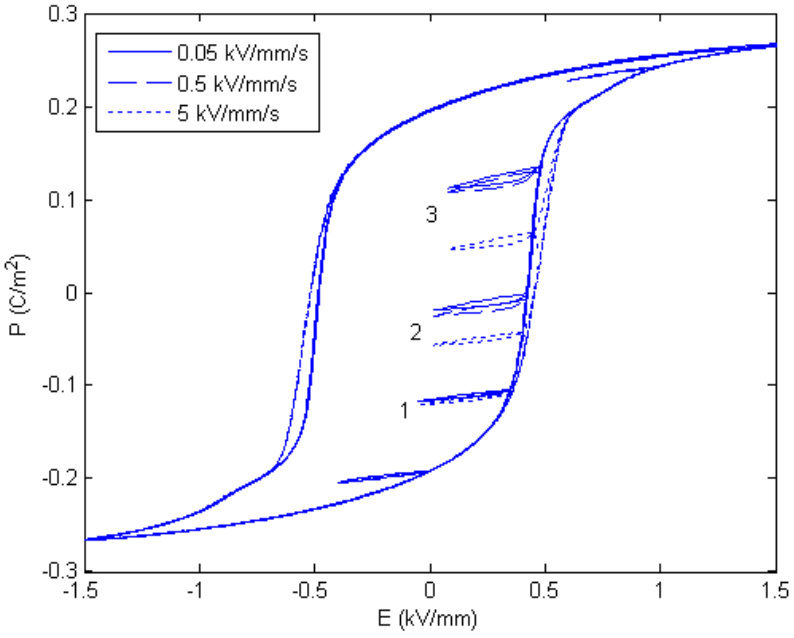


Figure 2.19: Second order reversal at different rates.

2.4.3 Relaxation Behaviors

Another important time dependent behavior of the PZT actuator is the relaxation or creep. The relaxation behavior is observed when the applied electric field is held constant and the polarization continues to change over time. To study the relaxation behavior, the electric field is held constant at different levels for the time period of $20s$ as shown in Figure 2.20 (a)-(c). The relaxation behavior is shown in the P vs. E diagram in Figure 2.20 (g)-(i). The simulations qualitatively show the rate dependent relaxation behavior in the P-E plots. But from the time responses of the polarization as in Figure 2.20 (d)-(f), the relaxations happen instantaneously. This does not reflect the slow and asymptotic relaxation over time behaviors as shown in the experimental results in Figure 2.21 (d)-(f). The two parameters in the free energy model related to the time behaviors of the PZT materials are the activation volume V_D and the relaxation time τ_x, which dictate the extent and rate of the relaxation. Unfortunately, we are not able to choose appropriate values of the activation volume V_D and the relaxation time τ_x to reflect the asymptotic relaxation behavior of the PZT actuator. One possible mechanism behind this is that the 90° phase undergo a slower reorientation process than the $\pm 180^\circ$ phases [64], which results in a slow and asymptotic relaxation behavior as shown in Figure 2.21 (d)-(f).

2.5 Summary

In this chapter, we have developed a modified parametrization method to model the rate dependent minor loop behaviors of the PZT materials. The robust implementation of the model in Fortran program is computationally efficient compared to the quadrature implementation of the homogenized energy model (2.22). Compared to the experimental results, the simplified model has good represent the complicated minor loops behaviors of the polycrystalline PZT materials and reflects some of the rate dependent effects. The parametrized model, however, cannot represent relaxation behaviors of the PZT actuator correctly. The simulations qualitatively shows the relaxation in P-E hysteresis but the relaxation of polarization is not in the same time scale of the experimental results. Further research is needed to address this issue.

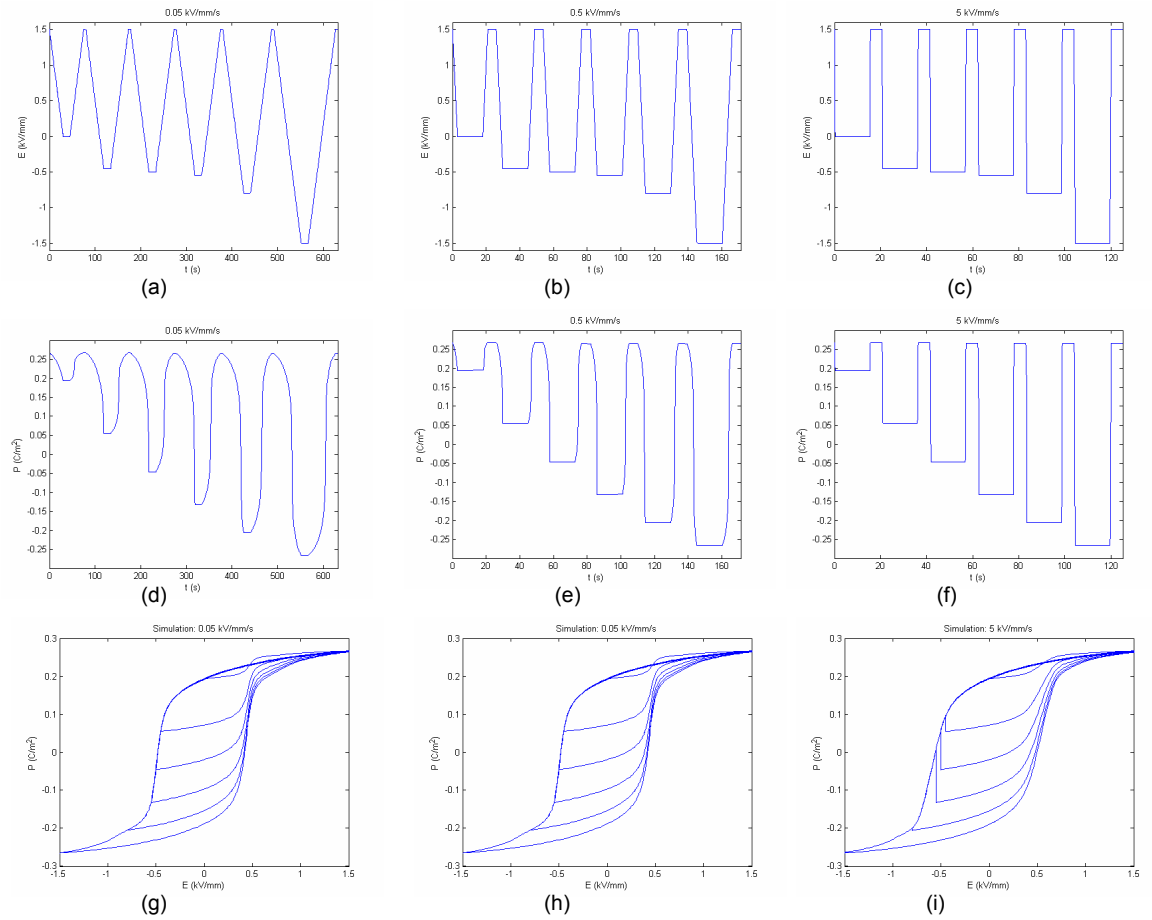


Figure 2.20: Relaxation simulations for $V_D = 1.0e-21/m^3$ and $\tau_x = 0.2s$: (a)-(c) applied fields at rates of $0.05kV/mm/s$, $0.5kV/mm/s$, $5.0kV/mm/s$; (d)-(f) time responses of the polarization at respecitive loading rates; (g)-(i) P vs. E at different rates

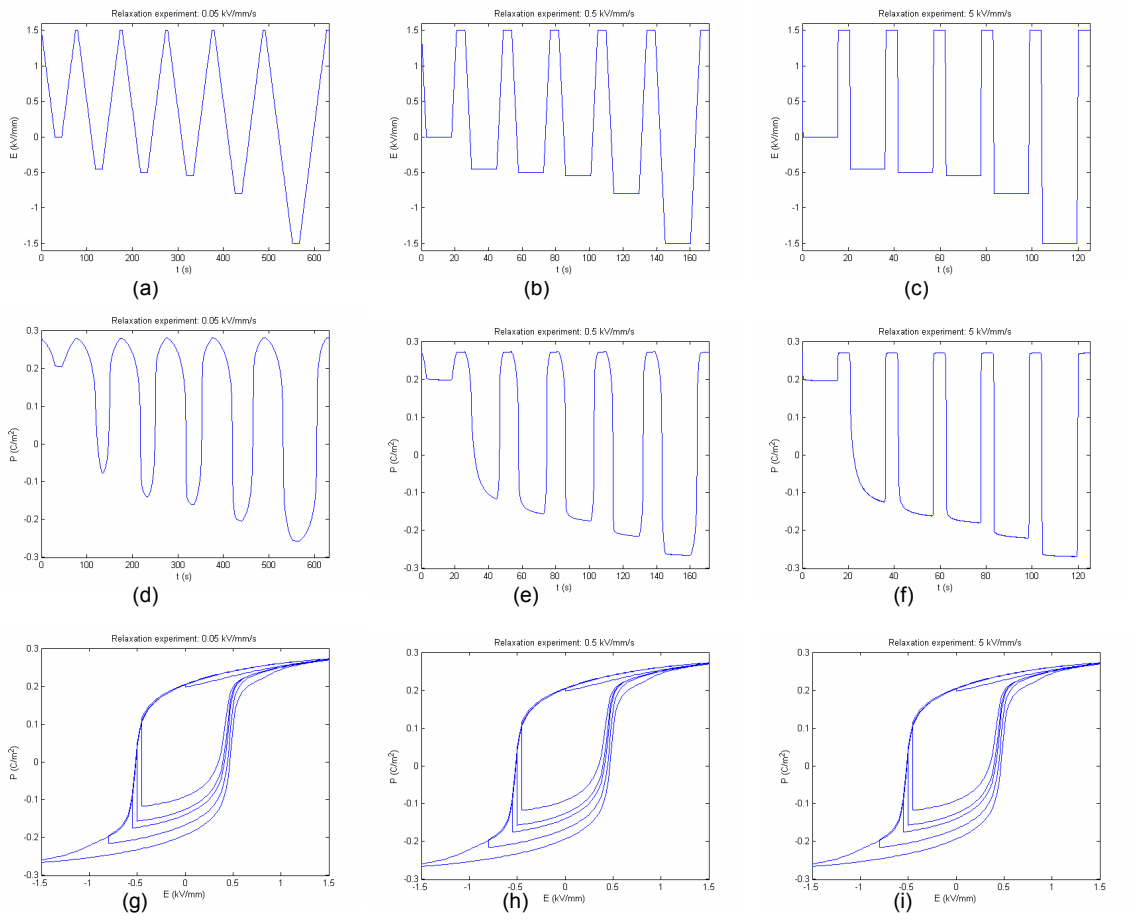


Figure 2.21: Relaxation experiments: (a)-(c) applied fields at rates of $0.05kV/mm/s$, $0.5kV/mm/s$, $5.0kV/mm/s$; (d)-(f) time responses of the polarization at respecitive loading rates; (g)-(i) P vs. E at different rates

Chapter 3

Finite Element Analysis of SMA Components

Due to their unique features, the superelasticity and shape memory effect, SMAs can produce large recoverable deformations and generate large forces. They have been widely used in many applications. Medical device applications include endovascular stent [10], etc. They are also used as hysteresis-induced damping materials in civil structures [12, 13, 14]. More recently, thin film SMAs have become very promising candidates for microacutors due to their high work output density [15, 16, 17]. Some interesting applications include microgrippers, micropumps, microcantilever switches and scanners [18, 19, 20, 21]. SMA components also exhibit highly nonlinear, loading-history and temperature dependent behaviors due to the inhomogeneities of stress and temperature fields in the structures. Typically, SMA actuators are driven by electric current heating and convective cooling to trigger phase transformations between martensite and austenite to generate the actuator deformations/forces. These are strong thermo-mechanically coupled problems due to the latent heats released and absorbed during austenite-martensite phase transformations. To facilitate the development of these new devices and obtain a better understanding of their working mechanism, an efficient computational tool such as finite element method (FEM) has to be used.

In this chapter, a 1-D free energy perfect single crystal model is implemented into finite element programs to simulate SMA components, such as bar, wire and beam. First, an overview of the free energy perfect single crystal SMA model is given. Then this model is implemented into multiphysics finite element program FEMLAB to analyze behaviors of SMA bar and wire components under isothermal, non-isothermal quasistatic loadings. By including latent heat effect, the responses of an SMA wire actuator driven by electric current

heating and convective cooling under different thermal boundary conditions is investigated. Then based on the small deformation Euler-Bernoulli beam theory, the 1-D SMA model is also implemented into the FEMLAB using its PDE general form and study the quasistatic inhomogeneous bending behaviors of a cantilever SMA beam under the isothermal conditions. Finally, using a different scheme, the 1-D SMA model is also implemented to the finite element code ANSYS using its BEAM188 element and user defined material subroutine USERMAT to study the beam bending problem of an SMA cantilever beam, which also serves as a validation tool for the FEMLAB implementation. Convergence behavior and accuracy are studied systematically for different convergence criteria in ANSYS as well as other relevant parameters such as element, substep and integration point number.

3.1 Free Energy SMA Model

In this section, an overview is given for the basic equations of the 1D free energy SMA model developed by Muller, Achenbach and Seelecke [22, 23, 24]. The 1-D SMA model can be used to model SMA wire, bar and beam structures. Motivated by macroscopic observations, a lattice layer is treated as the basic element of the model. Under uniaxial loading, apart from austenite A there are only two martensitic variants, denoted as M_+ and M_-. Figure (3.1) illustrates three equilibrium configurations for corresponding phases. M_+ and M_- may be considered as sheared versions of A with large shear strain. The phase fractions of austenitic and martensitic layers are denoted as x_A, x_+ and x_-, respectively and satisfy the following relationship

$$x_A + x_+ + x_- = 1 \tag{3.1}$$

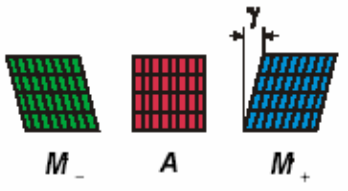


Figure 3.1: Lattice configurations in austenitic phase A and martenstic twin phases M_+, M_-.

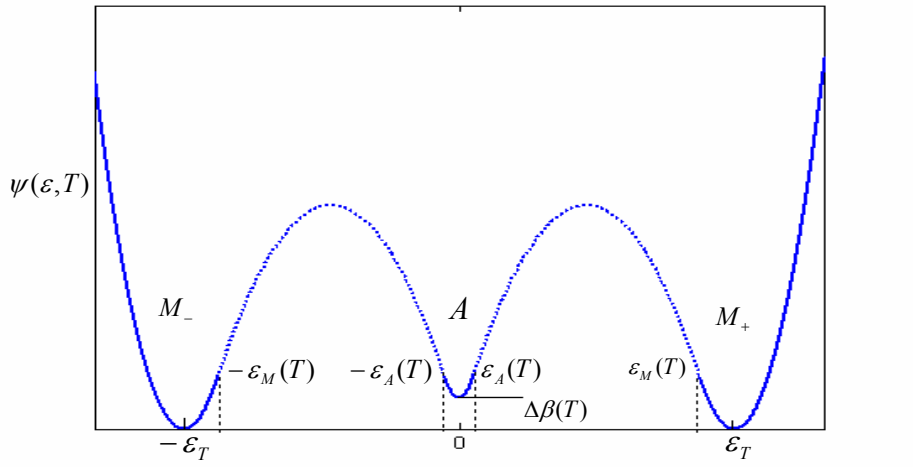


Figure 3.2: Piecewise quadratic Helmholtz free energy function $\psi(\varepsilon, T)$.

3.1.1 Free Energy

The piecewise quadratic Helmholtz free energy function $\psi(\varepsilon, T)$ is constructed by five parabolae using the measured material properties as [24, 33, 65]

$$\psi(\varepsilon,T) = \begin{cases} \frac{E_M}{2}(\varepsilon+\varepsilon_T)^2 & , \quad \varepsilon \le -\varepsilon_M(T) \\ a\varepsilon^2 + b\varepsilon + c & , \quad -\varepsilon_M(T) < \varepsilon < -\varepsilon_A(T) \\ \frac{E_A}{2}\varepsilon^2 + \triangle\beta(T) & , \quad |\varepsilon| \le \varepsilon_A(T) \\ a\varepsilon^2 - b\varepsilon + c & , \quad \varepsilon_A(T) < \varepsilon < \varepsilon_M(T) \\ \frac{E_M}{2}(\varepsilon-\varepsilon_T)^2 & , \quad \varepsilon \ge \varepsilon_M(T)\,. \end{cases} \tag{3.2}$$

where E_M, E_A are elastic moduli of martensite and austenite, respectively. The quantity ε_T is the maximum recoverable quasiplastic residual strain, which can be identified from experiment. The temperature dependent transformation strains are denoted as $\varepsilon_M(T)$ and $\varepsilon_A(T)$, which connect the the concave parabolae to the convex parabolae. As shown in Figure 3.2, the lateral wells of the free energy correspond to the martensitic variants M_+ and M_-, and the central well corresponds to the austenite A. The local minimum of the austenite well $\triangle\beta(T)$ is assumed to vary linearly with temperature [24, 65] as

$$\triangle\beta(T) = \triangle u - \triangle\eta T \tag{3.3}$$

where $\triangle u$ and $\triangle\eta$ can be identified using tensile test data at two different temperatures. Using the C^1 continuity conditions in (3.2) at the inflection points $\varepsilon_M(T)$ and $\varepsilon_A(T)$, we have the following relation

$$\triangle\beta(T) = \triangle u - \triangle\eta T = \frac{1}{2}E_M\varepsilon_T^2 + \frac{1}{2}(E_M - E_A)\varepsilon_M(T)\varepsilon_A(T) - \frac{1}{2}E_M\varepsilon_T[(\varepsilon_M(T)+\varepsilon_A(T)] \tag{3.4}$$

Under a mechanical load, the associated effective potential energy, the Gibbs free energy is

$$G(\varepsilon,\sigma,T) = \psi(\varepsilon,T) - \sigma\varepsilon \tag{3.5}$$

where $\sigma\varepsilon$ is the elastic potential energy due to the applied stress σ. Phase transitions occur once the barriers between phase specific Gibbs free energy minimums are eliminated by

thermal-mechanical loading as illustrated in Figure 3.3. The barriers may be eliminated by the transformation stresses

$$\sigma_A(T) = E_A \varepsilon_A(T) \tag{3.6}$$

$$\sigma_M(T) = E_M \left[\varepsilon_M(T) - \varepsilon_T\right] \tag{3.7}$$

These two stresses can be identified as pseudoelastic yield and recovery stresses in the tensile experiment, and from the experimental observation, the width of the stress strain hysteresis loop is assumed to be constant

$$\sigma_A(T) - \sigma_M(T) = \triangle\sigma \tag{3.8}$$

Two tensile tests as shown in Figure 3.4 are conducted at different temperatures T_L and T_U to identify the material properties used to construct the Helmholtz free energy (3.2). Once the parameters E_A, E_M, ε_T, $\sigma_A(T_L)$, $\sigma_A(T_U)$ and $\triangle\sigma$ are identified, from (3.4) and (3.6-3.8), $\triangle u$, $\triangle\eta$, $\sigma_A(T)$ and $\sigma_M(T)$ can be calculated as

$$\triangle\eta = \frac{-1}{2(T_U - T_L)} \left[\sigma_A(T_U)^2 - \sigma_A(T_L)^2\right] C_E - \left[\sigma_A(T_U) - \sigma_A(T_L)\right] \left[2\varepsilon_T + \triangle\sigma C_E\right] \tag{3.9}$$

$$\triangle u = \frac{1}{2} \left[\sigma_A(T_U)^2 C_E - \sigma_A(T_U)(2\varepsilon_T + \triangle\sigma C_E) + \triangle\sigma\varepsilon_T\right] + \triangle\eta T_U \tag{3.10}$$

$$\sigma_A(T) = \frac{2\varepsilon_T + \triangle\sigma C_E - \sqrt{\left(2\varepsilon_T + \triangle\sigma C_E\right)^2 - 4C_E \left[\triangle\sigma\varepsilon_T - 2\triangle\beta(T)\right]}}{2C_E} \tag{3.11}$$

$$\sigma_M(T) = \sigma_A(T) - \triangle\sigma \tag{3.12}$$

where $C_E = \frac{1}{E_A} - \frac{1}{E_M}$ is a constant.

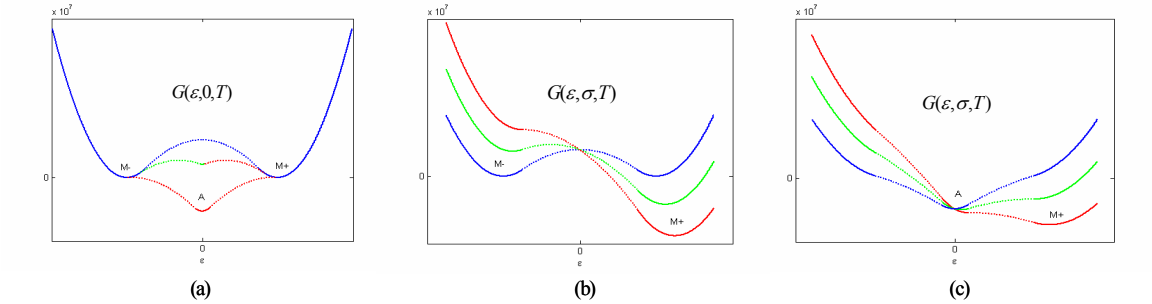


Figure 3.3: Gibbs free energy landscapes under thermo-mechanical loadings: (a) Under zero stress: temperature induced transformation; (b) At low temperature: stress induced marternsitic transformation; (c) At high temperature: stress induced martensitic transformation.

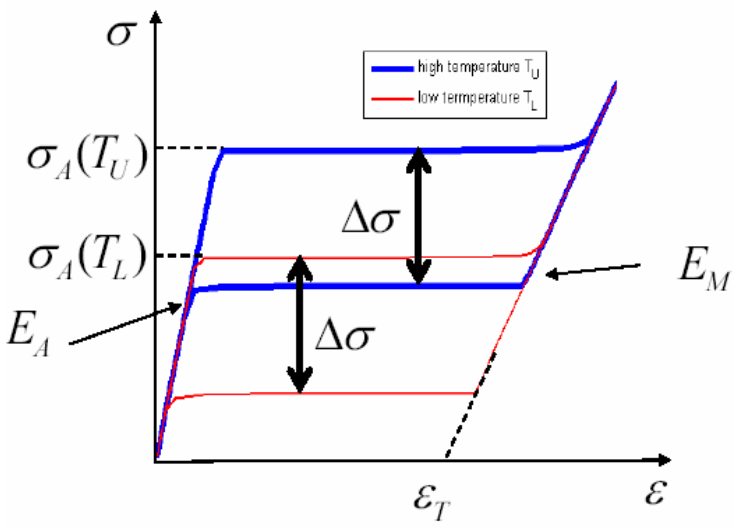


Figure 3.4: Material parameters identification through two tensile tests at different temperature T_L and T_U.

3.1.2 Constitutive Stress-Strain Relationship

The average strain of the specimen is the sum of the strains in each phase weighted by their fractions

$$\varepsilon = x_A \langle \varepsilon_A \rangle + x_+ \langle \varepsilon_+ \rangle + x_- \langle \varepsilon_- \rangle \tag{3.13}$$

$\langle \varepsilon_A \rangle$, $\langle \varepsilon_+ \rangle$, $\langle \varepsilon_- \rangle$ are the average strains in each phase, which can be calculated according to Boltzmann statistics [24, 33]

$$\langle \varepsilon_A \rangle = \frac{\int_{-\varepsilon_A}^{\varepsilon_A} \varepsilon e^{-G(\varepsilon,\sigma,T)V_D/kT}\, d\varepsilon}{\int_{-\varepsilon_A}^{\varepsilon_A} e^{-G(\varepsilon,\sigma,T)V_D/kT}\, d\varepsilon} \approx \frac{\sigma}{E_A} \tag{3.14}$$

$$\langle \varepsilon_+ \rangle = \frac{\int_{\varepsilon_M}^{\infty} \varepsilon e^{-G(\varepsilon,\sigma,T)V_D/kT}\, d\varepsilon}{\int_{\varepsilon_M}^{\infty} e^{-G(\varepsilon,\sigma,T)V_D/kT}\, d\varepsilon} \approx \frac{\sigma}{E_M} - \varepsilon_T \tag{3.15}$$

$$\langle \varepsilon_- \rangle = \frac{\int_{-\infty}^{-\varepsilon_M} \varepsilon e^{-G(\varepsilon,\sigma,T)V_D/kT}\, d\varepsilon}{\int_{-\infty}^{-\varepsilon_M} e^{-G(\varepsilon,\sigma,T)V_D/kT}\, d\varepsilon} \approx \frac{\sigma}{E_M} + \varepsilon_T \tag{3.16}$$

From (3.13-3.16), we can derive the explicit stress-strain relation as

$$\sigma(\varepsilon) = \frac{E_M \left[\varepsilon - (x_+ - x_-)\varepsilon_T\right]}{x_+ + x_- + \frac{E_M}{E_A} x_A} \tag{3.17}$$

This is the constitutive stress-strain equation that will be used in the finite element implementation. The stress is a function of strain and phase fractions.

3.1.3 Evolution of Phase Fractions

The evolution of the phase fractions x_α ($\alpha = A, +, -$) is governed by the rate laws

$$\begin{aligned} \dot{x}_+ &= -x_+ p^{+A} + x_A p^{A+} \\ \dot{x}_- &= -x_- p^{-A} + x_A p^{A-} \end{aligned} \tag{3.18}$$

and from (3.1), the phase fraction of austenite x_A is given as

$$x_A = 1 - x_+ - x_- \tag{3.19}$$

The rate of change of $x_\pm$ is the sum of a loss that due to layers jumping from the $M_\pm$ phase to the A phase, and a gain that due to layers jumping from the A phase phase to the $M_\pm$ phase. The number of jumps are proportional to the phase fractions x_+, x_-. The quantities $p^{\alpha\beta}$ in 3.18 are called transition probabilities. For instance, p^{+A} is the transition probability from M_+ phase to A phase. Transition probabilities are computed as the product of the probability of achieving the energy required to overcome the energy barrier and the frequency at which jumps are tempted. They are given as

$$\begin{aligned} p^{+A}(\sigma,T) &= \tfrac{1}{\tau}\frac{e^{-G(\varepsilon_M,\sigma,T)V_D/kT}}{\int_{\varepsilon_M}^{\infty} e^{-G(\varepsilon,\sigma,T)V_D/kT}d\varepsilon} \\ p^{A+}(\sigma,T) &= \tfrac{1}{\tau}\frac{e^{-G(\varepsilon_A,\sigma,T)V_D/kT}}{\int_{-\varepsilon_A}^{\varepsilon_A} e^{-G(\varepsilon,\sigma,T)V_D/kT}d\varepsilon} \\ p^{-A}(\sigma,T) &= \tfrac{1}{\tau}\frac{e^{-G(-\varepsilon_M,\sigma,T)V_D/kT}}{\int_{-\infty}^{-\varepsilon_M} e^{-G(\varepsilon,\sigma,T)V_D/kT}d\varepsilon} \\ p^{A-}(\sigma,T) &= \tfrac{1}{\tau}\frac{e^{-G(-\varepsilon_A,\sigma,T)V_D/kT}}{\int_{-\varepsilon_A}^{\varepsilon_A} e^{-G(\varepsilon,\sigma,T)V_D/kT}d\varepsilon} \end{aligned} \tag{3.20}$$

where τ is the relaxation time for the process. Transition probabilities $p^{\alpha\beta}$ are functions of stress σ and temperature T. The integrals in (3.20) can be expressed as

$$\begin{aligned} p^{\pm A}(\sigma,T) &= \tfrac{1}{\tau}\frac{e^{-\frac{V_D}{2E_M KT}(\sigma_M \mp\sigma)^2}}{\operatorname{erf} c\left[\sqrt{\frac{V_D}{2E_M KT}}(\sigma_M \mp\sigma)\right]} \\ p^{A\pm}(\sigma,T) &= \tfrac{1}{\tau}\frac{e^{-\frac{V_D(\sigma_A \mp\sigma)^2}{2E_A KT}}}{\operatorname{erf}\left[\sqrt{\frac{V_D}{2E_A KT}}(\sigma_A+\sigma)\right]+\operatorname{erf}\left[\sqrt{\frac{V_D}{2E_A KT}}(\sigma_A-\sigma)\right]} \end{aligned} \tag{3.21}$$

where

$$\operatorname{erf}(x) = \frac{2}{\sqrt{\pi}}\int_0^x e^{-t^2}dt \tag{3.22}$$

is the standard error function and

$$\operatorname{erf} c(x) = 1 - \operatorname{erf}(x) \tag{3.23}$$

is the complement error function.

3.1.4 Balance of Internal Energy

SMA actuators are typically driven by electric current heating and convective cooling. Coupled with the mechanical loading, the temperature changes trigger the phase transformations between martensite and austenite, and consequently, generate the deformation of the SMA actuator. For the modeling purpose, this necessitates the inclusion of the balance of the internal energy. Assuming uniform temperature changes throughout the SMA material, the heat transfer equation reads [24]

$$\rho c\dot{T} = -\alpha S_V(T - T_0) + j(t) - (h_{M_+} - h_A)\dot{x}_+ - (h_{M_-} - h_A)\dot{x}_- \tag{3.24}$$

where ρ is the density and c is the specific heat. We assume the same specific heats for austenite and martensite. The first term on the right hand side (RHS) of (3.24) is the heat convection to the environment with temperature T_0. The heat transfer coefficient between the SMA actuator surface and its surrounding environment is denoted by α and the surface area to volume ratio is S_V. The Joule heating is denoted by $j(t)$. The last two terms in RHS of (3.24) account for the rate dependent heat generation and loss due to phase transformations, where $h_{M_\pm} - h_A$ are called the latent heats of the transformations and given as

$$h_{M_\pm} - h_A = -\frac{\sigma^2}{2}\frac{E_M - E_A}{E_M E_A} \mp \sigma\varepsilon_T - \triangle u \tag{3.25}$$

where $\triangle u$ is given in (3.10). Detailed discussion about latent heats is presented in [24, 65].

3.1.5 Summary of Model Equations

The model can be summarized as the stress-strain relation (3.13)complemented by a system of nonlinear ODEs, which govern the evolution of the martensite phase fractions (3.18)and the temperature (3.24):

$$\varepsilon = x_A\frac{\sigma}{E_A} + x_+\left(\frac{\sigma}{E_M} - \varepsilon_T\right) + x_-\left(\frac{\sigma}{E_M} - \varepsilon_T\right) \tag{3.26}$$

$$\begin{aligned}\dot{x}_+ &= -x_+ p^{+A} + x_A p^{A+}\\ \dot{x}_- &= -x_- p^{-A} + x_A p^{A-}\end{aligned} \tag{3.27}$$

$$\rho c\dot{T} = -\alpha S_V(T - T_0) + j(t) - (h_{M_+} - h_A)\dot{x}_+ - (h_{M_-} - h_A)\dot{x}_- \tag{3.28}$$

where the transition probabilities $p^{\alpha\beta}(\sigma, T)$ are given in (3.21). So for given applied stress $\sigma(t)$ and Joule heat $j(t)$, we can evaluate phase fraction $x_\alpha(t)$ and temperature $T(t)$ by integrating the ODEs of (3.27) and (3.28) simultaneously, and then calculate the resulted strain $\varepsilon(t)$ from (3.26). Alternatively, prescribing strain $\varepsilon(t)$ and Joule heat $j(t)$, we can calculate $x_\alpha(t), T(t)$ and $\sigma(t)$. Initial conditions of phase fractions $x_+(0)$, $x_-(0)$ and temperature $T(0)$ need to be given to start the integration.

We summarize this section by illustrating the temperature dependent stress-strain hysteresis behaviors of the perfect single crystal SMA material predicted by the model. Figure 3.5 demonstrates the stress-strain behaviors of the material at different temperatures. At low temperature, the model predicts the quasiplastic deformation and phase transformations only occur between the two martensite variants M_+ and M_- because the austenite is unstable at this low temperature. At high temperature, the model predicts the superelastic behavior of SMA materials and phase transformations occur between austenite A and martensite $M_\pm$. The stress level of the hysteresis shifts as the temperature changes, which is dictated by the temperature dependent transformation stresses given in (3.11-3.12). As we can see, the free energy model can describe the temperature dependent quasiplastic and superelastic behavior of the SMA material and the hysteresis loops are characterized by sharp transitions as expected for single crystal behavior. This temperature dependent stress-strain behaviors forms the basis for the subsequent finite element analysis of SMA structures.

3.2 Finite Element Analysis of SMA Bars and Wires Using FEMLAB

The constitutive model given in (3.26-3.28) for SMA material is highly nonlinear, loading-history dependent, which is governed by the evolution of phase fractions and thermo-mechanical coupling. A numerical method is necessary to simulate the complex responses of SMA structures governed by space and time dependent partial differential equations

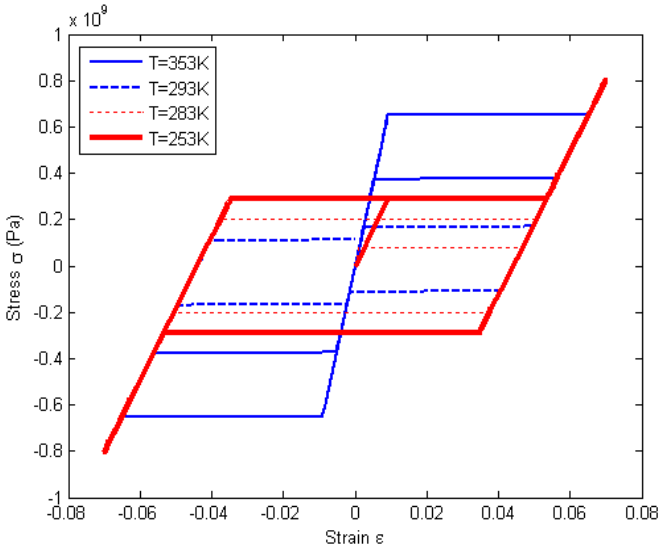


Figure 3.5: Temperature dependent stress-strain relation.

(PDEs). In this section, we implement the free energy SMA model developed in the previous section into the multiphysics finite element software package FEMLAB to model SMA bar/wire structures. FEMLAB is an open and flexible system used to solve different types of scientific and engineering problems based on PDEs by using finite element method. In the implementation, the ODEs of phase fraction evolution (3.27) are treated as degenerated PDEs which are coupled with the mechanical deformation and heat transfer equations to form a PDE system. The system is solved using a fully coupled approach.

First, under the isothermal assumption, we use a homogenous SMA bar as an example to validate the FE implementation and illustrate the model capabilities. Then SMA bars with varying cross-section and nonuniform temperature distribution are studied, respectively, inducing non-homogeneous phase transformations through the length of the SMA bar. They are followed by thermo-mechanical coupled analysis of tensile simulations of an SMA wire under insulated and fixed temperature boundary conditions with different loading rates, in which the only heat source is due to the phase transformation induced latent heats. Under insulated boundary condition, the temperature field along the SMA wire changes uniformly, and under fixed temperature boundary conditions, the temperature distribution along the

SMA wire is non-uniform, which induces non-homogeneous phase transformation along the SMA wire. We also study the performance of an SMA wire-spring actuator system driven by electric current heating and convective cooling under different thermal boundary conditions.

3.2.1 Implementation

FEMLAB is a modeling package for the simulation of general, coupled multifield physical processes based on balanced laws using finite element method. For a single solution variable u, the general form PDE reads [66]

$$d_a \frac{\partial u}{\partial t} + \nabla \cdot \Gamma = f \tag{3.29}$$

where d_a is the mass coefficient ; f is the source term; $\nabla \cdot \Gamma$ is the flux term with the divergence operator $\nabla = \begin{bmatrix} \frac{\partial}{\partial x} & \frac{\partial}{\partial y} & \frac{\partial}{\partial z} \end{bmatrix}$ and flux $\Gamma = \begin{bmatrix} \Gamma_x & \Gamma_y & \Gamma_z \end{bmatrix}$. For 1-D problems, we have $\nabla = \frac{\partial}{\partial x}$, and the general form PDE reads

$$d_a \frac{\partial u}{\partial t} + \frac{\partial \Gamma}{\partial x} = f \tag{3.30}$$

Typically, boundary conditions are given as either Dirichlet boundary condition or Neumann boundary conditions.

•Dirichlet boundary condition:

$$r = hu + b = 0 \tag{3.31}$$

•Neumann boundary condition:

$$-n \cdot \Gamma = g \tag{3.32}$$

In structure mechanics, Dirichlet and Neumann boundary conditions correspond to displacement and force boundary conditions, respectively.

Using the finite element method, the solution variable u within a discretized element is approximated as

$$u(x) = \sum_{i=1}^{k} U_i \varphi_i(x) \tag{3.33}$$

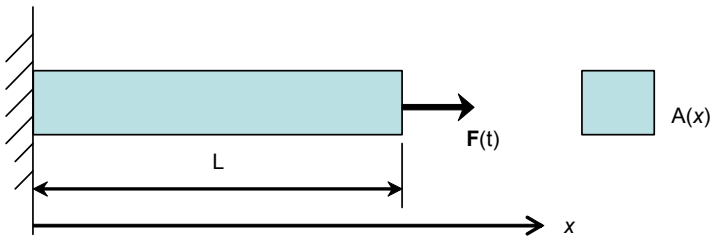


Figure 3.6: SMA bar

where $U_i = u(x_i)$ are the degrees of freedom to be solved for, and $\varphi_i(x)$ are the shape functions satisfying

$$\varphi_i(x_j) = \begin{cases} 1, i = j \\ 0, i \neq j \end{cases} \tag{3.34}$$

$$\sum_{i=1}^{k} \varphi_i(x) = 1 \tag{3.35}$$

The SMA bar is modeled as a PDE system using FEMLAB's general form PDE module. Considering an SMA bar structure shown in Figure 3.6 with varying cross section $A(x)$ and $u(x,t)$ as displacement, we can derive the equilibrium equation for the quasistatic case, neglecting the inertia as

$$\frac{\partial A(x)\sigma(x,t)}{\partial x} = 0 \tag{3.36}$$

and the boundary conditions as

$$u(0,t) = 0 \tag{3.37}$$

$$A(L)\sigma(L,t) = F(t) \tag{3.38}$$

where the cross section stress $\sigma(x,t)$ is given in (3.17)

$$\sigma(\varepsilon) = \frac{E_M\left[\varepsilon - (x_+ - x_-)\varepsilon_T\right]}{x_+ + x_- + \frac{E_M}{E_A}x_A} \tag{3.39}$$

The strain ε is defined as

$$\varepsilon = \frac{\partial u}{\partial x} = u_x \tag{3.40}$$

Then the stress can be expressed as a function of displacement as

$$\sigma = \frac{E_M \left[u_x(x) - (x_+ - x_-)\varepsilon_T\right]}{x_+ + x_- + \frac{E_M}{E_A} x_A} \tag{3.41}$$

And the phase fractions are governed by

$$\begin{aligned} \dot{x}_+ &= -x_+ p^{+A}(\sigma, T) + (1 - x_+ - x_-) p^{A+}(\sigma, T) \\ \dot{x}_- &= -x_- p^{-A}(\sigma, T) + (1 - x_+ - x_-) p^{A-}(\sigma, T) \end{aligned} \tag{3.42}$$

Due to the varying cross section $A(x)$, different cross sections see different stresses and consequently different evolutions of phase fractions. The phase fractions $x_+(x)$, $x_-(x)$ are also implicit functions of position x because of $\sigma(x)$. We treat the phase fractions x_+, x_- together with the displacement as the solution variables, which are discretized using FEM as

$$u(x) = \sum_{i=1}^{k} U_i \varphi_i(x)$$

$$x_\alpha(x) = \sum_{i=1}^{k} X_{\alpha i} \varphi_i(x)$$

where U_i, $X_{\alpha i}$ are the degrees of freedom, which are the values of u and x_α at the discretized finite element nodes to be solved.

Compared with the FEMLAB general form PDE, we can model the SMA bar under quasistatic loading as the following coupling PDE system

$$\begin{aligned} General\ form:\ d_{a1} \tfrac{\partial u}{\partial t} + \tfrac{\partial \Gamma_1}{\partial x} &= f_1 \\ 0 + \tfrac{\partial A(x)\sigma(x,t)}{\partial x} &= 0 \\ \Rightarrow\ d_{a1} = 0, \quad \Gamma_1 = A(x)\sigma(x,t), \quad f_1 &= 0 \end{aligned} \tag{3.43}$$

$$\begin{aligned} General\ form:\ d_{a2} \tfrac{\partial u}{\partial t} + \tfrac{\partial \Gamma_2}{\partial x} &= f_2 \\ \tfrac{\partial x_+}{\partial t} + 0 &= -x_+ p^{+A}(\sigma, T) + (1 - x_+ - x_-) p^{A+}(\sigma, T) \\ \Rightarrow\ d_{a2} = 1, \quad \Gamma_1 = 0, \quad f_2 &= -x_+ p^{+A}(\sigma, T) + (1 - x_+ - x_-) p^{A+}(\sigma, T) \end{aligned} \tag{3.44}$$

$$\begin{aligned} &General\ form:\ d_{a3}\tfrac{\partial u}{\partial t} + \tfrac{\partial \Gamma_3}{\partial x} = f_3 \\ &\tfrac{\partial x_-}{\partial t} + 0 = -x_- p^{-A}(\sigma, T) + (1 - x_+ - x_-)p^{A-}(\sigma, T) \\ \Rightarrow\ & d_{a3} = 1, \quad \Gamma_3 = 0, \quad f_3 = -x_- p^{-A}(\sigma, T) + (1 - x_+ - x_-)p^{A-}(\sigma, T) \end{aligned} \tag{3.45}$$

The stress is calculated using the following FEMLAB expression

$$\sigma(u_x, x_+, x_-) = \frac{E_M\left[u_x - (x_+ - x_-)\varepsilon_T\right]}{x_+ + x_- + \frac{E_M}{E_A}x_A} \tag{3.46}$$

where the strain $u_x = \frac{\partial u}{\partial x}$ is a default variable in FEMLAB, which is free to be used as solution variables u, x_+ and x_-. The expressions of transition probabilities $p^{\alpha\beta}$ are given in (3.21).

The corresponding boundary conditions are

Dirichlet condition at $x = 0$:

$$r_1 = hu + b = 0 : u(0, t) = 0 \Rightarrow r_1 = u \tag{3.47}$$

Neumann condition at $x = L$:

$$-n \cdot \Gamma_1 = g_1 : A(L)\sigma(L, t) = F(t) \Rightarrow g_1 = F(t) \tag{3.48}$$

And there is no restriction on the phase fractions at both ends, so boundary conditions for x_α are implemented as $r_\alpha = 0$.

The initial conditions to complete the model are given as

$$u(x, 0) = \overline{u}(x)$$

$$x_+(x, 0) = x_{+0} \tag{3.49}$$

$$x_-(x, 0) = x_{-0} \tag{3.50}$$

An extension to include the heat transfer equation (3.28) will be given in the subsequent subsection.

3.2.2 Quasi-static Analysis without Latent Heat

First, without including the heat transfer equation (3.28) and under the homogenous temperature assumption, we use a homogenous SMA bar as an example to validate the FE implementation and illustrate the model capabilities. For an SMA bar with uniform cross-section, each cross-section will have the same stress, which induces uniform phase transformation throughout the bar.

Then SMA bars with varying cross-section and nonuniform temperature distribution are studied, respectively. For an SMA bar with varying cross-section at constant temperature, different positions along the bar will see different stresses, which induces nonuniform phase transformation along the bar during the loading and unloading process. For an SMA bar with nonuniform temperature distribution, due to the temperature dependent stress-strain relation as illustrated in Figure 3.5, different positions along the SMA bar with different temperatures correspond to different transformation stresses, which also induces inhomogeneous phase transformation along the SMA bar.

The material properties used for the SMA material are: $E_A = 71.1GPa$, $E_M = 30.9GPa$, $\varepsilon_T = 0.044$, $\sigma_A(T_U = 353K) = 663.16MPa$, $\sigma_A(T_L = 323K) = 431.58MPa$, $\Delta\sigma = 295MPa$, volume of a layer $V_D = 5 \times 10^{-23}m^3$ and relaxation time $\tau_x = 10^{-2}s$. The geometry parameters of the SMA bar with square cross-section are: length $L = 200mm$, width and height $h = 10mm$.

Quasiplastic and superelastic behavior

To validate the FEMLAB implementation, a mechanical loading is applied at the free end of the SMA bar at different fixed temperatures.

We start with the low temperature case at $T = 273K$. The simulation starts with $x_+(0) = x_-(0) = 0.5$. At low temperature, the austenite state is unstable and the SMA material exhibits quasiplastic behavior. Figure 3.7(a) shows the time history of the applied tip force. Figures 3.7(b) and (c) show strain distributions along x during the loading and unloading processes, respectively. For the uniform SMA bar, the strain changes uniformly along the entire SMA bar during the loading and unloading processes. Figures 3.7(d) and (e) show the global force-displacement response and the local stress-strain hysteresis at point $x = 0$, respectively. The local stress-strain response is a scaled version of the global force-displacement response, and the hysteresis loops are characterized by sharp transitions

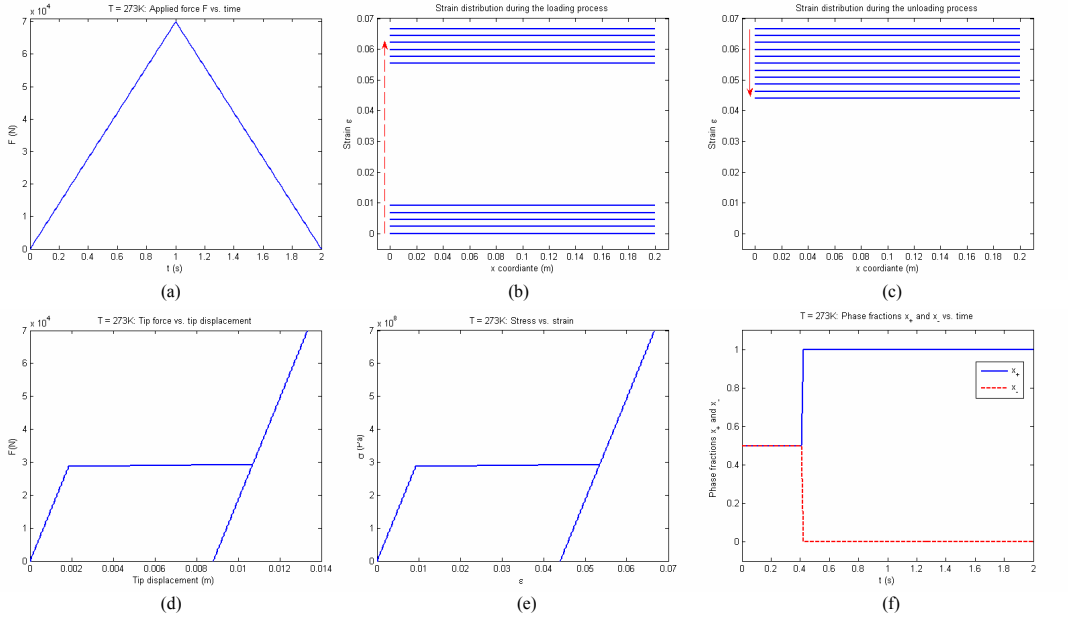


Figure 3.7: Quasiplasticity at low temperature T=273K: (a) Applied force; (b) Strain distribution along x during the loading process; (c) Strain distribution along x during the unloading process; (d) Global tip force vs. tip displacement; (e) Stress-strain relation at point $x = 0$; (c) Time histories of phase fractions x_+ and x_-.

as expected for single crystal behavior. Time histories of phase fractions are shown in Figure 3.7(f). When the tensile stress reaches the critical value of transformation stress σ_M, the SMA bar transforms from martensite M_- to martensite $M+$ as illustrated in Figure 3.7(e). After unloading, there is a residual strain ε_T.

At high temperature $T = 353K$, the SMA material exhibits superelastic behavior as shown in Figure 3.8. During the loading process, when the applied tensile stress reaches transformation stress σ_A, the SMA material transforms from austenite A to martensite $M+$ and during the unloading process, the material undergoes the reverse transformation from M_+ to A and recovers its original shape. So the model can capture the stress induced transformations of the SMA material at both low and high temperatures.

Shape memory effect

Another important property of SMA materials is the shape memory effect, which is due

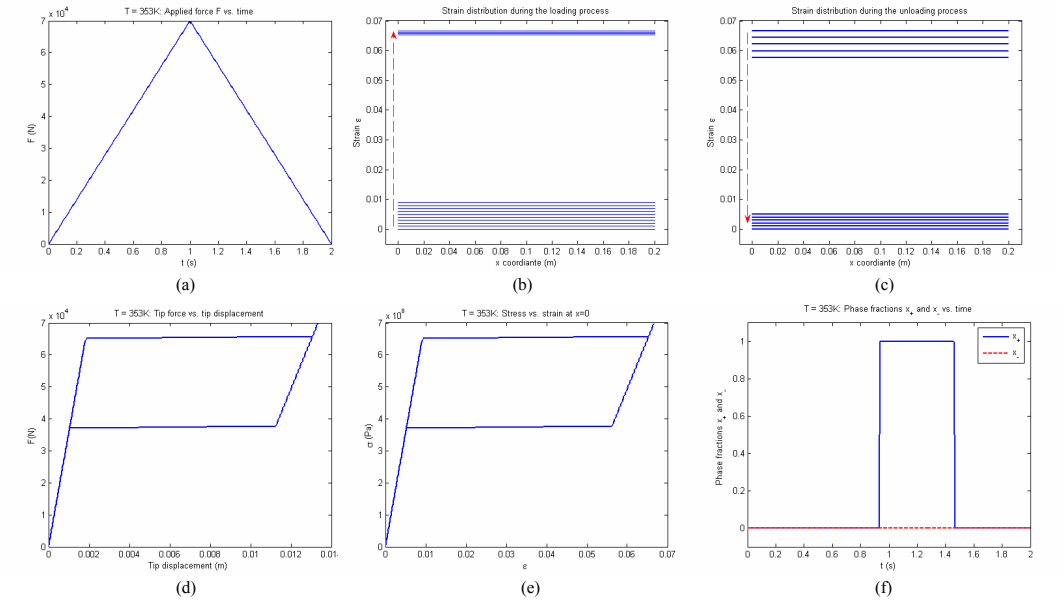


Figure 3.8: Superelasticity at high temperature T=353K: (a) Applied force vs. time; (b) Strain distribution along x during the loading process; (c) Strain distribution along x during the unloading process; (d) Global tip force vs. tip displacement; (e) Stress-strain relation at point $x = 0$; (c) Time histories of phase fractions x_+ and x_-.

to the temperature-induced phase transformations in SMA materials. Figures 3.9 and 3.10 illustrate the SME under thermomechanical loadings. First, under constant low temperature $T = 250K$, where martensite states are stable, upon loading and unloading at the free end, the SMA bar transforms from martensite M_- to martensite M_+ and generates a residual deformation. Then under zero mechanical loading and after being heated up to a high temperature, the SMA material transforms from martensite M_+ to austenite A and recovers to the original undeformed shape as shown in Figure 3.9(c) and (d). And then after being cooled down to a low temperature, the austenite A becomes unstable and transforms to martensite $M_\pm$. As predicted by the free energy model, under zero stress state, the layers have equal opportunities to jump from A to M_+ and M_- as illustrated by the evolution of phase fractions shown in Figure 3.10. The SME is the basis for the application of SMA actuators. The results show that the free energy SMA model can represent the temperature-induced phase transformation behavior of SMA materials.

Thermo-mechanical loading

Typically, SMA actuators are subjected to thermal and mechanical loadings simultaneously. Figures 3.11 and 3.12 show the response of an SMA bar to a cooling and heating cycle under a relative small constant tensile stress $\sigma = 100MPa$. The simulation starts at high temperature $T = 400K$ with $x_A(0) = 1$. Then, under the constant mechanical loading, the SMA bar is cooled down to $250K$ and then heated up to $T = 400K$ again. As we can see that even under a small constant stress, the SMA experiences a complete phase transformation from austenite A to martensite M_+ and thus generates a very large actuation stroke in a cooling and heating cycle. This behavior is due to the landscape of the Gibbs free energy (3.5) being tilted to favor the martensite M_+ and thus the energy barrier between austenite A and martensite M_+ is always lower than the one between austenite A and martensite M_- as illustrated in Figure 3.12(d). During the cooling and heating process, the energy barrier between austenite A and martensite M_+ will thus be eliminated first and phase transformations only occur between A and M_+, consequently generating very large deformations.

Non-homogeneous problems: geometry and temperature

First, we consider an SMA bar with varying cross-section as shown in Figure 3.13. The cross-section area is expressed as a function of x as $A(x) = A_0 + 0.1 \cdot A_0 \cdot \sin(\frac{x}{L}\pi)$ with

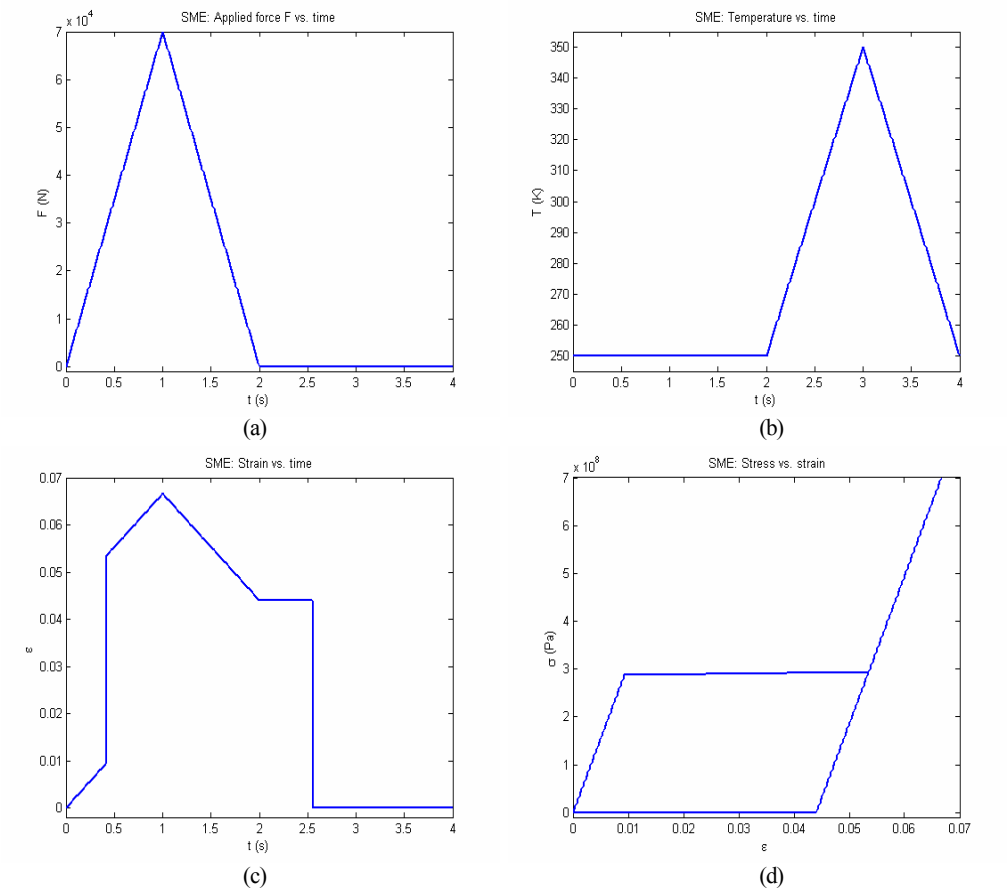


Figure 3.9: Shape memory effect (SME): (a) F vs. time; (b) T vs. time; (c). Strain reponse vs. time; (d) Stress-stain relation.

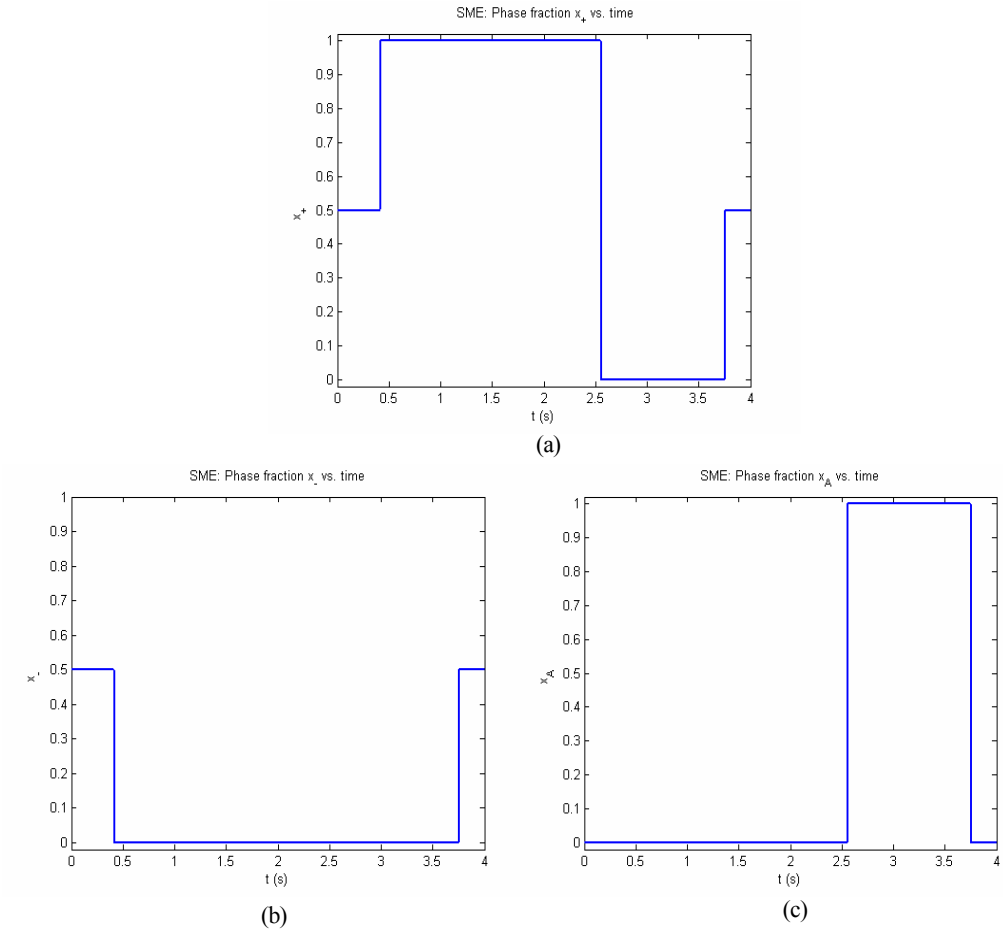


Figure 3.10: Evolution of phase fractions of shape memory effect (SME): (a) x_A vs. time; (b) x_+ vs. time; (c). x_- vs. time.

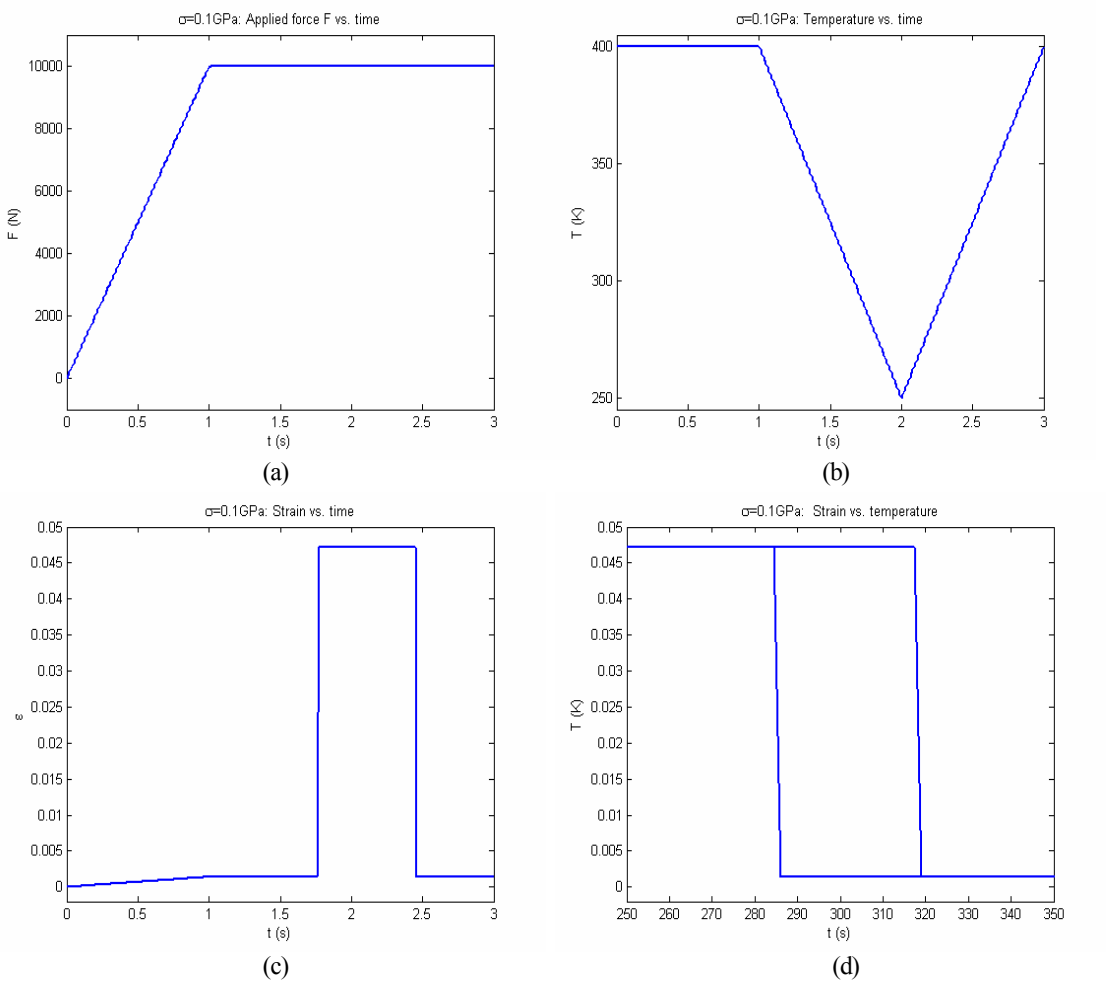


Figure 3.11: Themomechanical coupling with constant mechanical loading: (a) F vs. time; (b) T vs. time; (c) strain vs. time; (d) strain-temperature diagram.

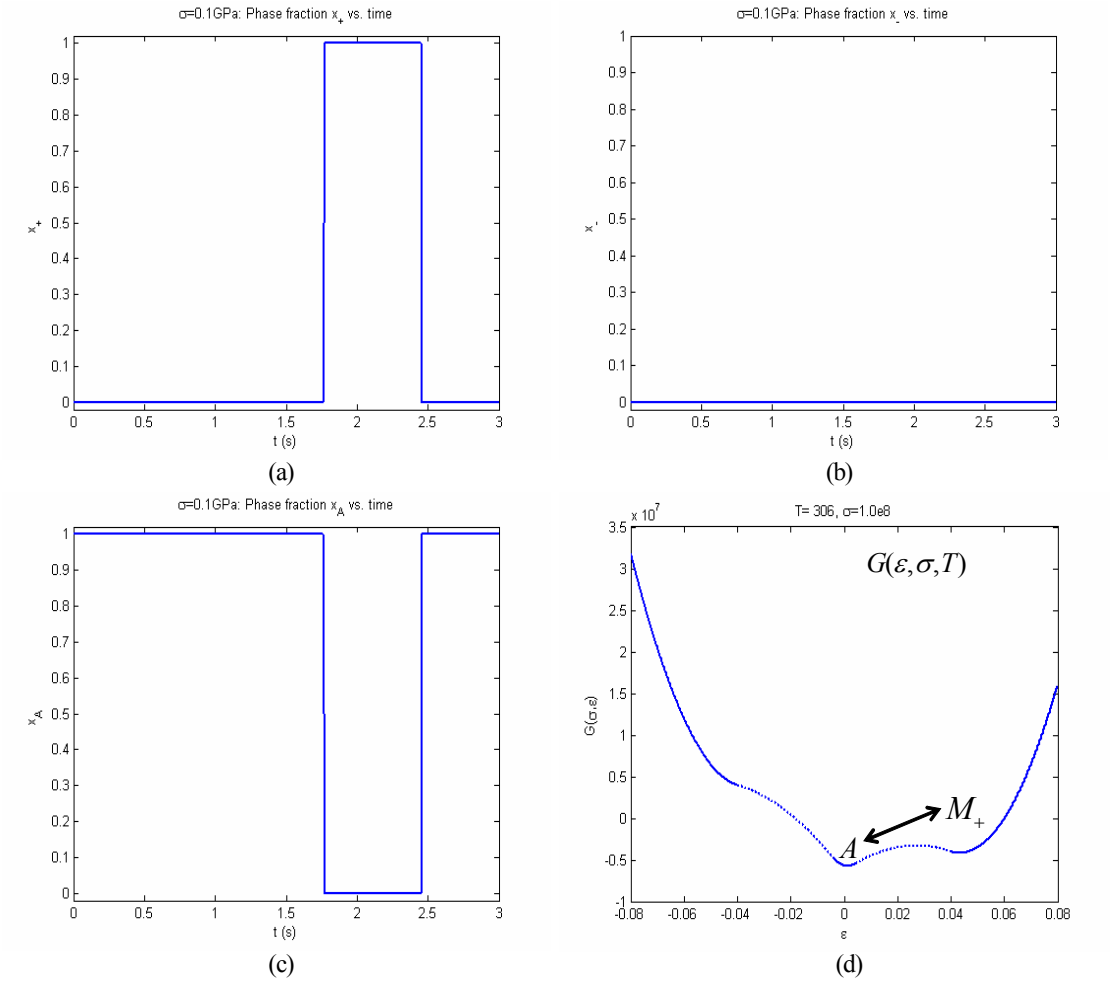


Figure 3.12: Evolution of phase fractions of themomechanical coupling: (a) x_+ vs. time; (b) x_- vs. time; (c) x_A vs. time; (d) Gibbs free energy landscape favoriting M_+ well.

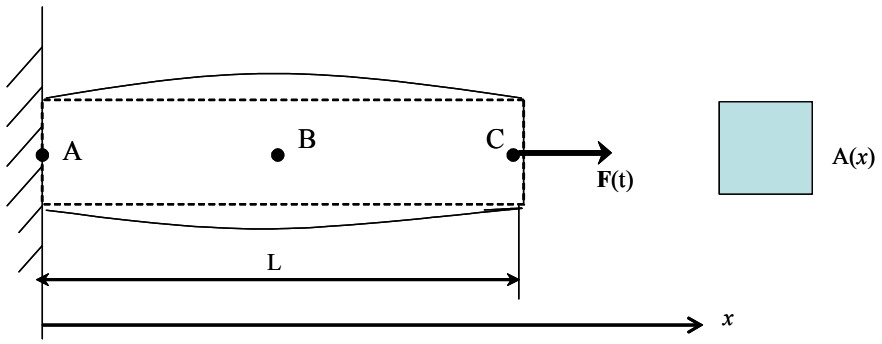


Figure 3.13: SMA bar with varying cross-section

$A_0 = 1.0 \times 10^{-4} m^2$, such that the center of the bar B at $x = \frac{L}{2}$ has the largest area $1.1 \times 10^{-4} m^2$ and the length is chosen as $L = 0.2m$.

This geometric non-homogeneity induces non-homogeneous phase transformations through the length of the SMA bar due to the non-homogeneous stress distribution with $\sigma(x) = \frac{F}{A(x)}$. Figures 3.14 and 3.16 show the responses of the tip displacement, stress, strain and phase fractions under quasi-static loading at a constant low temperature $T = 273K$. The smaller cross-section with larger stress will transform first followed by the larger cross-section with smaller stress. The simulation starts with the initial condition $x_+ = x_- = 0.5$. As we can see from Figure 3.15 and Figure 3.16, under tensile loading, the SMA bar transforms from M_- to M_+. This process starts from the smallest ends A and C and propagates towards B with the largest cross-section area. Due to the symmetry, point A and point C with the same cross-section area are subjected to the same stress. At high temperature ($T = 350K$), as shown in Figures 3.18 and 3.19, during the loading process, the smaller cross-section will transform from the austenite A into the martensite M_+ first followed by the larger cross-section, but during the unloading process, the larger cross-section will reach the critical transformation stress first and thus transform from M_+ back to A, eventually followed by the smaller cross-sections. The non-homogenous transformation behavior due to the geometric non-homogeneity of the SMA bar is also illustrated by the force-displacement relations without sharp transitions shown in Figures 3.14(b) and 3.17(b).

Secondly, we study a uniform SMA bar with a nonuniform temperature distribution as

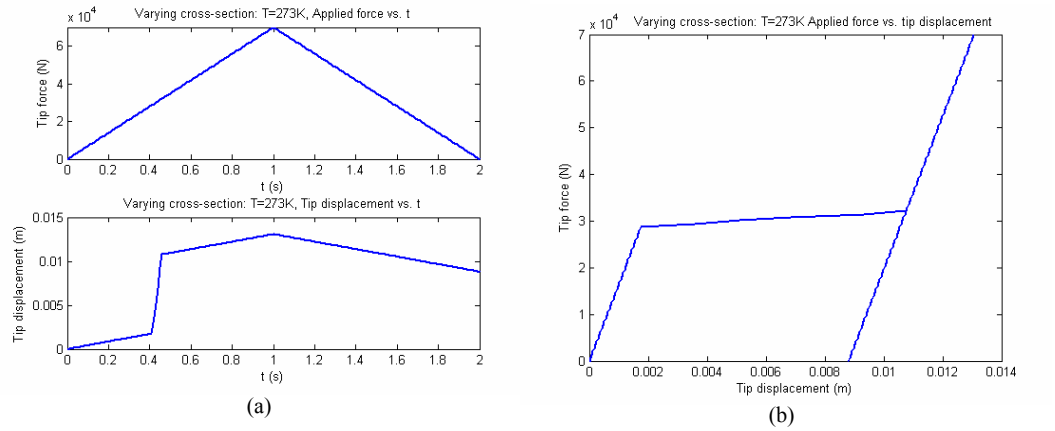


Figure 3.14: SMA bar with varying cross-section at $T = 273K$: (a) Force and displacement vs. time; (b) Force vs. displacement.

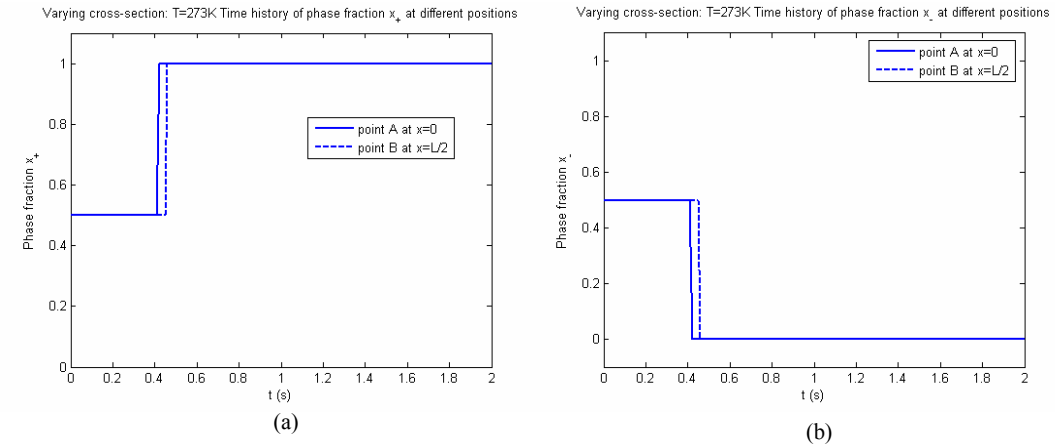


Figure 3.15: Phase fraction evolution of different positions A and B for a SMA bar with varying cross-section at $T = 273K$: (a) x_+ vs. time; (b) x_- vs. time

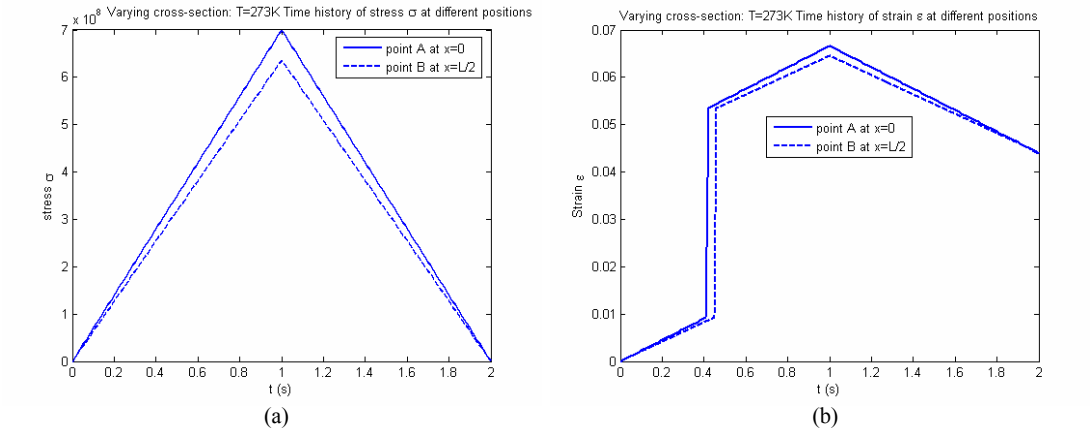


Figure 3.16: Stress and strain responses of different positions A and B for a SMA bar with varying cross-section at $T = 273K$: (a) stress vs. time; (b) strain vs. time.

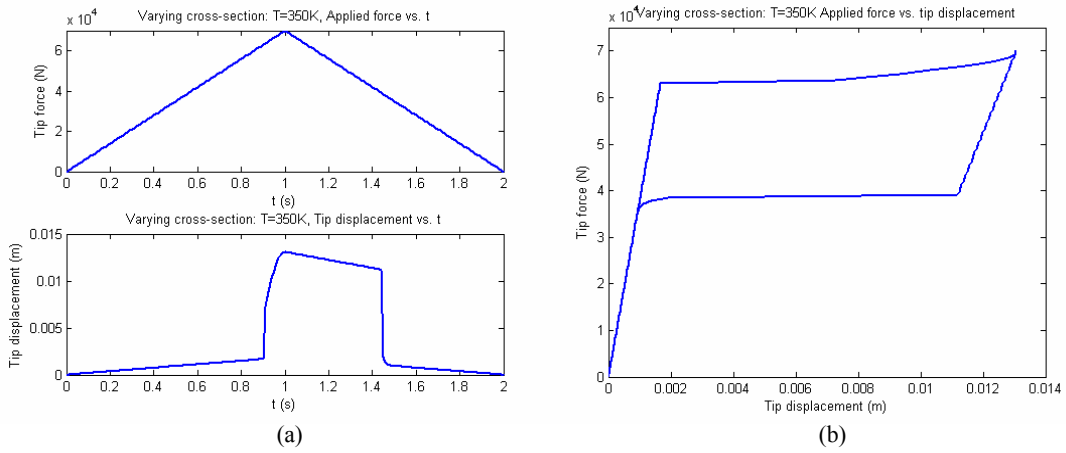


Figure 3.17: SMA bar with varying cross-section at $T = 350K$: (a) Force and displacement vs. time; (b) Force vs. displacement.

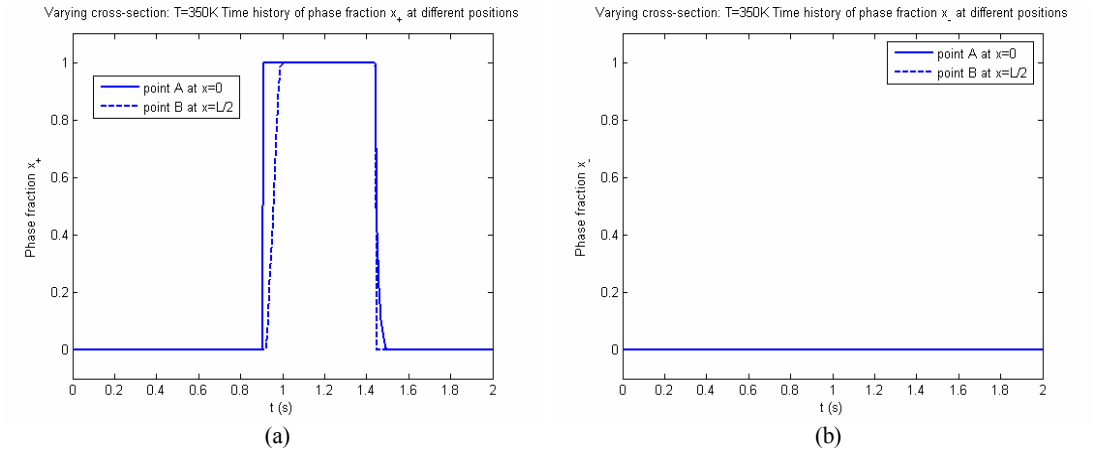


Figure 3.18: Phase fraction evolution of different positions A and B for a SMA bar with varying cross-section at $T = 350K$: (a) x_+ vs. time; (b) x_- vs. time

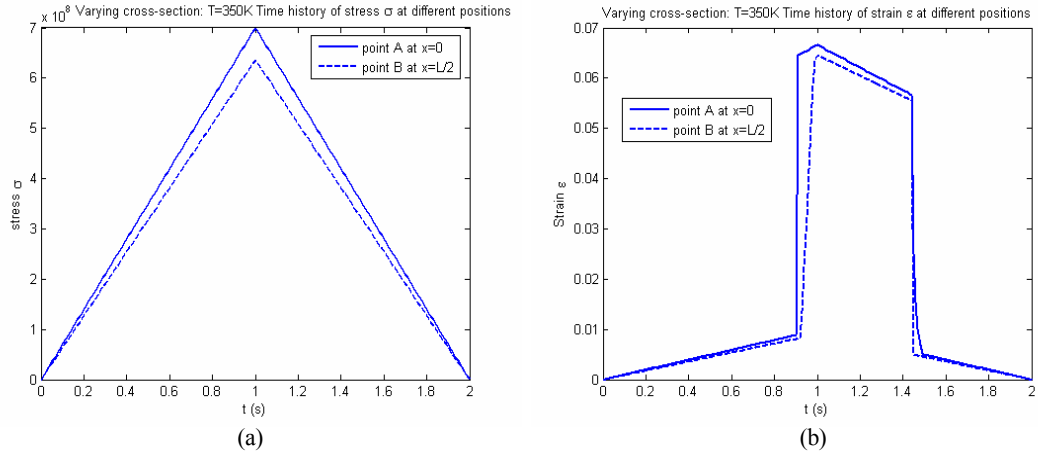


Figure 3.19: Stress and strain responses of different positions A and B for a SMA bar with varying cross-section at $T = 350K$: (a) stress vs. time; (b) strain vs. time.

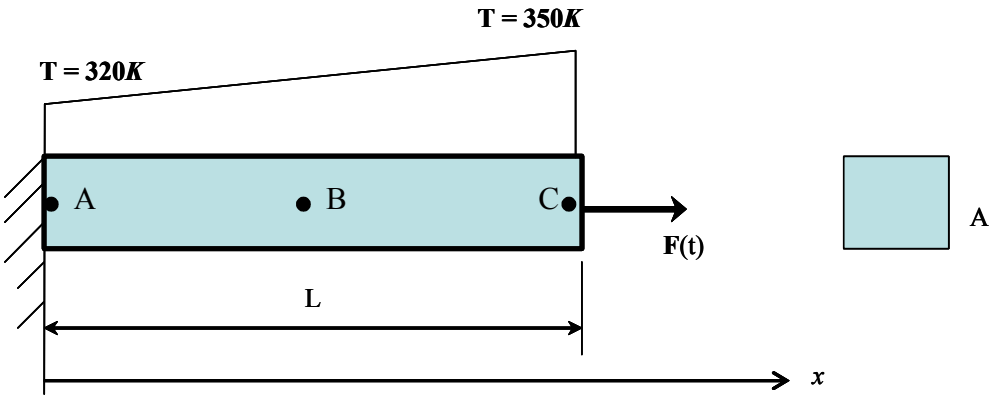


Figure 3.20: SMA bar with nonuniform temperature distribution

shown in Figure 3.20. The temperature distribution is assumed to be a function of position x as $T(x) = 320 + \frac{30}{L}x$. Each cross-section sees the same stress $\sigma = \frac{F}{A_0}$. Since the temperature distribution is non-homogeneous, the different positions have different temperatures and thus have different transformation stresses, see (3.11) and (3.12). The cross-section with the lowest temperature has the lowest transformation stress, and the phase transformation will start there first. In this example with temperature $T \geq 320K$, the SMA bar demonstrates superelastic behavior. Figure 3.21 shows the loading process, the tip displacement response and the corresponding force-displacement relation. There is no sharp transition compared with the homogeneous uniform SMA bar example, demonstrating the non-homogeneous transformation behavior of the SMA bar. This non-homogenous behavior is further illustrated by evolution of phase fractions and strain responses at different positions A, B, C shown in Figures 3.22 and 3.23, respectively. During the loading process, point A has the lowest temperature $T = 320K$ and thus lowest transformation stress. The transformation from austenite to martensite M_+ starts here followed by point B with $T = 335K$ and then point C with $T = 350K$. During the unloading process, the sequence of transformation from martensite M_+ back to the austenite is reversed as $C \rightarrow B \rightarrow A$. Figure 3.23 presents the stress-strain relation of different positions with different temperatures, which illustrates the temperature dependent stress-strain relation of the SMA material.

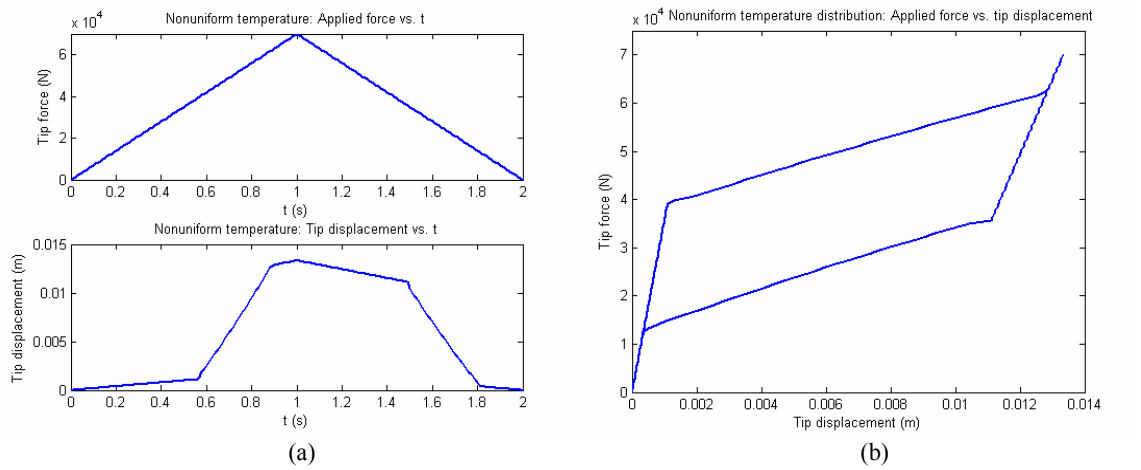


Figure 3.21: Displacement response for a SMA bar with nonuniform temperature distribution: (a) Applied tip force and tip displacement vs. time; (b) Applied tip force vs. tip displacement.

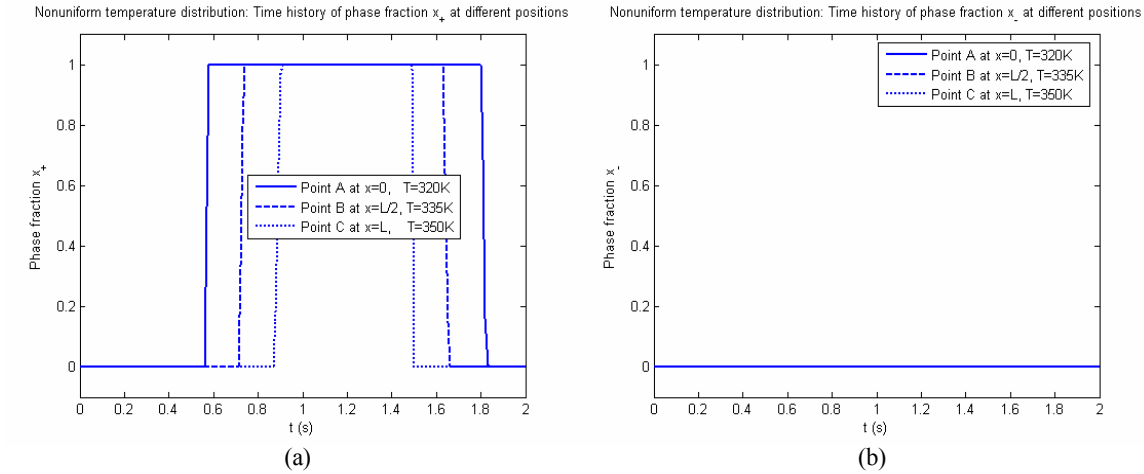


Figure 3.22: Phase fraction evolution of different positions A, B and C for a SMA bar with nonuniform temperature distribution : (a) x_+ vs. time; (b) x_- vs. time

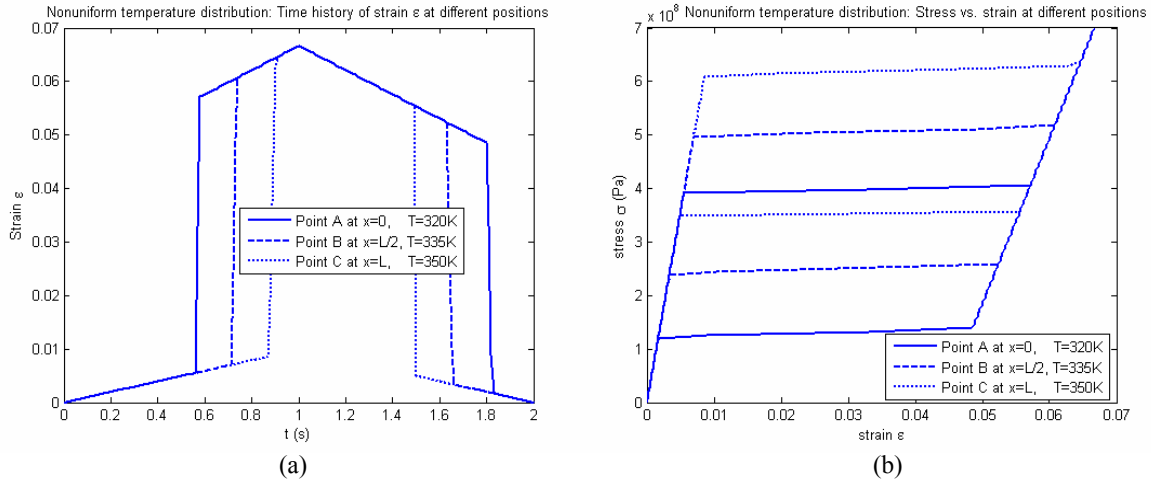


Figure 3.23: Strain reponse and stress-strain relation of different positions A, B and C for a SMA bar with nonuniform temperature distribution : (a) strain vs. time; (b) stress-strain relation.

3.2.3 Coupled Thermo-mechanical Analysis

The behavior of SMA materials is characterized by the strong thermo-mechanical coupling due to the rate-dependent latent heats released and absorbed during austenite-martensite phase transformations. SMA actuators are typically driven by direct electric current heating and convective cooling. The heat transfer equation given in (3.28) is under assumption of uniform temperature throughout the SMA devices. In reality, however, due to factors such as non-homogeneous geometry, boundary conditions, temperature dependent resistivity, localized self-heating or self-cooling due to latent heat effects, the temperature distribution along the SMA bar/wire will be non-homogeneous. A space dependent nonlinear transient thermo-mechanical coupled problem has to be solved.

According to the first law of thermodynamics, we re-derive the 1-D heat transfer equation by including axial heat conduction as

$$\rho c\frac{\partial T}{\partial t} - \frac{\partial}{\partial x}(\lambda\frac{\partial T}{\partial x}) = -\alpha\frac{l_c(x)}{A(x)}(T - T_0) + j(x,t) - (h_{M_+} - h_A)\dot{x}_+ - (h_{M_-} - h_A)\dot{x}_- \quad (3.51)$$

where the second term on the left hand side of equation (3.51) is the gradient of the axial

heat flow and $\lambda(W/m\cdot K)$ is the heat conductivity. $l_c(x)$ and $A(x)$ are the circumference and cross-section area of the SMA bar/wire, respectively. $j(x,t)$ (W/m^3) is the Joule heating density. For conduction media like SMA material, we have [67]

•Conservation of current:

$$\boldsymbol{\nabla}\cdot\mathbf{J}=\mathbf{0} \tag{3.52}$$

•Ohm's law:

$$\mathbf{J}=\eta\mathbf{E} \tag{3.53}$$

•Relationship between electric field $\mathbf{E}$ and electric potential V

$$\mathbf{E}=-\boldsymbol{\nabla}V \tag{3.54}$$

where $\mathbf{J}$ (A/m^2), $\mathbf{E}$ (V/m) and V are the current density vector, the electric field and electric potential, respectively. To avoid confusing with the symbol of stress σ, here we use η (S/m) to denote the electric conductivity, the reciprocal of the resistivity ρ_e $(\Omega\cdot m)$. From (3.52) to (3.54), we have

$$-\boldsymbol{\nabla}\cdot(\frac{\boldsymbol{\nabla}V}{\rho_e})=0 \tag{3.55}$$

and the expression of the Joule heating density is given as

$$j(t)=\mathbf{J}\cdot\mathbf{E}=\frac{|\boldsymbol{\nabla}V|^2}{\rho_e}$$

In the 1-D case, we have

$$-\frac{\partial}{\partial x}(\frac{1}{\rho_e}\frac{\partial V}{\partial x})=0 \tag{3.56}$$

and

$$j(t)=\frac{(\frac{\partial V}{\partial x})^2}{\rho_e} \tag{3.57}$$

Typically, the resistivity of SMA materials are temperature and phase dependent. Variations in resistivity with temperature are complex functions of composition and thermomechanical processing. For the sake of simplicity, we express the phase dependent resistivity as

$$\rho_e(t) = \sum_{\alpha} \rho_{e\alpha} x_\alpha(t) \tag{3.58}$$

If the resistivity ρ_e of the SMA bar/wire is assumed to be constant, the Joule heating can be expressed as

$$j(t) = \frac{(\frac{\partial V}{\partial x})^2}{\rho_e} = \frac{(V/L)^2}{\rho_e} = \frac{V^2}{\frac{\rho_e L}{A} LA} = \frac{V^2}{RV_0} \tag{3.59}$$

where $R = \frac{\rho_e L}{A}$ is the resistance of the SMA bar/wire with length L and cross-section area A and $V_0 = LA$ is the volume of the SMA bar/wire.

Combining the equations (3.36), (3.42) with (3.51) and (3.56), we can implement the resulting mechanical-phase evolution-thermal-electric coupled problem into FEMLAB general form PDEs with five solution variables $\mathbf{U} = \begin{bmatrix} u & x_+ & x_+ & T & V \end{bmatrix}^T$ as

$$\mathbf{d}_\alpha \frac{\partial \mathbf{U}}{\partial t} + \frac{\partial \mathbf{\Gamma}}{\partial x} = \mathbf{F} \tag{3.60}$$

with

$$\mathbf{d}_\alpha = \begin{bmatrix} 0 & 0 & 0 & 0 & 0 \\ 0 & 1 & 0 & 0 & 0 \\ 0 & 0 & 1 & 0 & 0 \\ 0 & (h_{M_+} - h_A) & (h_{M_-} - h_A) & \rho c & 0 \\ 0 & 0 & 0 & 0 & 0 \end{bmatrix} \tag{3.61}$$

$$\mathbf{\Gamma} = \begin{bmatrix} A(x)\sigma(x) \\ 0 \\ 0 \\ -\lambda \frac{\partial T}{\partial x} \\ -\frac{1}{\rho} \frac{\partial V}{\partial x} \end{bmatrix} \tag{3.62}$$

$$\mathbf{f} = \begin{bmatrix} 0 \\ -x_+ p^{+A}(\sigma, T) + (1 - x_+ - x_-) p^{A+}(\sigma, T) \\ -x_- p^{-A}(\sigma, T) + (1 - x_+ - x_-) p^{A-}(\sigma, T) \\ -\alpha \frac{l_c(x)}{A(x)} (T - T_0) + j(x, t) \\ 0 \end{bmatrix} \tag{3.63}$$

The above implementation is used to simulate a quasistatic tensile test of an SMA wire with different thermal boundary conditions and loading rates as well as to study the response of a electrically heated SMA wire actuator with different thermal boundary conditions. The strong thermo-mechanical coupling is due to the rate-dependent latent heats released and absorbed during the phase transformations

Tensile Simulations of SMA wire

To illustrate self-cooling and self-heating of the SMA material due to the latent heat, we use an SMA wire under tensile tests as examples as shown in Figure 3.24. The governing equations are the same for both bar and wire structures except that the wire can only sustain tensile loading. The parameters of the SMA wire are: length $L = 60mm$, radius $r = 0.4mm$, density $\rho = 6500kg/m^3$, specific heat $c = 0.5 \times 10^3 J/kg \cdot K$, heat conductivity $\lambda = 18W/m \cdot K$ and the heat transfer coefficient α between the SMA wire surface and its surrounding environment is assumed to be $90W/m^2K$. The mechanical properties are the same as those used in the last section.

Two different heat transfer boundary conditions, insulated ends with $\frac{\partial T}{\partial x}(0, t) = 0$ and $\frac{\partial T}{\partial x}(L, t) = 0$ and fixed temperature at both ends with $T(0, t) = T(L, t) = T_0$ are studied in sequence.

For the insulated boundary conditions, the temperature of the SMA wire changes uniformly. Figures 3.25 shows the results for the case with insulated boundary conditions at low ambient temperature $T_0 = 253K$. Figure 3.25(a) is the controlled displacement input. Figure 3.25(b) is the temperature response of the SMA wire. Figure 3.25(c) and (d) are the stress response and the evolution of phase fractions,respectively. During the transformation between martensite variants M_- and M_+, the SMA wire releases heat and the temperature increases slightly by $0.45K$. Figure 3.26 shows the results for the simulation at high ambient temperature $T_0 = 333K$, which shows that during the transformation from austenite to



Figure 3.24: Tensile test of SMA wire with controlled displacement.

martensite, the SMA wire releases heat and thus the temperature increases by $4K$, while during the transformation from austenite to martensite, the SMA wire absorbs heat, and thus the temperature of the SMA wire drops below the environment temperature T_0 to $329K$. The latent heat between the martensite twins is much smaller than the latent heat between martensite and austenite.

For fixed temperature boundary conditions with both ends contacting thermal heat sinks at low ambient temperature, the temperature distribution along the SMA wire is non-uniform. The case with high ambient temperature $T_0 = 333K$ is studied first. The controlled displacement inputs for three different loading rates of $\dot{u}\ (t)/L_0 = 0.7 \times 10^{-4}/s$, $0.7 \times 10^{-3}/s$ and $0.7 \times 10^{-2}/s$ are shown in Figure 3.27.

Figure 3.28 illustrates the evolution of temperature distribution along the SMA wire for three different loading rates during the loading and unloading processes. The temperature evolution is caused by the corresponding evolution of the latent heat shown in Figure 3.29, the only heat source in the heat transfer equation (3.51) with Joule heat $j(x,t) = 0$. Figure 3.30 presents the evolution of phase fraction x_+ distribution along the SMA wire during the loading and unloading processes, and Figure 3.31 illustrates the corresponding evolution of strain distribution. During the loading process, initially the entire SMA wire with the same temperature $T_0 = 333K$ and the same transformation stress $\sigma_A(333K)$ transforms together from austenite A to martensite M_+ once the stress reaches the value of $\sigma_A(333K)$ and releases heat, which causes the temperature of the SMA wire except the fixed end temperature to increase. With the controlled displacement increasing, the portions close to the

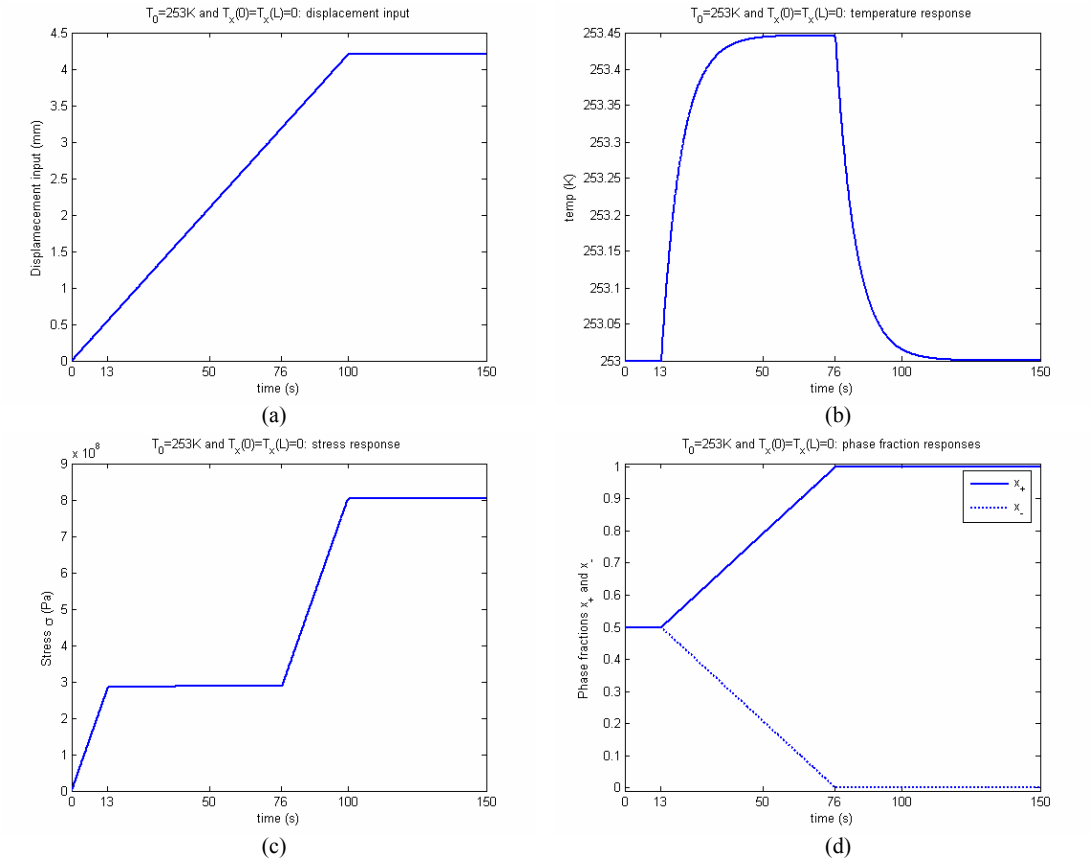


Figure 3.25: Tensile test of SMA wire with insulated boundary condtion at temperature $T_0 = 253K$: (a) controlled displacement input; (b) temperature response of the SMA wire; (c) stress response of the SMA wire; (d) evolution of phase fractions x_+ and x_-.

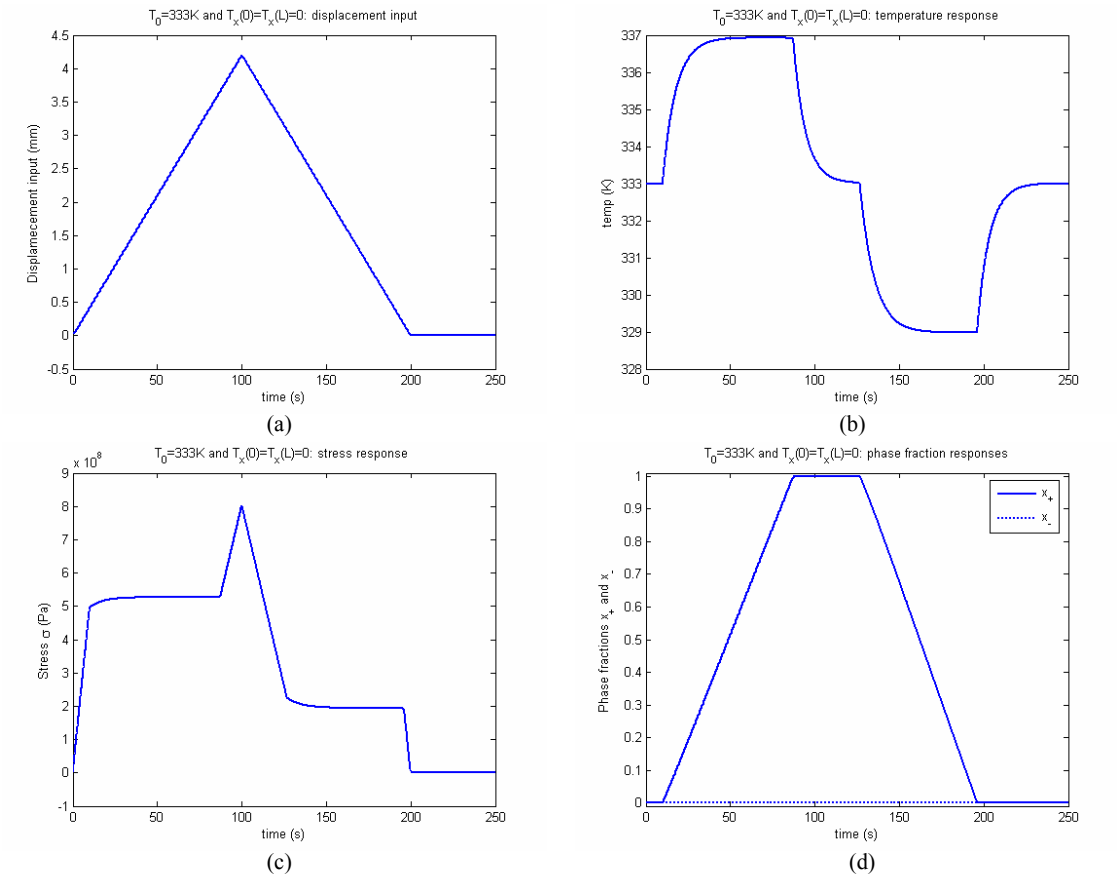
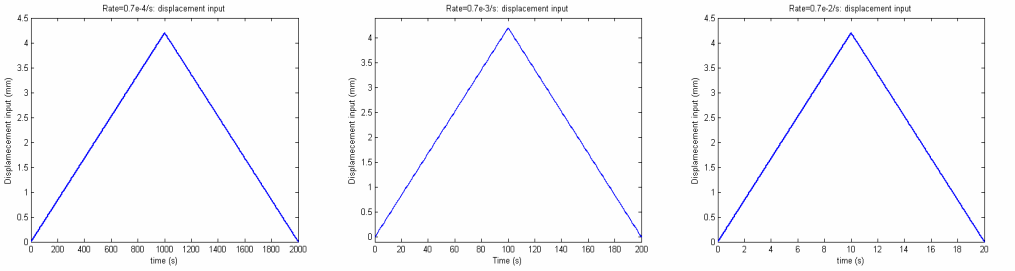


Figure 3.26: Tensile test of SMA wire with insulated boundary condtion at temperature $T_0 = 333K$: (a) controlled displacement input; (b) temperature response of the SMA wire; (c) stress response of the SMA wire; (d) evolution of phase fractions x_+ and x_-.



(a) (b) (c)

Figure 3.27: Controlled displacement input for three different rates: (a) $\dot{u}(t)/L_0 = 0.7 \times 10^{-4}/s$;(b) $\dot{u}(t)/L_0 = 0.7 \times 10^{-3}/s$;(c) $\dot{u}(t)/L_0 = 0.7 \times 10^{-2}/s$.

fixed temperature ends with lower ambient temperature and thus with lower transformation stress will transform first from austenite A to martensite M_+ and release latent heat. Due to the axial heat conduction, the heat flows from high temperature region to low temperature region. With the loading increasing, the latent heat propagates from outside into middle and also the middle portion of the SMA wire already in the phase transition region continues to transform from austenite A to martensite M_+ and release latent heat to increase the temperature as illustrated in Figure 3.28 (a), (c) and (e). Once the transformation is finished, the latent heat drops to zero and the temperature of the SMA wire decreases due to heat exchange with the environment. The transformation process from austenite A to martensite M_+ during the loading process are clearly illustrated by the evolution of phase fraction x_+ distribution in Figures 3.30 (a), (c) and (e) and the corresponding strain distribution in Figures 3.31 (a), (c) and (e).

Similarly, the results of the unloading process are illustrated by the evolution of the phase fraction x_+ in Figures 3.30 (b), (d) and (f) and strain evolution in Figures 3.31 (b), (d) and (f). The portions of the SMA wire with lower temperature and thus with lower transformation stress $\sigma_M\ (T)$ will first transform back from martensite M_+ to austenite A and absorb heat. At high temperature and under tensile loading, the phase fraction x_- of martensite M_- is always 0.

Figures 3.32 (a), (c) and (e) present the time histories of the temperature responses at the center point of the SMA wire. Due to the rate dependent latent heat effect, faster

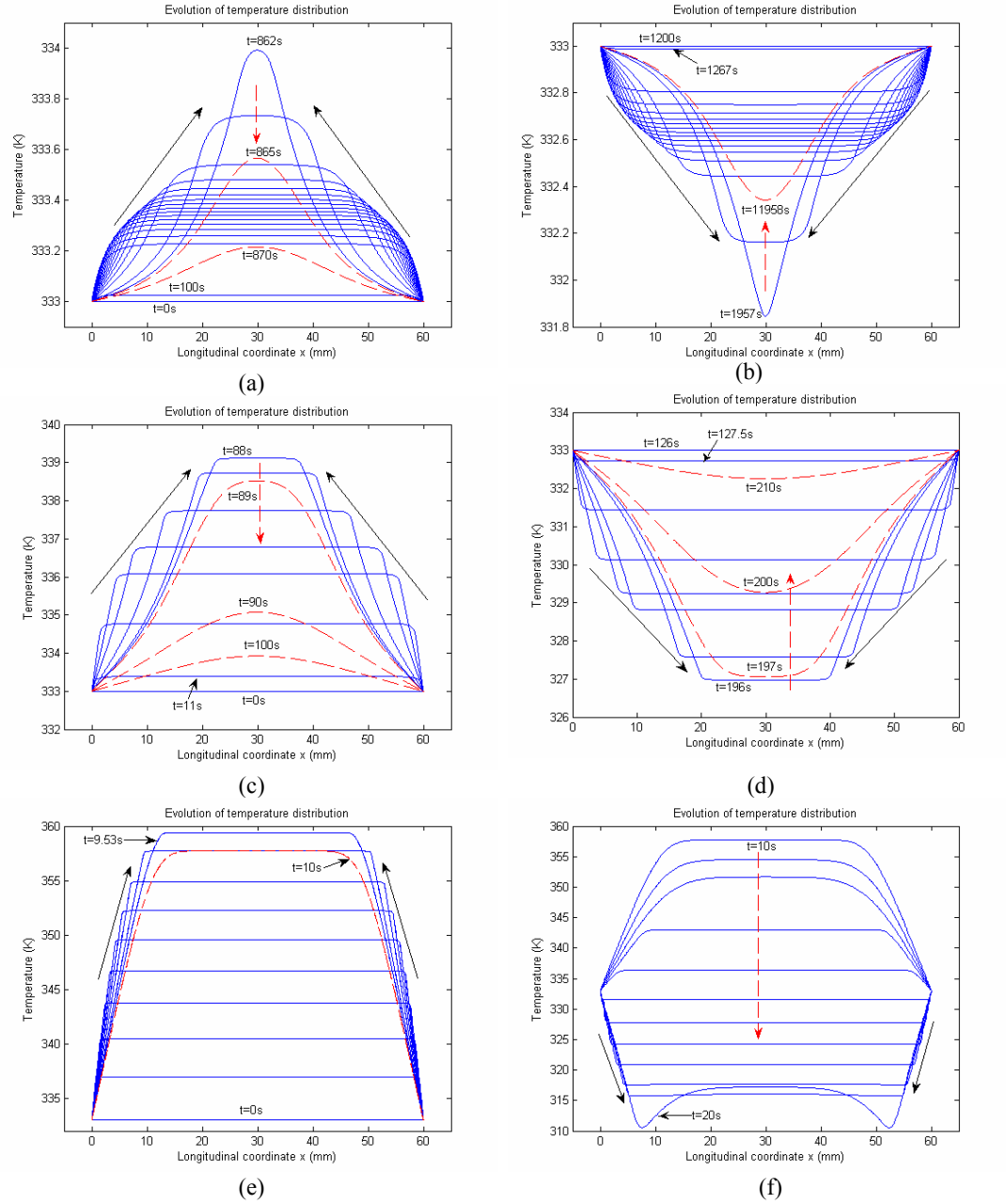


Figure 3.28: Evolution of temperature distribution along the SMA wire for three different loading rates during the loading and unloading processes: (a) and (b) for the loading rate of $0.7 \times 10^{-4}/s$; (c) and (d) for the loading rate of $0.7 \times 10^{-3}/s$;(e) and (f) for the loading rate of $0.7 \times 10^{-2}/s$.

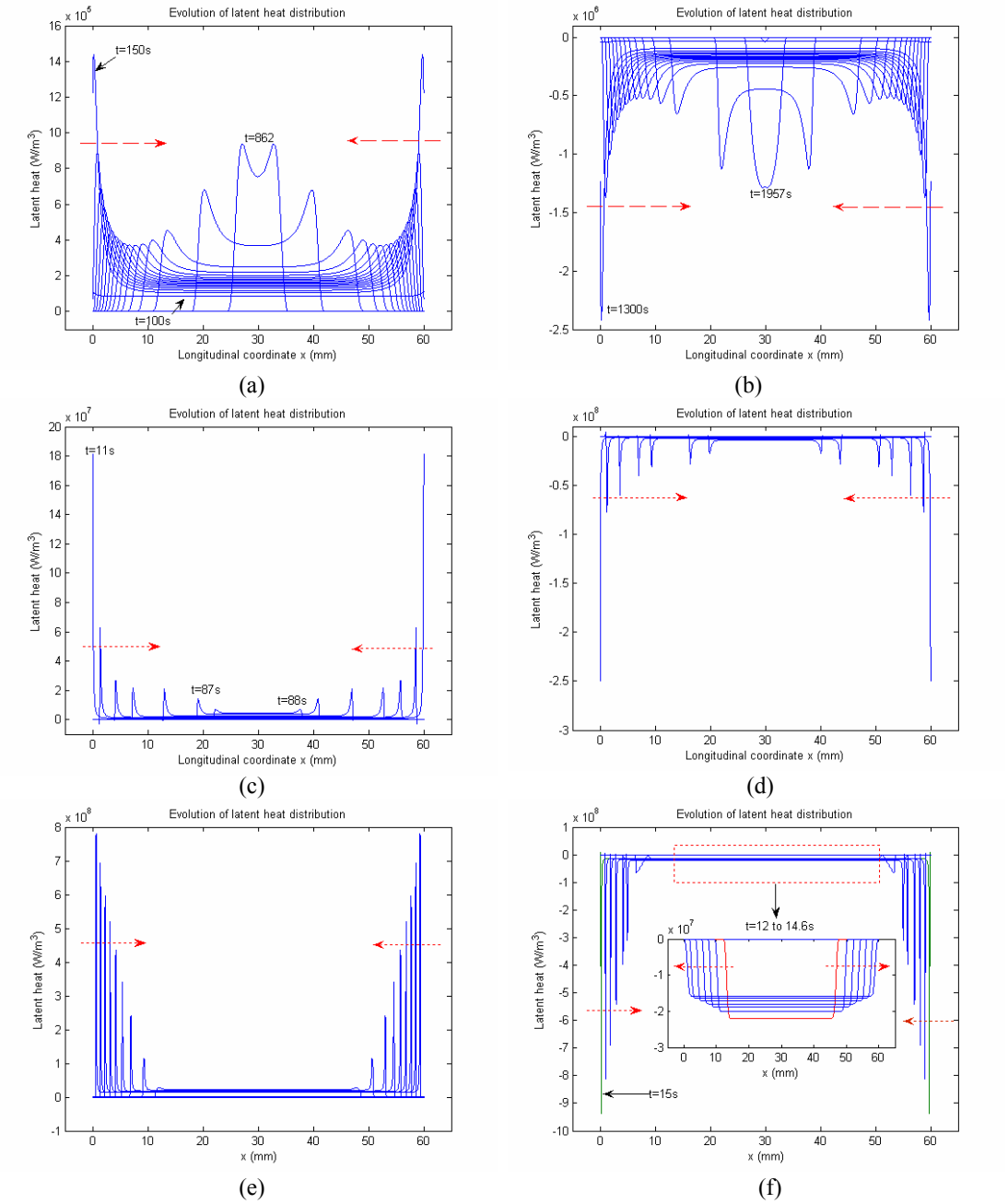


Figure 3.29: Evolution of latent heat distribution along the SMA wire for three different loading rates during the loading and unloading processes: (a) and (b) for the loading rate of $0.7 \times 10^{-4}/s$; (a) and (b) for the loading rate of $0.7 \times 10^{-3}/s$;(a) and (b) for the loading rate of $0.7 \times 10^{-2}/s$.

rate generate more latent heat to cause bigger temperature change, which results in different stress responses as shown in Figures 3.32 (b), (d) and (f). The stress response of the faster rate changes more gradually during the phase transformation periods. Due to the nonuniform temperature distribution along the SMA wire during the loading and unloading processes, different positions of the SMA wire have different stress-strain responses as shown in Figure 3.33. The end with fixed ambient temperature has sharp transition and the middle with gradual temperature change has corresponding gradual transition stress-strain relation. Figure 3.34 shows the rate dependent global stress σ-strain $\frac{u(t)}{L_0}$(engineering strain) relations for three different loading rates and their comparisons with the local stress σ-strain $\frac{\partial u}{\partial x}$ relations at different positions for corresponding loading rates. Typically, in tensile experiments of SMA wires, global stress-strain responses are used to characterize the material properties of SMA materials. For the very slow loading rate of $0.7 \times 10^{-4}/s$, the global stress-strain response represents the stress-strain relation of the SMA wire. The global stress-strain responses of the faster loading rates are close to the stress-strain responses at the middle point.

The simulation results of global stress-strain responses shown in Figure 3.34(a) are quite similar to the experimental results [68] shown in Figure 3.35. The stress-strain responses change from sharp transition to gradual transition with increasing loading rates. The simulation result of the fastest rate in Figure 3.34(a) also predicts the unsymmetrical loading and unloading behavior as illustrated by the experimental result in Figure 3.35(c).

The results of the case with fixed temperature boundary conditions at low ambient temperature $T_0 = 253K$ are presented in Figure 3.37 for the displacement input with loading rate of $0.7 \times 10^{-3}/s$ given in Figure 3.36. Figures 3.37(a) and (b) illustrate the temperature distribution along the wire during the phase transformation process from M_- to M_+ and the cooling process after the transformation, respectively. During the transformation process from M_- to M_+, due to the latent heat distribution as shown in Figure 3.37(c), the SMA wire the releases heat to cause the temperature of the wire to increase except the fixed low temperature ends to increase and the center of the SMA wire has the highest temperature as shown in Figure 3.37(d). With this small temperature perturbation (less than $0.45K$), the SMA wire is still in the fully martensite state. According to the free energy model, below certain temperature, the whole SMA wire has the same transformation stress σ_M.

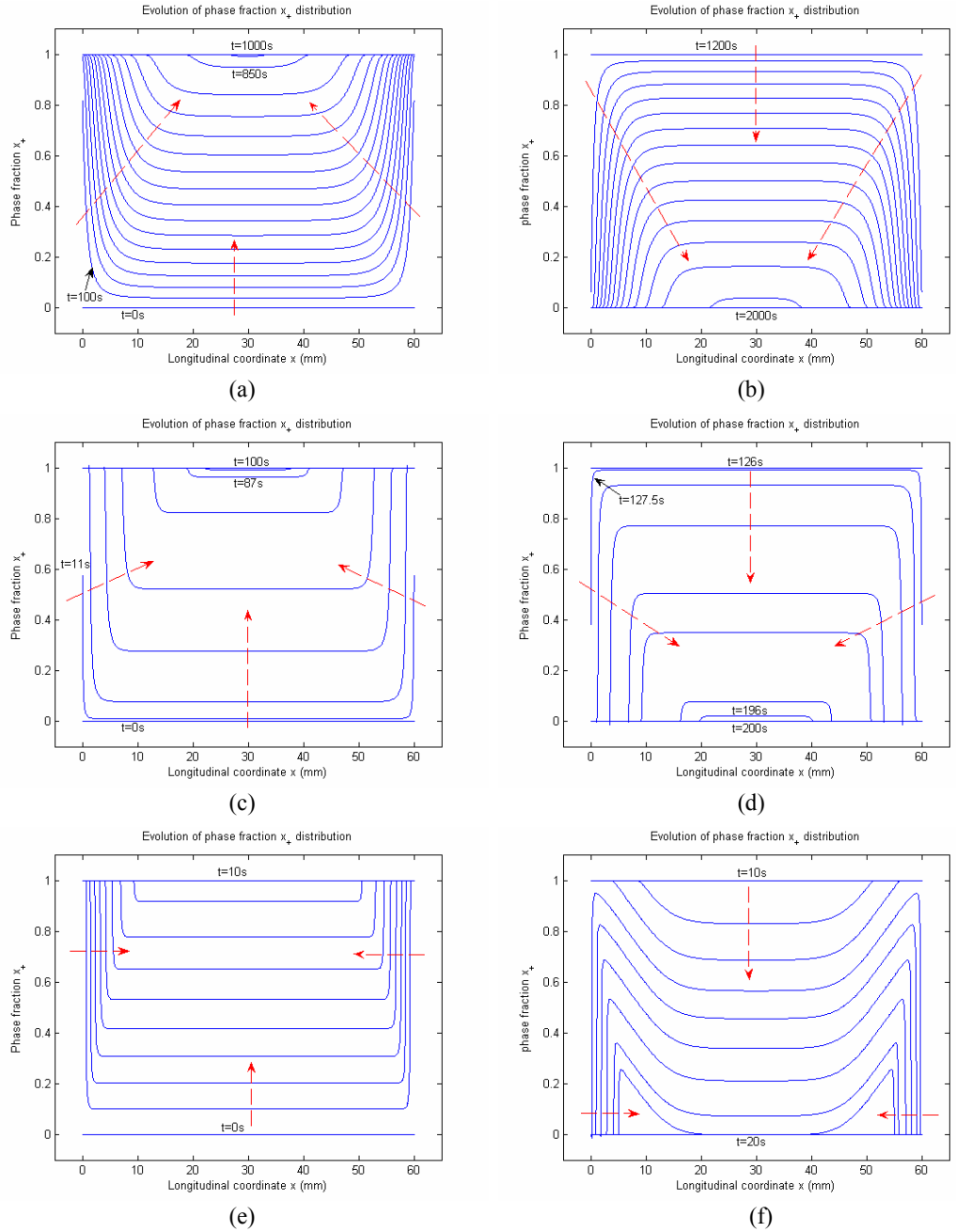


Figure 3.30: Evolution of phase fraction x_+ distribution along the SMA wire for three different loading rates during the loading and unloading processes: (a) and (b) for the loading rate of $0.7 \times 10^{-4}/s$; (a) and (b) for the loading rate of $0.7 \times 10^{-3}/s$;(a) and (b) for the loading rate of $0.7 \times 10^{-2}/s$.

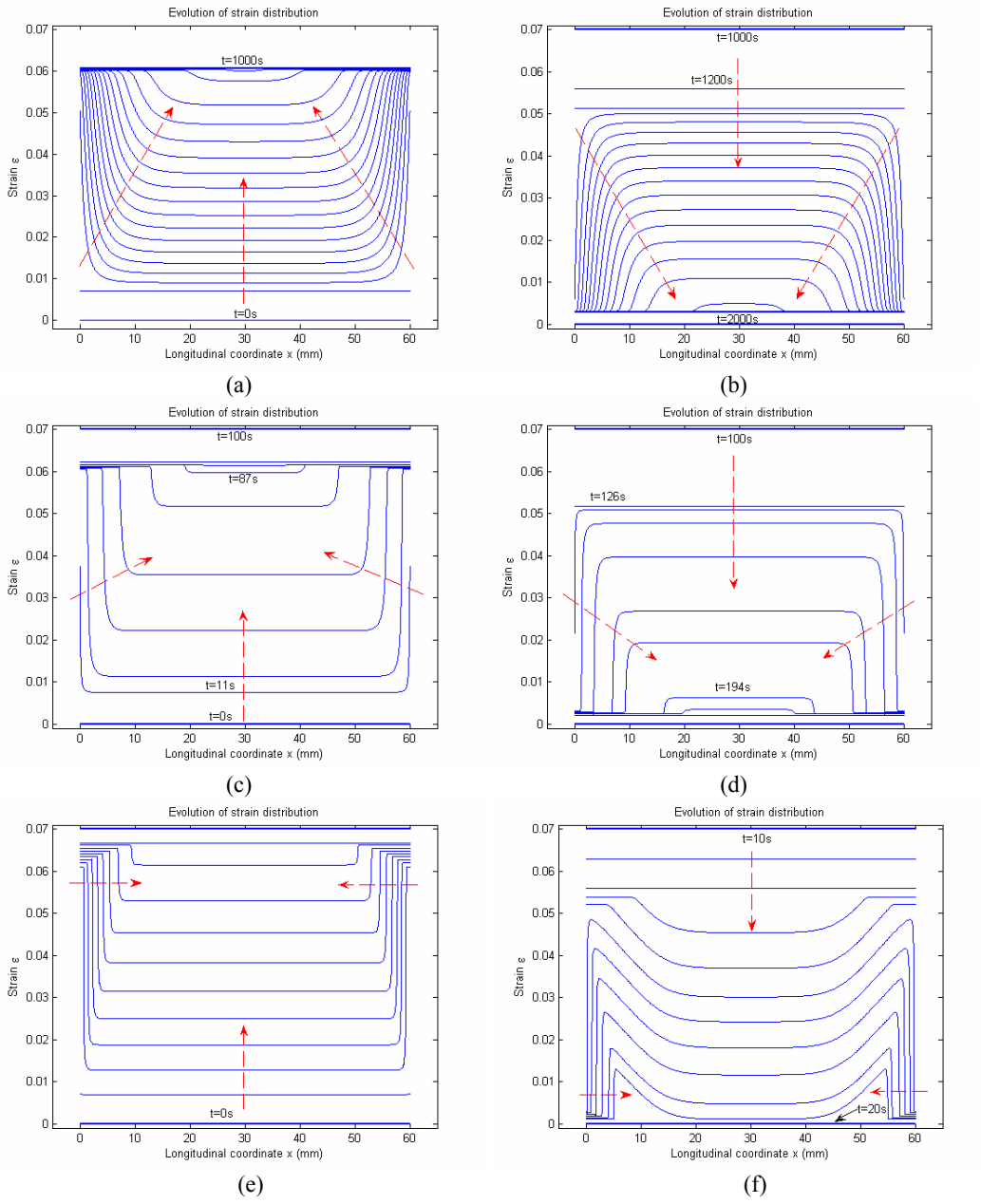


Figure 3.31: Evolution of strain distribution along the SMA wire for three different loading rates during the loading and unloading processes: (a) and (b) for the loading rate of $0.7 \times 10^{-4}/s$; (a) and (b) for the loading rate of $0.7 \times 10^{-3}/s$;(a) and (b) for the loading rate of $0.7 \times 10^{-2}/s$.

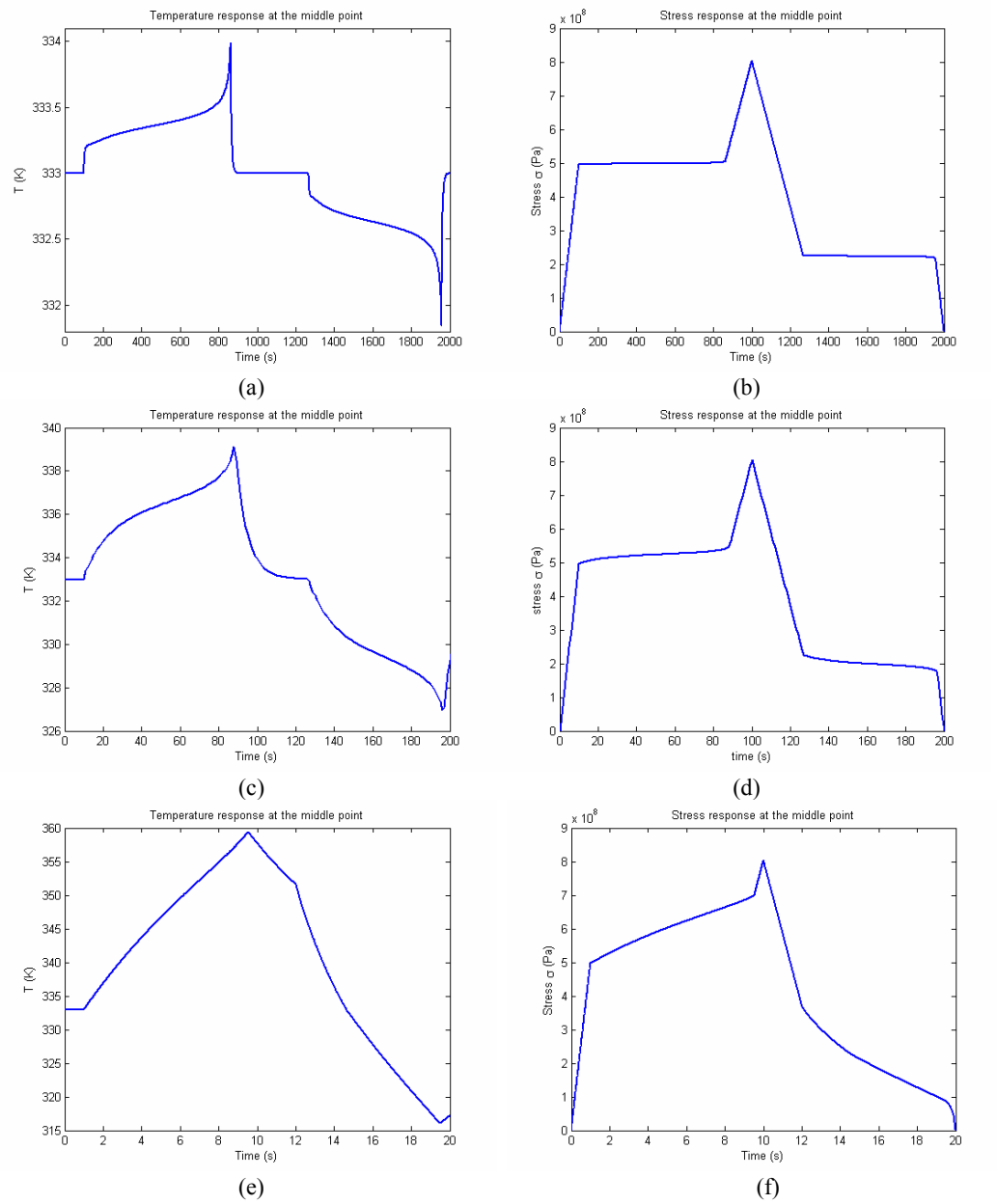


Figure 3.32: Time responses of temperature and stress at the middle point of the SMA wire for three different loading rates: (a) and (b) for the loading rate of $0.7 \times 10^{-4}/s$; (a) and (b) for the loading rate of $0.7 \times 10^{-3}/s$;(a) and (b) for the loading rate of $0.7 \times 10^{-2}/s$; (a), (c) and (e) are temperature responses; (b), (d) and (f) are stress responses.

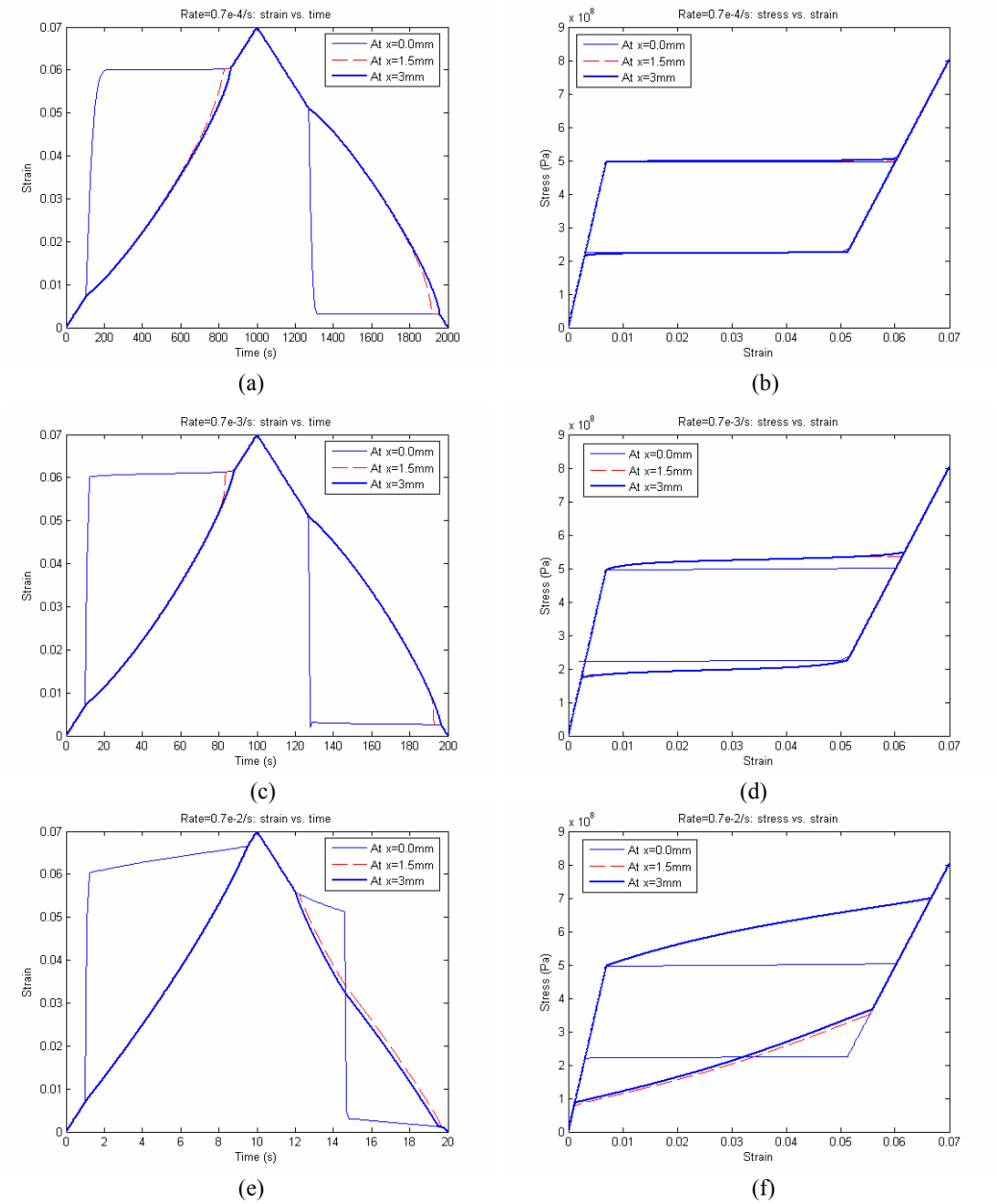


Figure 3.33: Time responses of strain of the SMA wire at three different points $x = 0mm$, $x = 1.5mm$ and $x = 3mm$, and their corresponding stress-strain relations: (a) and (b) for the loading rate of $0.7 \times 10^{-4}/s$; (a) and (b) for the loading rate of $0.7 \times 10^{-3}/s$;(a) and (b) for the loading rate of $0.7 \times 10^{-2}/s$.

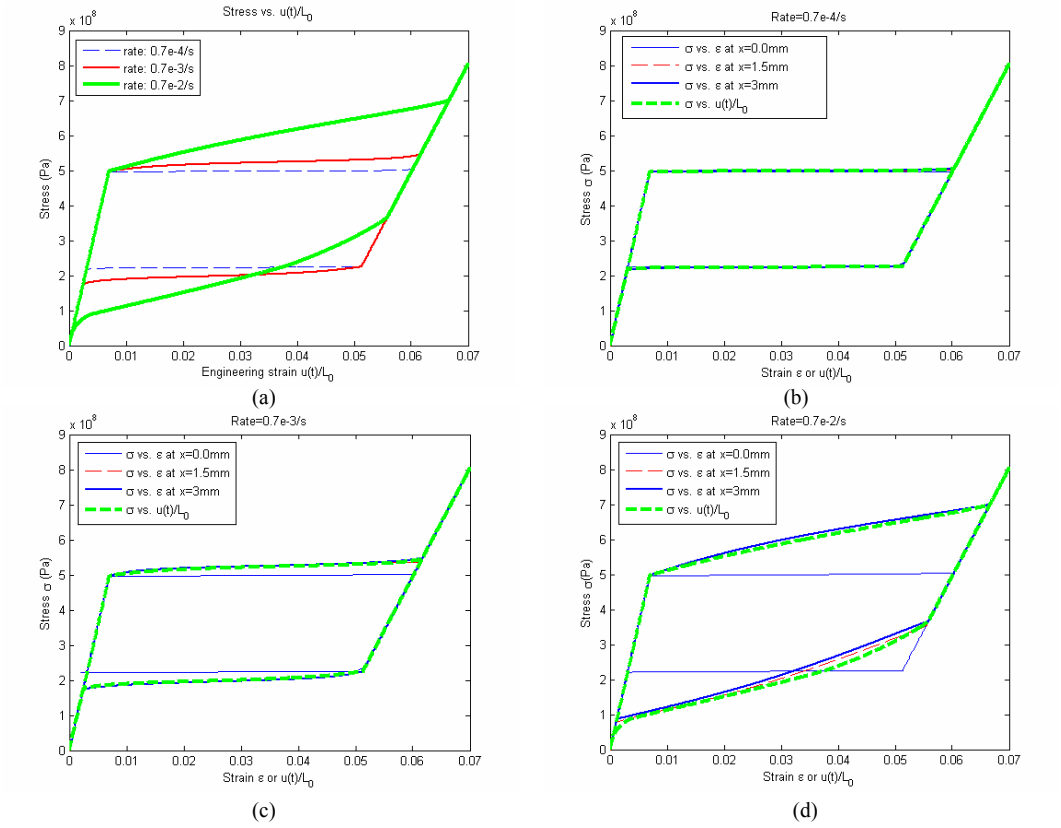


Figure 3.34: Stress-strain relations: (a) engineering stress-strain responses of three different loading rates; (b) engineering stress-strain response vs. stress-strain respones at three different position for rate $\dot{u}(t)/L_0 = 0.7 \times 10^{-4}/s$; engineering stress-strain response vs. stress-strain respones at three different position for rate $\dot{u}(t)/L_0 = 0.7 \times 10^{-3}/s$; engineering stress-strain response vs. stress-strain respones at three different position for rate $\dot{u}(t)/L_0 = 0.7 \times 10^{-2}/s$.

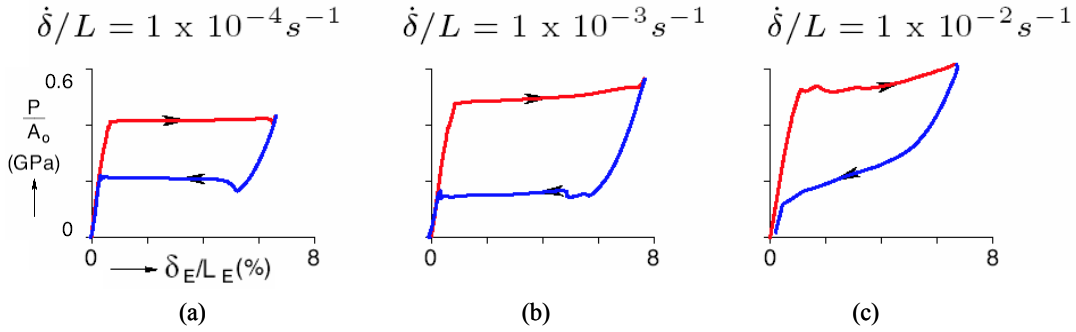


Figure 3.35: Superelastic responses of SMA wire tensile experiments at different displacement rates (Shaw et al [68]): (a) $1 \times 10^{-4}/s$; (b) $1 \times 10^{-3}/s$; (c) $1 \times 10^{-2}/s$.

So the whole SMA wire will transform simultaneously and stress keeps constant during the phase transformation. Figure 3.38 (a) and (b) illustrate the evolution of phase fractions and the stress response of the SMA wire.

SMA wire actuator

Here we study the behaviors of an SMA wire actuator coupled with a linear elastic spring as shown in Figure 3.39 under different boundary conditions. The SMA wire is pre-stretched into fully martensite M_+ phase and then connected with the spring. Upon electric current heating above the transformation temperature, SMA transforms from martensite M_+ to austenite A, which results in contraction and tensile stress in the SMA wire. And upon convective cooling below the transformation temperature and under tensile stress, the SMA wire transforms from austenite A back into martensite M_+ and recovers to the original position. Resistivities of the wire used in the simulations are assumed to be $\rho_{eM} = \rho_{eA} = 0.80 \times 10^{-6}\Omega m$. Other parameters used for the SMA wire are the same as those used in above tensile simulations.

Two different heat transfer boundary conditions, insulated ends with $\frac{\partial T}{\partial x}(0,t) = 0$ and $\frac{\partial T}{\partial x}(L,t) = 0$ and fixed temperature at both ends with $T(0,t) = T(L,t) = T_0$ are studied in sequence.

First, we assume the SMA actuator has insulated thermal boundary conditions as $\frac{\partial T}{\partial x}(0,t) = 0$ and $\frac{\partial T}{\partial x}(L,t) = 0$. The applied voltage $V(t)$ is given in Figure 3.40(a). Starting at $t = 0s$, the voltage is ramped up to $0.4V$ at $t = 1s$ and held for $10s$ to $t = 11s$. From

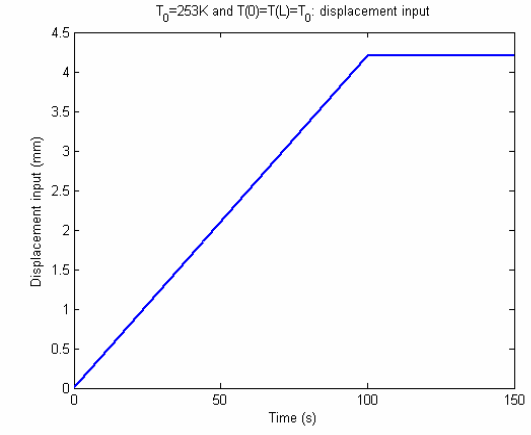


Figure 3.36: Controlled displacement input at low temperature $T_0 = 253K$ with fixed temperature boundary conditions.

$t = 11s$ to $12s$, the voltage is ramped down to 0 and then held for $28s$ up to $t = 50s$. The ambient temperature is assumed to be $T_0 = 253K$. Under insulated boundary conditions, the temperature distribution and thus phase transformation are uniform along the SMA wire actuator. Figure 3.40(b), (c) and (d) present the results of temperature responses, displacement responses and corresponding displacement-temperature diagrams for two different values of the spring stiffness $K_{B1} = 0.1E_MA/L$ and $K_{B2} = 0.4E_MA/L$, respectively. The regions with reduced rates in heating and cooling processes shown in Figure 3.40(b) are due to the latent heat is absorbed or released during the phase transformation processes from M_+ to A or from A to M_+ as illustrated in Figure 3.41(c). As indicated by the evolution of phase fraction in Figure 3.41 (a) and (b), for the system with spring stiffness $K_{B2} = 0.4E_MA/L$, the SMA wire are partially transformed from martensite M_+ into austenite A and has smaller actuation stroke under the same applied voltage input because the stiffer spring causes the larger stress as shown in Figure 3.41(d), which thus requires the temperature to increase to much higher value to overcome the energy barrier between martensite M_+ and austenite A. The system with the softer spring has much sharper transition as illustrated in Figure 3.40(c) and (d).

For the SMA wire actuator with fixed temperature boundary conditions with $T(0,t) = T(L,t) = T_0$, the same applied voltage as before (see Figure 3.40(a)) is used to heat the SMA

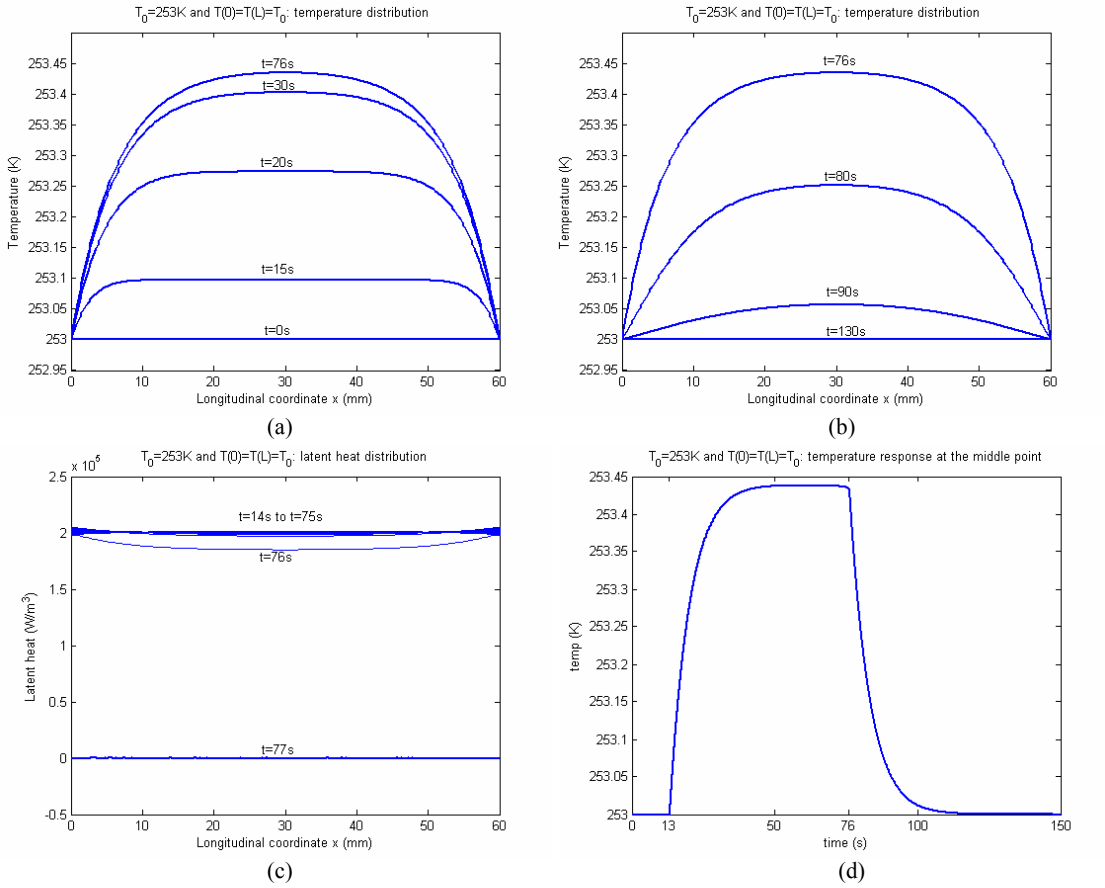


Figure 3.37: Tensile test of SMA wire with fixed temperature boundary condtions at $T_0 = 253K$: (a) evolution of temperature distribution along x during the loading process; (b) evolution of temperature distribution along x during the cooling process; (c) evolution of laten heat distribution along x; (d) temperature response at the middle point $x = 30mm$.

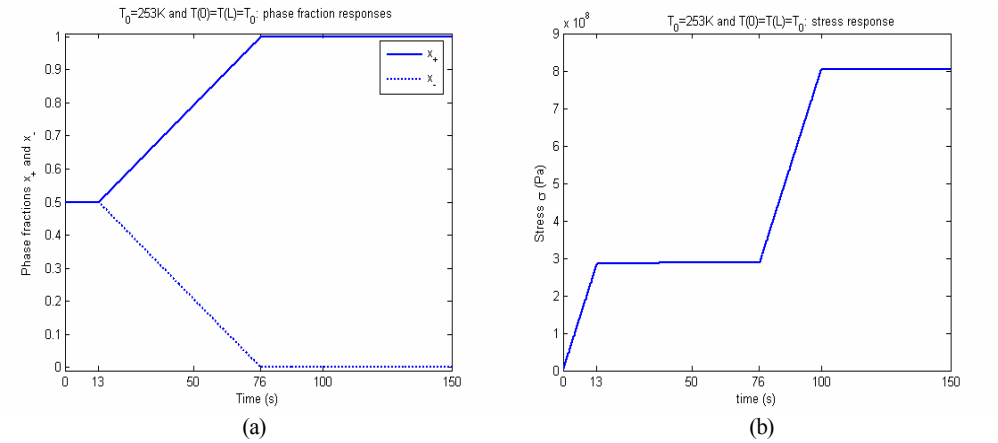


Figure 3.38: Tensile test of SMA wire with fixed temperature boundary condtions at $T_0 = 253K$: (a) evolution of phase fractions x_+ and x_-; (b) stress response.

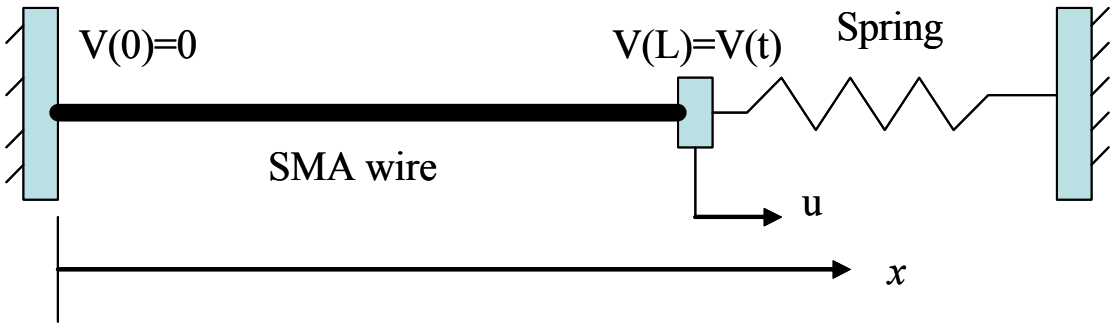


Figure 3.39: SMA wire actuator

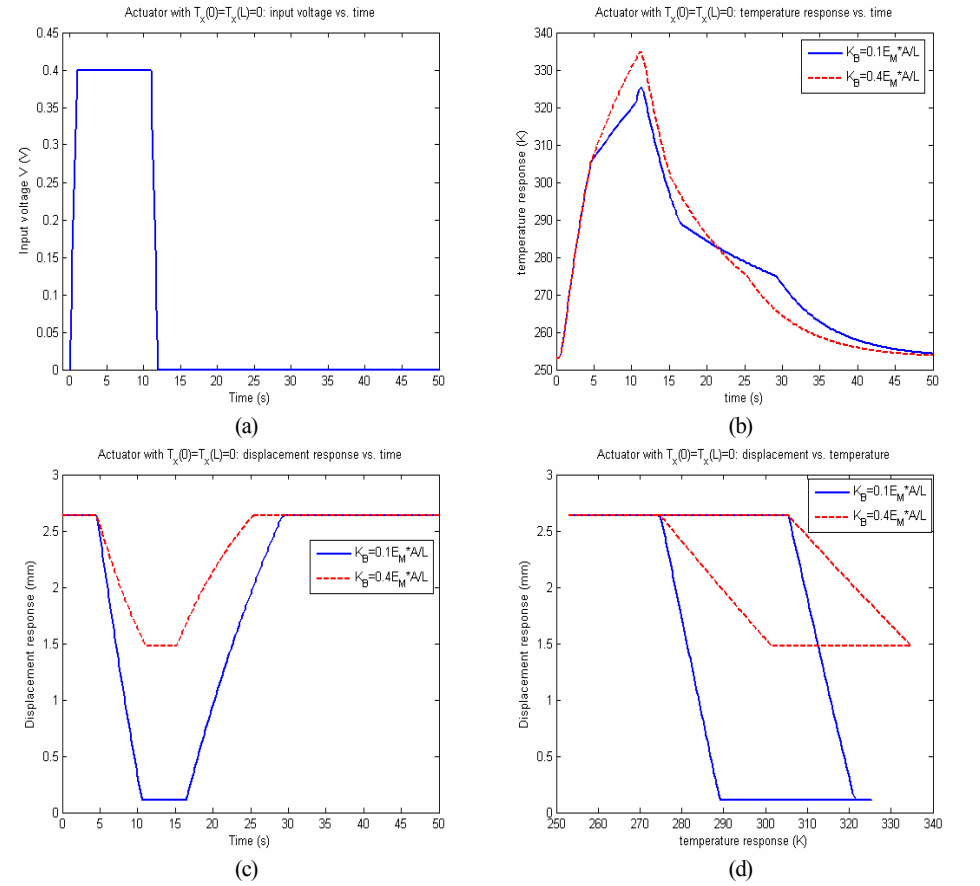


Figure 3.40: SMA wire actuator with insulated boundary conditions: (a). applied voltage vs. time; (b) temperature responses vs. time for different spring stiffness; (c) displacement reponses for different spring stiffness; (d) displacment-temperature relations for different spring stiffness.

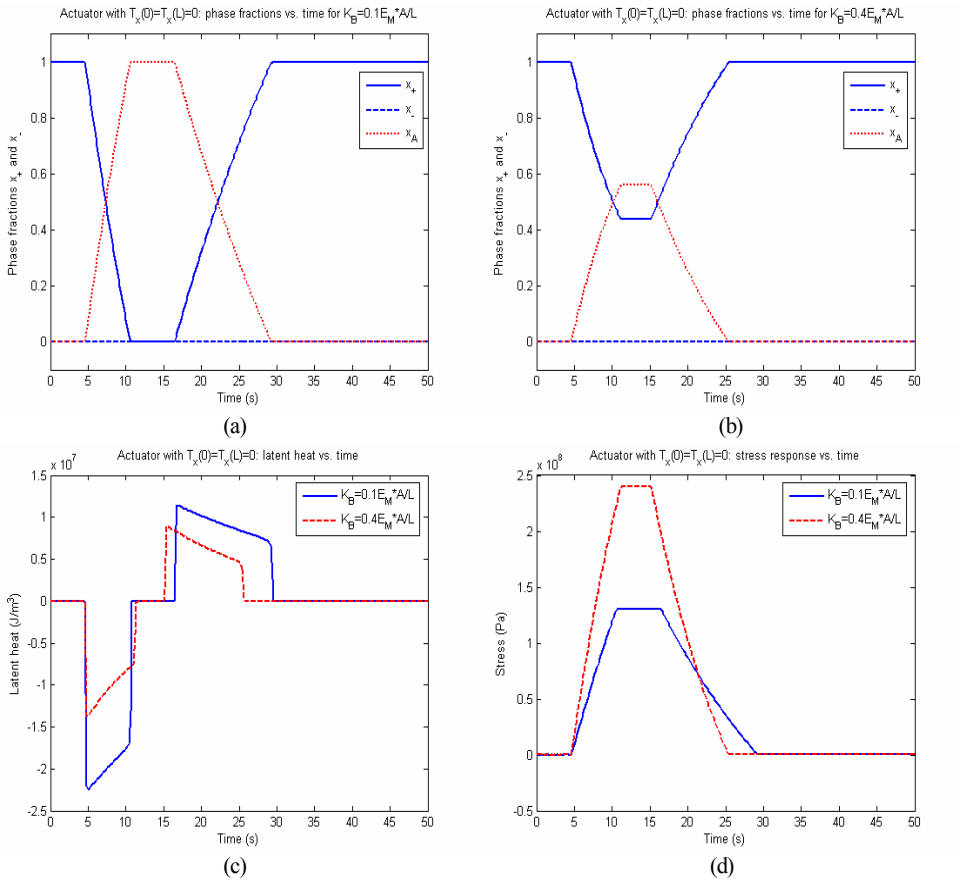


Figure 3.41: SMA wire actuator with insulated boundary conditions: (a) evolution of phase fractions for the case with $K_B = 0.1E_M A/L$; (b) evolution of phase fractions for the case with $K_B = 0.4E_M A/L$; (c) time history of latent heat absorbed and released; (d) stress reponses vs. time.

wire to trigger the phase transformation from martensite M_+ to austenite A. The stiffness of the spring is assumed to be $K_B = 0.1E_M A/L$. Due to the fixed low temperature $T_0 = 253K$ at both ends of the SMA wire, the temperature distribution along the wire is non-uniform as illustrated in Figure 3.42(a) and (b). Figure 3.42(a) and (b) show the temperature history at the middle point and the displacement output of the SMA actuator. During the heating process, the center part of the SMA wire sees higher temperature and starts the transformation from martensite to austenite first and the transformation propagates toward the ends with temperature increasing as indicated by the evolutions of phase fraction x_+ and strain shown in Figure 3.43(a) and Figure 3.43(c). The phase transformation process is reversed during the cooling process as illustrated in Figure 3.43(b) and Figure 3.43(d). The portions close to the fixed low temperature ends do not have phase transformation and only experience elastic deformation. We can see that the stroke of the SMA actuator with the fixed temperature boundary conditions is smaller than that of the SMA actuator with the insulated boundary conditions as illustrated in Figure 3.44. In [69], Chang et al also reported similar finite element simualtion results as illustated in Figure 3.45, which further validates the current FEMLAB implementation.

3.3 Finite Element Analysis of SMA Beam Bending Using FEMLAB

Beam structure is another important application structure form of SMA materials. Structures of some SMA devices, such as thin-film microactuators **??**, can be modeled using beam element instead of 3D element to improve the computational efficiency. SMA beam bending problem is much more complicated than the SMA bar problem due to its inhomogeneous stress and temperature distributions through the thickness and along the axis direction under the thermo-mechanical coupled loading. Phase transformations occur not only along the longitudinal direction but also through the thickness. In this section, based on the small deformation Euler-Bernoulli beam theory and by treating an SMA beam as consisting of several layers, we implement the 1-D SMA model into the FEMLAB using its PDE general form and study the quasistatic inhomogeneous bending behaviors of a cantilever SMA beam under the isothermal and non-isothermal conditions.

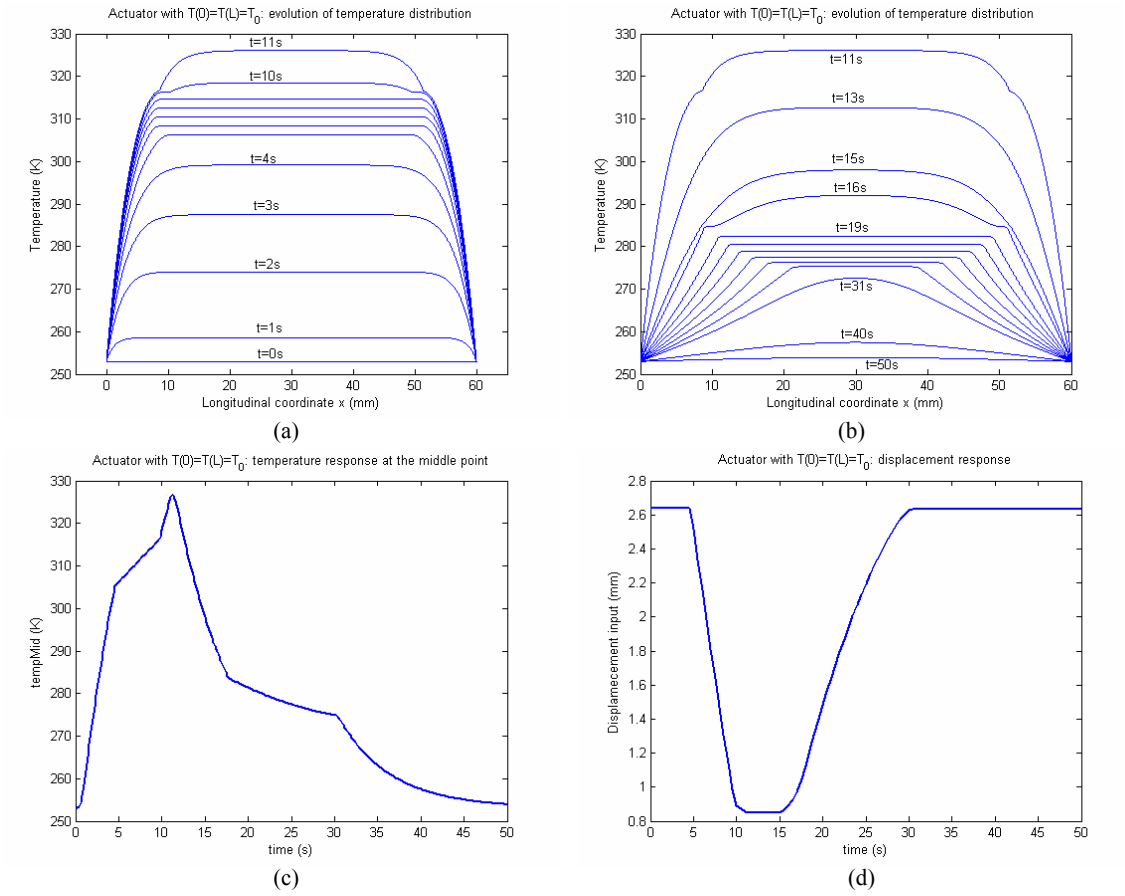


Figure 3.42: SMA wire actuator with fixed temperature boundary conditions: (a) temperature distribution along the wire during the heating process; (b) temperature distribution along the wire during the cooling process; (c) temperature history at the middle point $x = 30mm$; (d) displacement response of SMA actuator.

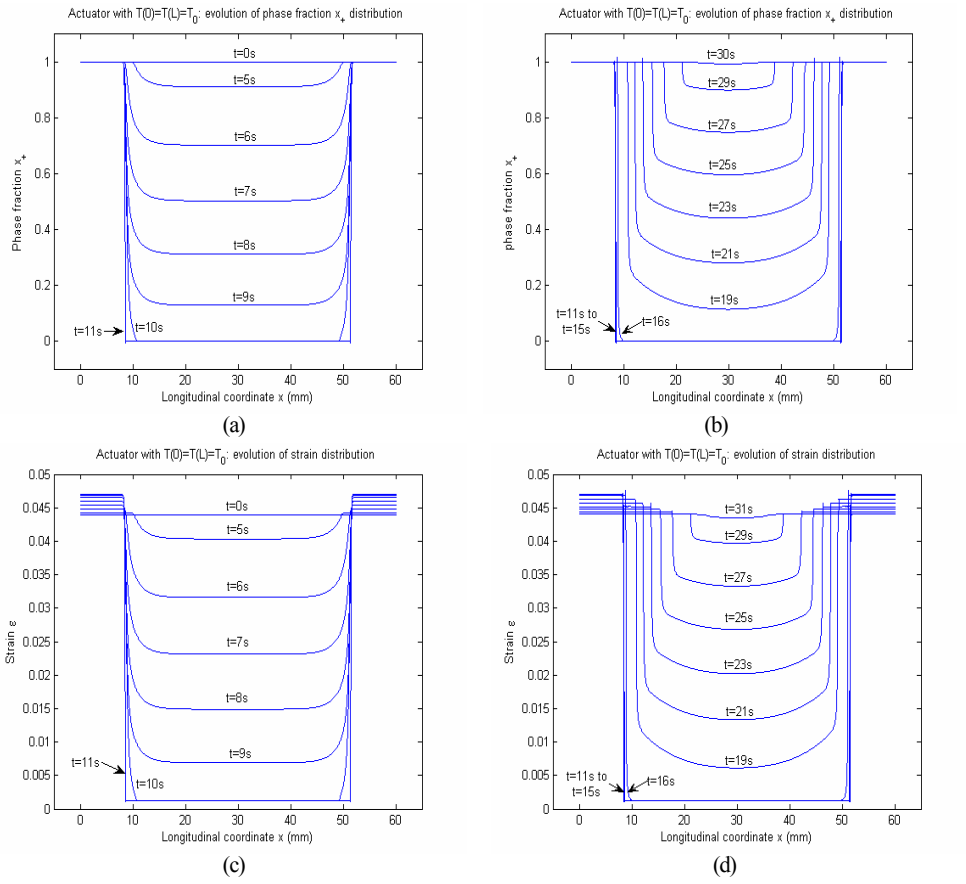


Figure 3.43: SMA wire actuator with fixed temperature boundary conditions: (a) phase fraction x_+ distribution along the wire during the heating process; (b) phase fraction x_+ distribution along the wire during the cooling process; (c) strain distribution along the wire during the heating process; (d) strain distribution along the wire during the cooling process;

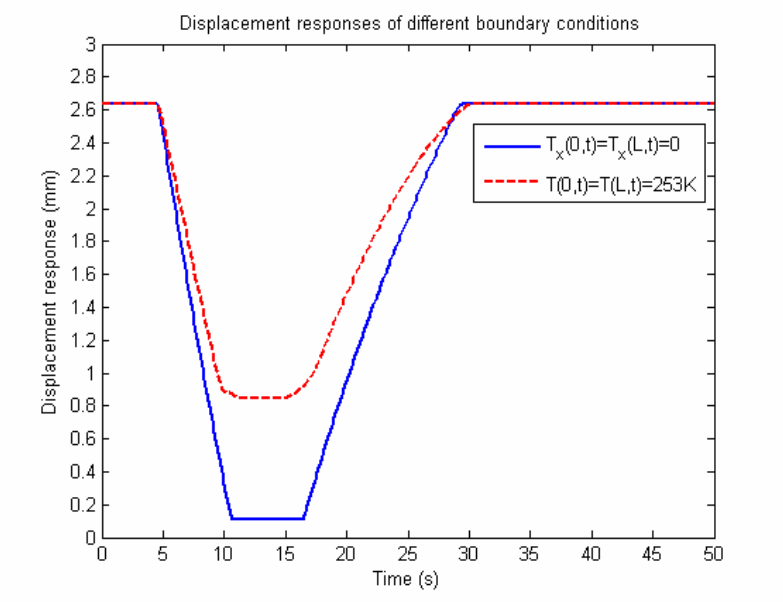


Figure 3.44: Comparison of SMA actuator displacement reponses between the insulated boundary conditions and fixed temperature boundary conditions under the same applied voltage.

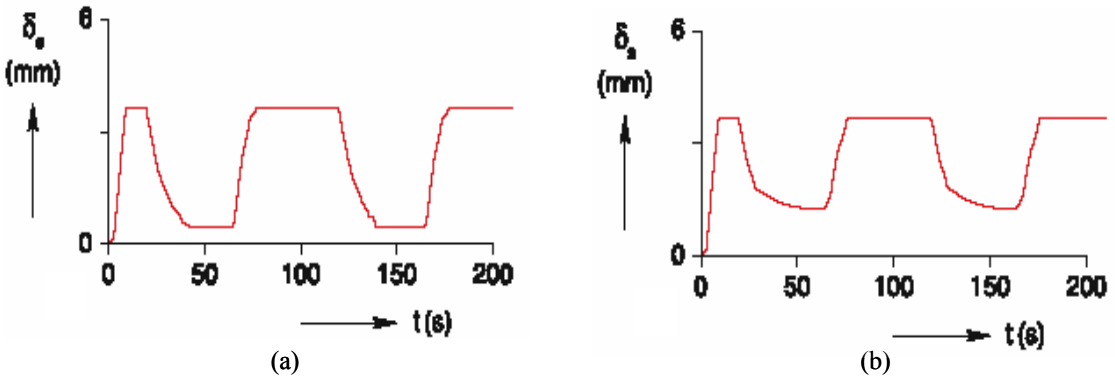


Figure 3.45: Displacement responses of a SMA wire actuator (Chang et al [69]): (a) insulated boundary condition; (b) fixed temperature boundary condition.

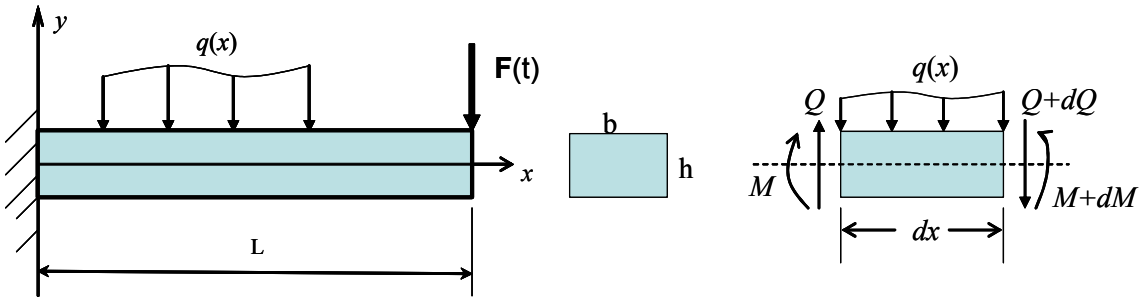


Figure 3.46: SMA cantilever beam

First, we study the quasiplastic and superelastic behaviors of an SMA cantilever beam under a constant low temperature and a constant high temperature, respectively. The non-homogeneous phase transformation along the SMA beam is caused by mechanical loading.

Then detail analysis of the SMA beam bending under thermo-mechanical loading is presented by using the temperature dependent stress-strain relation of the free energy SMA model.

By including the nonlinear transient heat transfer equation with phase transformation induced latent hearts included, the rate-dependent responses of an SMA cantilever beam under thermo-mechanical coupling loadings are studied.

3.3.1 Implementation

The classical Euler-Bernoulli beam theory is based on the hypothesis that cross-sections perpendicular to the neutral axis of the beam before deformation remain plane and perpendicular to the neutral axis throughout the deformation. These assumptions neglects the Poisson effect and transverse strain and lead to a one dimensional stress and strain state in the beam. So the 1-D SMA model developed in the section (3.1) can be applied to model the Euler-Bernouli beam bending problem by assuming an SMA beam to consist of several layers. For the cantilever beam shown in Figure 3.46, we can derive the equilibrium equation as

$$\frac{\partial Q}{\partial x} = -q(x) \tag{3.64}$$

and the relation between the shear force $Q(x)$ and the cross-section moment $M(x)$

$$\frac{\partial M}{\partial x} = Q \tag{3.65}$$

The cross-section moment $M(x)$ is calculated as

$$M(x) = b \int_{-h/2}^{h/2} y\sigma(x,y)dy \tag{3.66}$$

where $\sigma(x,y)$ is the cross-section stress. For SMA material, the stress-strain relation is given in (3.17) as

$$\sigma(x,y) = \frac{E_M\left[\varepsilon(x,y) - (x_+ - x_-)\varepsilon_T\right]}{x_+ + x_- + \frac{E_M}{E_A}x_A} \tag{3.67}$$

Due to the inhomogeneity of the SMA beam bending, the phase fractions $x_\alpha(x,y)$ are also functions of position (x,y). For the kinematic assumptions of the Euler-Bernoulli Beam theory, the strain $\varepsilon(x,y)$ is calculated as

$$\varepsilon(x,y) = -y\frac{\partial\theta}{\partial x} \tag{3.68}$$

with the deflection angle $\theta(x)$ following from the transverse deflection $W(x)$ of the beam as

$$\frac{\partial W}{\partial x} = \theta \tag{3.69}$$

The cross-section moment in (3.66) can be computed by using Gauss integration as

$$\begin{aligned} M(x) &= b\textstyle\int_{-h/2}^{h/2} y\sigma(x,y)dy \\ &= \tfrac{bh^2}{4}\textstyle\int_{-1}^{1} \xi\sigma(x,\xi)d\xi \quad (y = \tfrac{h}{2}\xi) \\ &= \tfrac{bh^2}{4}\textstyle\sum_{i=1}^{n} w_i\xi_i\sigma(x,\tfrac{h}{2}\xi_i) \end{aligned} \tag{3.70}$$

where ξ_i and w_i are Gauss integration points and corresponding weights, respectively. From (3.67) and (3.68), we have

$$\sigma(x,\frac{h}{2}\xi_i) = \frac{E_M\left[\varepsilon(x,\frac{h}{2}\xi_i) - (x_+^i - x_-^i)\varepsilon_T\right]}{x_+^i + x_-^i + \frac{E_M}{E_A}x_A^i} \tag{3.71}$$

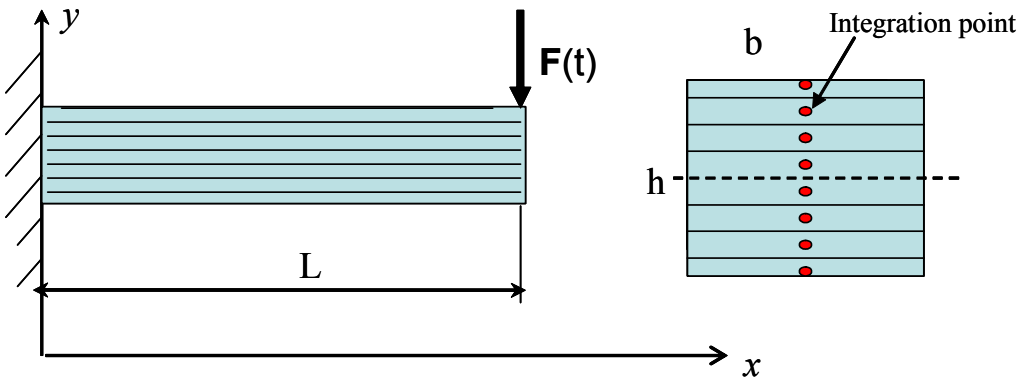


Figure 3.47: Illustration of Gauss integration

$$\varepsilon(x, \frac{h}{2}\xi_i) = -\frac{h}{2}\xi_i \frac{\partial \theta}{\partial x} \tag{3.72}$$

As illustrated in Figure 3.47, we consider the SMA beam to consist of n thin layers. Each integration point $y_i = \frac{h}{2}\xi_i$ represents one layer and the evolution of phase fractions at each layer is governed by

$$\begin{aligned} \dot{x}^i_+ &= -x^i_+ p^{+A}(\sigma(x, \tfrac{h}{2}\xi_i), T) + (1 - x^i_+ - x^i_-) p^{A+}(\sigma(x, \tfrac{h}{2}\xi_i), T) \\ \dot{x}^i_- &= -x^i_- p^{-A}(\sigma(x, \tfrac{h}{2}\xi_i), T) + (1 - x^i_+ - x^i_-) p^{A-}(\sigma(x, \tfrac{h}{2}\xi_i), T) \end{aligned} \quad i = 1, \cdots, n \tag{3.73}$$

Substituting (3.71) and (3.72) into (3.70), we can express the cross-section moment $M(x)$ as an affine function of the curvature of the neutral axis $\frac{\partial \theta}{\partial x}$ as

$$M(x) = \beta \frac{\partial \theta}{\partial x} + \gamma \tag{3.74}$$

with

$$\begin{aligned} \beta &= \tfrac{bh^2}{4} \sum_{i=1}^{n} w_i \xi_i \beta_i \\ \gamma &= \tfrac{bh^2}{4} \sum_{i=1}^{n} w_i \xi_i \gamma_i \end{aligned} \tag{3.75}$$

and

$$\begin{aligned}\beta_i &= \frac{E_M(-\frac{h}{2}\xi_i)}{x_+^i + x_-^i + \frac{E_M}{E_A}x_A^i} \\ \gamma_i &= \frac{E_M\varepsilon_T(-x_+^i + x_-^i)}{x_+^i + x_-^i + \frac{E_M}{E_A}x_A^i}\end{aligned} \tag{3.76}$$

Using the shear force Q, moment M, deflection angle θ, deflection W and phase fractions x_+^i, x_-^i $(i = 1, \cdots, n)$ as solution variables

$$U = \begin{bmatrix} Q & M & \theta & W & x_+^1 & x_-^1 & \cdots & x_+^n & x_-^n \end{bmatrix}^T$$

we can implement the quasistatic bending problem of the SAM cantilever beam into the FEMLAB general form PDEs as

$$\mathbf{d}_a\frac{\partial \mathbf{U}}{\partial t} + \frac{\partial \mathbf{\Gamma}}{\partial x} = \mathbf{f} \tag{3.77}$$

with

$$\mathbf{d}_a = diag(\begin{bmatrix} 0 & 0 & 0 & 0 & 1 & 1 & \cdots & 1 & 1 \end{bmatrix})$$

$$\mathbf{\Gamma} = \begin{bmatrix} 0 & 0 & 0 & 0 & 0 & 0 & \cdots & 0 & 0 \end{bmatrix}^T$$

$$\mathbf{f} = \begin{bmatrix} Q_x + q(x) \\ -M_x + Q \\ -\theta_x + \frac{M-\gamma}{\beta} \\ -W_x + \theta \\ -x_+^1 p^{+A}(\sigma(x, \frac{h}{2}\xi_1), T) + (1 - x_+^1 - x_-^1)p^{A+}(\sigma(x, \frac{h}{2}\xi_1), T) \\ -x_-^1 p^{-A}(\sigma(x, \frac{h}{2}\xi_1), T) + (1 - x_+^1 - x_-^1)p^{A-}(\sigma(x, \frac{h}{2}\xi_1), T) \\ \vdots \\ -x_+^n p^{+A}(\sigma(x, \frac{h}{2}\xi_n), T) + (1 - x_+^n - x_-^n)p^{A+}(\sigma(x, \frac{h}{2}\xi_n), T) \\ -x_-^n p^{-A}(\sigma(x, \frac{h}{2}\xi_n), T) + (1 - x_+^n - x_-^n)p^{A-}(\sigma(x, \frac{h}{2}\xi_n), T) \end{bmatrix}$$

Dirichlet boundary conditions are

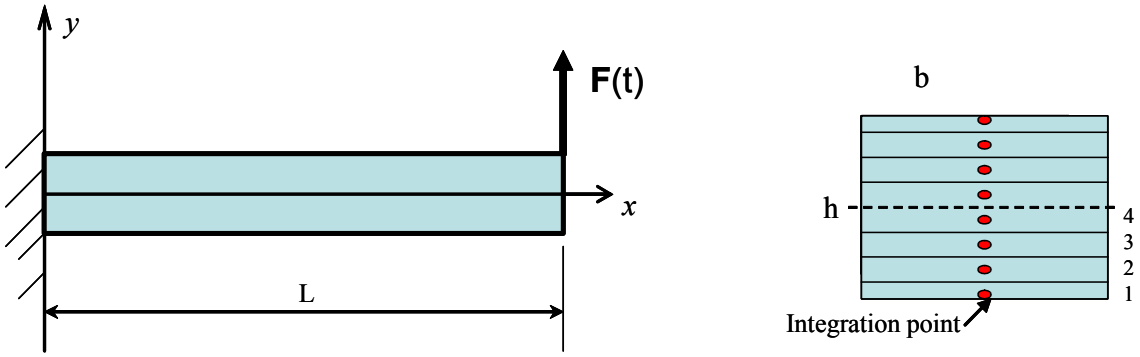


Figure 3.48: SMA cantilever beam with 8 integration points

$$\begin{aligned} W(0,t) = 0: &\qquad r = W \\ \theta(0,t) = 0: &\qquad r = \theta \\ Q(L,t) = F(t): &\qquad r = Q - F(t) \\ M(L,t) = 0: &\qquad r = M \end{aligned}$$

No restriction on phase fractions $x^i_{\pm}$ on both ends is implemented as $r = 0$. Initial conditions need to be given for phase fractions as

$$\begin{bmatrix} x^1_+(x,0) = x^1_{+0}(x) \\ x^1_-(x,0) = x^1_{-0}(x) \\ \vdots \\ x^n_+(x,0) = x^n_{+0}(x) \\ x^n_-(x,0) = x^n_{-0}(x) \end{bmatrix}$$

3.3.2 Inhomogeneous Bending Analysis under Constant Temperatures

The geometry parameters of the uniform SMA cantilever beam with rectangular cross section shown in Figure 3.48 are: length $L = 10cm$, width $b = 1.5cm$ and height $h = 1cm$. The material parameters of the SMA material are the same as those used in the bar problems as: $E_A = 71.1GPa$, $E_M = 30.9GPa$, $\varepsilon_T = 0.044$, $\sigma_A(T_U = 353K) = 663.16MPa$, $\sigma_A(T_L = 323K) = 431.58MPa$, $\Delta\sigma = 295MPa$, volume of a layer $V_D = 5 \times 10^{-23}m^3$ and

relaxation time $\tau_x = 10^{-2}s$. In this and subsequent examples, eight integration points are used to calculate the cross-section moment given in Eq. (3.70). The cross-section is divided into 8 layers and each layer is represented by a Gauss integration point as shown in 3.48 (right).

Low temperature case with $T = 273K$: quasiplastic behavior

First, under isothermal assumptions, we study the quasiplastic behavior of the inhomogeneous quasistatic SMA beam bending at the constant low temperature $T = 273K$, at which the SMA material is in the martensitic state. A concentrated force is applied at the free end of the SMA cantilever beam and the simulation starts with $x_+ = x_- = 0.5$.

Figure 3.49 presents the time histories of the applied force, displacement response and the corresponding force displacement diagram. After unloading, a residual deformation is generated. The force displacement diagram in Figure 3.49(b) indicates the gradual phase transform behavior of the SMA beam bending. Compared to the uniform bar problem in Figure 3.7, there is no sharp transition due to the inhomogeneity of the beam bending problem.

From the contour plots of the stress, strain and phase fractions shown in Figure 3.50 during the loading process at $F = 1200N$, $2100N$ and $3000N$, we can see that, due to the nonuniform stress distribution throughout the SMA beam, the phase transformation starts from the outer layer at the clamped end with the maximum stress and propagates through the thickness and along the length of the beam with increasing loading. The section below the neutral axis is subjected to tensile stresses and phase transformation occurs from martensite M_- to M_+. The section above the neutral axis is subjected to compression stresses and transforms from M_+ to M_-. These have the same effect for the global beam deflection.

Figure 3.51 shows the contour plots of the stress, strain and phase fractions during the unloading process at $F = 3000N$, $1500N$ and $0N$. From the global force-displacement response shown in 3.49(b), we can see that the unloading process follows an elastic deformation path. The phase fraction contour plots in Figure 3.51(c) and 3.51(d) are essentially unchanged during the unloading process. Thus after the unloading is completed with $F = 0N$, and there is a residual strain distribution as shown in Figure 3.51(b), which contributes to the global residual deformation of the SMA beam as shown in Figure 3.49(b).

The stresses in each cross-section are re-distributed to satisfy the 0 cross-section moment, which generates a complex residual stress distribution as illustrated by the stress contour plot shown in Figure 3.51(a). Detail analysis of the quasiplastic behavior of the SMA beam bending is given below.

Figures 3.52 (a)-(d) show the phase fraction, stress and strain distributions of different layers along the length of the beam at $t = 1s$ with $F = 3000N$, respectively. The layer numbers are labeled in sequence as shown in 3.48 (right). Considering the anti-symmetry of the bending problem as shown in Figures 3.50 and 3.51, only the half section data are presented. These are also presented as contour plots in Figure 3.50. We can see that the portions of layers without complete transformation have the same constant stress, which is equal to the transformation stress σ_M.

Figures 3.53(a) and (b) show the phase fractions distributions along the length of the beam at $t = 2s$ with $F = 0N$, respectively. These are also shown as contour plots in Figures 3.51(c) and 3.51(d). Compared to the results in Figures 3.52 (a) and (b), only small portion of the layer 3 near the clamped end are transformed back into the martensite M_- and the distributions of other layers are the same as those at the maximum loading moment $t = 1s$. After the unloading is completed with the applied force $F = 0N$, the stresses in each cross-section are re-distributed to satisfy the 0 cross-section moment given in (3.70), which generates the residual stress distributions of different layers along the length of the beam as shown in Figure 3.53(c) and the corresponding residual strain distributions shown in 3.53(d). This results in the global residual deformation of the SMA cantilever beam as illustrated in Figure 3.49

Figure 3.54 shows the time histories of the phase fractions of different layers at the clamped end. The layers 1 and 2 at the clamped end transform completely from martensite M_- to M_+ and the layers 3 and 4 partially transform only. As shown in the zoom-in Figures 3.54(b) and (d) from $t = 0.25s$ to $0.4s$, the phase transformation starts gradually from the layer 1 followed by the layer 2 and then the layer 3. Only until the phase transformation starts at the layer 4 from $t = 0.36s$ to $t = 0.37s$, the layer 1 transforms completely from martensite M_- to M_+.

Figure 3.55 shows the time histories of stress and strain of different layers at the clamped end. During the loading process, the layer 1 reaches the transformation stress first and

maintains at the same level. The increasing of the applied load is sustained by other layers that are still in elastic deformation region. According to the plane assumption of the Euler-Bernoulli beam theory, the strain varies linearly through the height of the beam cross-section given in (3.68). Thus, the outer layer 1 always has the maximum strain and the inner layer 4 has the minimum strain. As shown in the zoom-in Figure 3.55(b) from $t = 0.25s$ to $0.4s$, the layer 4 reaches the transformation stress from $t = 0.36s$ to $0.37s$. Once all the layers are in the unstable transition region, the layers transform together with strain varying linearly through the height of the cross-section. The outer layer 1 transforms completely from martensite M_- to M_+ first. After the complete transformation, the layer 1 re-gains its stiffness E_M and sustains the increasing of the applied load with small increasing change of strain. This is also clearly illustrated in the stress and strain distributions at the clamped end through the thickness of the beam shown in Figure 3.56.

Figure 3.57 shows the stress-strain responses at the clamped end. Each layer of the SMA beam is governed by the same stress-strain relation at $T = 273K$. During the unloading process, we can see that all the layers follow the elastic deformation paths with the same elastic modulus E_M, and the amount the stress decreases in each layer is given by $E_M(-y_i\Delta\theta_x)$ with $\Delta\theta_x$ is the curvature of the neutral axis and $(-y_i\Delta\theta_x)$ is the corresponding strain change of the i-th layer. So during the unloading process, an inner layer could see a higher stress value than an outer layer. When the layer 3 reaches zero stress first, other layers still have tensile stresses. Due to the constraint of linearly varying strains through the thickness, the layer 3 is forced to sustain compression stress with the unloading process continuing in order to satisfy the decreasing global cross-section moment. At the clamped end, after the unloading is completed with the applied force $F = 0N$, the stresses are re-distributed to satisfy the 0 cross-section moment with layers 1, 2 and 4 in tension, and the layer 3 in compression as illustrated in Figure 3.57.

High temperature case with $T = 333K$: superelastic behavior

Similarly, now we study the superelastic behavior of the SMA beam bending at high temperature $T = 333K$. The SMA material is in austenite state at this temperature under zero mechanical loading. So the simulation starts with the initial phase fractions as $x_+ = x_- = 0$. Figure 3.58 shows the time histories of the applied force, displacement response and the corresponding force displacement diagram. The force displacement diagram in Figure

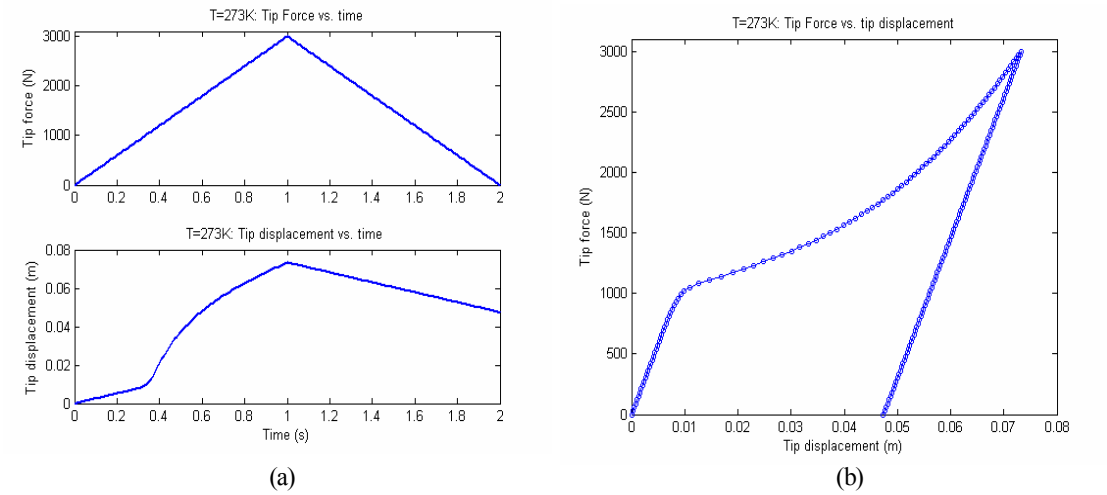


Figure 3.49: Quasiplastic behavior of SMA beam bending at low temperature $T = 273K$: (a) Applied tip force and tip displacement response vs. time; (b) Tip force vs. tip displacment.

3.58(b) illustrates the superelastic behavior of the SMA beam bending with gradual phase transform at high temperature. This qualitatively matches the result reported by Auricchio and Sacco [55] as shown in Figure 3.59. The SMA beam is able to recover large deformation after unloading.

The gradual and inhomogeneous phase transformation of the SMA beam bending is illustrated in the contour plots of the stress, strain and phase fractions during the loading process and unloading process in Figures 3.60 and 3.61. Upon loading, some portion of the SMA beam below the neutral axis subjected to tensile stresses transforms from austenite A to martensite M_+ and some portion above the neutral axis subjected to compression stresses transforms from austenite A to martensite M_- and together result in a large deflection of the SMA beam as shown in Figure 3.58. Upon unloading, the SMA beam transforms back into austenite A and recovers its original shape. During the loading process, the outer layers at the clamped end reach the transform stress σ_A first and the phase transformation starts from there and propagates longitudinally and transversely. The reverse process occurs during the unloading process.

Figure 3.62 shows the time histories of phase fractions, stress and strain of different

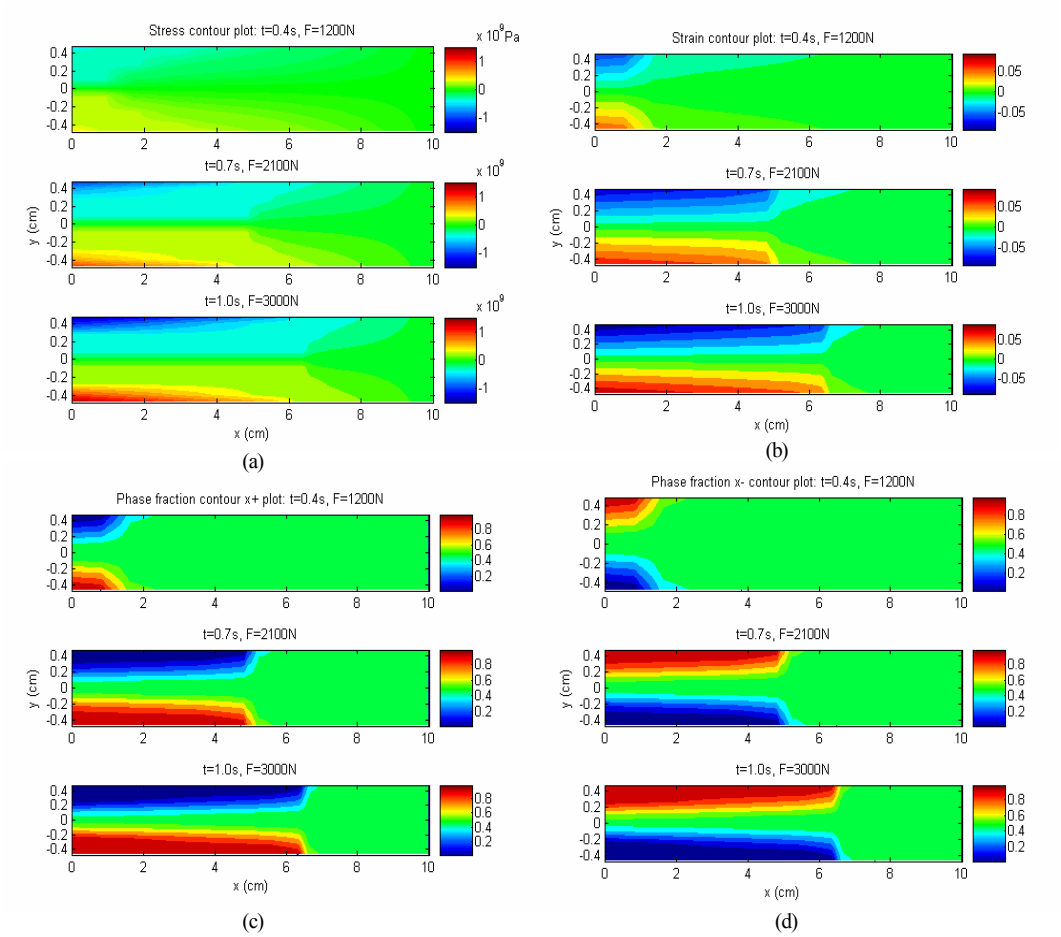


Figure 3.50: Contour plots of SMA beam bending at low temperature $T = 273K$ during the loading process: (a) stress contour plots; (b) strain contour plots; (c) phase fraction x_+ contour plots; (d) phase fraction x_- contour plots at $F = 1200N$, $2100N$, $3000N$, respectively.

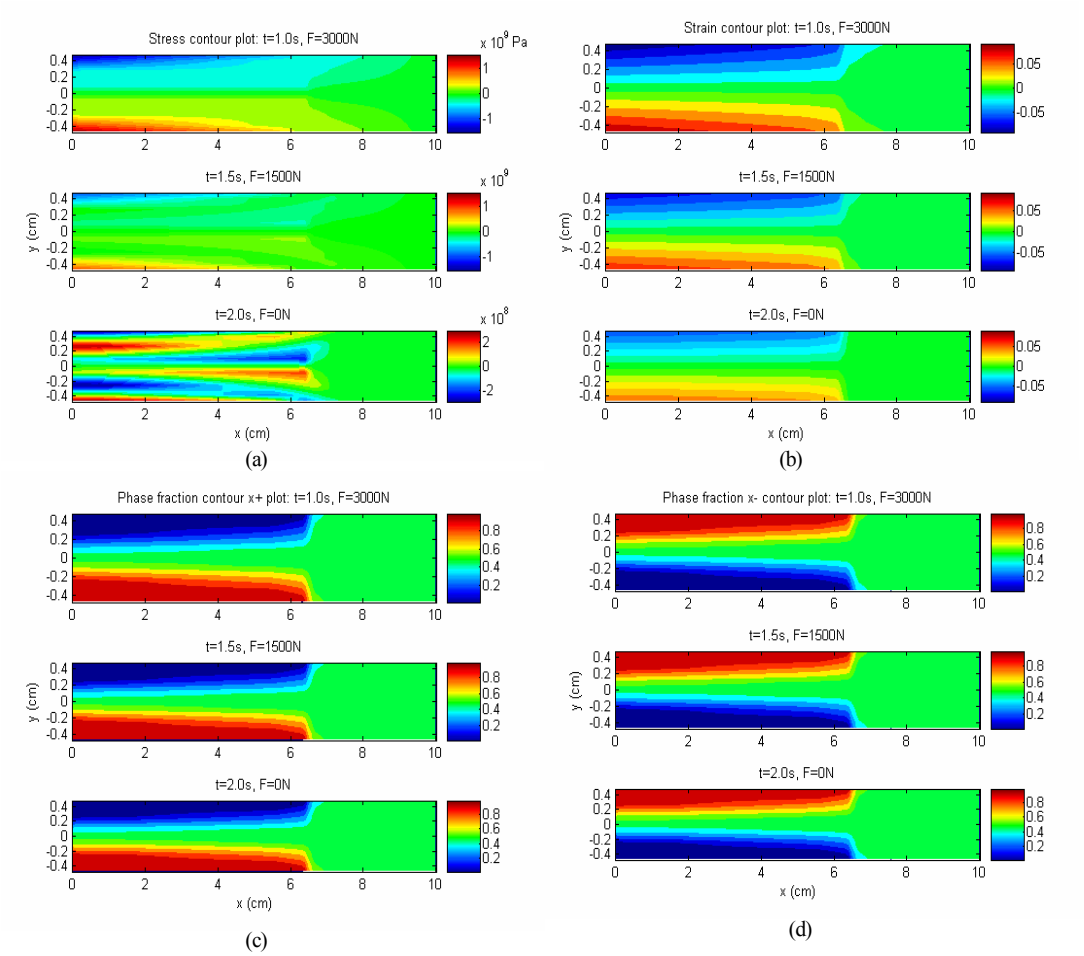


Figure 3.51: Contour plots of SMA beam bending at low temperature $T = 273K$ during the unloading process: (a) stress contour plots; (b) strain contour plots; (c) phase fraction x_+ contour plots; (d) phase fraction x_- contour plots at $F = 3000N$, $1500N$, $0N$, respectively.

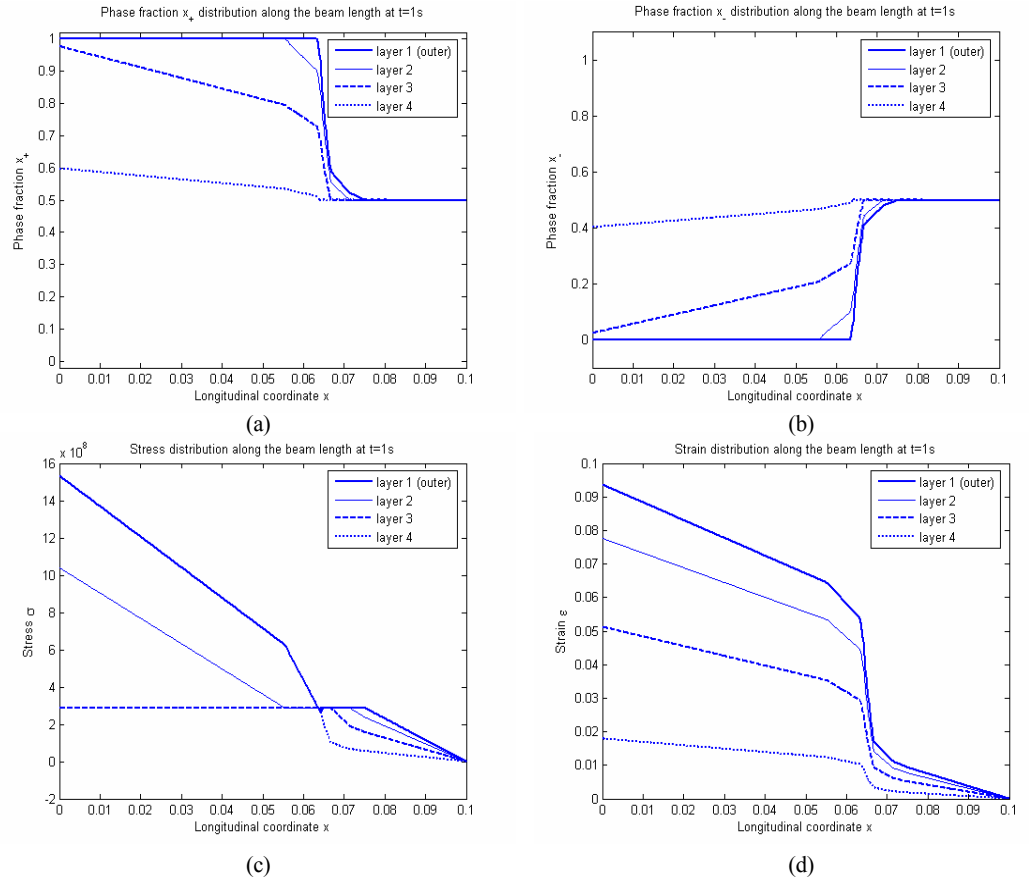


Figure 3.52: SMA beam bending at low temperature $T = 273K$: phase fraction, stress and strain distributions of different layers along the length of the beam at $t = 1s$ with $F = 3000N$: (a) x_+ vs. x; (b) x_- vs. x; (c) stress vs. x; (d) strain vs. x.

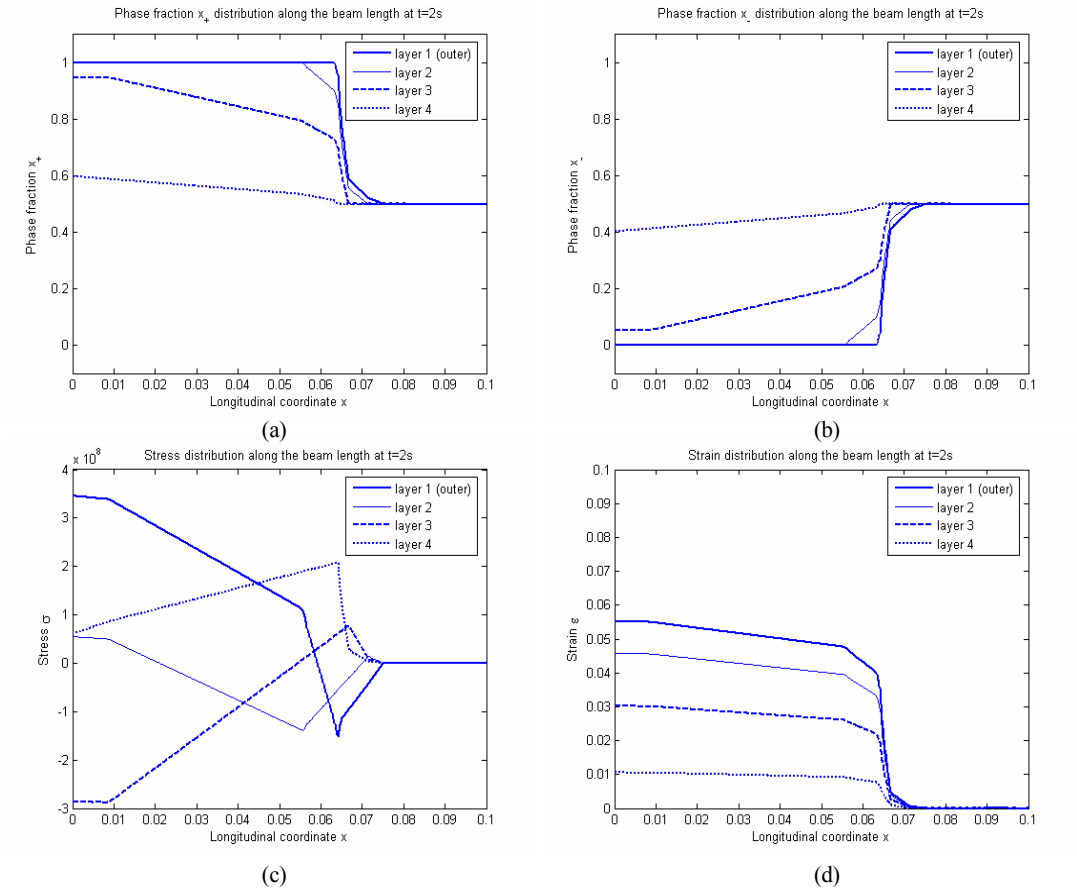


Figure 3.53: SMA beam bending at low temperature $T = 273K$: phase fraction, stress and strain distributions of different layers along the length of the beam at $t = 2s$ with $F = 0N$: (a) x_+ vs. x; (b) x_- vs. x; (c) stress vs. x; (d) strain vs. x.

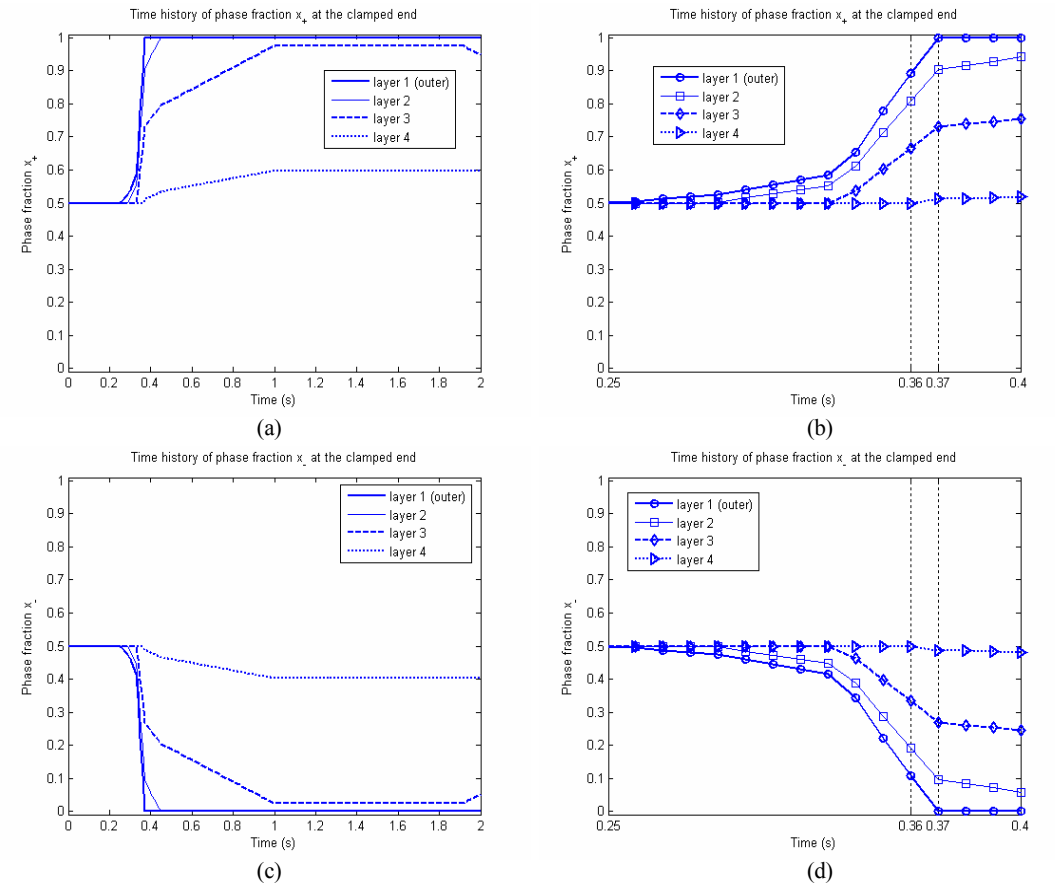


Figure 3.54: SMA beam bending at low temperature $T = 273K$: evolution of phase fractions for different layers at the clamped end: (a) x_+ vs. time; (b) x_+ vs. time from $t = 0.25$ to $0.4s$; (c) x_- vs. time; (d) x_- vs. time from $t = 0.25$ to $0.4s$.

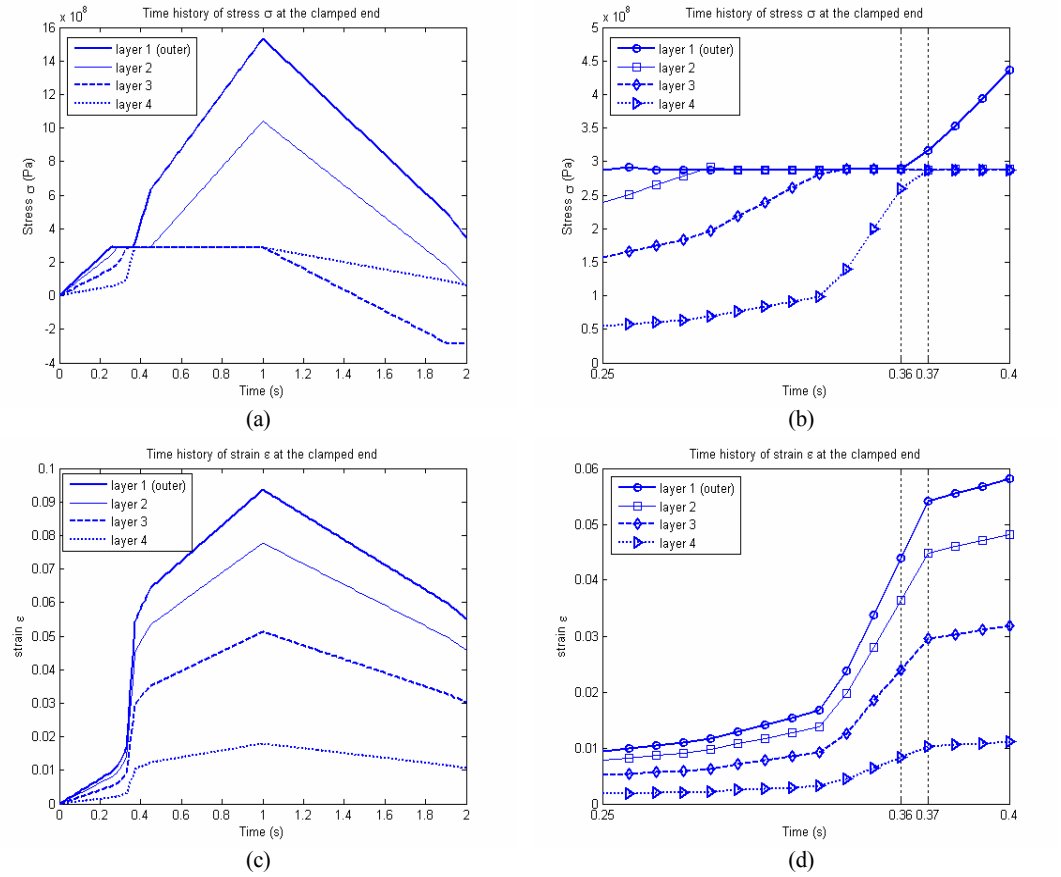


Figure 3.55: SMA beam bending at low temperature $T = 273K$: time history of stress and strain responses of different layers at the clamped end: (a) stress vs. time; (b) stress vs. time from $t = 0.25$ to $0.4s$; (c) strain vs. time; (d) strain vs. time from $t = 0.25$ to $0.4s$.

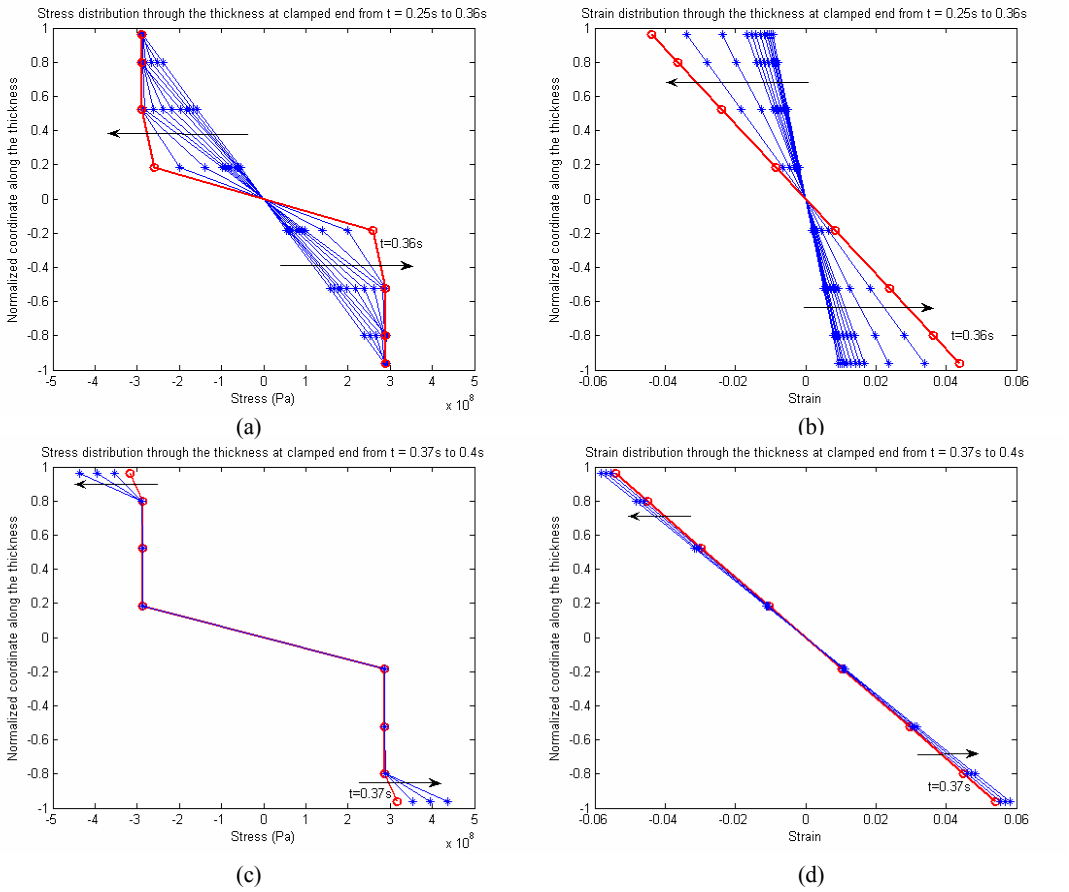


Figure 3.56: SMA beam bending at low temperature $T = 273K$: stress and strain distribution of different layers through the thickness at the clamped end: (a) stress distribution from $t = 0.25$ to $0.36s$; (b) strain distribution from $t = 0.25$ to $0.36s$; (c) stress distribution from $t = 0.37s$ to $0.4s$; (d) strain distribution from $t = 0.37s$ to $0.4s$.

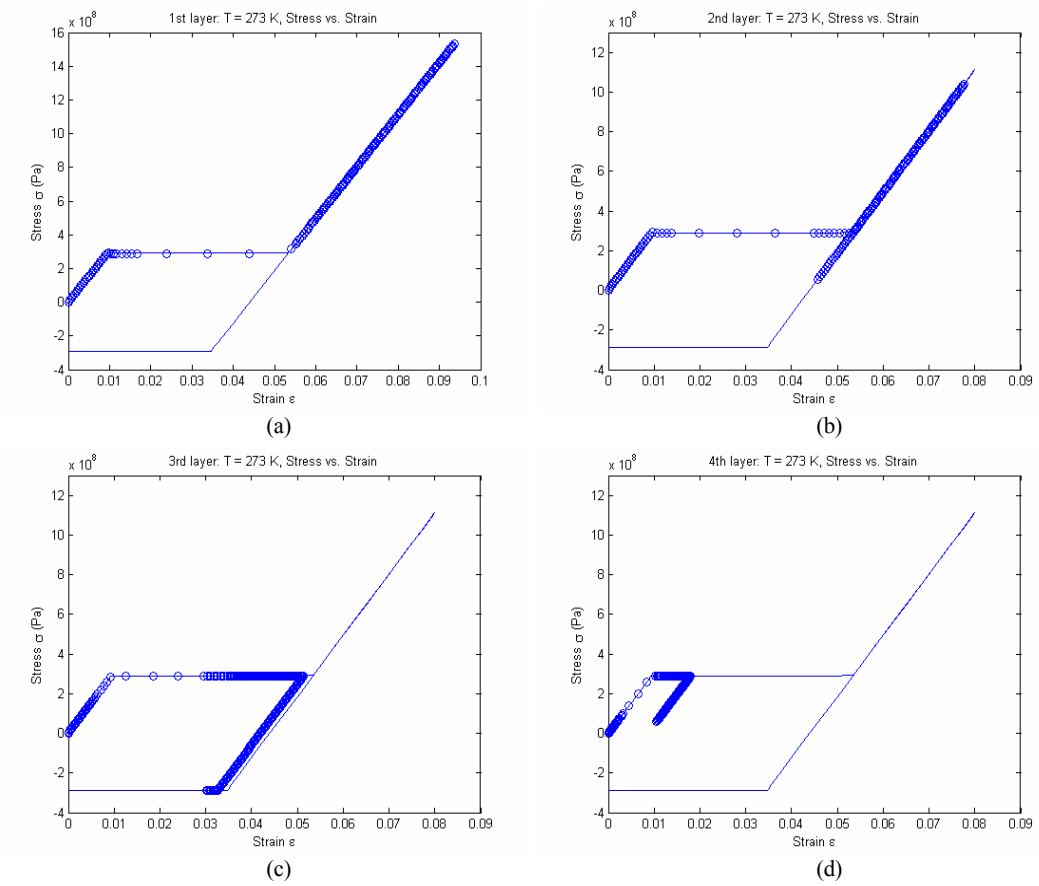


Figure 3.57: Quasiplastic behavior of SMA beam bending at low temperature $T = 273K$: (a) stress-strain response of the $1st$ layer; (b) stress-strain response of the $2nd$ layer; (c) stress-strain response of the $3rd$ layer; (d) stress-strain response of the $4th$ layer.

layers at the clamped end. Using the anti-symmetry of the beam bending behavior, only the data of the section below the beam neutral axis are presented. The layer numbers are labeled in sequence as shown in 3.48 (right). Similar to the above quasiplastic beam bending behavior at low temperature, during the loading process, the outer layer 1 seeing the maximum stress starts to transform first, followed by the subsequent layers. Due to the constraint of plane assumption of the Euler-Bernoulli Beam theory, the strain varies linearly across the section and the layer 1 cannot complete its phase transformation until the layer 4 reaches the transformation stress σ_A. During the unloading process, each layer follows a elastic path and the layer 3 drops to the transformation stress σ_M first, followed by the layers $4, 2$ and 1 in sequence, and the amount the stress decreases in each layer is given by $E_i(-y_i\Delta\theta_x)$ with E_i is the Young's modulus of the $i-th$ layer and $\Delta\theta_x$ is the curvature of the neutral axis. So during the unloading process, an inner layer could see a higher stress value than an outer layer. After finishing phase transformation, each layer re-gain its stiffness and is able to sustain the change of the applied loading. These are clearly illustrated in the time history of stress at the clamped end in Figure 3.62(c). There are two stress plateaus which corresponds to the critical transformation stresses σ_A and σ_M, respectively.

Figure 3.63 shows the stress strain hysteresis loops of different layers at the clamped end. Each layer is governed by the same stress strain hysteresis loop at $T = 333K$. During loading process, a layer starts to transform from A to M_+ when the stress of the layer reaches the critical transformation stress σ_A and during the unloading process, all the layers follow elastic deformation paths. A layer starts to transform from M_+ to A when the stress of the layer drops to the critical transformation stress σ_M as illustrated in Figure 3.63(a).

As noticed that in contour plots shown in Figure 3.60, there is a sharp transformation front in the strain and phase fraction contour plots. To study the effects of integration point number and element number on the transformation front, the contour plots of stress, strain, phase fractions at $t = 0.75s$ with $F = 1950N$ are presented in Figures 3.64-3.67 for four combinations of two integration point numbers 8 and 16, and two element numbers 250 and 500. Figure 3.64 shows the stress contour plots. The two cases with 16 integration points have smooth stress contour plots for both 250 and 500 elements at the region that corresponds to the transformation front. Figure 3.65(a) and (b) show the strain contour plots

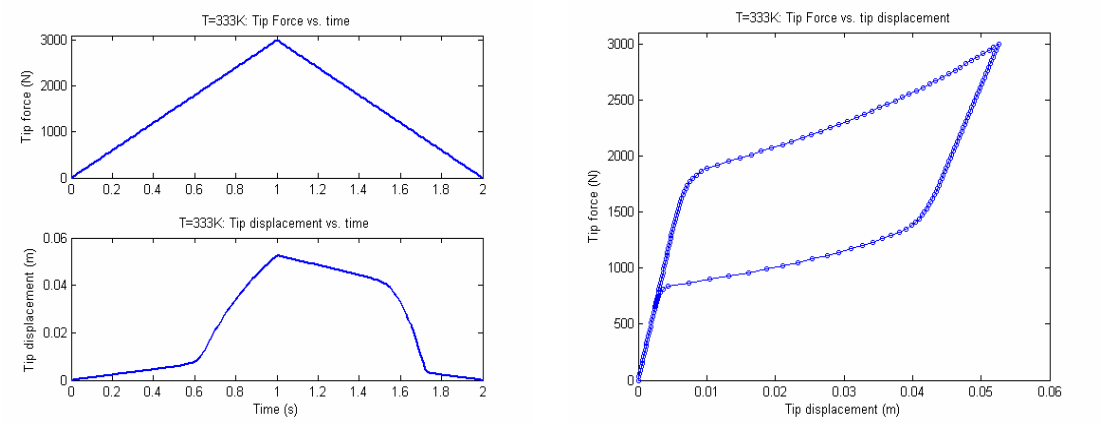


Figure 3.58: Superelastic behavior of SMA beam bending at high temperature $T = 333K$: (a) Applied tip force and tip displacement response vs. time; (b) Tip force vs. tip displacment.

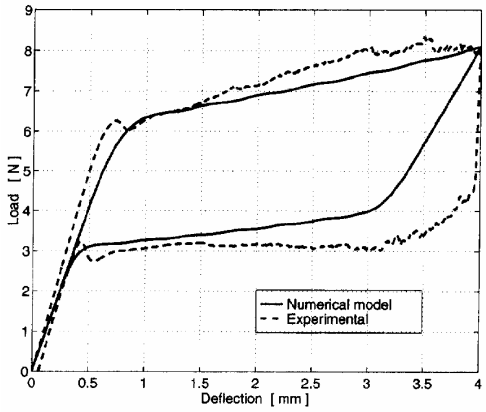


Figure 3.59: Superelastic behavior of three point bending test: applied force vs. midspan deflection (Auricchio and Sacco [55]).

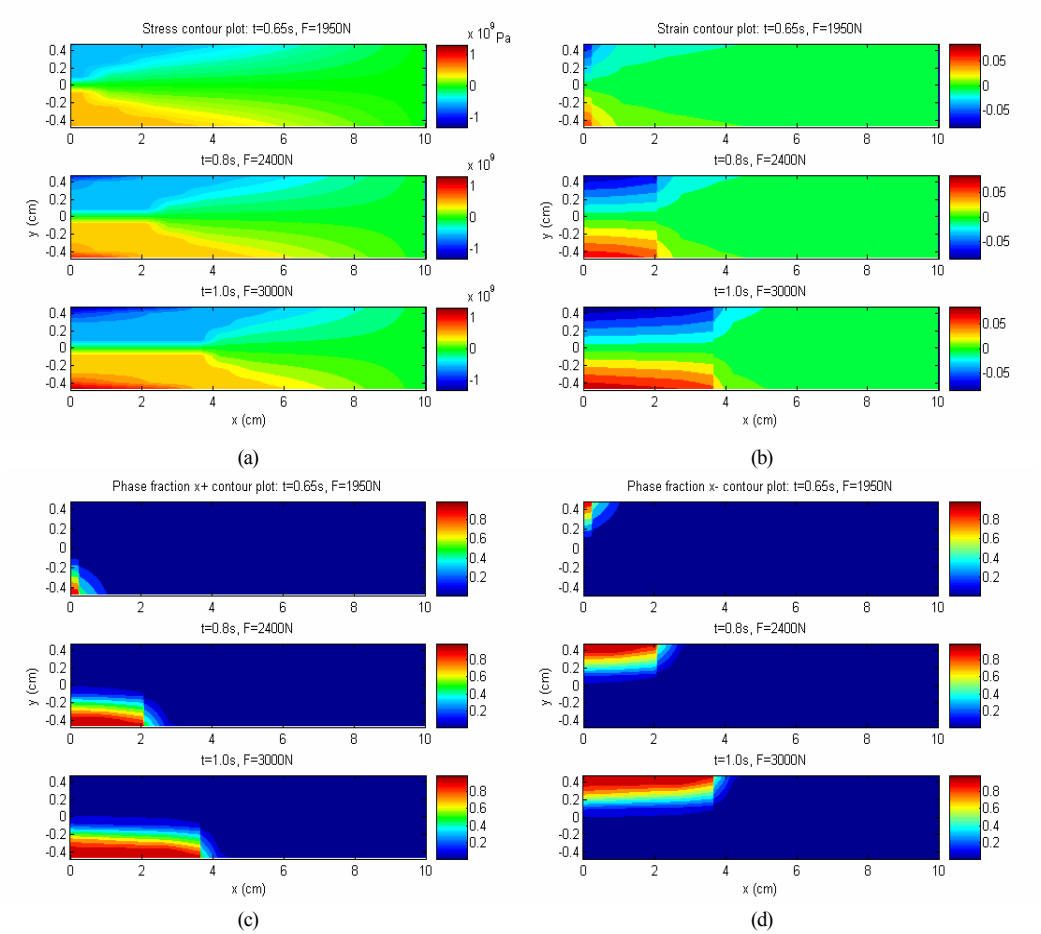


Figure 3.60: Contour plots of SMA beam bending at high temperature $T = 333K$ during the loading process: (a) stress contour plots; (b) strain contour plots; (c) phase fraction x_+ contour plots; (d) phase fraction x_- contour plots at $F = 1950N$, $2400N$, $3000N$, respectively.

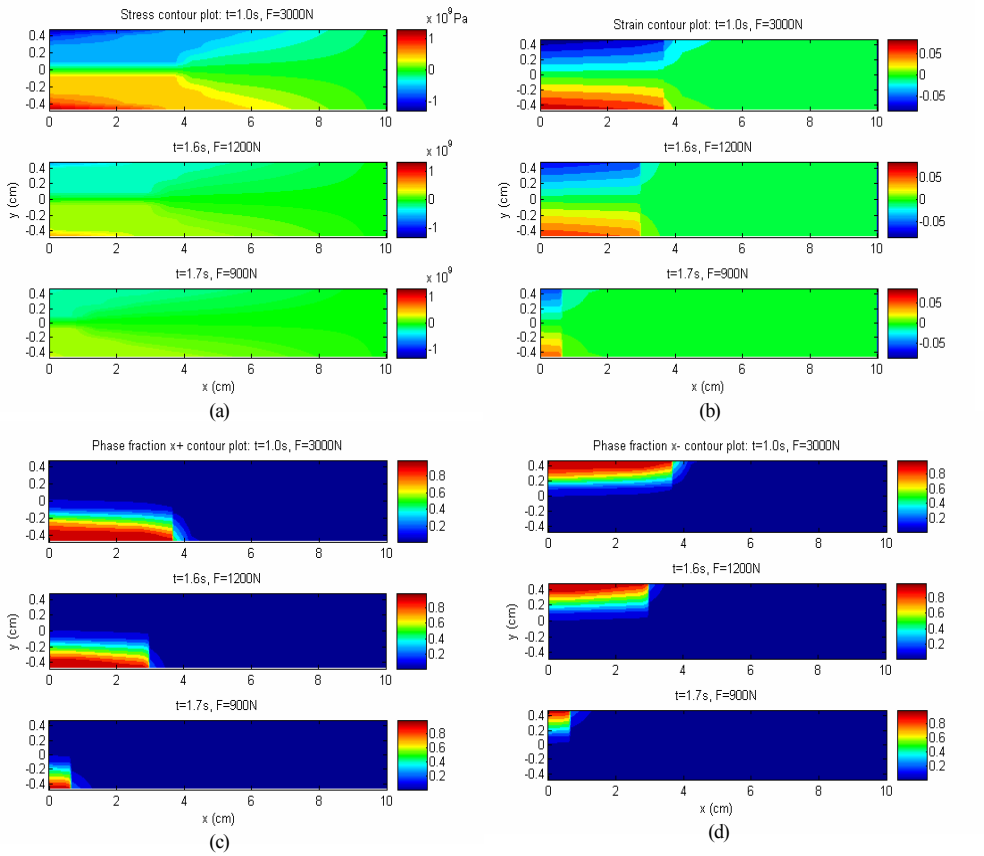


Figure 3.61: Contour plots of SMA beam bending at high temperature $T = 333K$ during the unloading process: (a) stress contour plots; (b) strain contour plots; (c) phase fraction x_+ contour plots; (d) phase fraction x_- contour plots at $F = 3000N$, $1200N$, $900N$, respectively.

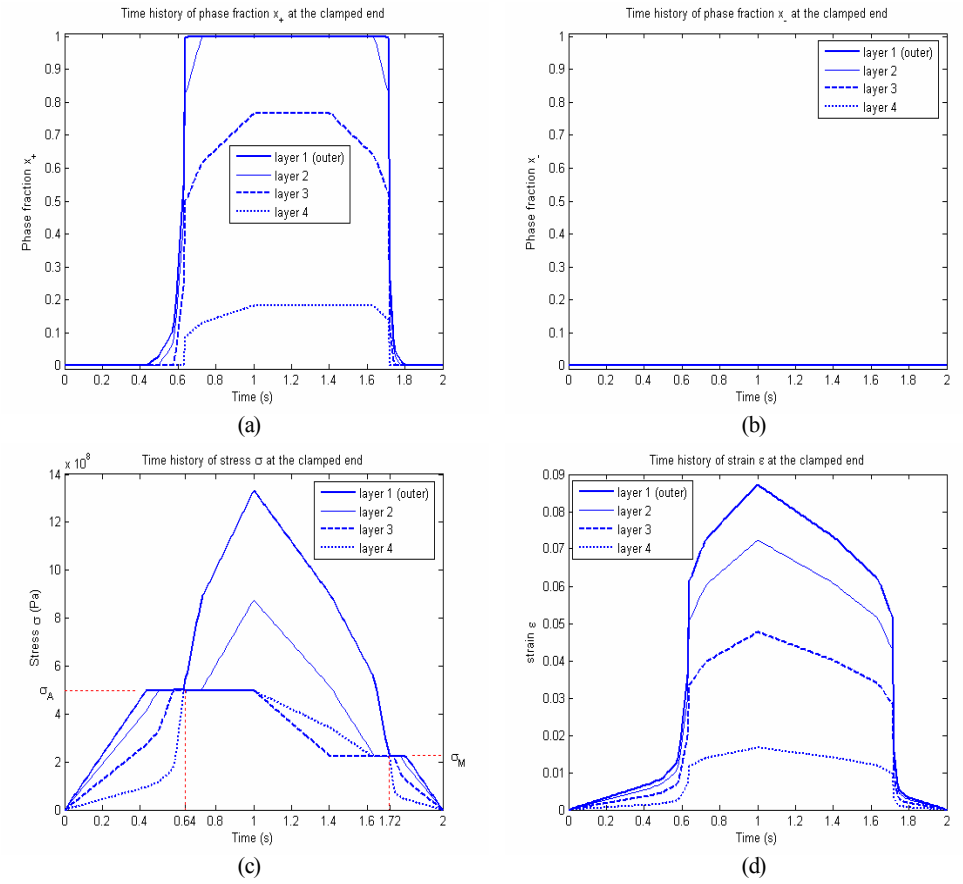


Figure 3.62: SMA beam bending at high temperature $T = 333K$: (a) evolution of phase fraction x_+ for different layers at the clamped end; (b) evolution of phase fraction x_- for different layers at the clamped end; (c) time history of stress for different layers at the clamped end; (d) time history of strain for different layers at the clamped end.

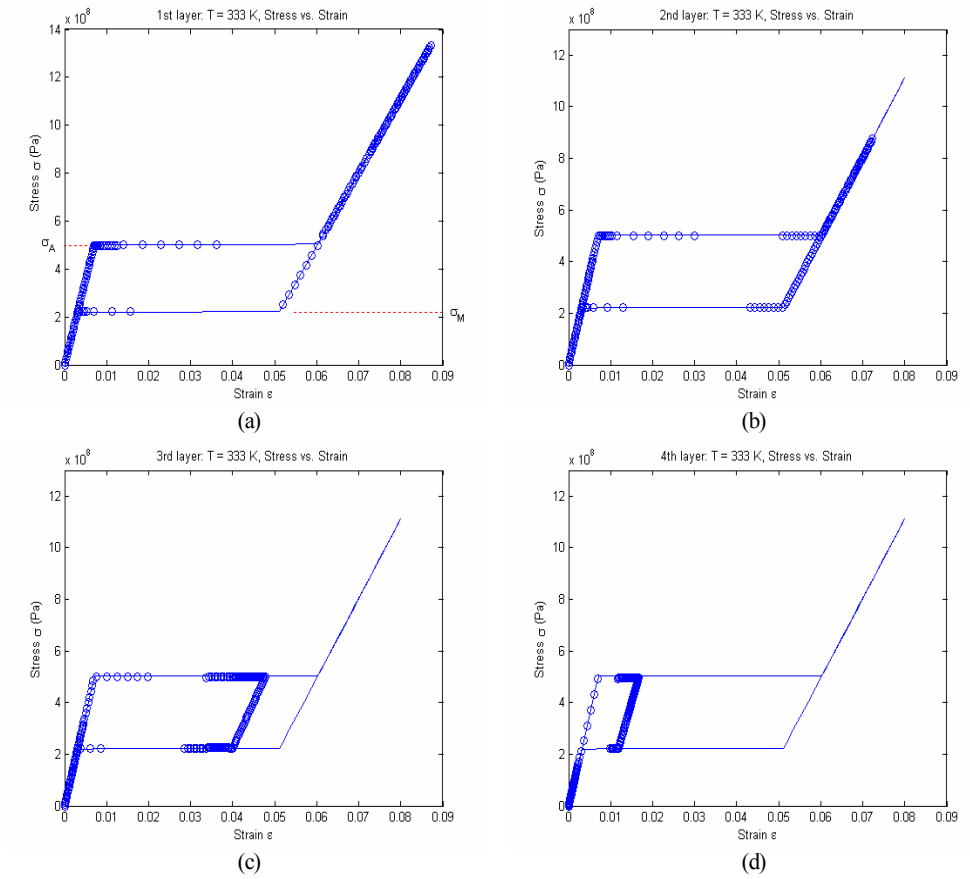


Figure 3.63: Superelastic behavior of SMA beam bending at high temperature $T = 333K$: (a) stress-strain response of the $1st$ layer; (b) stress-strain response of the $2nd$ layer; (c) stress-strain response of the $3rd$ layer; (d) stress-strain response of the $4th$ layer.

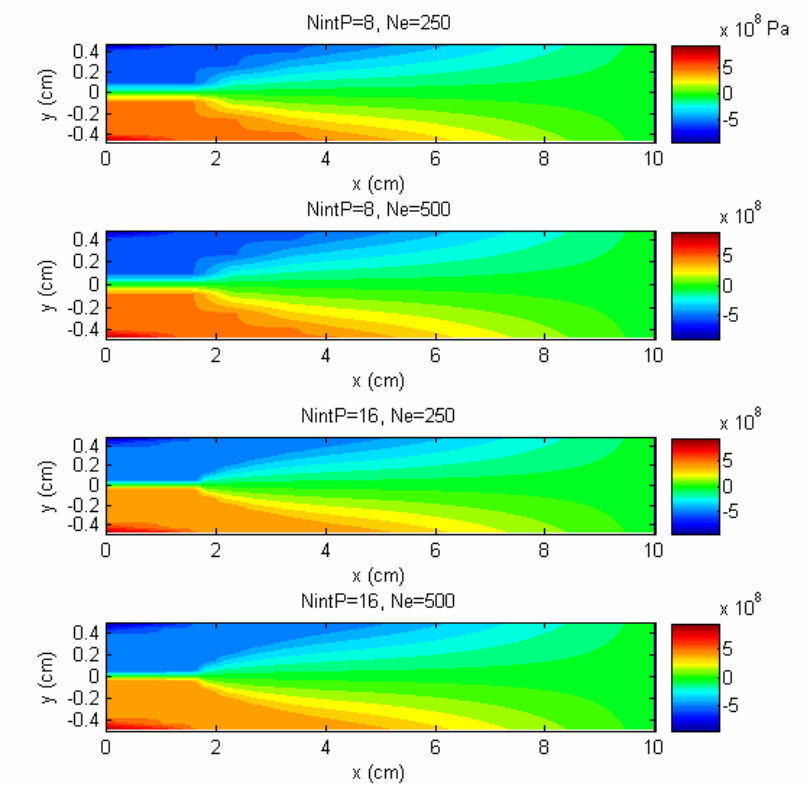


Figure 3.64: Stress contour plots of SMA beam bending at high temperature $T = 333K$ during the loading process at $F = 1950N$ for two different numbers of integration points ($NintP = 8, 16$) and two different numbers of elements ($Ne = 250, 500$).

and their corresponding zoom-in plots, respectively. Figure 3.66 and 3.67 show the contour plots of the phase fraction x_+ and x_-, respectively. We can see that the two cases with 16 integration point give essentially the same results with smooth transformation fronts for both 250 elements and 500 elements. For the cases with 8 integration point , the one with 500 elements has smooth zoom-in plots, but both still present sharp transformation fronts, and from the zoom-in plots, we can see that they do not have the exact location of the transformation fronts. In order to capture the inhomogeneous phase transformation behavior of SMA beam bending accurately, sufficient integration points through the thickness has to be used together with sufficient elements.

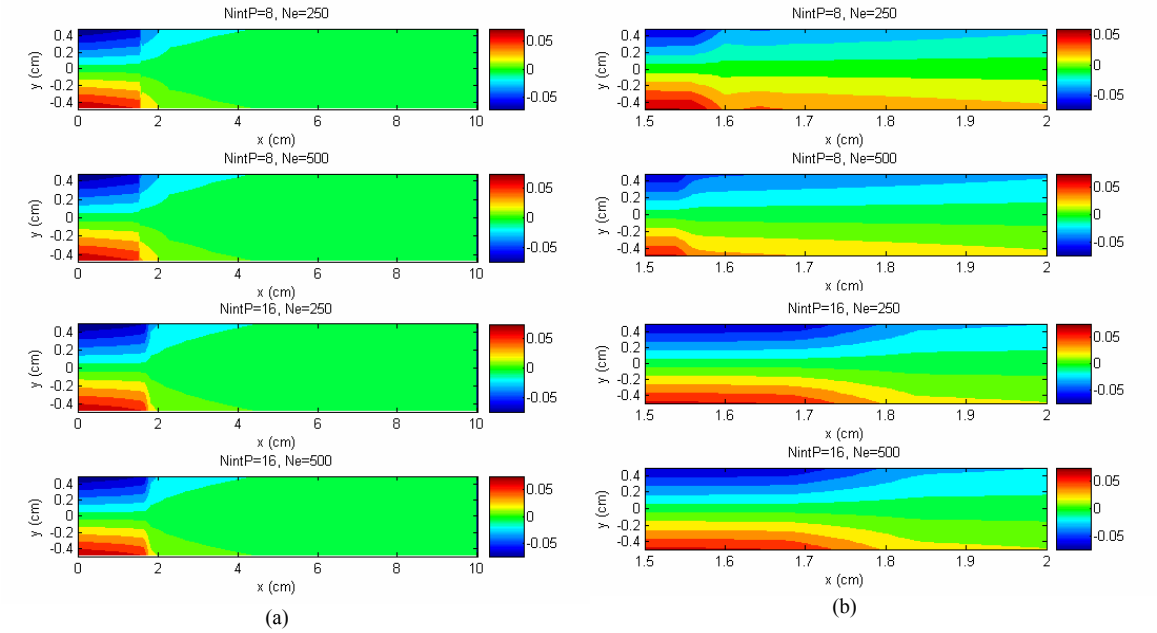


Figure 3.65: Strain contour plots of SMA beam bending at high temperature $T = 333K$ during the loading process at $F = 1950N$ for two different number of integration points ($NintP = 8, 16$) and two different number of elements ($Ne = 250, 500$): (a) complete plots; (b) zoom-in plots.

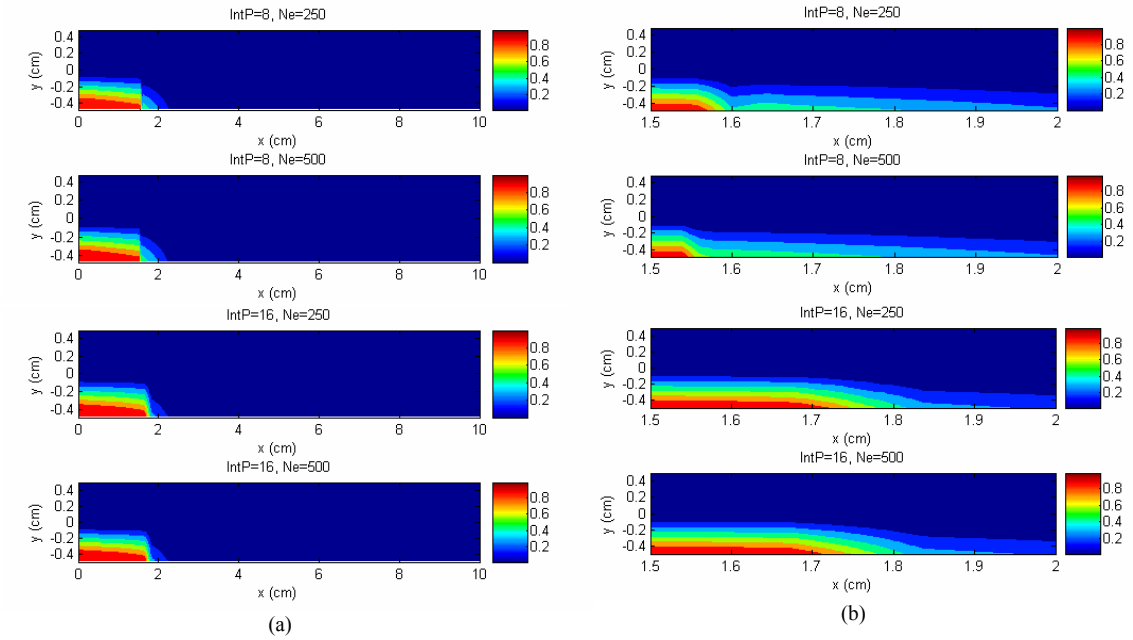


Figure 3.66: Phase fraction x_+ contour plots of SMA beam bending at high temperature $T = 333K$ during the loading process at $F = 1950N$ for two different numbers of integration points ($NintP = 8, 16$) and two different numbers of elements ($Ne = 250, 500$): (a) complete plots; (b) zoom-in plots.

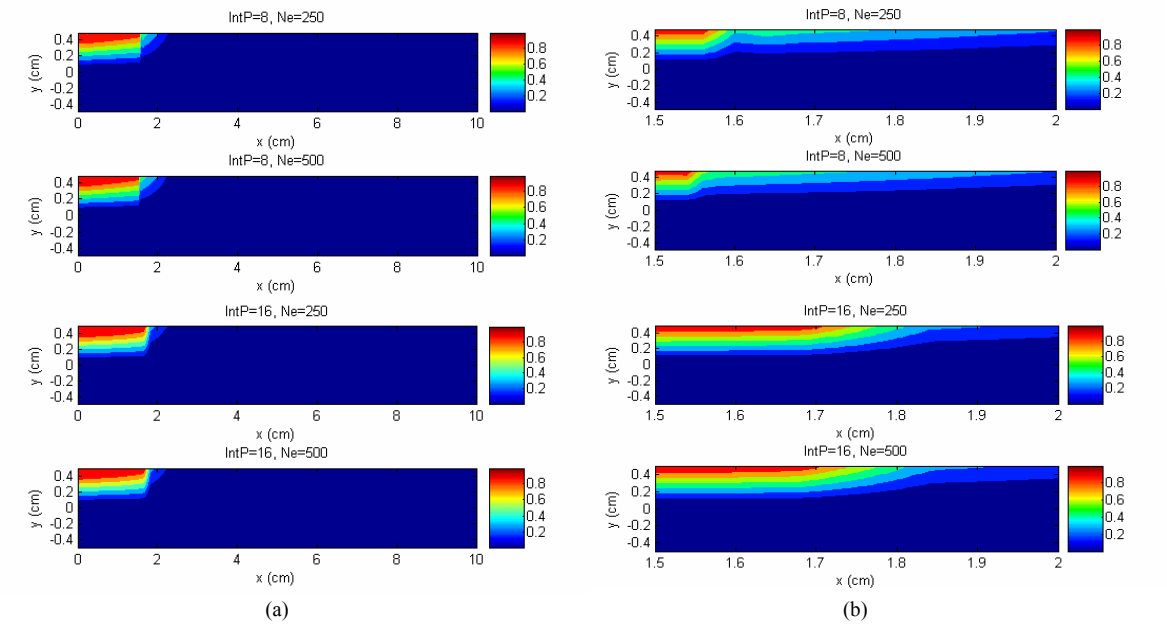


Figure 3.67: Phase fraction x_- contour plots of SMA beam bending at high temperature $T = 333K$ during the loading process at $F = 1950N$ for two different numbers of integration points ($NintP = 8, 16$) and two different numbers of elements ($Ne = 250, 500$): (a) complete plots; (b)

3.3.3 Thermo-mechanical Loading

Considering an SMA cantilever beam as shown in Figure 3.48 under thermo-mechanical loading as given in 3.68(a). The simulation starts at high temperature $T = 400K$ with $x_+(t = 0) = x_-(0) = 0$. Under the constant mechanical loading with $F = 1000N$, the SMA beam is cooled down to $250K$ and then heated up to $T = 400K$.

As presented in the previous subsection, under constant low temperature, $F = 1000N$ can only generate relatively small elastic deflection of the SMA beam as shown in Figure 3.49(b). In the present case, under constant force $F = 1000N$ and upon a cooling and heating cycle, the SMA beam generates a large stroke as illustrated in the displacement-temperature diagram shown in Figure 3.68(b).The mechanism behind this is similar to the SMA bar case illustrated in Figure 3.11-3.12. Under the constant tip force $F = 1000N$ as shown in 3.48, the section above the beam neutral axis is subjected to compression stresses and the section below the neutral axis is subjected to tensile stresses. For the perfect single crystal SMA free energy model, under constant compression (or tensile) stress, the landscape of the Gibbs free energy (3.5) is tilted to favor martensite M_- (or M_+) and thus the energy barrier between austenite A and martensite M_- (or M_+) is always lower than the one between austenite A and martensite M_+ (or M_-). Upon cooling and heating, the section above the neutral axis subjected to compression stresses transforms between austenite A and martensite M_- and the section below the neutral axis subjected to tensile stress transforms between austenite A and martensite M_+, and these together consequently generate a large deformation as shown in Figure 3.58(b).

Figures 3.69 and 3.70 present the contour plots of the stress, strain and phase fractions during the cooling and heating processes, respectively. As illustrated in the phase fraction contour plots in Figures 3.69(c) and 3.69(d) at low temperature $T = 250K$, most part of the outer layers below the neutral axis subjected to tensile stresses has fully A to M_+ transformation and most part of the outer layers above the neutral axis subjected to compression stresses has fully A to M_- transformation. The central portion of the SMA beam transforms from austenite A to both martensite M_+ and M_-. The stress contour plot at $T = 250K$ in 3.69(a) shows that the central portion of the SMA beam has zero stress state and the external applied load is sustained by the outer portion of the SMA beam, which re-gains its stiffness after fully transforming from A to M.

Figure 3.71 shows the distributions of phase fractions x_+ and x_-, stress and strain of different layers at the moment of $t = 2s$, $T = 250K$. Again only the data of the section below neutral axis are presented and the layer label sequence is given in Figure 3.48(right). At $t = 2s$ with cooling to low temperature $T = 250K$, the phase transformation of the SMA beam is already completed as indicated by the steady displacement response shown in Figure 3.68(a). From the phase fraction distributions in Figure 3.71(a) and (b), we can see that the layer 1 transforms completely from austenite A to martensite M_+ with $x_+ = 1$ and has tensile stress distribution along the length of the beam. Most part of the layer 2 transforms from austenite A to martensite M_+ except a small portion near the free end of the beam, which corresponds to zero stress distribution as shown in Figure 3.71(c). The layers 3 and 4 transforms into both martensite M_+ and M_- and have zero stress distributions as illustrated in Figure 3.71(c). Under zero stress, the SMA material has equal probability to transform from austenite A into martensite M_+ and M_-.

Figure 3.72 shows the evolution of the phase fractions x_+ and x_- of different layers at the clamped end. And Figure 3.73 shows the stress and strain responses of different layers at the clamped end. The layer 1 transforms first with stress decreasing in the layer 1 and increasing in other layers. With the temperature decreasing, the transformation stress $\sigma_A(T)$ is decreasing. Following the layer 1, the phase transformation starts next in the layer 2 and the stresses decrease in both the layers 1 and 2 and continue to increase in both the layers 3 and 4. The layer 3 is the next layer to reach the transformation stress and starts to transform. The stress values in the transforming layers are equal to the transformation stress $\sigma_A(T)$. As shown in zoom-in Figures 3.72(b) and 3.73(b), upon cooling, once the increasing stress in the inner layer 4 also reaches the the decreasing transformation stress $\sigma_A(T)$, the outer layer 1 is able to finish its phase transformation from austenite A to martensite M_+ at $t = 1.64s$ and re-gains its stiffness with elastic modulus E_M and its stress starts to increase with small change of elastic strain to compensate the stress decreasing in other layers with continuous cooling. When the cooling is continued, the layer 2 follows the layer 1 to finish its phase transformation and re-gains its stiffness. The stresses keep increasing in both the layers 1 and 2 and keep decreasing in both the layers 3 and 4 until the moment at $t = 1.84s$ the stress in the layers 3 and 4 reaches zero (see 3.72(b)) and the remaining un-transformed austenite particles have equal probability to jump into martensite M_+ and M_- as illustrated

in zoom-in Figures 3.73(b) and (d). Figure 3.74 shows the stress and strain distributions along the thickness of the cross-section from $t = 1.5s$ to $1.85s$ during the cooling precess. After phase transformations from austenite to martensite in all the layers are finished, the SMA beam reaches its largest deformation and only the outer layers sustain the applied load. This is clearly illustrated by the stress contour plots shown in Figure 3.69(a).

Similarly, the heating process is illustrated in Figure 3.75. During the heating process, the stress-strain hysteresis loop shifts up with temperature increasing. The inner layers 3 and 4 reach the transformation stress $\sigma_M(T)$ first and start to transform from martensite to austenite with stress increasing, followed by the layers 2 and 1 subsequently with stress decreasing. Once all the layers reach the same transformation stress $\sigma_M(T)$ (which increases with temperature increasing), the inner layer 4 is able to finish the transformation and jumps to the elastic deformation branch with Young's modulus E_A. With continuous heating, the stresses of different layers along the cross-section are re-distributed to satisfy the global constant cross-section moment produced by the constant tip force. The layers in the transition region will have the same stress increasing with temperature increasing, which is compensated by the stress decreasing in the layers already in the elastic deformation branch. The evolution of the heating process is also illustrated by the contour plots of the stress, stain, and phase fractions in Figure 3.70. Once the phase transformation from martensite to austenite is finished by heating up to a high temperature, the SMA beam recovers back to its original elastic deformation generated by the constant tip force.

Figure 3.76 shows the stress-strain responses of different layers at the clamped end fitted with the temperature dependent stress-strain hysteresis loops. The stress-strain hysteresis loop shifts down with the decreasing of temperature dictated by the temperature dependent transformation stresses given (3.11-.3.12). Upon cooling, when the transformation stress $\sigma_A(T)$ given in (3.11) shifts below the stress of the layer 1, the layer 1 starts to transform. And other layers with stresses smaller than $\sigma_A(T)$ are still in elastic deformation region and due to the constraint of the plane assumption of the Euler-Bernoulli beam theory with strain varying linearly through the cross-section, the layer 1 is restricted with a small change of strain which is not large enough to trigger the fully transformation from austenite A to martensite M_+ and stays in the unstable transition region that corresponds to a lower stress value. The stress decreasing in the transforming layer with the hysteresis loop shifting down

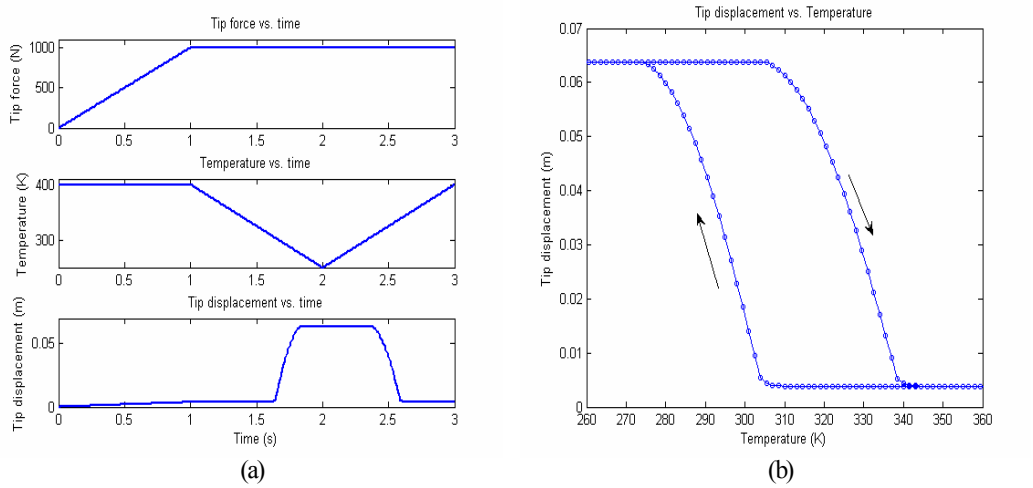


Figure 3.68: SMA beam bending under thermo-mechanical loading: (a) applied force, temperature and displacement response vs. time; (b) displacement vs. temperature.

during cooling is compensated by the stress increasing in the un-transformed layers to satisfy the global equilibrium equation with the constant cross-section moment under the constant tip force. The heating process is the reverse process of the cooling process.

3.3.4 Coupled Thermo-mechanical Analysis

In the prevoius subsection, we studied the inhomogenous bending problems of a SMA cantilever beam by neglecting the thermo-mechanical coupling without including the phase transformation induced latent heats. The behavior of SMA materials, however, is characterized by strong thermo-mechanical coupling due to the latent heats released and absorbed during austenite-martensite phase transformations.

For an SMA beam with small thickness, such as a thin-film SMA microactuator, the temperature through each cross-section is assumed to be uniform such that we can still use the 1-D heat transfer equation (3.51) to approximate the 2-D heat transfer problem of the SMA beam bending. By treating the total effect of latent heats as a sum of the latent heats released or absorbed at each integration point through the thickness, we can write the 1-D heat transfer equation (3.51) as

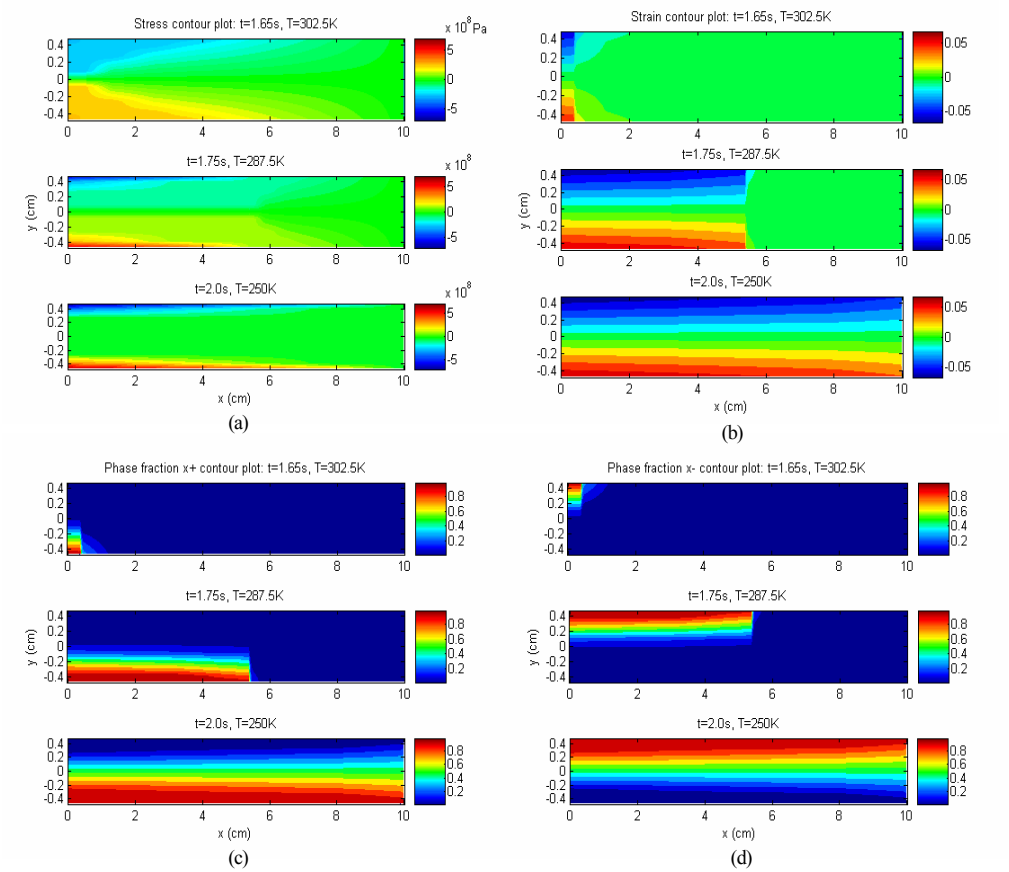


Figure 3.69: Contour plots of SMA beam bending under thermo-mechanical loading during the cooling process: (a) stress contour plots; (b) strain contour plots; (c) phase fraction x_+ contour plots; (d) phase fraction x_- contour plots at $T = 302.5K$, $287.5K$, $250K$, respectively.

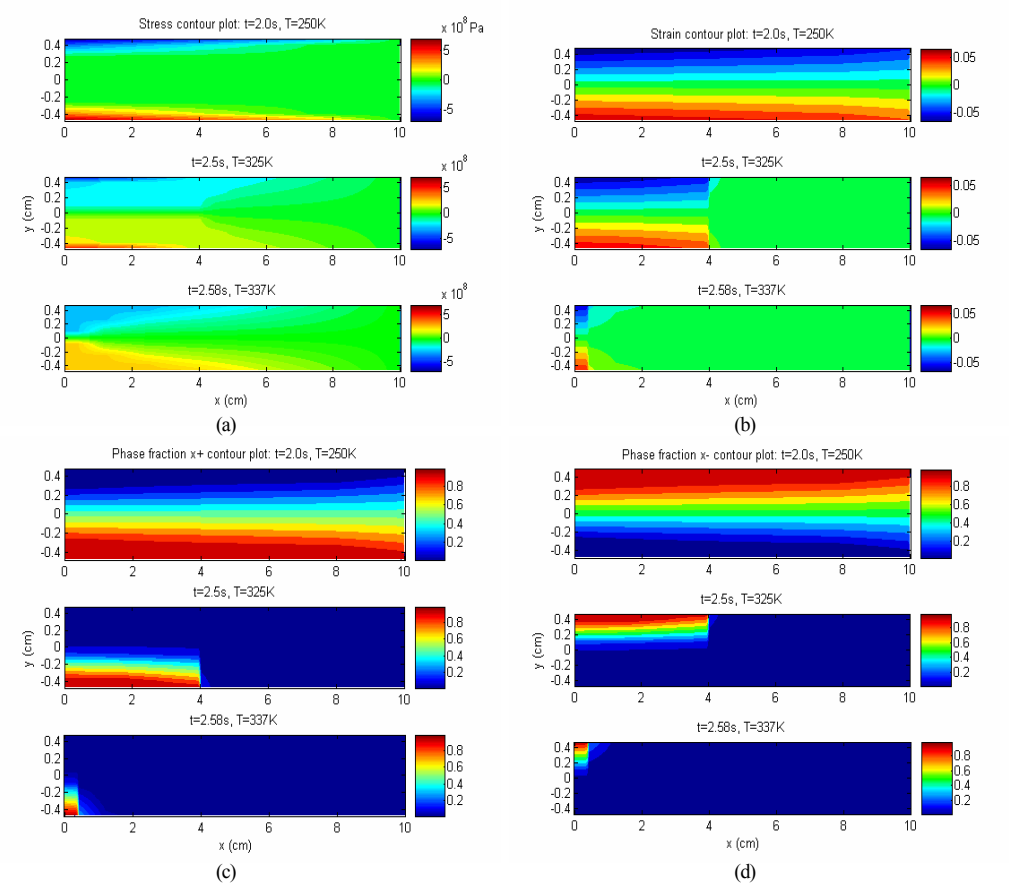


Figure 3.70: Contour plots of SMA beam bending under thermo-mechanical loading during the heating process: (a) stress contour plots; (b) strain contour plots; (c) phase fraction x_+ contour plots; (d) phase fraction x_- contour plots at $T = 250K,\ 325K,\ 337K$, respectively.

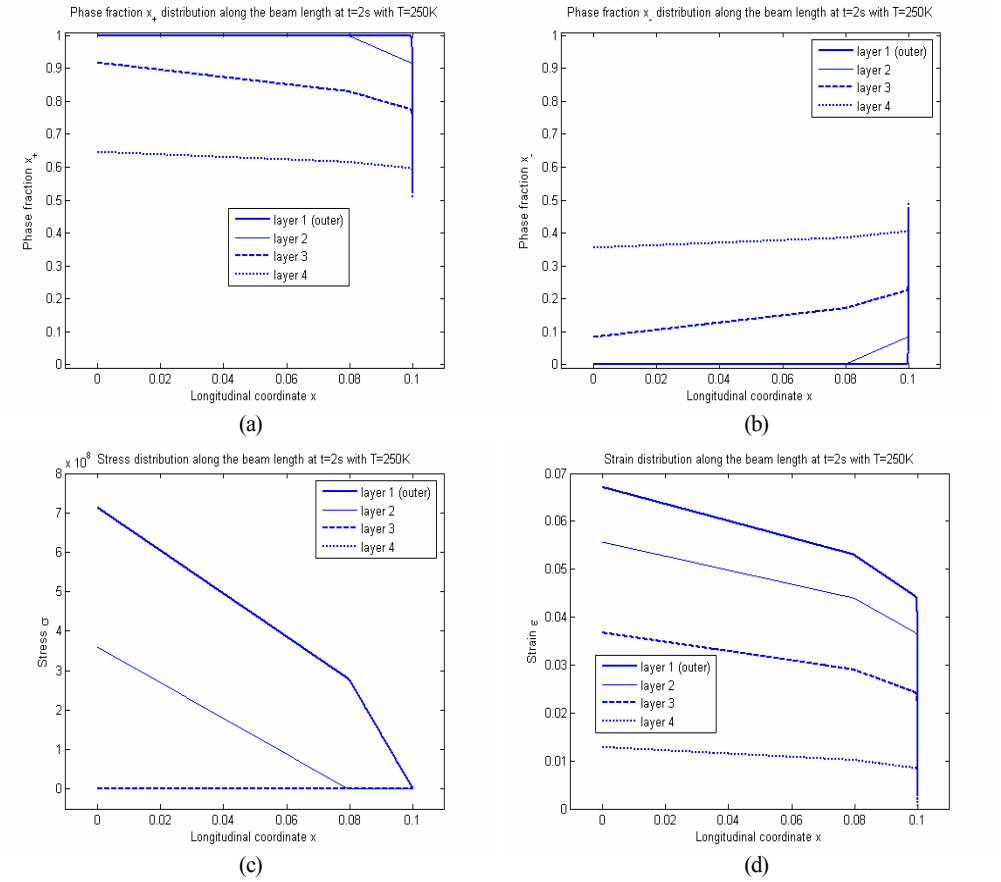


Figure 3.71: SMA beam bending under thermo-mechanical loading: phase fractions, stress and strain distribution of different layers along the length of the beam at $t = 2s$ with low tempature $T = 250K$: (a) x_+ vs. x; (b) x_- vs. x; (c) stress vs. x; (d) strain vs. x.

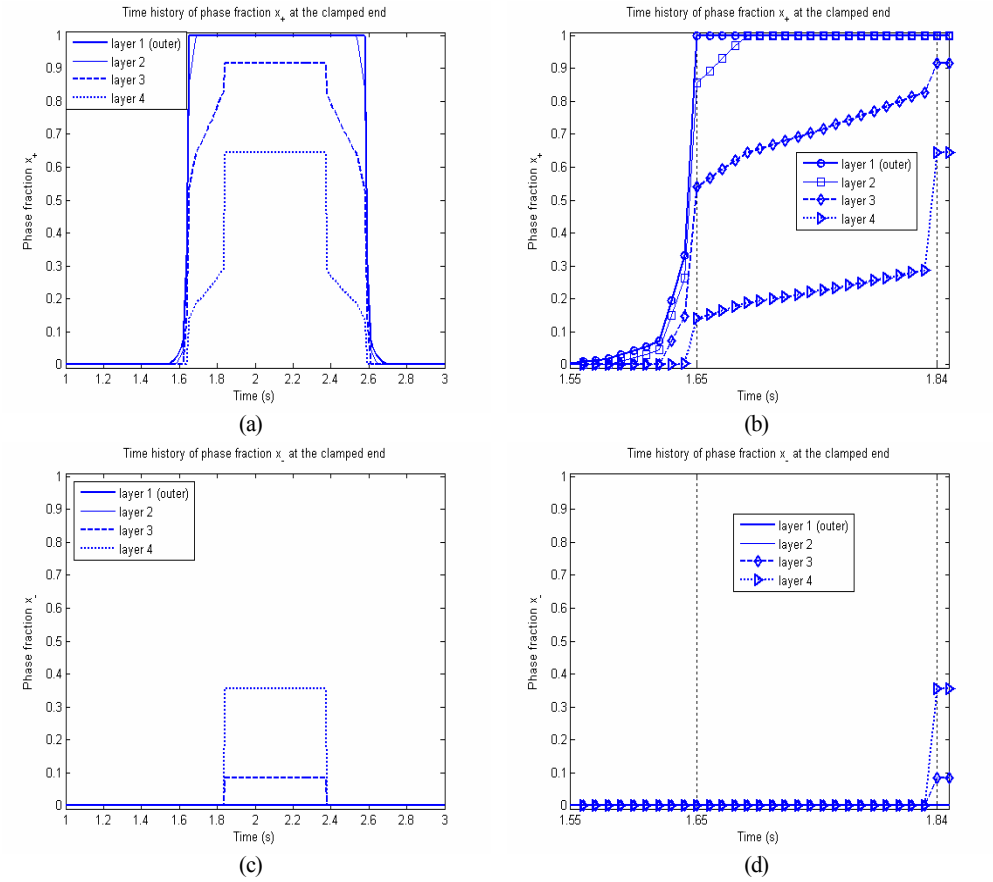


Figure 3.72: SMA beam bending under thermo-mechanical loading: evolution of phase fractions for different layers at the clamped end: (a) x_+ vs. time; (b) x_+ vs. time from $t = 1.55s$ to $1.85s$; (c) x_- vs. time; (d) x_- vs. time from $t = 1.55s$ to $1.85s$.

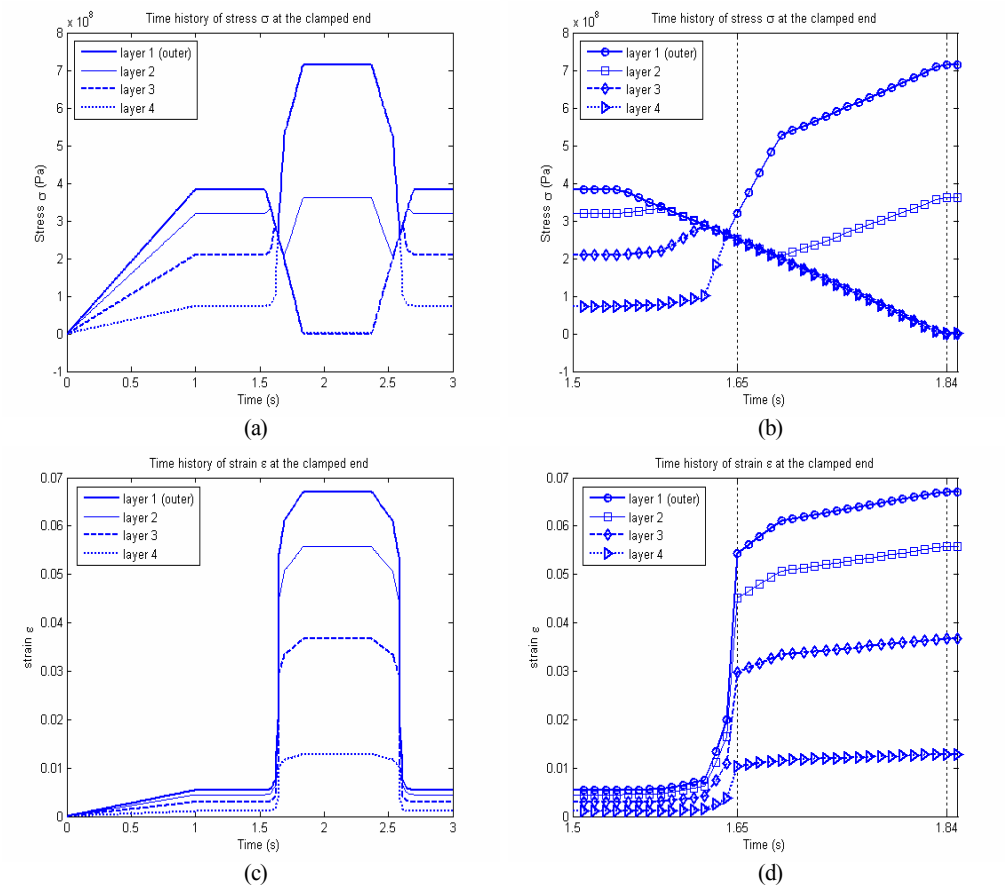


Figure 3.73: SMA beam bending under thermo-mechanical loading: time history of stress and strain responses of different layers at the clamped end: (a) stress vs. time; (b) stress vs. time from $t = 1.5$ to $1.85s$; (c) strain vs. time; (d) strain vs. time from $t = 1.5$ to $1.85s$.

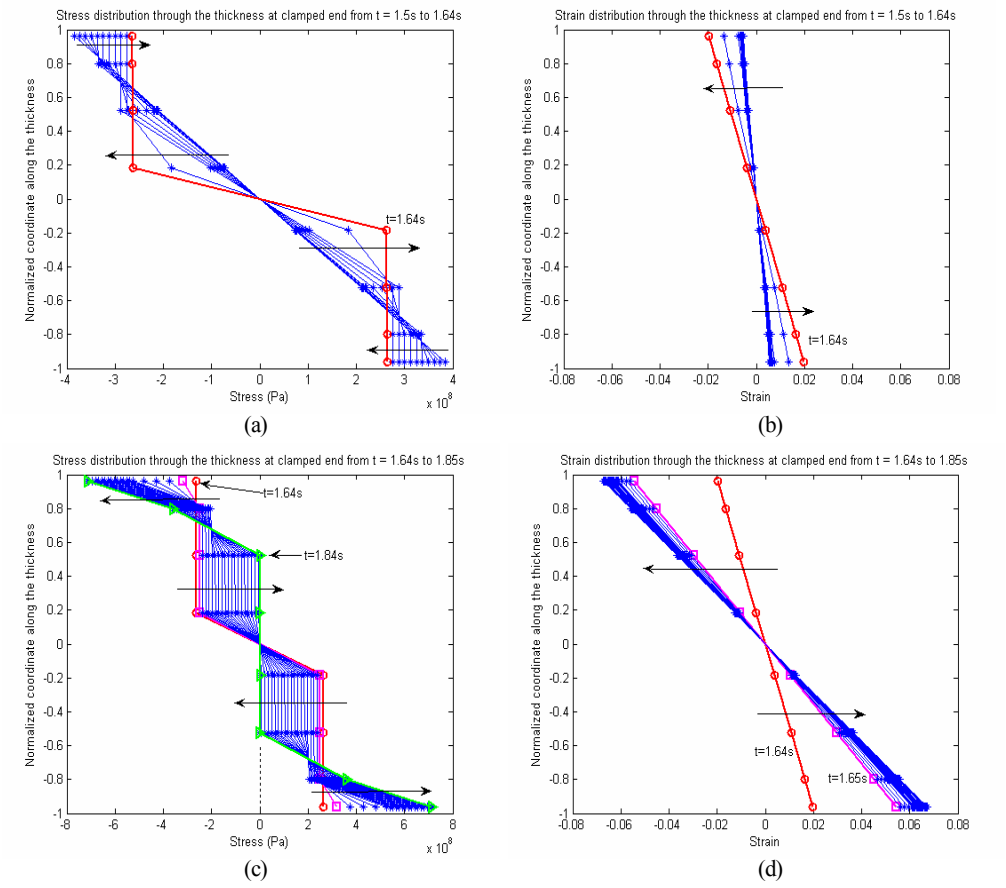


Figure 3.74: SMA beam bending under thermo-mechanical loading: stress and strain distribution of different layers through the thickness at the clamped end: (a) stress distribution from $t = 1.5s$ to $1.64s$; (b) strain distribution from $t = 1.5s$ to $1.64s$; (c) stress distribution from $t = 1.64s$ to $1.85s$; (d) strain distribution from $t = 1.64s$ to $1.85s$.

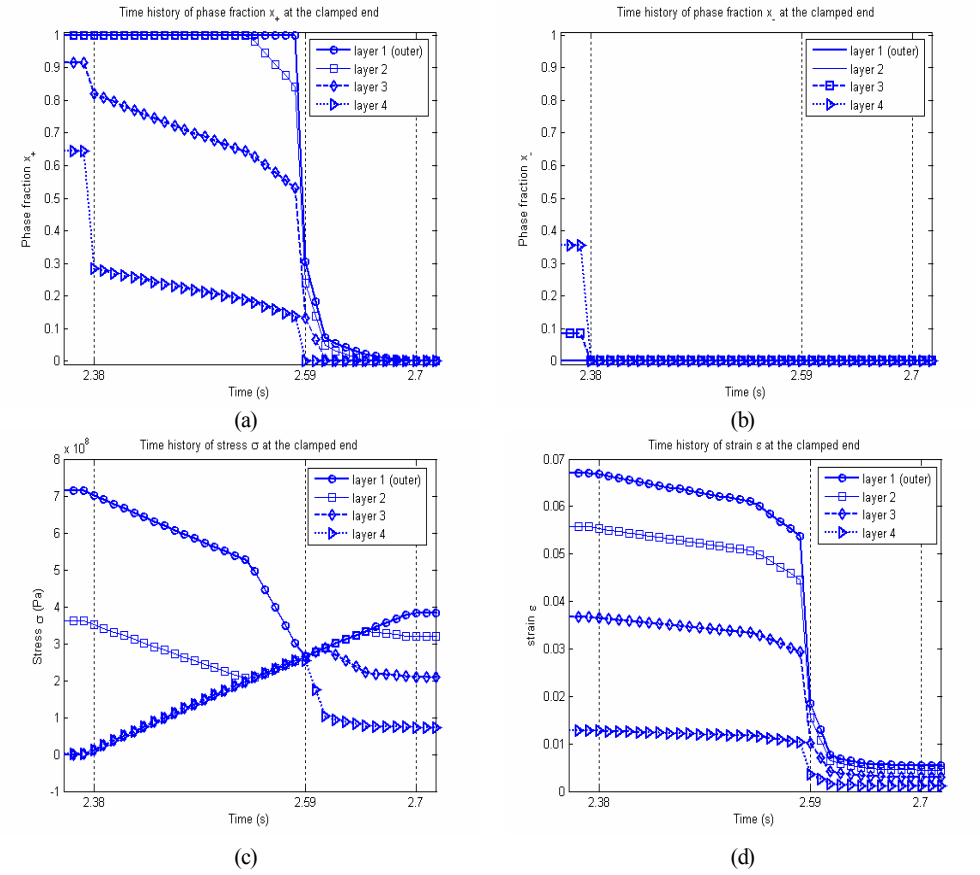


Figure 3.75: SMA beam bending under thermo-mechanical loading: time history of phase fraction, stress and strain responses of different layers at the clamped end during heating from $t = 2.35s$ to $2.72s$: (a) x_+ vs. time; (b) x_- vs. time (c) stress vs. time; (d) strain vs. time.

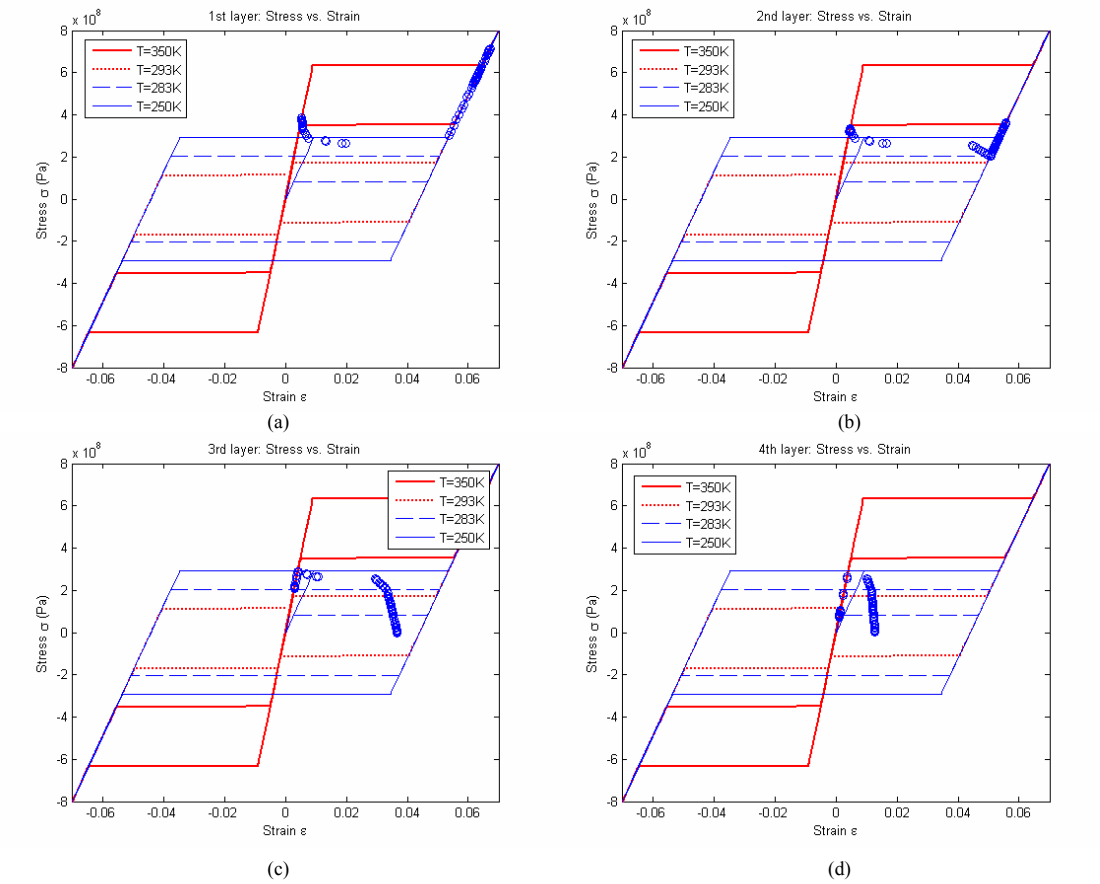


Figure 3.76: SMA beam bending under thermo-mechanical loading: stress-strain responses at the clamped end (starts from $t = 1s$): (a) the $1st$ layer; (b) the $2nd$ layer; (c) the $3rd$ layer; (d) the $4th$ layer.

$$\rho c\frac{\partial T}{\partial t} - \frac{\partial}{\partial x}(\lambda\frac{\partial T}{\partial x}) = -\alpha\frac{l_c(x)}{A(x)}(T - T_0) + j(x,t) - \sum_{i=1}^{n}\left[(h_{M_+} - h_A)^i\dot{x}_+^i + (h_{M_-} - h_A)^i\dot{x}_-^i\right] \tag{3.78}$$

where the term $\left[-(h_{M_+} - h_A)^i\dot{x}_+^i - (h_{M_-} - h_A)^i\dot{x}_-^i\right]$ is the latent heats released or absorbed at the $i-th$ layer during phase transformations. Using the shear force Q, moment M, deflection angle θ, deflection W, phase fractions x_+^i, x_-^i $(i = 1, \cdots, n)$ and temperature T as solution variables,

$$\mathbf{U} = \left[\begin{array}{cccccccccc} Q & M & \theta & W & x_+^1 & x_-^1 & \cdots & x_+^n & x_-^n & T \end{array}\right]^T \tag{3.79}$$

we can implement the quasistatic bending problem of the SAM cantilever beam with latent heats included into FEMLAB general form PDEs by using the same scheme presented in (3.60-3.63).

A small SMA cantilever beam (see Figure 3.77) under mechanical loading is used as an example to illustrate rate dependent latent heat effects on inhomogenous SMA beam bending problems. The parameters of the SMA beam are: length $L = 3mm$, width $b = 0.8mm$, height $h = 0.1mm$, density $\rho = 6500kg/m^3$, specific heat $c = 0.5 \times 10^3 J/kg \cdot K$, heat conductivity $\lambda = 18W/m \cdot K$ and the heat transfer coefficient α between the SMA beam surface and its surrounding environment is assumed to be $100W/m^2K$. The mechanical properties are the same as those used in the last subsection. The beam cross-section is divided into 8 layers (8 integration points). The following two cases of superelastic responses with different loading rates and different thermal boundary conditions are studied, respectively.

Case 1: two different loading rates of $\dot{F}(t) = 0.35N/s$ and $\dot{F}(t) = 0.035N/s$ under the same insulated boundary conditions with $\frac{\partial T(0,t)}{\partial x} = \frac{\partial T(L,t)}{\partial x} = 0$.

Case 2: two different thermal boundary conditions of $(\frac{\partial T(0,t)}{\partial x} = \frac{\partial T(L,t)}{\partial x} = 0)$ and $(T(0,t) = T_0, \frac{\partial T(L,t)}{\partial x} = 0)$ under the same loading rate at $\dot{F}(t) = 0.35N/s$.

Both cases start with the same initial ambient temperature $T_0 = 333K$ and the SMA beam is in fully austenite state at this temperature with $x_\pm^i(x,0) = 0$. Figure 3.78 shows the time histories of the applied forces for two different loading rates at $0.35N/s$ and $0.035N/s$, respectively.

The results of the case 1 are shown in Figures 3.79-3.80. Figure 3.79 shows the tip force-tip displacement responses of the two different loading rates under the same insulated boundary conditions. We can see that the responses are strongly rate-dependent with different hysteresis reponses corresponds to different loading rates. The SMA beam has smaller stiffness, larger deformation and wider hysteresis loop for the slower loading rate. This is the result of the rate-dependent stress-strain responses of the SMA material. SMA material has steeper stress-strain response in the transition regions for the faster loading rate, which is demonstrated in Figure 3.34 of the tensile simulations of a SMA wire at different loading rates. Thus under the same level of applied forces, the SMA beam undergoes a larger extent of phase transformations for the slower loading rate as illustrated by the contour plots of the evolution of phase fraction x_+ for different layers in Figure 3.80. This results in larger deformation of the SMA beam for the slower loading rate. Due to the anti-symmetry of the beam bending, only the data of the half section subjected to tensile stresses are presented. The label sequence of the layers is illustrated in Figure 3.77(right). The half section below the neutral axis subjected to tensile stresses transforms from austenite to martensite M_+. Figure 3.81 shows the contour plots of the evolution of latent heats and temperatures along the length of the SMA beam for the two different loading rates. The latent heat is the only heat source in the heat transfer equation (3.78). During the loading process, the SMA beam transforms from austenite to martensite and releases heat. The phase transformations start at the clamped end, and due to the axial heat conduction, the heat flows from high temperature region to low temperature region. With the loading increasing, the heat propagates from the clamped to the free end. During the unloading process, the SMA beam transforms from martensite back to austenite and absorbs heat, which causes the temperature near the clamped end to drop below the ambient temperature. Due to the inhomogenous phase transformation along the SMA beam, the temperature distributions along the beam are nonuniform under insulated boundary conditions. The faster loading causes larger temperature change.

The results of the case 2 are shown in Figures 3.82-3.84. Figure 3.82 shows the tip force-tip displacement responses of the two different thermal boundary condition under the same loading rate at $0.35N/s$. The SMA beam with fixed temperature clamped end has larger deformation than the one with insulated clamped end. Both free ends have insulated

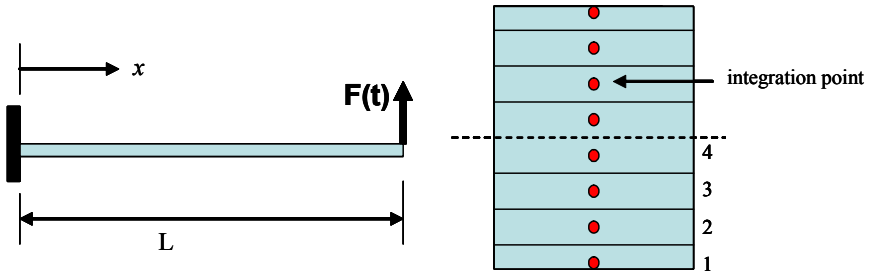


Figure 3.77: SMA cantilever beam

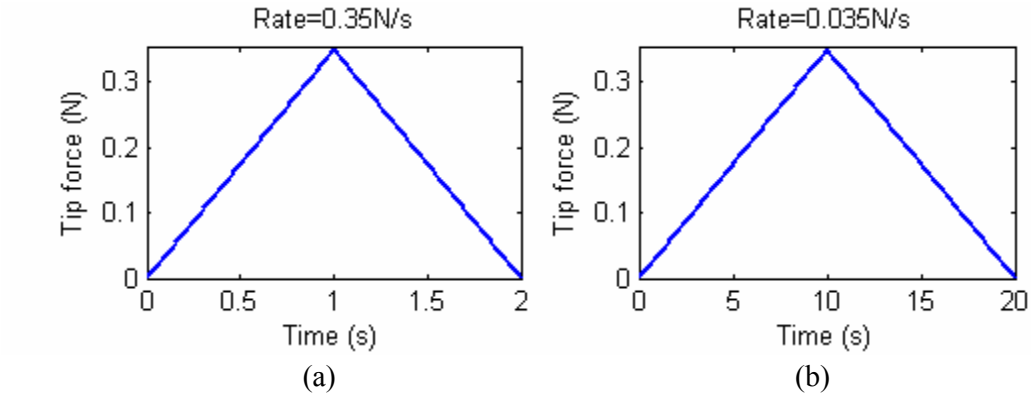


Figure 3.78: Applied tip forces vs. time: (a) $rate = 0.35N/s$; (b) $rate = 0.035N/s$.

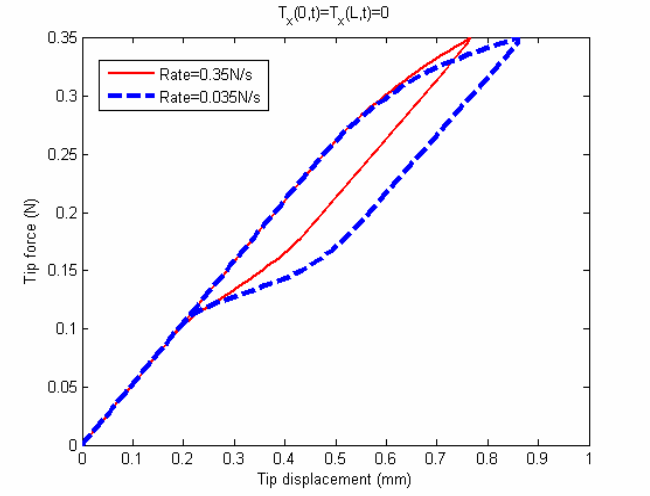


Figure 3.79: Tip force-tip displacement responses under the thermal boundary condition of $T_x(0,t) = T_x(L,t) = 0$.

boundary conditions. The clamped end with fixed ambient temperature always sees the same stress-strain relation with sharp transition regions. Governed by the temperature-dependent stress-strain relation, the clamped end with insulated boundary condition has a stress-strain relation with gradual transition regions due to the continuous change of temperature during the phase transformations. Thus under the same level of applied forces, the SMA beam undergoes a much larger extent of phase transformations at the fixed temperature clamped end as illustrated by the contour plots of the evolution of phase fraction x_+ for different layers in Figure 3.83. In this case, the clamped end with fixed temperature acts like a "hinge" and thus the SMA beam with fixed temperature clamped end generates much larger deformation than the one with insulated clamped end. From the contour plots of the evolution of latent heats and temperatures along the length of the SMA beam in Figure 3.81, we can see that the SMA beam with the temperature fixed at the clamped end undergoes relatively smaller change in temperature along the length due to the fixed temperature clamped end..

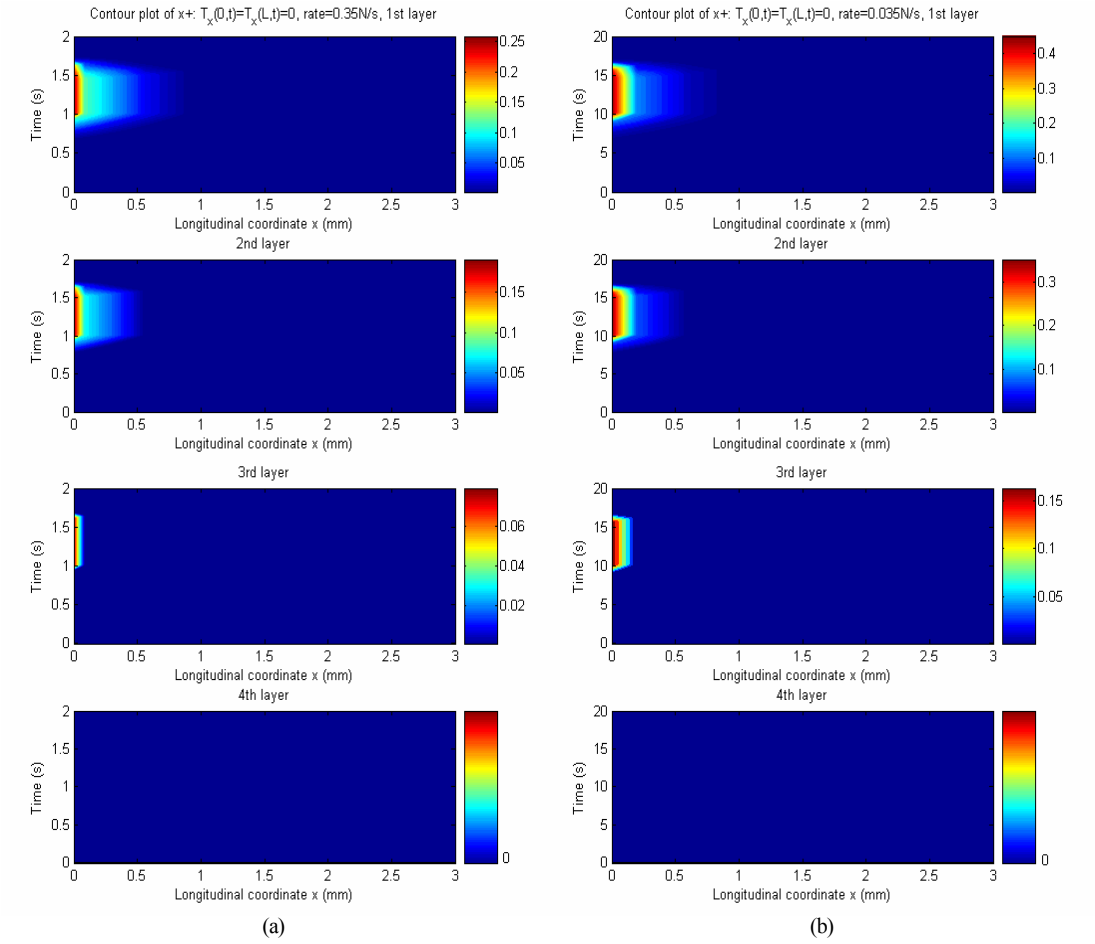


Figure 3.80: Evolution of phase fraction x_+ along the length of the SMA beam at different layers (in the half section subjected to tensile stresses) under the thermal boundary condition of $T_x(0,t) = T_x(L,t) = 0$: (a) $rate = 0.35N/s$; (b) $rate = 0.035N/s$.

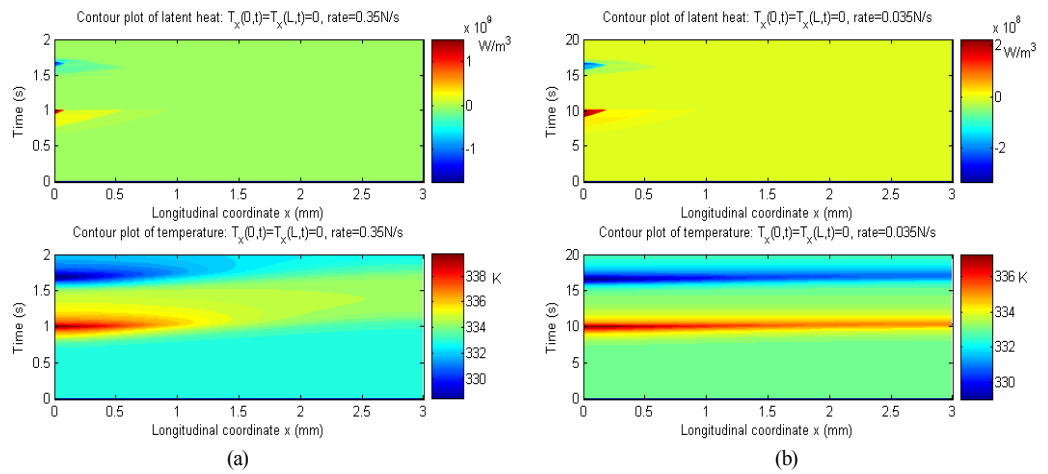


Figure 3.81: Evolution of latent heat and temperature along the length of the SMA beam under the thermal boundary condition of $T_x(0,t) = T_x(L,t) = 0$: (a) $rate = 0.35N/s$; (b) $rate = 0.035N/s$.

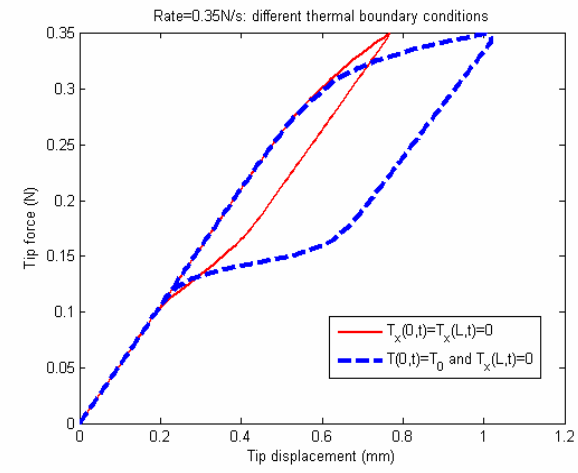


Figure 3.82: Tip force-tip displacement responses under the loading rate at $0.35N/s$ for two different thermal boundary conditions.

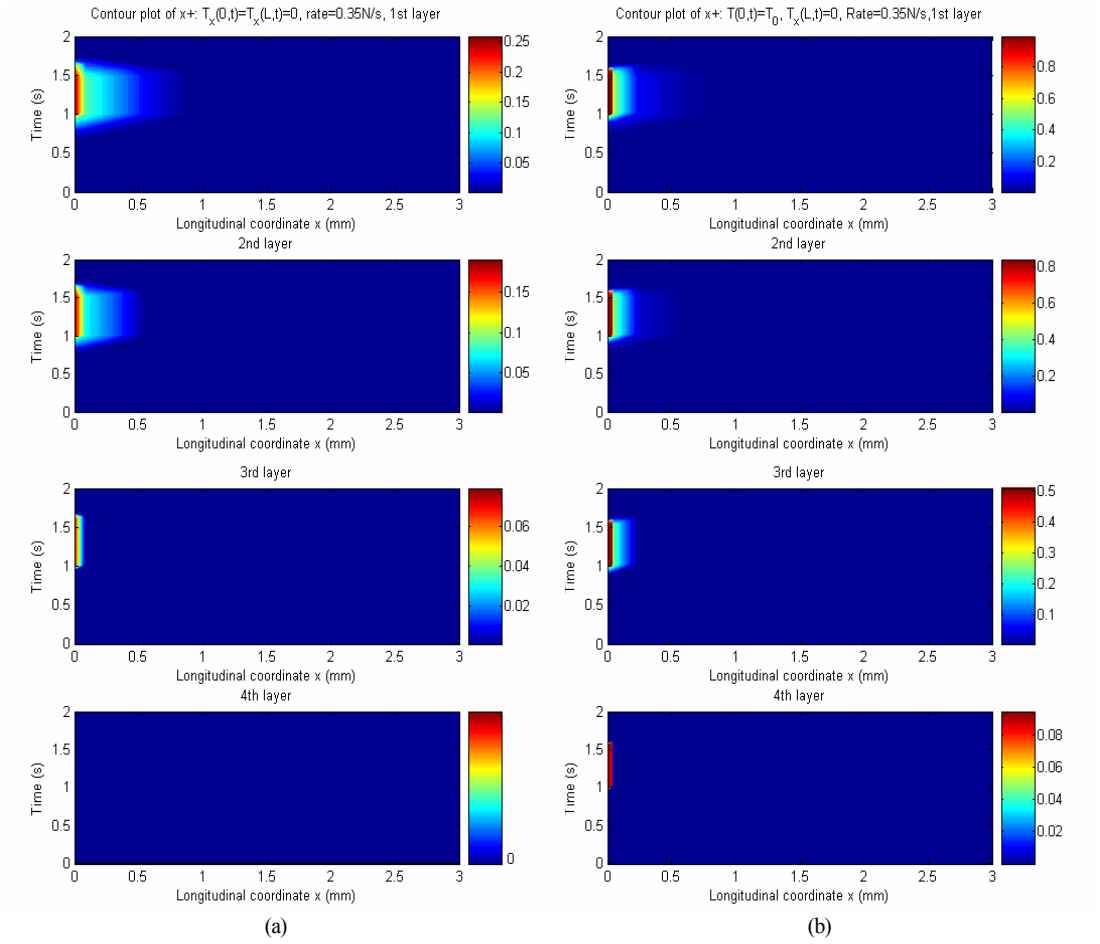


Figure 3.83: Evolution of phase fraction x_+ along the length of the SMA beam at different layers (in the half section subjected to tensile stresses) under the loading rate at $0.35N/s$: (a) $T_x(0,t) = T_x(L,t) = 0$; (b) $T(0,t) = T_0$ and $T_x(L,t) = 0$.

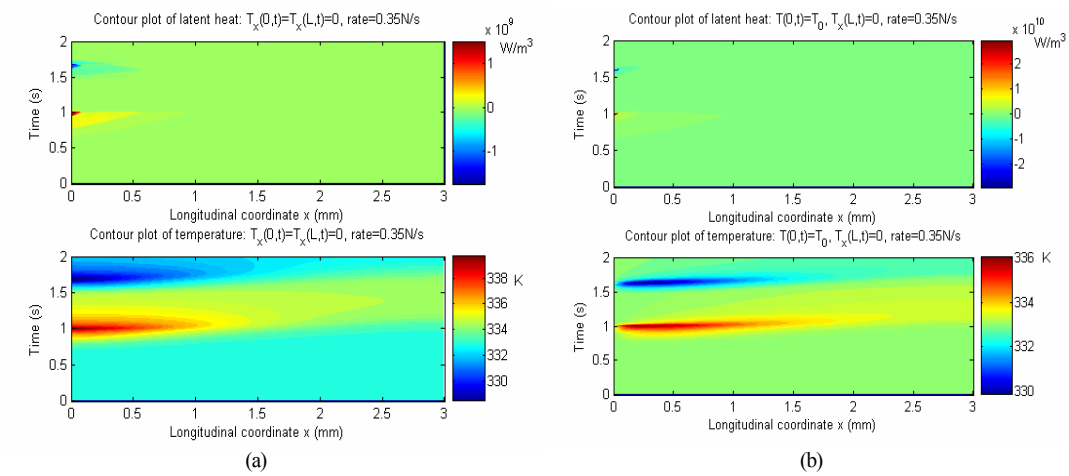


Figure 3.84: Evolution of latent heat and temperature along the length of the SMA beam under the loading rate at $0.35N/s$: (a) $T_x(0,t) = T_x(L,t) = 0$; (b) $T(0,t) = T_0$ and $T_x(L,t) = 0$.

3.4 Finite Element Analysis of SMA Beam Bending Using ANSYS

In the above FEMLAB implementation, the phase fractions x_+ and x_- are treated as solution variables as the displacement u and they are discretized together to form a global differential-algebraic equation (DAE) and solved as a direct coupling problem. In this section, 1-D free energy SMA model is implemented into finite element code ANSYS using its BEAM188 element and its user defined material Fortran subroutine USERMAT to study the beam bending problem of an SMA cantilever beam. Different from the FEMLAB implementation, in the ANSYS implementation, only the displacement u is discretized to form a global finite element algebraic equation, which is solved by the Newton-Raphson method. The subroutine USERMAT is used to define the stress-strain relation, the mechanical constitutive behavior of SMA materials. During each Newton-Raphson iteration, USERMAT is called at very integration point and the phase fractions are stored as state variables at each integration point and ANSYS passes in the values of the stresses, strains, current strain

increment and state variables at the beginning of the time increment. The USERMAT integrates the constitutive model of the SMA material to update the values of stresses, state variables and material Jacobian matrix $\left[\frac{d\sigma_{ij}}{d\varepsilon_{ij}}\right]$. The ANSYS implementation also serves as a validation tool for the FEMLAB implementation.

First, in this section, we derive the expression for the tangent modulus for the 1-D SMA model and present detail implementation of the SMA model into ANSYS BEAM188 element via its user defined material subroutine USERMAT. The implementation is validated by axial loading for an SMA cantilever beam. The results of bending at low and high temperatures are also compared with those of FEMLAB implementation. Finally, we study the convergence behavior of the SMA cantilever beam bending problem under different factors such as different convergence criteria, number of elements, number of integration points, etc.

3.4.1 Finite Element Implementation

The weak form of the balance of momentum reads [70]

$$\int \mathbf{B}^T \boldsymbol{\sigma}(\mathbf{a}) dv = \mathbf{P}^{ext}(\mathbf{a}) \tag{3.80}$$

where $\mathbf{B}$ is the divergence matrix, and $\boldsymbol{\sigma}$ and $\mathbf{P}^{ext}$ are stresses and external loads,respectively. Due to the nonlinearity of the shape memory behavior, Eq. (3.80) is highly nonlinear even for the small deformation. Also the hysteretic behavior makes it necessary to calculate the solution at time t_{n+1} through a series of incremental steps of magnitude Δt_{n+1}. A standard procedure in ANSYS to solve Eq. (3.80) for the displacement $\mathbf{a}_{n+1}$ is the Newton-Raphson method. It is linearized about a found approximation to the solution $\mathbf{a}_{n+1}^{(i)}$, and neglecting the dependence of the external loads on the displacement $\mathbf{a}$, it gives an iterative improvement $\delta\mathbf{a}_{n+1}^{(i)} = \mathbf{a}_{n+1}^{(i+1)} - \mathbf{a}_{n+1}^{(i)}$ by solving the set of linear algebraic equations

$$\mathbf{K}_{n+1}^{(i)\ T} \delta\mathbf{a}_{n+1}^{(i)} = \mathbf{P}_{n+1}^{ext} - \mathbf{I}_{n+1}^{(i)} \tag{3.81}$$

where

$$\mathbf{K}_{n+1}^{(i)} = \int \mathbf{B}^T \left(\frac{\partial \boldsymbol{\sigma}}{\partial \boldsymbol{\varepsilon}}\right)_{n+1}^{(i)} \mathbf{B} dv$$

is the so-called tangential stiffness matrix, and the right hand side of (3.81) is the difference between the internal forces due to the stresses in the elements $\mathbf{I}_{n+1}^{(i)} = \int \mathbf{B}^T \boldsymbol{\sigma}(\mathbf{a}_{n+1}^{(i)}) dv$ and the external loads $\mathbf{P}_{n+1}^{ext}$. An appropriate norm of this out-of-balance force or displacement increment has to be smaller than some tolerance for a convergence solution, which are corresponding to the force convergence and displacement convergence criteria in ANSYS. So according to (3.81), for each iteration, we need to update the tangential stiffness matrix $\mathbf{K}_{n+1}^{(i)}$ and internal force $\mathbf{I}_{n+1}^{(i)}$ by using the new tangential Young's modulus (Jacobian matrix) $\left(\frac{\partial \boldsymbol{\sigma}}{\partial \boldsymbol{\varepsilon}}\right)_{n+1}^{(i)}$ and stresses $\boldsymbol{\sigma}(\mathbf{a}_{n+1}^{(i)})$.

In order to implement the 1D SMA model into the 3D ANSYS element BEAM188 to simulate the 2D bending problem, we set the shear modulus to a large number and set the shear stresses equal to zeros such that we can use the 3D Timoshenko beam element BEAM188 approximately as a 2D Euler-Bernoulli beam element. Hence, we only need to update the tangential Young's modulus $\left(\frac{d\sigma}{d\varepsilon}\right)_{n+1}^{(i)}$and the longitudinal stress $\sigma_{n+1}^{(i)}$, which can be calculated using (3.17)

$$\sigma(\varepsilon) = \frac{E_M \left[\varepsilon - (x_+ - x_-)\varepsilon_T\right]}{x_+ + x_- + \frac{E_M}{E_A} x_A} \tag{3.82}$$

And the tangential Young's modulus is computed as

$$\frac{d\sigma}{d\varepsilon} = \frac{\partial \sigma}{\partial \varepsilon} + \frac{\partial \sigma}{\partial x_+}\frac{dx_+}{d\varepsilon} + \frac{\partial \sigma}{\partial x_-}\frac{dx_-}{d\varepsilon} \tag{3.83}$$

The important aspect with respect to the implementation of the above model is the integration of the ODEs of the phase fraction evolution (3.18)

$$\begin{aligned} \dot{x}_+ &= -x_+ p^{+A}(\sigma, T) + x_A p^{A+}(\sigma, T) \\ \dot{x}_- &= -x_- p^{-A}(\sigma, T) + x_A p^{A-}(\sigma, T) \end{aligned} \tag{3.84}$$

The system exhibits a strongly varying stiffness behavior due to the nonlinearity, is unpredictable a priori. For stability, this requires the application of an implicit integration scheme. Additionally, the scheme needs to perform an adaptive time step control in order to be independent of the size of the global finite element time step. This is called a subincrementation method, and it requires an assumption about the time dependence of strain during , which is taken to vary linearly from to ε_n to ε_{n+1}.An unconditionally stable and

very efficient code for moderate accuracy requirements is the Radau5 routine by Harrier and Wanner [**?**]. It is based on an implicit Runge-Kutta scheme (Radau IIa) and is particularly suited for stiff systems.

In order to preserve the quadratic convergence of the Newton-Raphson method, the tangent modulus needs to be computed in a manner consistent with the integration algorithm. To this purpose, we re-write the expression from (3.83), in the following manner:

$$\frac{d\sigma}{d\varepsilon} = \max\left(\frac{\partial\sigma}{\partial\varepsilon} + \frac{\partial\sigma}{\partial x_+}\frac{\dot{x}_+}{\dot{\varepsilon}} + \frac{\partial\sigma}{\partial x_-}\frac{\dot{x}_-}{\dot{\varepsilon}},\ Et_{\min}\right) \tag{3.85}$$

where the strain rate $\dot{\varepsilon}$ can be approximated as $\frac{\Delta\varepsilon}{\Delta t}$, and $\dot{x}_+$, $\dot{x}_-$can be calculated exactly at time by integrating (3.84). To avoid a zero tangential Young's modulus for the perfect single crystal SMA model in the unstable phase transition region, and to improve the convergence behavior of the FE implementation, we set the tangential Young's modulus equal to the larger of the exact expression and a cut-off value $Et_{\min}$, which will be determined later in the course of this section.

The whole ANSYS implementation using the BEAM188 element and the user defined material subroutine USERMAT can be summarized in Figure 3.85. The subroutine USERMAT is used to define the stress-strain relation, the mechanical constitutive behavior of the SMA material. During each Newton-Raphson iteration, USERMAT is called at very integration point and the phase fractions are stored as state variables at each integration point and ANSYS passes in the values of the stresses, strains, current strain increment and state variables at the beginning of the time increment. Then the USERMAT integrates the constitutive model of the SMA material to update the values of stresses, state variables and the material tangential Young's modulus $\frac{d\sigma}{d\varepsilon}$.

For ANSYS's BEAM188 element, the element output is available at element integration stations and at section integration points [72]. Each element has one integration station, and the cross section is divided by cross section cells. Each cross section cell has 2 by 2 integration points as show in Figure 3.86, each of which calculates stresses from the above 1D model. In order to capture the inhomogeneous phase transformation behavior of the SMA through the thickness of the beam cross section, we need to subdivide the cross section with a sufficiently large number of cells (layers). Note, that ANSYS automatically places a

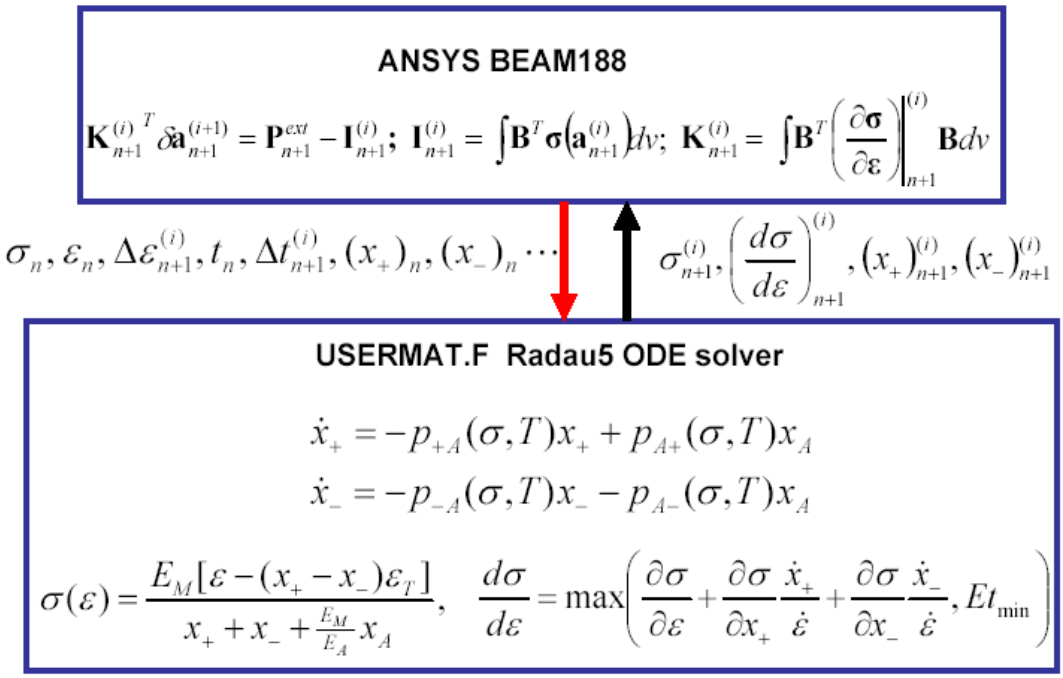


Figure 3.85: ANSYS implmentation using the element beam188 and usermat.f

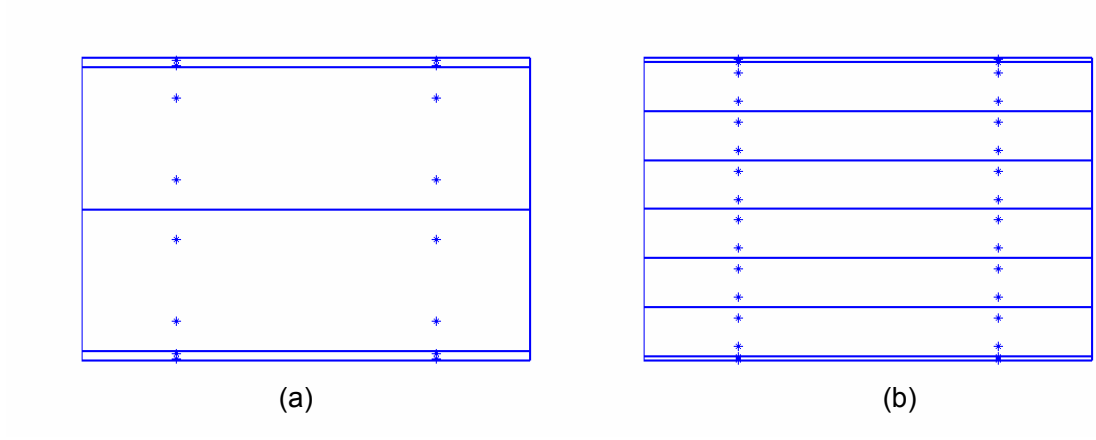


Figure 3.86: ANSYS beam section cell mesh(* - integration point): (a) 1x 4 cells; (b) 1x 8 cells.

fine cell near the top and bottom of the cross section in order to capture the onset of the transformation.

3.4.2 Parameter Study

A SMA cantilever beam is used as an example to validate the above finite element implementation and study the convergence behavior under different convergence criteria, element numbers and cross section integration points. The geometry parameters of the uniform SMA cantilever beam with rectangular cross section are: length $L = 10cm$, width $b = 1.5cm$ and height $h = 1cm$.The material parameters of the SMA material are the same as those used in the bar problems as: $E_A = 71.1GPa$, $E_M = 30.9GPa$, $\varepsilon_T = 0.044$, $\sigma_A(T_U = 353K) = 663.16MPa$, $\sigma_A(T_L = 323K) = 431.58MPa$, $\Delta\sigma = 295MPa$, volume of a layer $V_D = 5 \times 10^{-23}m^3$ and relaxation time $\tau_x = 10^{-2}s$, which are the same as before.

Implementation validation

First, to validate the FE implementation into ANSYS using BEAM188, we apply an axial loading at the free end of the cantilever beam at low temperature T = 273 K and high temperature T = 333K, respectively. Results shown in the Figure 3.87 represent the hysteresis behaviors of the SMA material at different temperatures under the uniaxial loading and match the setting of the above material parameters. Figure 3.88 shows the

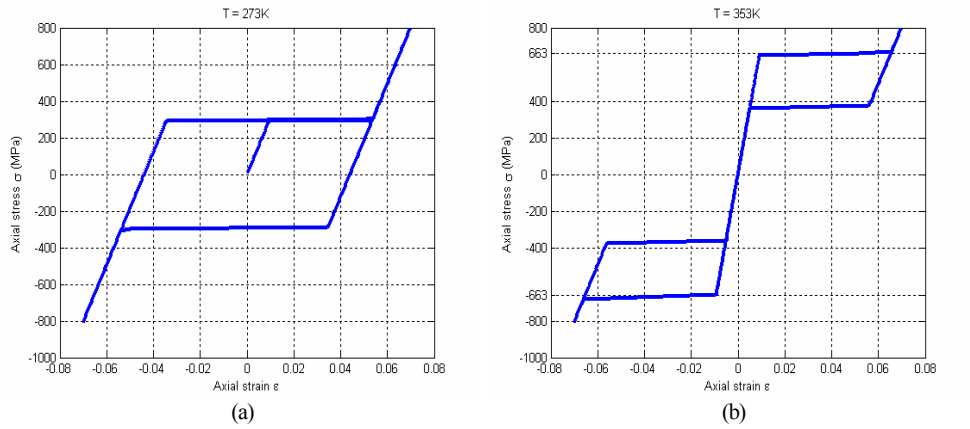


Figure 3.87: Axial loading at low and high temperatures: (a) Low temperature at $T = 273K$; (b) High temperature at $T = 353K$.

comparison between the results of ANSYS and FEMLAB implementation. The results match very well for these two different implementation schemes.

Effects of Different Convergence Criterion

After the validation of the implementation, we study the quasi-static bending behavior of the SMA cantilever beam by applying a transverse tip force F given in Figure 3.88(a) at the free end of the beam. First, we study the convergence behavior using a force convergence criterion by setting the element number $Ne = 40$, cross section cells $=1 \times 16$ and varying the substep numbers ($Nsubst$). In contrast to the axial loading case, we now observe a gradual and smooth transformation regime for the global behavior (tip force vs. tip displacement). It also exhibits a continuously increasing slope, even though the local stress-strain curve is still the box-shaped one with a horizontal plateau. This is a consequence of the inhomogeneous stress distribution in the bending case, and reflects a gradually triggered transformation along the length of the beam and through its thickness. Results in Figure 3.89, however, show that even with a very large number of substeps (> 500), we still do not obtain a reasonably converged result for both, low and high temperature cases. Compared to the results of the force control criterion, the results of the displacement control criterion in Figure 3.90 show that it requires a considerably smaller number of substeps (i.e. 40 for this specific example) to obtain a converged solution. This is due to the almost horizontal

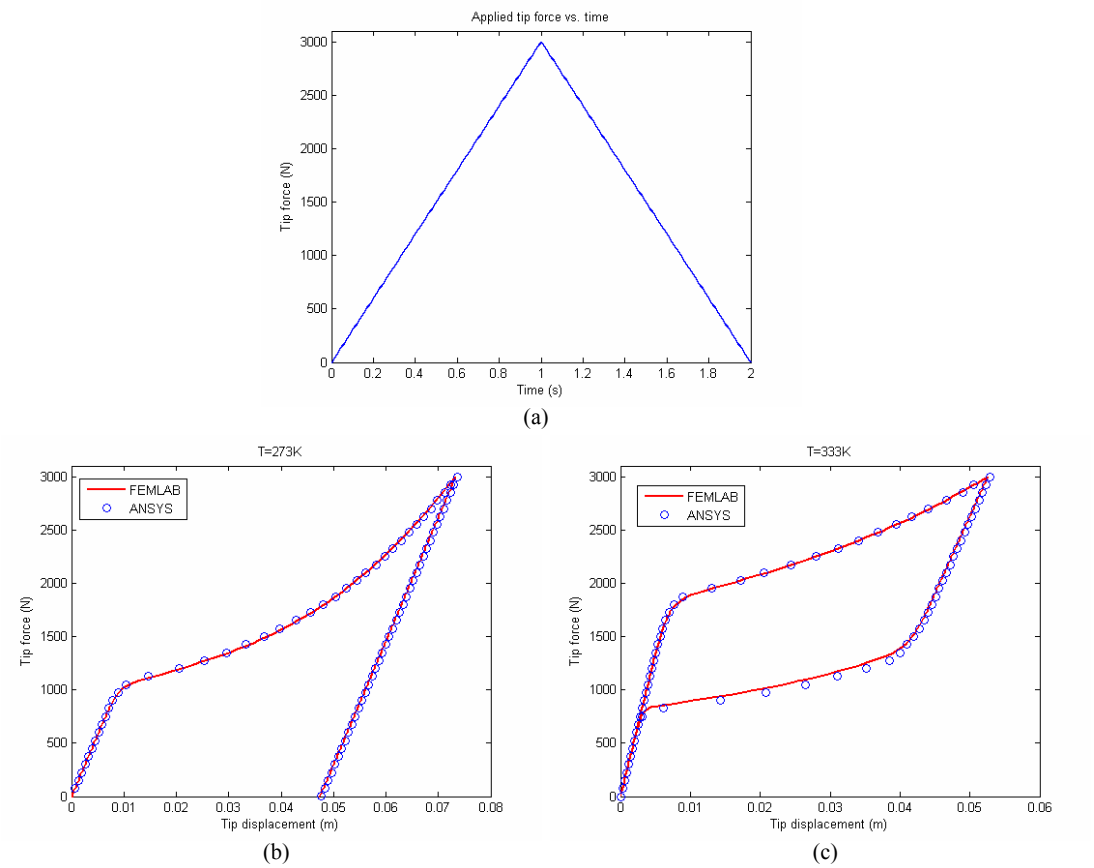


Figure 3.88: Comparison between the results of ANSYS and FEMLAB for the SMA cantilever beam bending: (a) Applied tip force vs. time; (b) force-displacement diagram at low temperature $T = 273K$; (c) force-displacement diagram at high temperature $T = 333K$.

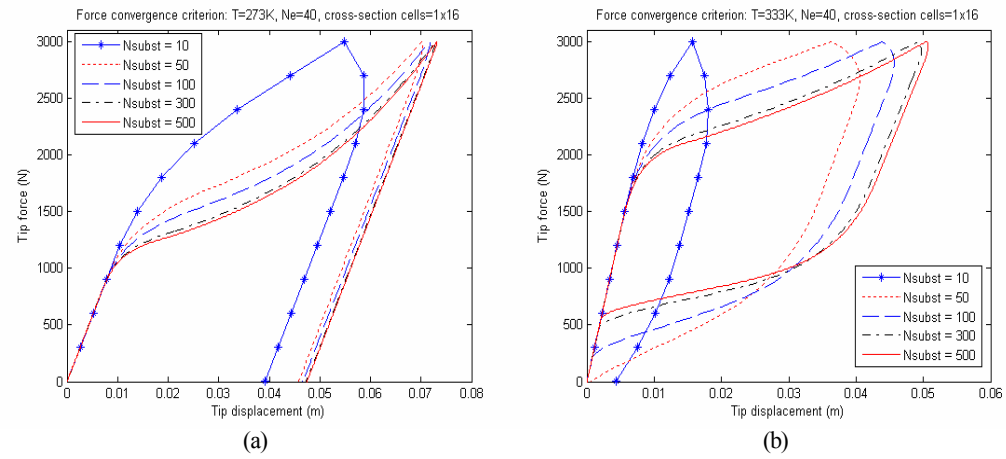


Figure 3.89: Force convergence criterion with different substeps: (a) Low temperature at $T = 273K$; (b) High temperature at $T = 333K$.

plateau in the stress-strain behavior, which makes the force very insensitive to changes in the deformation. For the SMA beam bending case, once the outer layers start to transform from M_+ to M_-, M_- to M_+ and A to M_+ or M_-, a small change in the external force could cause a large change in deformation. We thus need to choose the appropriate convergence criterion carefully and use enough substeps in order to capture the hysteresis behavior of the SMA material accurately. In all of the following cases, we use the displacement convergence criterion to study the convergence behavior as a function of several other factors, such as element number, etc.

Effects of Element Number

Using the displacement convergence criterion, setting a fixed number of substeps ($Nsubst = 40$) and a fixed number of cross section cells (1×16), we now study the convergence behavior of the bending of the SMA cantilever beam by varying the element numbers as shown in Figure 3.91. As expected, increasing the number of elements makes the beam softer, because the propagation of the phase transformation zone can be captured more accurately. For this specific case, 30 to 40 elements of equal length are needed to produce a converged solution. It would be most efficient to only increase the element density in the vicinity of the clamped end.

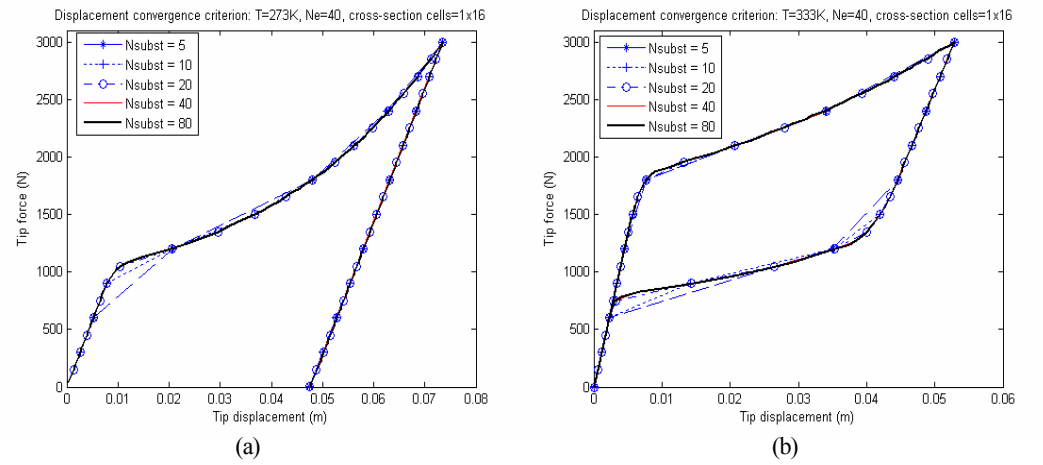


Figure 3.90: Displacement convergence criterion with different substeps: (a) Low temperature at $T = 273K$; (b) High temperature at $T = 333K$.

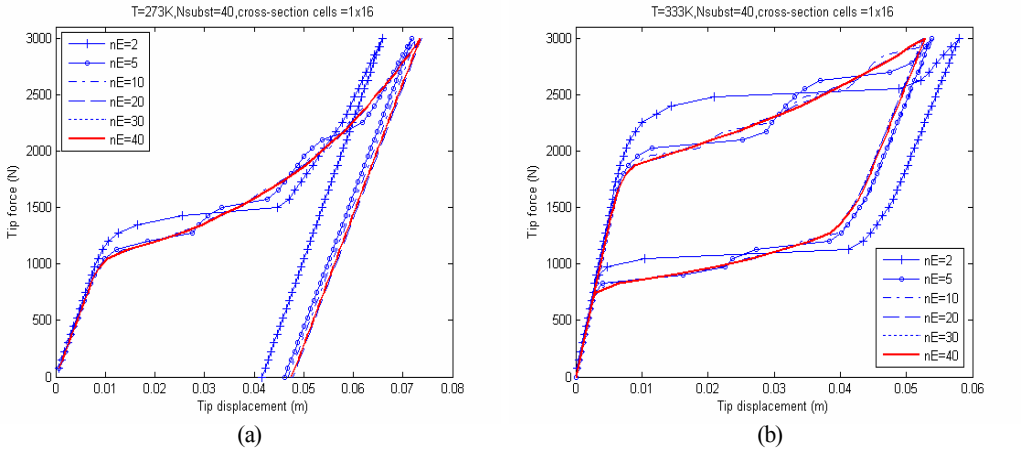


Figure 3.91: Displacement convergence criterion with different element numbers: (a) Low temperature at $T = 273K$; (b) High temperature at $T = 333K$.

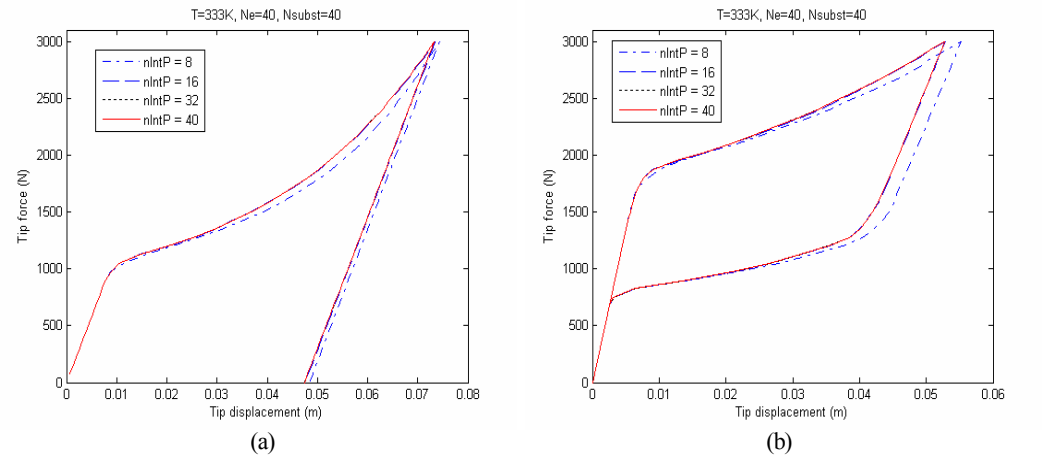


Figure 3.92: Displacement convergence criterion with different integration points: (a) Low temperature at $T = 273K$; (b) High temperature at $T = 333K$.

Effects of Integration Point Number

Another important factor in the bending of an SMA cantilever beam is the number of integration points through the thickness of the cross section. In addition to propagating longitudinally from the clamped end, the phase transformation also propagates through the thickness direction starting form the outer layers, which are always subjected to the maximum stresses. A layer will also harden again once it finishes the phase transformation as can be seen from Figure 3.87. In order to represent this inhomogeneous behavior, a sufficient number of integration points (cells) is needed. As shown in Figure 3.92, 16 integration points (8 cells with two outer thin layers) through the thickness give a converged solution for this specific case.

Effects of Cut-off Young's modulus

We also study the impact of the minimum tangential Young's modulus given in (3.85). Even though the consistent tangent modulus required by the Newton Raphson method for optimal convergence is equal to zero during the transformation phase, this would produce a singular stiffness matrix and is thus prohibited. It is even difficult to obtain a converged solution, if is non-zero but too small; but on the other hand, using too large a value for requires an excessive number of iterations to converge and is not efficient. Figure 3.93(b)

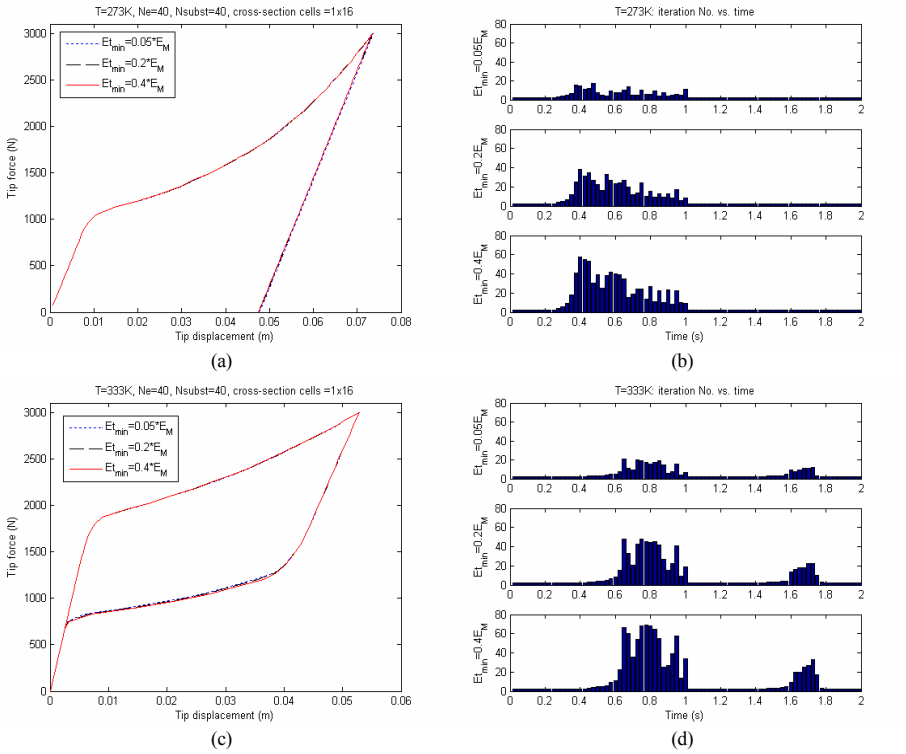


Figure 3.93: Effects of minimum cutoff tangential Young's modulus $Et_{\min}$: (a) force-displacement diagrams at low temperature at $T = 273K$; (b) iteration number vs. time at low temperature $T = 273K$; (c) force-displacement diagrams at high temperature at $T = 333K$; (d) iteration number vs. time at high temperature $T = 333K$.

and Figure 3.93(d) illustrate this behavior, both showing that the global results are not affected as indicated in Figure 3.93(a) and Figure 3.93(c).

3.5 Summary

In this chapter, finite element method is used to study the behavior of SMA components under isothermal and non-isothermal conditions, respectively. In particular, by treating the evolution equations of phase fractions as degenerated PDEs, thermo-mechanical coupled problems of the SMA components are implemented to FEMLAB gerneral form PDEs,

which are solved as fully coupled problems. The convergence behavior of the ANSYS implementation using traditional incremental finite element method is also studied systematically. The performed analyses give interesting insights about the complex responses of SMA components, and show that the proposed coupled multi-field implementation of the free energy model is an efficient tool for simulating SMA component applications.

Chapter 4

Conclusions

In the fist part of the dissertation, a modified parametrization method has been developed to model the rate dependent minor loop behaviors of the PZT materials. The parameterization model preserves the simple structure and efficiency of the original perfect single crystal model with only one ODE has to be solved. The effective barrier is parametrized as a function of the phase fraction and identified from experimental data. The robust implementation of the model in Fortran program is computationally efficient compared to the quadrature implementation of the homogenized energy model. The simulation results are also compared with experimental data. The simplified model has quantitative reproduction of outer-loop behavior and has good representation of the features of the complicated minor loop behaviors of polycrystalline PZT materials and reflects some of the rate dependent effects. The parametrized model, however, cannot represent relaxation behaviors of the PZT actuator correctly. The simulations qualitatively show the relaxation in P-E hysteresis but the relaxation of polarization is not in the same time scale of the experimental results. One possible mechanism behind this is that the 90° phase undergoes a slower reorientation process than the ±180° phases [64], and this results in a slow and asymptotic relaxation behavior of PZT actuators. Future research will be conducted to extend the two-phase parametrized model to a three-phase model by including the 90° phase.

In the second part of the dissertation, a 1-D free energy SMA model is implemented into finite element software package FEMLAB using its general PDE form by treating the evolution equations of phase fractions as degenerated PDEs coupled with the mechanical equilibrium equation and the nonlinear transient heat transfer equation. The system is

solved as a direct thermo-mechanically coupled problem. Simulation results demonstrate that the model can predict the low temperature quasiplastic and high temperature superelastic behaviors as well as shape memory effect of SMA materials. Tensile simulations of an SMA wire under different thermal boundary conditions with different loading rates are conducted to demonstrate the inhomogeneity and rate effects of the system responses, and the results are also compared to experimental data qualitatively. By including the Joule heating, the performance of an SMA wire actuator under different thermal boundary conditions is studied. For the fixed temperature boundary conditions, only the center portion of the SMA wire participates in the phase transformation and the actuation stroke is smaller compared to that of the insulated boundary condition case.

The 1-D free energy model is also implemented into FEMLAB by using the Euler-Bernoulli beam bending theory to study the inhomogeneous SMA beam bending problems under isothermal and non-isothermal conditions. The SMA beam bending problem is modeled as a system of first order PDEs and boundary conditions are implemented as Dirichlet boundary conditions. After the implementation, we present the detailed analysis of inhomogeneous bending behaviors of an SMA cantilever beam under constant temperatures. During the loading process, the phase transformations start from the outer layers at the clamped end and propagate longitudinally and transversely due to the nonuniform stress field of the beam bending. The global response of the SMA beam is characterized by gradual transitions even though the governing stress-strain relation is characterized by a sharp transition. At high temperature, the SMA beam demonstrates superelastic behavior. At low temperature, the SMA beam demonstrates quasiplastic behavior and after complete unloading, stresses through cross-sections are redistributed to satisfy the global equilibrium equation with zero cross-section moment, and this results in a complex residual stress distribution along the SMA beam.

The behavior of the SMA cantilever beam under thermo-mechanical loading is also studied. Upon cooling and heating, most part of the section above the neutral axis subjected to compression stresses transforms between austenite A and martensite M_- and most part of the section below the neutral axis subjected to tensile stress transforms between austenite A and martensite M_+, and these together consequently generate a very large deformation. Governed by the temperature-dependent stress-strain relation, stresses in the SMA beam

are redistributed to satisfy the global equilibrium equation during the cooling and heating processes. The center portion of the SMA beam has zero stress state after the transformation from austenite to martensite is finished, and under zero stress state, the center portion of the SMA beam transforms from austenite to both martensite M_+ and M_-. The outer layers below and above the neutral axis transform fully from austenite to M_+ or M_- and regain their stiffness and sustain the external applied load. It is noteworthy that the beam exhibits an extremely large deformation even for small loads during a heating/cooling cycle. This is in part due to the sharp single crystal transition at constant stress, but also the temperature dependence of the transformation stress needs to be revealed by future experimental study.

Thermo-mechanically coupled analyses is also conducted for a thin SMA cantilever beam by including the phase transformation induced the latent heats. The responses of the SMA beam strongly depend on the loading rates and thermal boundary conditions due to the temperature-dependent stress-strain relation of the SMA material, and the inhomogeneous phase transformations generate nonuniform temperature fields along the length of the SMA beam. SMA beam generates larger deformation under isothermal conditions than under non-isothermal conditions.

Finally, using the traditional incremental finite element method, the 1D free energy model is also implemented into the finite element program ANSYS using its BEAM188 element and the user defined material subroutine USERMAT, which also serves as a validation tool for the FEMLAB implementation. We study convergence behavior and accuracy for different convergence criteria in ANSYS as well as other relevant parameters such as element, substep and integration point number.

Future research will be conducted to obtain a better understanding of the physical mechanisms of the transition between the superelastic and quasiplastic region to improve the current single crystal SMA model, to extend the finite element implementation to include geometry nonlinearity and a polycrystalline SMA model as well as to study the dynamic behavior of SMA structures.

List of References

[1] P. K. Hansma, V. B. Elings, O. Marti and C. E. Bracker. Scanning tunning microscopy and atomic force microscopy: Application to biology and technology. Science, 242, pp. 209-242, 1988.

[2] D. Croft, G. Shed and S. Devasia. Creep, hysteresis, and vibration compensation for piezoactuators: Atomic force microscopy application. Journal of Dynamic Systerms, Measurement, and Control, 123, pp. 35-43, 2001.

[3] H. Jung and D. Gweon. Creep charateristics of piezoelectric actuators. Reviews of Scientific Instruments, 17, pp. 1896-1900, 2000.

[4] S. Salapaka, A. Sebastian, J. P. Cleveland and M. v. Salapaka. High bandwidth nano-positioner: A robust control approach. Reviews of Scientific Instruments, 73, pp. 3232-3241, 2002.

[5] G. Schitter, G. E. Fantner, J. H. Kindt, P. J. Thurner and P. K. Hansma. On recent developments for high-speed atomic force microscopy. Proceedings of the 2005 IEEE/ASME International Conference on Advanced Intelligent Mechatronics, pp. 261-264, Monterey, CA, USA, 24-28 July, 2005.

[6] B. Clephas. Adaptronics and Smart Structures, chapter Piezoelectric Actuators. Springer Verlag, 1999.

[7] J. Zhong, S. Seelecke, R. C. Smith and C. Buskens. Optimal control of piezoceramic actuators. Proceedings of the SPIE, Smart Structures and Materials, 5049, pp. 264-274, 2003.

[8] H. Funakubo (ed.), Shape Memory Alloys. Gordon and Breach Science Publishers, 1984.

[9] K. Otsuka and C. M. Wayman (eds.), Shape Memory Materials. Cambridge University Press, UK, 1998.

[10] T. W. Duerig, D. E. Tolomeo and M. Wholey. An overview of superelastic stent design. Min. Invas. Ther. & Allied Technol., 9, pp. 235-246,2000.

[11] T. W. Duerig, K. N. Melton and C. M. Wayman. Engineering aspects of shape memory alloys. Butterworth-Heinemann, 1990.

[12] S. Aizawa, T. Kakizawa and M. Higashino. Case studies of smart materials for civil structures. Smart Mater. Struct., 7, pp. 617-626, 1998.

[13] R. DesRoches and R. Delemont. Seismic retrofit of simply supported bridges using shape memory alloys. Eng. Struct., 24, pp325-332, 2002.

[14] M. Dolce and D. Cardone. Mechanical behavior of shape memory alloys for seismic applications: 2. Austenite NiTi wires subjected to tension. Int. J. Mech. Sci., 43, pp. 2657-2677, 2001.

[15] P. Krulevitch, A. P. Lee et al. Thin film shape memory alloy microactuators. Journal of Microelectromechanical Systems, 5, pp. 270-282, 1996.

[16] B. Winzek, S. Schmitz et al. Recent development in shape memory thin film technology. Materials Science and Engineering A, 378, pp. 40-46, 2004.

[17] Y. Q. Fu, H. J. Du et al. TiNi-based thin films in MEMS applications: a review. Sensors and Actuators A, 112, pp. 395-408, 2004.

[18] M. Kohl, B. Krevet and B. Just. SMA microgripper system. Sensors and actuators A, 97-98, pp. 646-652, 2002.

[19] M. Kohl, Y. Liu et al. SMA microactuators for microvalve applications. J. Phys. IV France, 115, pp. 333-342, 2004.

[20] M. Kohl, D. Brugger, M Ohtsuka and T. Takagi. A novel actuation mechanism on the basis of ferromagnetic SMA thin films. Sensors and Actuators A, 114, pp. 445-450, 2004.

[21] W. L. Benard, H. Kahn et al. Thin film shape memory alloy actuated micropumps. Journal of mircoelectromechanical systems, 7, pp.245-251, 1998.

[22] M. Achenbach and I. Muller. Simulation of material behavior of alloys with shape memory. Arch Mech, 37, pp. 573-585, 1985.

[23] M. Achenbach. A model for an alloy with shape memory. Int. J. Plast., 5, pp.371-395, 1989.

[24] S. Seelecke and I. Muller. Shape memory alloy actuators in smart structures-modeling and simulation. ASME Applied Mechanics Reviews, 57, pp. 23-46, 2004.

[25] R. C. Smith, S. Seelecke, Z. Ounaies, and J. Smith. A free energy model for hysteresis in ferroelectric materials. Journal of Intelligent material systems and structures, 14, pp. 719-739, 2003.

[26] M. Omura, H.Adachi and Y, Ishibashi. Simulations of ferroelectric charateristics using a one-dimensional lattice model. Japanese Journal of Applied Physics,30, 2384-2387, 1991.

[27] P. Ge and M. Jouaneh. Modeling hysteresis in piezoceramic actuators. Precision Engineering, 17, 211-221, 1995.

[28] G. Robert, D. Damjanovic and N. Setter. Preisach modeling of piezoelectric nonlinearity in ferroelectric ceramics. Journal of Applied Physics, 89, 5067-5074, 2001.

[29] I. D. Mayergoyz. Mathematical Models of Hysteresis and their Applications, 2nd Edition. Academic Press, 2003.

[30] W. Chen and C. S. Lynch. A model for simulating polarization switching and AF-F phase changes in ferroelectric ceramics. Journal of Intelligent Material Systems and Structures, 9, pp. 427-431, 1998.

[31] R. C. Smith and C. L. Hom. Domain wall theroy for ferroelectric hysteresis. Journal of Intelligent Material Systems and Structures, 10, pp.195-213, 1999.

[32] R. C. Smith and Z. Ounaies. A domain wall model for hysteresis in piezoelectric materials. Journal of Intelligent Material Systems and Structures, 11, pp. 62-79, 2000.

[33] R. C. Smith, S. Seelecke, M. Dapino and Z. Ounaies. A unified framework for modeling hysteresis in ferroic materials. Journal of the Mechanics and Physics of Solids, 54, pp. 46-85, 2006.

[34] T. R. Braun and R. C. Smith. Efficient implementation algorithms for homogenized energy models. Continumm Mechanics and Thermodynamics, 18, pp. 137-155, 2006.

[35] R. C. Smith, A. G. Hatch, B. Mukherjee and S. Liu. A homogenized energy model for hysteresis in ferroelectric materials: general density formulation. Journal of Intelligent Material Systems and Structures, 16, pp. 713-732, 2005.

[36] R. C. Smith. Smart Material Systems: Model Development. SIAM, 2005.

[37] K. Tanaka and S. NagaKi. A thermomechanical description of materials with internal variables in the process of phase transition. Ingenieur Archiv Arch Appl Mech, 51, pp. 287-299, 1982.

[38] K. Tanaka. A thermomechanical sketch of shape memory effect: one-dimensional tensile behavior. Res Mech, 18, pp. 251-263, 1986.

[39] K. Tanaka, S. Kobayashi and Y. Sato. Thermomechanics of transformation, pseudoelasticity and shape memory effect in alloys. Int. J. Plast, 2, pp. 59-72.

[40] C. Liang and C. A. Rogers. One-dimensional thermomechanical constitutive relations for shape memory materials. Journal of Intelligent Material Systerms and Structures, 1, pp. 207-234, 1990.

[41] L. C. Brinson. One-dimentional constitutive behavior of shape memory alloys: thermomechanical derivation with non-constant material functions and redefined martensite internal variable. Journal of Intelligent Material Systerms and Structures, 4, pp. 229-242, 1993.

[42] A. Bekker and L. C. Brinson. Temperature-induced phase transformation in a shape memory alloy: phase diagram based kenetics approach. Journal of the Mechanics and Physics of Solids, 45, pp. 946-988, 1997.

[43] A. Bekker and L. C. Brinson. Phase diagram based description of the hysteresis behavior of shape memory alloys. Acta Mater., 46, pp. 3649-3665, 1998.

[44] J. G. Boyd and D. C. Lagoudas. Thermomechanical response of shape memory composites. Journal of Intelligent Material Systerms and Structures, 5, pp. 333-346, 1994.

[45] F. Auricchio and R. Taylor. Shape memory alloys: modeling and numerical simulations of the finite-strain superelastic behavior. Computer Methods in Applied Mechanics and Engineering, 143, pp. 175-194, 1997.

[46] Z. K. Lu and G. J. Weng. A self-consistent model for the stress-strain behavior of shape memory alloy polycrystal. Acta Metall., 46, pp. 5423-5433, 1998.

[47] E. Patoor, A. Eberhardt and M. Berveiller. Micromechanical modeling of the superelasticity in shape memory alloys. J. Phys. IV, 6, C1-277-292, 1996.

[48] X. Gao and L. C. Brinson. A simplified multivariant SMA model based on invariant plane nature of martensitic transformation. Journal of Intelligent Material Systerms and Structures, 13, pp. 795-810, 2002.

[49] M. Brocca, L. C. Brinson and Z. P. Bazant. Three-dimentional constitutive model for shape memory alloys based on microplane model. J. Mech. Phys. Solids, 50, pp. 1051-1077,2002.

[50] Y. Ivshin and T. J. Pence. A constitutive model for hysterestic phase transition behavior. Int J Eng Sci.,32, pp. 681-704, 1994.

[51] Y. Ivshin and T. J. Pence. A thermomechanical model for a one variant shape memory material. Journal of Intelligent Material Systems and Structures, 5, pp. 455-473.

[52] X. C. Wu and T. J. Pence. Two variant modeling of shape memory materials: unfolding a phase diagram triple point. Journal of Intelligent Material Systems and Structures, 9, pp. 335 - 354, 1998.

[53] J. A. Shaw. A thermomechanical model for a 1-D shape memory alloy wire with propagating instabilities. Int. J. Solids Struct., 39, pp. 1275-1305, 2002.

[54] L. C. Brinson and R. Lammering. Finite element analysis of the behavior of shape memory alloys and their applications. Int. J. Solids Structures, 30, pp. 3261-3280, 1993.

[55] F. Auricchio and E. Sacco. A temperature-dependent beam for shape memory alloys: constitutive modelling, finite element implemenation and numerical simulations. Comput. Methods Appl. Mech. Engrg., 174, pp. 171-190, 1999.

[56] F. Auricchio. A robust integration-algorithm for a finite-strain shape-memory-alloy superelastic model. International Journal of Plasticity, 17, pp. 971-990, 2001.

[57] F. Trochu and Y. Qian. Nonlinear finite element simulation of superelastic shape memory alloy parts. Computers and Structures, 62, pp. 799-810, 1997.

[58] M. A. Qidwai and D. C. Lagoudas. Numerical implementation of a shape memory alloy thermomechanics constitutive model using return mapping algorithms. Int. J. Numer. Meth. Eng., 47, pp. 1123-1168, 2000.

[59] D. C. Lagoudas, K. Ravi-Chandar, K. Sarh and P. Popov. Dynamic loading of polycrystalline shape memory alloy rods. Mechanics of Materials, 35, pp. 689-716, 2003.

[60] B. Peultier, T. B. Zineb and E. Patoor. Macroscopic constitutive law of shape memory alloy thermomechanical behavior. Application to structure application by FEM. Mechanics of Materials, 38, pp. 510-524, 2006.

[61] J. J. Amalraj, A Bhattacharyya and M. G. Faulkner. Finite-element modeling of phase transformation in shape memory alloy wires with variable material properties. Smart Mater. Struct., 9, pp. 622-631, 2000.

[62] B. Krevet and M. Kohl. Finite element simulation of SMA microactuators with large deflection. J. Phys. IV France, 115, pp. 365-373, 2004.

[63] J. H. Zhong. Modeling and Control of Piezoceramic Actuators for Nanopositioning. Master thesis, NC State University, Department of Mechanical and Aerospace Engineering, 2003.

[64] A. York. Experimental investigation of rate-dependent inner hysteresis loops in PZT. Master thesis, NC State University, Department of Mechanical and Aerospace Engineering, 2005.

[65] J. E. Massad and R. C. Smith. A homogenized free energy model for hysteresis in thin-film shape memory alloys. Thin Solid Films, 489, pp. 266-290, 2005.

[66] FEMLAB help documentation, COMSOL Inc.

[67] M. N. Sadiku. Elements of Electromagnetics. 3rd edition, Oxford University Press, Inc., 2001.

[68] J. A. Shaw, B. C. Chang, M. A. Iadicola and Y. M. Leroy. Thermodynamics of a 1-D shape memory alloy: modeling, experiments, and application. Proceedings of the SPIE 10th Annual International Symposium on Smart Structures and Materials. San Diego, CA, 2-6 March, 2003.

[69] B. C. Chang, J. A. Shaw and M. A. Iadicola. Thermodynamics of shape memory alloy wire: modeling, experiments, and application. Continumm Mechanics and Thermodynamics, 8, pp. 83-118, 2006.

[70] O. C. Zienkiewicz and R. L. Taylor. The finite element method. 4th edition, vol. 2, McGraw-Hill, 1989.

[71] E. Harrier and G. Wanner. Solving ordinary differential equations II: stiff and differential-algebraic Problems. Springer Verlag, 1991.

[72] ANSYS version 9.0 help documentation, ANSYS Inc.